Theory of resonant light-matter interactions in nanophotonic sensing

Steffen Both

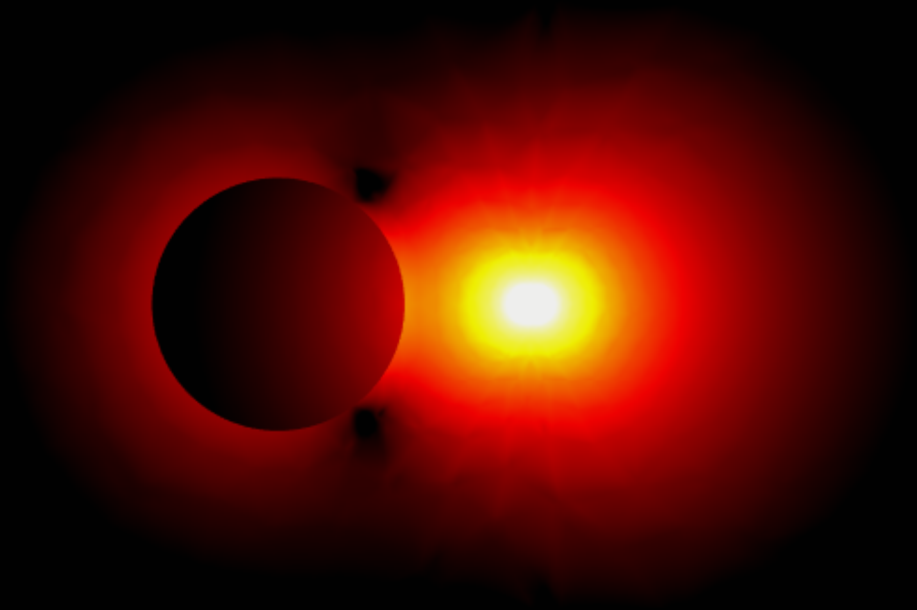

University of Stuttgart
2022

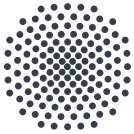

Universität Stuttgart

Theory of resonant light-matter interactions in nanophotonic sensing

Von der Fakultät Mathematik und Physik
der Universität Stuttgart zur Erlangung der Würde
eines Doktors der Naturwissenschaften (Dr. rer. nat.)
genehmigte Abhandlung

vorgelegt von

Steffen Both

aus Königheim

Hauptberichter:	Prof. Dr. Thomas Weiss
Mitberichter:	Prof. Dr. Eric Lutz
Mitberichter:	Prof. Dr. Carsten Rockstuhl
Prüfungsvorsitzender:	Prof. Dr. Sebastian Loth

Tag der mündlichen Prüfung: 25.07.2022

4. Physikalisches Institut der Universität Stuttgart
2022

Steffen Both: *Theory of resonant light-matter interactions in nanophotonic sensing*, 2022

CONTENTS

ABSTRACT

Detecting and analyzing substances is of crucial relevance in numerous areas of our modern lives, including industrial process control, environmental monitoring, forensic science, and medical diagnostics. Many of the above-indicated applications would drastically benefit from improving the sensitivities compared to what is currently achievable by conventional sensing approaches. In this context, a promising technique that is experiencing rapidly increasing interest in recent times is nanophotonic sensing. The idea is to exploit the strong light-matter interactions that can occur in nanophotonic resonators to realize optical sensing schemes with extremely high sensitivities. The approach has proven to be highly useful for the detection of gases, biomolecules, and much more. It also has been demonstrated that one can utilize this scheme for the analysis of specific molecular properties, such as chirality. Countless kinds of nanophotonic platforms have been and are investigated, including numerous types of plasmonic nanostructures, photonic crystals, dielectric resonators, etc.

With the increasing popularity of nanophotonic sensing techniques, it becomes more and more important to have a solid understanding of the involved light-matter interactions. This is not only relevant for designing and optimizing such systems, but also for interpreting optical signals, as well as for the development of new sensing applications. In this thesis, we present a thorough theoretical description of the involved light-matter interactions. In particular, we approach the problem via the concept of resonant states, which denote a specific subset of eigensolutions of Maxwell's equations and provide a physically meaningful basis to describe resonant optical phenomena.

We start by explaining how resonant states are defined and provide a detailed overview from literature on how they can be used to model all sorts of light-matter interactions. Then, we explain that in most sensing scenarios, one is dealing with small material changes in an initial system and thus, a natural theoretical approach consists in the use of perturbation theories. While literature already provides a simple perturbation theory that allows for predicting resonance shifts under local material variations, this theory is only valid for variations inside a given resonator geometry. However, there

are many sensing applications where changes in the resonator's surrounding are relevant. Consequently, we present an extended theory that is capable of handling these kinds of changes. Afterwards, we explain that resonance shifts are not the only effects that can be important in nanophotonic sensing. In order to have a more general description, we derive a perturbation theory that allows for predicting the change of optical far-field spectra. We apply the theory to many example systems and demonstrate that it allows us to gain deep fundamental insights in the heart of the light-matter interactions. In this context, we also extensively discuss a very specific application, which is experiencing a lot of attention lately: nanophotonic chiral sensing. We use our theory to clarify the involved enhancement mechanisms and reveal a surprising finding concerning the relevance of frequency shifts. Furthermore, we explain that the perturbative approach has many practical benefits for sensor modeling in terms of computational efficiency.

Finally, we unveil that substance detection and characterization are not the only nanophotonic sensing applications. Instead, one can also exploit nanophotonic approaches to track motions on the nanoscale. This motion sensing is based on the interaction between nanostructures and quantum emitters. While the idea of exploiting the above interaction for the manipulation of quantum emitters has become extremely popular in recent years, the motion-sensing application is less well-known. We provide a detailed theoretical model of the underlying light-matter interaction and employ it to describe and elucidate observations from experiments on DNA-based molecular nanodevices. Furthermore, we show that by combining the model of the light-matter interactions with a kinetic model of chemical reactions, one can obtain deep insights into the dynamics of such nanosystems. In the end, we shortly discuss the inclusion of another effect into the equations, known as Förster resonance energy transfer, and investigate a complex nanosystem where both effects (Förster resonance energy transfer and emitter-nanostructure interactions) are occurring simultaneously.

DEUTSCHE ZUSAMMENFASSUNG

Die Detektion und Analyse von Substanzen ist in zahlreichen Bereichen unseres modernen Lebens von entscheidender Bedeutung, z. B. in der industriellen Prozesskontrolle, der Umweltbeobachtung, der Forensik und der medizinischen Diagnostik. Viele der oben genannten Anwendungen würden von einer drastischen Verbesserung der Sensitivität im Vergleich zu dem, was derzeit mit konventionellen Ansätzen möglich ist, profitieren. Eine vielversprechende Technik, die in letzter Zeit große Beachtung findet, ist in diesem Zusammenhang die nanophotonische Sensorik. Die Grundidee besteht darin, die starken Licht-Materie-Wechselwirkungen, die in nanophotonischen Resonatoren auftreten können, auszunutzen, um optische Messverfahren mit extrem hoher Sensitivität zu realisieren. Dieser Ansatz hat sich als äußerst nützlich für den Nachweis von Gasen, Biomolekülen und vielem mehr erwiesen. Es wurde auch gezeigt, dass dieses Verfahren für die Analyse spezifischer Moleküleigenschaften, wie z. B. der Chiralität, eingesetzt werden kann. Unzählige Arten von nanophotonischen Plattformen wurden und werden untersucht, darunter zahlreiche Arten von plasmonischen Nanostrukturen, photonischen Kristallen, dielektrischen Resonatoren usw.

Mit der zunehmenden Popularität nanophotonischer Sensortechniken wird es immer wichtiger, die zugrundeliegenden Licht-Materie-Wechselwirkungen gut zu verstehen. Dies ist nicht nur für den Entwurf und die Optimierung solcher Systeme von Bedeutung, sondern auch für die Interpretation optischer Signale sowie für die Entwicklung neuer Sensoranwendungen. In dieser Arbeit präsentieren wir eine gründliche theoretische Beschreibung der zugrundeliegenden Licht-Materie-Wechselwirkungen. Im Besonderen gehen wir das Problem über das Konzept der sogenannten Resonanzzustände an. Diese stellen eine spezielle Untermenge von Eigenlösungen der Maxwellschen Gleichungen dar und bieten eine physikalisch sinnvolle Basis für die Beschreibung resonanter optischer Phänomene.

Zunächst erläutern wir, wie Resonanzzustände definiert sind, und liefern einen ausführlichen Literaturüberblick, wie diese zur Modellierung aller möglicher Arten von Licht-Materie-Wechselwirkungen verwendet werden

können. Dann erklären wir, dass man es bei den meisten Sensoranwendungen mit kleinen Materialänderungen in einem Ausgangssystem zu tun hat und daher ein natürlicher Beschreibungsansatz in der Verwendung von Störungstheorien besteht. Zwar gibt es in der Literatur bereits eine einfache Störungstheorie, mit der sich Resonanzverschiebungen bei lokalen Materialänderungen vorhersagen lassen, doch gilt diese Theorie nur für Änderungen innerhalb der vorgegebenen Resonatorgeometrie. Es existieren jedoch viele Anwendungen in der Sensorik, bei denen Änderungen in der Umgebung des Resonators von Bedeutung sind. Aus diesem Grund stellen wir eine erweiterte Theorie vor, die diese Art von Veränderungen mitberücksichtigen kann. Anschließend erläutern wir, dass Resonanzverschiebungen nicht die einzigen Effekte sind, die in der nanophotonischen Sensorik von Bedeutung sein können. Um eine allgemeinere Beschreibung zu erhalten, leiten wir eine Störungstheorie für die Änderung von optischen Fernfeldspektren her. Wir wenden die Theorie auf viele Beispielsysteme an und zeigen, dass sie tiefe fundamentale Einblicke in die Licht-Materie-Wechselwirkungen ermöglicht. In diesem Zusammenhang diskutieren wir auch ausführlich eine sehr spezifische Anwendung, die in letzter Zeit viel Aufmerksamkeit erfährt: die nanophotonische chirale Sensorik. Wir nutzen unsere Theorie, um die beteiligten Signalverstärkungsmechanismen aufzuklären und zeigen ein überraschendes Ergebnis hinsichtlich der Relevanz von Frequenzverschiebungen auf. Darüber hinaus erklären wir, dass der störungstheoretische Ansatz viele praktische Vorteile für die Sensormodellierung hinsichtlich der Recheneffizienz hat.

Schließlich erläutern wir, dass die Detektion und Charakterisierung von Substanzen nicht die einzigen nanophotonischen Sensoranwendungen sind. Stattdessen kann man nanophotonische Ansätze auch nutzen, um Bewegungen auf der Nanoskala zu verfolgen. Diese Bewegungserfassung basiert auf der Wechselwirkung zwischen Nanostrukturen und Quantenemittern. Während die Idee, diese Wechselwirkung für die Manipulation von Quantenemittern auszunutzen, in den letzten Jahren große Popularität erreicht hat, ist ihre Anwendung zur Bewegungsverfolgung weniger bekannt. Wir stellen ein detailliertes theoretisches Modell der zugrundeliegenden Licht-Materie-Wechselwirkung vor und wenden dieses an, um Beobachtungen aus Experimenten an DNA-basierten molekularen Nanobauteilen zu beschreiben und zu erläutern. Darüber hinaus zeigen wir, dass man durch die Kombination des Modells der Licht-Materie-Wechselwirkung mit einem kinetischen Modell chemischer Reaktionen tiefe Einblicke in die Dynamik solcher Nanosysteme gewinnen kann. Abschließend erörtern wir kurz, wie

man einen weiteren Effekt in die Gleichungen miteinbeziehen kann, bekannt als Förster-Resonanzenergietransfer, und untersuchen ein komplexes Nanosystem, in dem beide Effekte (Förster-Resonanzenergietransfer und Emitter-Nanostruktur Wechselwirkungen) gleichzeitig auftreten.

PUBLICATIONS

Parts of this thesis and associated work have been published in scientific journals, have been submitted to a journal, are being prepared for publication, and/or have been presented at national and international conferences.

JOURNAL PUBLICATIONS

[P1] M. J. Urban, S. Both, C. Zhou, A. Kuzyk, K. Lindfors, T. Weiss, and N. Liu: *Gold nanocrystal-mediated sliding of doublet DNA origami filaments.* Nature Communications **9**, 1454 (2018).
DOI 10.1038/s41467-018-03882-w.

[P2] L. Xin, M. Lu, S. Both, M. Pfeiffer, M. J. Urban, C. Zhou, H. Yan, T. Weiss, N. Liu, and K. Lindfors: *Watching a single fluorophore molecule walk into a plasmonic hotspot.* ACS Photonics **6**, 985-993 (2019).
DOI 10.1021/acsphotonics.8b01737.

[P3] P. Zhan, M. J. Urban, S. Both, X. Duan, A. Kuzyk, T. Weiss, and N. Liu: *DNA-assembled nanoarchitectures with multiple components in regulated and coordinated motion.* Science Advances **5**, eaax6023 (2019).
DOI 10.1126/sciadv.aax6023.

[P4] P. Zhan, S. Both, T. Weiss, and N. Liu: *DNA-assembled multilayer sliding nanosystems.* Nano Letters **19**, 6385–6390 (2019).
DOI 10.1021/acs.nanolett.9b02565.

[P5] S. Both and T. Weiss: *First-order perturbation theory for changes in the surrounding of open optical resonators.* Optics Letters **44**, 5917–5920 (2019).
DOI 10.1364/OL.44.005917.

[P6] S. Both, M. Schäferling, F. Sterl, E. A. Muljarov, H. Giessen, and T. Weiss: *Nanophotonic chiral sensing: How does it actually work?* ACS Nano **16**, 2822–2832 (2022).
DOI 10.1021/acsnano.1c09796.

[P7] S. Both and T. Weiss: *Resonant states and their role in nanophotonics.* Semiconductor Science and Technology **1**, 013002 (2022).
DOI 10.1088/1361-6641/ac3290.

[P8] A. Peil, L. Xin, S. Both, L. Shen, Y. Ke, T Weiss, P. Zhan, and N. Liu: *DNA assembly of modular components into a rotary nanodevice.* ACS Nano **16**, 5284–5291 (2022).
DOI 10.1021/acsnano.1c10160.

PUBLICATIONS NOT DIRECTLY PART OF THIS THESIS

[P9] F. Sterl, N. Strohfeldt, S. Both, E. Herkert, T. Weiss, and H. Giessen: *Design principles for sensitivity optimization in plasmonic hydrogen sensors.* ACS Sensors **5**, 917–927 (2020).
DOI 10.1021/acssensors.9b02436.

[P10] T. Herzog, S. Böhrkircher, S. Both, M. Fischer, R. Sittig, M. Jetter, S. L. Portalupi, T. Weiss, and P. Michler: *Realization of a tunable fiber-based double cavity system.* Physical Review B **102**, 235306 (2020).
DOI 10.1103/PhysRevB.102.235306.

[P11] B. Jang, J. Gargiulo, J. Kim, J. Bürger, S. Both, H. Lehmann, T. Wieduwilt, T. Weiss, S. A. Maier, and M. A. Schmidt: *Fiber-integrated hollow-core light cage for gas spectroscopy.* APL Photonics **6**, 061301 (2021).
DOI 10.1063/5.0048501.

[P12] F. Sterl, E. Herkert, S. Both, T. Weiss, and H. Giessen: *Shaping the color and angular appearance of plasmonic metasurfaces with tailored disorder.* ACS Nano **15**, 10318–10327 (2021).
DOI 10.1021/acsnano.1c02538.

[P13] E. Herkert, F. Sterl, S. Both, T. Weiss, and H. Giessen: *The influence of structural disorder on plasmonic metasurfaces and their colors.* In preparation.

[P14] M. Hentschel, K. Koshelev, F. Sterl, S. Both, J. Karst, L. Shamsafar, T. Weiss, Y. Kivshar, and H. Giessen: *Dielectric Mie voids: Confining light in air.* Submitted (2022).
Preprint https://arxiv.org/abs/2205.07729.

[C1] S. Both, M. J. Urban, K. Lindfors, T. Weiss, and N. Liu: *Coupling of quantum emitters to plasmonic nanostructures in functional devices built from DNA*. Spring Meeting of the German Physical Society (DPG), Erlangen, Germany, 2018. Oral presentation.

[C2] S. Both, M. J. Urban, K. Lindfors, N. Liu, and T. Weiss: *Coupling of quantum emitters to plasmonic nanostructures in functional devices built from DNA*. The 7th International Topical Meeting on Nanophotonics and Metamaterials (NanoMeta), Seefeld, Austria, 2019. Oral presentation.

[C3] S. Both and T. Weiss: *First-order perturbation theory for material changes in the surrounding of open optical resonators*. Spring Meeting of the German Physical Society (DPG), Regensburg, Germany, 2019. Oral presentation.

[C4] S. Both and T. Weiss: *First-order perturbation theory for material changes in the surrounding of open optical resonators*. The 27th International Workshop on Optical Wave and Waveguide Theory and Numerical Modelling (OWTNM), Málaga, Spain, 2019. Oral presentation.

[C5] S. Both and T. Weiss: *First-order perturbation theory for material changes in the surrounding of open optical resonators*. The 14th International Conference on Mathematical and Numerical Aspects of Wave Propagation (WAVES), Vienna, Austria, 2019. Oral presentation.

[C6] S. Both and T. Weiss: *Modal expansion for chiral materials*. Recent Advances in Modal Expansions for Nanophotonic Systems, online symposium, 2020. Invited oral presentation.

[C7] S. Both, H. Giessen, and T. Weiss: *Nanophotonic chiral Sensing: How does it actually work?* Conference on Lasers and Electro-Optics (CLEO). Online conference, 2021. Oral presentation.

[C8] F. Sterl, T. Weiss, S. Both, and H. Giessen: *Tuning the visual appearance of plasmonic metasurfaces by controlled disorder.* Spring Meeting of the German Physical Society (DPG), Berlin, Germany, 2018. Oral presentation.

[C9] F. Sterl, T. Weiss, E. Herkert, S. Both, and H. Giessen: *Fourier-space spectroscopy of disordered plasmonic metasurfaces.* Materials Research Society (MRS) Fall Meeting, Boston, Massachusetts, USA, 2018. Oral presentation.

[C10] F. Sterl, E. Herkert, S. Both, T. Weiss, and H. Giessen: *Quantifying the optical properties of disordered plasmonic metasurfaces by Fourier-space microspectroscopy.* The 7th International Topical Meeting on Nanophotonics and Metamaterials (NanoMeta), Seefeld, Austria, 2019. Poster presentation.

[C11] M. Fischer, T. Herzog, S. Böhrkircher, S. Both, M. Jetter, S. L. Portalupi, T. Weiss, and P. Michler: *Improving the Purcell-enhancement for InAs-QDs in Fabry-Perot fiber-microcavities.* Spring Meeting of the German Physical Society (DPG), Regensburg, Germany, 2019. Poster presentation.

[C12] L. Xin, M. Lu, S. Both, M. Pfeiffer, M. J. Urban, C Zhou, H. Yan, T. Weiss, N. Liu, and K. Lindfors: *Watching a single fluorophore molecule walk into a plasmonic hotspot.* Spring Meeting of the German Physical Society (DPG), Regensburg, Germany, 2019. Oral presentation.

[C13] E. Herkert, F. Sterl, S. Both, T. Weiss, and H. Giessen: *Revealing the influence of structural disorder in plasmonic systems.* Spring Meeting of the German Physical Society (DPG), Regensburg, Germany, 2019. Oral presentation.

[C14] F. Sterl, E. Herkert, S. Both, T. Weiss, and H. Giessen: *Fourier microspectroscopy of disordered plasmonic metasurfaces.* AMOLF nanophotonics summer school, Amsterdam, The Netherlands, 2019. Poster presentation.

[C15] F. Sterl, E. Herkert, S. Both, T. Weiss, and H. Giessen: *Fourier microspectroscopy of disordered plasmonic metasurfaces.* Disordered Materials conference (DisoMAT), Potsdam, Germany, 2019. Oral presentation.

[C16] E. Herkert, F. Sterl, S. Both, T. Weiss, and H. Giessen: *Computing the influence of disorder in plasmonic metasurfaces.* London Plasmonics Forum, King's College London, UK, 2019. Poster presentation.

[C17] S. Both, E. A. Muljarov, and T. Weiss: *Nanophotonic chiral sensing: How does it actually work?*. The 12$^{\text{th}}$ International Conference on Metamaterials, Photonic Crystals and Plasmonics (META), Torremolinos, Spain, 2022, Oral presentation.

ABBREVIATIONS

TECHNICAL ABBREVIATIONS

C	Optical chirality
CD	Circular dichroism
FRET	Förster resonance energy transfer
TE	Transverse electric
TM	Transverse magnetic

SYMBOLS

c	Speed of light in vacuum
ε, μ	Permittivity and permeability
ξ, ζ	Bi-anisotropic contributions
κ	Pasteur parameter
$\mathbf{r}$	Position vector
t	Time
$\hbar$	Reduced Planck constant
ω	Angular frequency
k	Vacuum wavenumber
$\mathbf{E}$	Electric field
$\mathbf{H}$	Magnetic field
$\mathbf{J}_{\mathrm{E}}$	Generalized electric current
$\mathbf{J}_{\mathrm{H}}$	Generalized magnetic current
$\mathbb{F}$	Fields supervector
$\mathbb{J}$	Currents supervector
$\hat{\mathbb{P}}$	Material operator
$\hat{\mathbb{D}}$	Generalized curl operator

$\hat{\mathbb{M}}$	Maxwell operator
$\hat{\mathbb{G}}$	Green's dyadic
$\mathbb{I}$	Incoming basis function
$\mathbb{O}$	Outgoing basis function
Λ	Perturbation parameter
γ_{fl}	Fluorescence rate
γ_{exc}	Excitation rate
γ_{r}	Radiative decay rate
γ_{nr}	Internal nonradiative decay rate
γ_{abs}	Rate of energy absorption
τ	Fluorescence lifetime
q	Quantum yield
γ_{FRET}	FRET rate
q_{FRET}	FRET efficiency

1

INTRODUCTION

As written in the abstract, detecting and analyzing substances is of crucial relevance in numerous areas of our modern lives, including industrial process control, environmental monitoring, forensic science, and medical diagnostics. One can, for instance, think of the chemical company that needs to monitor the presence of potentially harmful or explosive gases in its production plants or of the Diabetes patient who needs to regularly determine his or her blood-sugar concentration.

In many cases, it is highly practical to carry out the detection optically, i.e., to utilize the interaction of the analyte substance with light in order to gain information about its nature or chemical composition. Depending on the application, there are several benefits of optical measurements [1–3]: They are typically very fast, cheap, reliable, easy to handle, and they usually do not alter the chemical composition of the analyte substance. In some scenarios, there exist even further specific advantages: For example when dealing with explosive gases, it is preferable to use purely optical read-out schemes in order to avoid any direct contact of the gas with electronic circuits, as this could induce sparking [4].

A lot of optical sensing applications are, however, hampered by the often intrinsically high detection limits of conventional approaches. A way to dramatically decrease the detection limits consists in the utilization of nanophotonic resonators in order to enhance the underlying light-matter interactions [5]. A typical example scheme for this kind of nanophotonic substance sensing is displayed in Fig. 1.1. The starting point is a resonant nanophotonic structure that can be brought in contact with the analyte substance. As an example, we depict an array of metallic nanoantennas that is covered by an analyte solution. The optical response of the nanophotonic

structure is probed before and after adding the analyte. In the example, the transmittance of the system is measured.

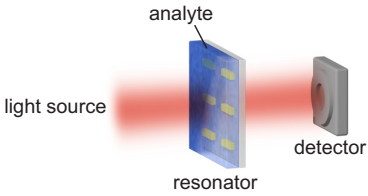

FIGURE 1.1. Typical example setup for resonant nanophotonic substance sensing. The starting point is a nanophotonic resonator that can be brought in contact with the analyte substance. In the depicted example, the resonator consists of an array of plasmonic nanoantennas. The optical response of the nanophotonic structure is probed before and after adding the analyte. The example sketches a setup that is made to measure the optical transmittance of the system. The change in the optical response provides information about the analyte substance. Typically, the signal strengths (and thus, the sensitivities) that are reached via this approach are orders of magnitude higher than the ones that would be achieved from measuring the analyte substance alone, due to the enhanced light-matter interaction that can take place in nanophotonic resonators. Adapted with permission from Ref. [6], copyright 2016, American Chemical Society.

The change in the optical response contains information about the analyte substance. Typically, the signals that are obtained via this approach can be orders of magnitude larger than the ones that would be achieved from measuring the analyte substance alone. The reason is that nanophotonic structures – if appropriately designed – can exhibit electromagnetic resonances with extremely strong electromagnetic near fields that allow for drastically enhancing the interaction of the light with the analyte medium. As a disclaimer, it should be mentioned that in some cases, it is not only necessary to have particularly strong near fields, but also that they are specially tailored. To give the reader some impressions about the kinds of signals that can be produced in this sensing scheme: One can, for instance, measure intensity changes at a fixed wavelength, track spectral shifts of resonant features, monitor shape changes of the features, or even look for new features popping up in the spectrum.

These nanophotonic-sensing approaches have proven to be highly efficient for countless applications: Examples include the ultra-sensitive detection and characterization of various kinds of biomolecules [5, 7–19], gases [20–22], and much more [23–25]. Even specific molecular properties, such as the so-called chirality [26–30], can be determined optically. It should also be emphasized that there are different possibilities to achieve selective detection of target substances: One option is to functionalize the surface of the nanostructures such that only the substance of interest can bind to it. This technique is often used in the case of biomolecules [5]. Another option is to built the resonator (or parts of it) of materials that selectively absorb the requested target substance. This technique is often employed in the case of gas sensing [20–22]. In recent years, a plethora of resonant nanosystems have been investigated, including whispering-gallery resonators [11, 31–33], metallic plasmonic structures [9, 10, 12, 13, 17, 18, 20–22, 25, 26, 28], photonic crystals [8, 14], dielectric nanoresonators [15, 16, 19, 29], and even exotic systems, such as graphene [34].

With the growing popularity of nanophotonic sensing schemes, it becomes more and more important to have available a thorough theoretical understanding of the underlying light-matter interactions. In this context, an approach that has started to experience increasing recognition is the theory of resonant states (also known under the term quasi-normal modes) [35–39]. These states are defined as a specific subset of eigensolutions of Maxwell's equation and constitute a physically meaningful basis to characterize resonant optical phenomena. The resonant-state approach has proven to be highly efficient for modeling numerous sorts of light-matter interactions, such as the interplay of emitters with nanostructures [36, 40–42], light scattering [43–45], light propagation in fibers [46, 47], and many others [38, 39, 48–52]. By exploiting the power of the above framework, in this thesis, we present a detailed theoretical description of the specific interactions that occur in nanophotonic sensing.

The thesis is structured as follows:

- We start in chapter 2 by giving a thorough introduction into the theory of resonant states as well as a broad literature overview of how resonant states can be utilized to describe all kinds of resonant optical phenomena. In this context, we also show that literature provides a simple perturbation theory that allows for efficiently predicting frequency shifts and linewidth changes under small local material variations in nanophotonic systems, as they occur in typical substance sensing schemes.

- In chapter 3, we reveal that the above-mentioned perturbation theory is only valid for material variations inside a given resonator geometry, but not for changes in the surrounding medium, which are often relevant in sensing as well. To close this gap, we present a generalization that is capable of rigorously accounting for such exterior changes and demonstrate its applicability at different example systems.
- Afterwards, in chapter 4, we explain that frequency shifts and linewidth changes are not the only effects that can be important in nanophotonic substance sensing. Consequently, we go one step further and develop a rigorous perturbation theory for predicting the change in any of the resonator's far-field under internal material variations. In order to be as universal as possible, the theory is formulated in the framework of the so-called optical scattering matrix. We test the power of the theory at a simple example from the field of dielectric sensing and show that it allows us to gain deep insights into the heart of the light-matter interactions.
- Then, in chapter 5, we apply the theoretical framework from the previous section to rigorously understand the enhancement mechanisms that occur in a very special sensing application, which has attracted a lot of attention in resent years: nanophotonic chiral sensing.
- In chapter 6, we unveil that substance detection and characterization are not the only nanophotonic sensing applications. Instead, one can also exploit nanophotonic effects for the tracking of movements on the nanoscale. This movement-sensing scheme is based on the interaction between nanostructures and quantum emitters. We present a detailed theoretical model of the involved interactions and apply it to understand and elucidate observations from experiments on DNA-based molecular nanodevices that had been carried out in several collaboration projects.
- Finally, chapter 7 is devoted to summarizing the main results of this thesis as well as to providing some suggestions for possible future works.

2

RESONANT STATES

A physically meaningful basis to describe resonant phenomena are the so-called resonant states. In optics, these states are defined as a specific subset of the eigensolutions of Maxwell's equations. Their physical meaningfulness comes from the fact that resonant states allow for a description of resonant phenomena without relying on any artificial frequency discretization as it is needed in conventional frequency-domain approaches. In this chapter, we will provide a detailed introduction into the framework of resonant states and show how exactly they can be used in practical calculations. Specifically, we discuss the pole expansion of the near and far field and outline related theoretical tools such as the resonant-state expansion and first-order perturbation theories. Furthermore, we will explain how the resonant-state approach can be employed for efficiently describing countless sorts of light-matter interactions in nanophotonics. Finally, we will briefly mention some related approaches.

The main goal of this chapter is to lay the theoretical basis for the rest of this thesis. However, in addition, it is also intended to give the reader some general overview on the broader context of works that this thesis is embedded in.

Parts of this chapter have been published beforehand in the following review article [P7]:

S. Both and T. Weiss: *Resonant states and their role in nanophotonics*. Semiconductor Science and Technology **1**, 013002 (2022).
DOI 10.1088/1361-6641/ac3290.

2.1 INTRODUCTION

In many fields of physics, we are used to describe systems via their eigenmodes, i.e, the eigensolutions of the underlying set of differential equations that characterize the system. In quantum mechanics, for instance, we are used to look at the eigensolutions of the Schrödinger equation. Similarly, in resonant mechanical systems, we are used to deal with the eigensolutions of the mechanical equations of motion. It turns out that also in optics, when investigating resonant phenomena, it is highly useful to approach the problem via the concept of eigenmodes [35–39]. In this case, the underlying differential equations are Maxwell's equations. There is, however, one complication: Many optical systems form so-called open resonators, meaning that they can leak energy to the environment. This makes the underlying physics non-Hermitian and complicates the mathematical analysis, as we will see later.

The eigenmodes of open resonators are typically referred to as resonant states or quasi-normal modes, in order to emphasize the non-Hermitian nature. The two expressions can be used equivalently. The term quasi-normal modes was probably arising the first time for describing tapered fibers [53]. Later, it was reframed in the context of damped mechanical oscillators [54] and stellar models [55]. In contrast, the term resonant states stems from quantum theory and scattering at nuclei [56]. Note that throughout this thesis, we will consistently use the term resonant states.

The strength of the theory of resonant states is to describe resonant phenomena. An overview over typical resonant optical systems is provided in Fig. 2.1. Common to all systems is some mechanism to confine light in a localized region in space. It turns out that this confinement becomes significantly amplified at certain resonance frequencies. Often, it is possible to identify a scaling behavior of the resonance frequencies with some geometrical parameters. In many cases, the scaling is linear and can be interpreted as the result of constructive interference. A prominent example [cf. panel (a)] is that of a whispering gallery mode [11], where light is confined inside a material with high refractive index by total internal reflection at the boundary to a low-index surrounding. This results in constructive interference of light at the resonance frequencies after one roundtrip. In spherical whispering gallery resonators, for instance, the resonance frequency scales linearly with the radius. Owing to their narrow linewidth, whispering gallery resonances are often used in sensing devices [11, 31–33]. Another important resonator type is based on collective electron oscillations, so-called surface-plasmon

polaritons, see Ref. [57] and references therein. When these surface-plasmon polaritons are bound to a finite geometry as depicted in panel (b), they form localized plasmon resonances with very large field enhancements in localized hotspot regions [58–64]. As an alternative to plasmonic structures, high-index dielectric nanoresonators have been investigated that support Mie resonances [65–69]. Their advantage is a reduced loss compared to plasmonic nanoresonators combined with a high flexibility to tailor the interaction of different electric and magnetic resonances [cf. panel (c)]. Interestingly, very recently, it has been demonstrated that similar phenomena can be observed in low-index nanoresonators that are embedded into a high-index surrounding [P14]. Finally, light can also be confined by regions with photonic bandgaps that arise in photonic crystals [70–73]. An example of such a photonic crystal cavity is shown in panel (d).

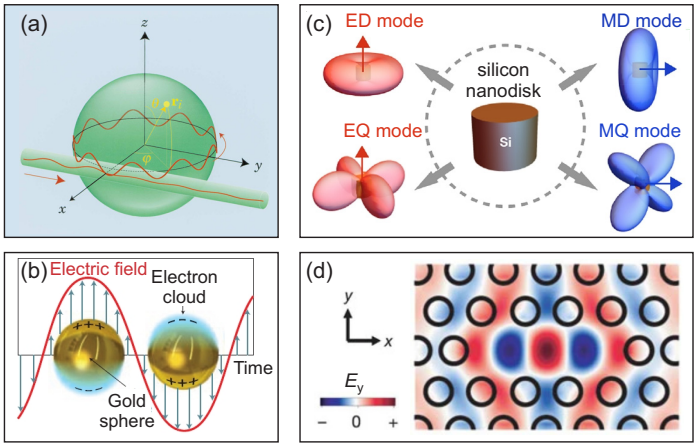

Figure 2.1. Examples of different resonant nanophotonic systems: (a) Dielectric sphere supporting whispering gallery resonances, reprinted with permission from Ref. [11], copyright 2003, Optica; (b) Plasmonic resonances in single gold spheres, reprinted with permission from Ref. [64], copyright 2011, Springer Nature; (c) Electric dipolar (ED), electric quadrupolar (EQ), magnetic dipolar (MD), and magnetic quadrupolar (MQ) Mie resonances in dielectric disks, reprinted with permission from Ref. [69], copyright 2020, American Chemical Society; (d) Photonic crystal cavity, reprinted with permission from Ref. [73], copyright 2003, Springer Nature.

As a side note, let us mention that resonant states in such systems can be categorized by carrying out a multipolar decomposition [74]. This yields three different contributions with typical near- and far-field properties: Electric, magnetic, and toroidal multipoles [75–77].[1] Often, only the lowest-order multipoles suffice to gain a better understanding of the underlying physics. For instance, the interference of toroidal and electric dipoles may lead to the occurrence of anapoles, which are nonradiating charge-current configurations that have been described in various systems [79–81].

At the beginning of this section, it was already stated that resonant states constitute eigensolutions of a non-Hermitian problem. Precisely, they are defined as the eigensolutions of the underlying differential equations at complex-valued eigenfrequencies that decay in time while exhibiting outgoing boundary conditions outside the given resonator geometry. One may wonder about the fact that the eigenfrequencies are in general not real numbers, while experimental observations are only carried out at real frequencies. What is then the implication of these resonant states at complex eigenfrequencies? As a picturesque analogy, consider an old alley, where trees are planted on one side of the road. If the roots of the trees have been growing below the bitumen, the road is no longer plain. Therefore, one feels the impact of the nearby trees, albeit staying always on the road. The same holds for resonant states. They typically occur at frequencies with negative imaginary parts, with few exceptions such as the exotic bound states in the continuum that have a real-valued eigenfrequency [82–88]. From a physical perspective, resonant states oscillate in time with the real part of the eigenfrequency, while twice the magnitude of the imaginary part corresponds to the decay rate in time domain and the resonance linewidth in frequency domain. The decay in time happens due to two possible loss channels: Intrinsic losses in the materials and radiation to the exterior. Particularly those resonant states with eigenfrequencies close to the real axis can have significant impact on the optical response at real frequencies.

Before we continue, let us have a short excursion about some interesting properties of related resonant phenomena: While anapoles suppress the far-field radiation only at certain frequencies due to the interplay of two resonant states, bound states in the continuum are resonant states that do not

1 It should be mentioned that this distinction – although often used in literature – is not truly physical. The reason is that toroidal multipoles do not form an independent multipolar faimily. Instead, it has been shown that they are simply higher-order terms of an expansion of the transverse multipolar coefficients of electric parity with respect to the electromagnetic size of the source [78].

couple to the far-field at all. They can be classified as symmetry-protected and accidental bound states in the continuum [84, 89]. The former can be found whenever the coupling with the far field is forbidden by symmetry constraints of the geometry and the incoming light, which can be, e.g., achieved in photonic crystal slabs [90]. In the latter case, we can understand the origin of the nonradiative properties by the coupling of two or more resonant states, which may yield a zero resonant linewidth under certain "accidental" conditions. Another interesting phenomenon that is attributed to the coupling of resonant states in open resonators is that of exceptional points [32, 91–93], where minimum two eigenstates in a system coalesce in field distribution and frequency. Finally, the arrangement of several resonators in periodic arrays also yields intriguing effects such as narrow surface-lattice resonances [94–97]. In that case, the interaction of the individual resonators is mediated by plane waves close to their diffraction opening, which is known as Rayleigh-Wood anomalies [98–100]. This interplay may result in extremely sharp spectral features, which can be exploited in optical sensors [62].

As already mentioned, resonant states exhibit complex eigenfrequencies with typically nonzero imaginary parts. If the negative imaginary part of the eigenfrequencies is partially correlated with radiative losses, this results in the peculiar behavior that the eigensolutions grow with distance to the resonator. The physical explanation is that light further away from the resonator has left the resonator at the time when more energy had been stored inside the resonator. As a consequence, conventional normalization schemes for these eigensolutions fail. However, the absence of a suitable normalization would render any theory of resonant states to be purely phenomenological. Several alternative approaches have been developed to solve this problem for quantum mechanics [101–103] and later applied to propagating modes in optical waveguides [46, 104–106] and resonant states in optical resonators [35–37, 41, 49, 50, 52, 107–115]. Owing to this plethora of different formulations, the question of how to correctly normalize resonant states was debated a lot in recent years [115–117]. Predominantly two normalization schemes became widely accepted: (i) Analytic normalizations and (ii) the application of complex coordinate transformations, which is equivalent to using so-called perfectly-matched layers for the mode normalization [36]. Interestingly, it appears that those authors who are using the term quasi-normal modes prefer the latter approach. In contrast, the term resonant states is mainly used in the context of analytic normalization schemes [35, 37]. While there are two reviews in literature that have been written from the perspective of quasi-normal modes [38, 39], in this chapter, we approach

the topic mainly from the perspective of resonant states. More specifically, we focus on the analytic normalization schemes and the derivation of the resonant expansion via the Mittag-Leffler theorem, which can be applied to the Green's dyadic.

Another relevant aspect that deserves to be discussed is how to derive the resonant states of a perturbed system based on the resonant states of an unperturbed reference system, which is known as the resonant-state expansion. Originally, the term resonant-state expansion was used in quantum mechanics for a general expansion of functions or operators in terms of resonant states [118, 119], but later refined to a perturbation theory in all orders by the Muljarov group [35, 37, 120]. In general, this perturbative approach can be applied to arbitrarily large perturbations, provided that enough basis states of the unperturbed system are taken into account. It results in a simple eigenvalue equation that can be solved much faster than conventional numerical schemes for determining the resonant states. Under certain simplifications such as the consideration of few modes, it boils down to the so-called coupled-mode theory [121]. However, care has to be taken, because the resonant states cannot be used as a complete set of basis functions far outside the resonator [39], so that the considered perturbations should be in general localized in the resonator. In the limit of a single resonant state, the resonant-state expansion yields a simple first-order perturbation theory. Thus, it is possible to describe the sensitivity of resonantly enhanced refractive-index sensors [51, 52, 111, 122, 123] and define a figure of merit that can be used for optimizing such systems [25].

The rest of the chapter is organized as follows: We begin with the derivation of the constitutive equation for resonant states, which requires searching for solutions of Maxwell's equations in the absence of sources and with outgoing boundary conditions. Afterwards, we show how the Green's dyadic can be expanded in terms of the resonant states. Then, we address the question of mode normalization, including a more general derivation of the analytic normalization (compared to Refs. [37, 45]) that is valid even for nonreciprocal materials. The next subsection is devoted to orthogonality relations, followed by an overview on how to expand the near fields in terms of the resonant states and a discussion of the completeness of the basis of resonant states. Section 2.2 concludes with the pole expansion of the optical scattering matrix. The next section contains an overview of the different applications: Resonant-state expansion, first-order perturbation theory and sensing, as well as Purcell enhancement. In the last section before the conclusion, we provide a brief introduction to related theories such as the expansion in

terms of permittivity eigenmodes or propagating modes. Finally, we discuss how to use these theories to describe nonlinear optical phenomena.

2.2 THEORY

We start with Maxwell's equations in frequency domain, which we obtain from time domain by using the Fourier transform

$$f(\mathbf{r};\omega) = \int_{-\infty}^{\infty} dt\, \mathrm{e}^{i\omega t} f(\mathbf{r},t). \tag{2.1}$$

Here, ω is the angular frequency. By making use of the compact matrix-vector notation introduced in Ref. [37], the resulting curl Maxwell's equations (Gaussian units) can be written as

$$\underbrace{\left[\underbrace{\frac{\omega}{c}\underbrace{\begin{pmatrix}\varepsilon(\mathbf{r};\omega) & -i\xi(\mathbf{r};\omega)\\ i\zeta(\mathbf{r};\omega) & \mu(\mathbf{r};\omega)\end{pmatrix}}_{\hat{\mathbb{P}}(\mathbf{r};\omega)} - \underbrace{\begin{pmatrix}0 & \nabla\times\\ \nabla\times & 0\end{pmatrix}}_{\hat{\mathbb{D}}(\mathbf{r})}\right]}_{\hat{\mathbb{M}}(\mathbf{r};\omega)} \underbrace{\begin{pmatrix}\mathbf{E}(\mathbf{r};\omega)\\ i\mathbf{H}(\mathbf{r};\omega)\end{pmatrix}}_{\mathbb{F}(\mathbf{r};\omega)} = \underbrace{\begin{pmatrix}\mathbf{J}_{\mathrm{E}}(\mathbf{r};\omega)\\ i\mathbf{J}_{\mathrm{H}}(\mathbf{r};\omega)\end{pmatrix}}_{\mathbb{J}(\mathbf{r};\omega)}. \tag{2.2}$$

Here, c is the vacuum speed of light, while ε, μ, ξ and ζ represent the material parameters, namely permittivity, permeability, and possible bi-anisotropic contributions, respectively. In general, ε, μ, ζ, and ξ are 3×3 tensors. It should be mentioned that in the special case of reciprocal materials, the material parameters obey $\xi^{\mathrm{T}} = -\zeta$, $\varepsilon^{\mathrm{T}} = \varepsilon$, and $\mu^{\mathrm{T}} = \mu$, with the superscript T denoting the matrix transpose [124]. The vectors $\mathbf{E}$ and $\mathbf{H}$ denote the electric and magnetic fields, respectively, while the vectors $\mathbf{J}_{\mathrm{E}}$ and $\mathbf{J}_{\mathrm{H}}$ represent generalized external electric and magnetic currents, respectively. Note that the generalized electric current is defined as $\mathbf{J}_{\mathrm{E}} = -4\pi i\mathbf{j}/c$, with the electric current density $\mathbf{j}$, while $\mathbf{J}_{\mathrm{H}}$ has only been introduced for symmetry purposes. In order to write the equations in a more compact form, we summarize all material parameters in a material operator $\hat{\mathbb{P}}$. In analogy, all curls are included in a generalized curl operator $\hat{\mathbb{D}}$. Furthermore, we introduced two six-dimensional supervectors $\mathbb{F}$ and $\mathbb{J}$ that consist of the fields and the generalized currents, respectively. By further abbreviating $\hat{\mathbb{M}} = \omega/c\,\hat{\mathbb{P}} - \hat{\mathbb{D}}$, the curl Maxwell's equations become a simple operator equation:

$$\hat{\mathbb{M}}(\mathbf{r};\omega)\mathbb{F}(\mathbf{r};\omega) = \mathbb{J}(\mathbf{r};\omega). \tag{2.3}$$

In the following, we will refer to $\hat{\mathbb{M}}$ as the Maxwell operator. For the sake of completeness, we want to remark that other authors have defined alternative

matrix-vector notation of Maxwell's equations [38, 39, 125], which are from a conceptual point similar to the above, but differ in the details, as they for instance do not contain a factor i in the definition of the field supervector.

One can introduce the so-called Green's dyadic $\hat{\mathbb{G}}$ of Eq. (2.3). This is defined as the solution of

$$\hat{\mathbb{M}}(\mathbf{r};\omega)\hat{\mathbb{G}}(\mathbf{r},\mathbf{r}';\omega) = \hat{\mathbb{I}}\delta(\mathbf{r}-\mathbf{r}'), \tag{2.4}$$

where $\hat{\mathbb{I}}$ is the six-dimensional unit matrix and $\delta(\mathbf{r})$ represents the delta function. If $\hat{\mathbb{G}}$ of a system is known, one can immediately calculate the fields $\mathbb{F}$ for a given source $\mathbb{J}$ as

$$\mathbb{F}(\mathbf{r};\omega) = \int dV'\, \hat{\mathbb{G}}(\mathbf{r},\mathbf{r}';\omega)\mathbb{J}(\mathbf{r}';\omega). \tag{2.5}$$

This equation will be relevant at several places within this thesis.

2.2.1 *Constitutive equation of resonant states*

In the following, we want to find an equation that defines the resonant states. To motivate this, we consider that our system experiences a very short excitation at time t_0 by a source $\mathbb{J}_0(\mathbf{r})\delta(t-t_0)$. The resulting time-dependent electric field is given by

$$\mathcal{E}(\mathbf{r},t) = \frac{1}{2\pi}\int_{-\infty}^{\infty} d\omega\, \mathrm{e}^{-i\omega(t-t_0)}\mathbf{E}(\mathbf{r};\omega), \tag{2.6}$$

where $\mathbf{E}(\mathbf{r};\omega)$ is the frequency-dependent electric field generated by $\mathbb{J}(\mathbf{r};\omega) = \mathbb{J}_0(\mathbf{r})$. Now, we assume that $\hat{\mathbb{G}}$ and, thus, $\mathbf{E}(\mathbf{r};\omega)$ has a countable number of simple poles at complex frequencies ω_n in the negative imaginary frequency half plane: $\omega_n = \Omega_n - i\Gamma_n$ with $\Omega_n, \Gamma_n \in \mathbb{R}, \Gamma_n > 0$. Furthermore, we restrict our considerations to times $t > t_0$. We note that Eq. (2.6) can be interpreted as a line integral in the complex frequency plane along a path C_1 that coincides with the real frequency axis. We now extend the integration path as indicated in Fig. 2.2 by adding a second section C_2 such that we obtain a closed loop that encompasses the negative imaginary frequency half plane. We can assume that the integral over C_2 vanishes [note that the integrand is exponentially damped for $\mathrm{Im}(\omega) \to -\infty$]. Therefore, the result

of Eq. (2.6) is not influenced by the change of the integration path. Since we have a closed contour, we can apply the residue theorem and obtain:

$$\mathcal{E}(\mathbf{r},t) = i\sum_n \mathrm{e}^{-i\omega_n(t-t_0)}\mathrm{Res}[\mathbf{E}(\mathbf{r};\omega),\omega_n]. \tag{2.7}$$

This result allows us to draw some important conclusions: First, the time-dependent field oscillates with frequencies Ω_n while decaying in time as $\exp[-\Gamma_n(t-t_0)]$. Second, the optical response of the system is solely determined by the fields at the complex poles ω_n. Third, since the time-dependent field $\mathcal{E}(\mathbf{r},t)$ must be real-valued, we infer that for every pole at a frequency ω_n, there must be another pole at $-\omega_n^*$ with residue $\mathrm{Res}[\mathbf{E}(\mathbf{r};\omega),-\omega_n^*] = -\mathrm{Res}[\mathbf{E}(\mathbf{r};\omega),\omega_n]^*$.

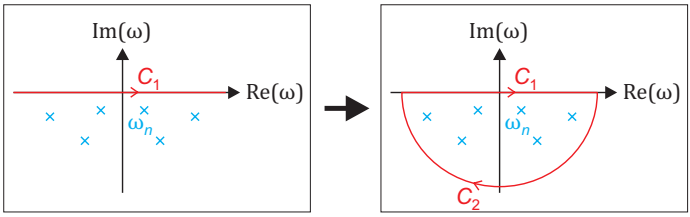

Figure 2.2. Change of the integration path in Eq. (2.6). The original path C_1 resembles a straight line along the real frequency axis. We add a second path C_2, such that we obtain a closed loop that encompasses the negative imaginary frequency half plane. We can assume that the integral over C_2 vanishes and therefore, the result of Eq. (2.6) is not altered. Note that for visualization, the sketch shows a loop of finite dimension; however, in reality the loop is meant to be infinitely extended such that it encloses the entire half plane.

A closely related visualization that indicates how the behavior of a function at real-valued arguments is determined by the poles in the complex argument plane can be found in Fig. 2.3. Plotted is the transmittance of a planar dielectric slab as a function of the complex wavenumber $k = \omega/c$. As it can be seen, the transmittance at real wavenumbers (orange solid line) is governed by the nearest poles on the complex wavenumber plane [45]. The depicted situation is somewhat analog to the situation in Eq. (2.7).

Equation (2.7) is quite descriptive. It means that a short excitation will store a finite amount of energy in the system, which will allow the resonator

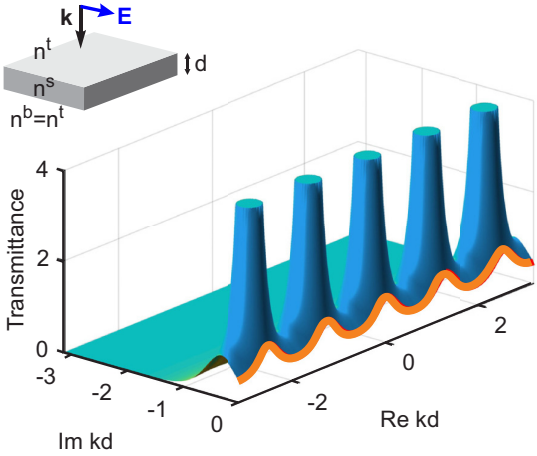

Figure 2.3. Analytic continuation of the transmittance of a planar dielectric slab of thickness d to the complex normalized wavenumber plane kd. The slab has a refractive index of $n = 2.5$ and is surrounded by air. The incidence direction is normal to the slab. It can bee seen that the transmittance maxima at real wavenumbers are manifestations of the poles at complex wavenumbers, which can be associated with Fabry-Perot modes of different orders. Reprinted with permission from Ref. [45], copyright 2018, American Physical Society.

to oscillate at the excited resonance frequencies. While doing that, it can lose energy via different loss channels, resulting in an exponential decay of the oscillations in time with a decay rate of Γ_n. This is exactly the same process as in acoustic resonators, e.g., in a bell or guitar string that is excited by a short strike. Direct experimental observations of this decay are often hampered in optics by the large decay rate of typical resonances, i.e., a rather short lifetime compared to the excitation pulse. However, for long-lived resonances, the exponential decay in time can be observed, as shown by Hergert et al. [126].

Let us now address the consequences of Eq. (2.4). If the Green's dyadic $\hat{\mathbb{G}}$ has poles at frequencies ω_n but the right-hand side of Eq. (2.4) does not depend on frequency, we can infer that the operator $\hat{\mathbb{M}}$ must have roots at these complex frequencies:

$$\hat{\mathbb{M}}(\mathbf{r};\omega_n)\mathbb{F}_n(\mathbf{r}) = 0. \tag{2.8}$$

Since this equation formally resembles an eigenvalue problem, we will from now on refer to ω_n as the eigenfrequencies. Equation (2.8) denotes the constitutive equation for resonant states. Since the Green's dyadic yields only outgoing fields for spatial regions outside a given source $\mathbb{J}$, it follows that the resonant fields $\mathbb{F}_n$ in Eq. (2.8) must possess purely outgoing boundary conditions outside the resonator. This is the reason why the above equation can be fulfilled only for a discrete set of eigenfrequencies ω_n. Without that restriction, there exist solutions of Eq. (2.8) for any frequency with a given incident field, which resembles the typical situation of a scattering problem in optics with a known incident field and the resulting scattered field [39].

Of course, the question is what outgoing boundary condition mean at complex frequencies. At real frequencies, we can use the Silver-Müller radiation condition [127] for isolated resonators embedded in a homogeneous and isotropic surrounding, which specify outgoing boundary conditions as

$$\lim_{r\to\infty} \mathbf{e}_r \times \mathbf{E} = Z\mathbf{H}, \tag{2.9}$$

$$\lim_{r\to\infty} \mathbf{e}_r \times Z\mathbf{H} = -\mathbf{E}, \tag{2.10}$$

where $\mathbf{e}_r$ is the radial unit vector and Z is the impedance of the surrounding medium. At complex frequencies, the situation is, however, more sophisticated. Most importantly, the Silver-Müller radiation condition does not hold for resonant states at complex frequencies [115]. Hence, it can be regarded for modal expansions in terms of resonant states only as the limiting case at real frequencies [39].

A straightforward way to extend the definition of outgoing boundary conditions to complex frequencies is to consider localized sources: If a source $\mathbb{J}$ is completely localized in a certain volume, then the fields generated by this source are purely outgoing outside that volume. The problem is that Eq. (2.8) does not contain any sources. Still, it is possible to test the boundary conditions of solutions of Eq. (2.8) by introducing a localized source that vanishes in the limit $\omega \to \omega_n$, i.e., $\mathbb{J} \propto O(\omega - \omega_n)$. The fields $\mathbb{F}$ generated by this source then have to obey $\mathbb{F} \to \mathbb{F}_n$ for $\omega \to \omega_n$. Note that this approach is also used for deriving the analytic normalization in the next section. Of course, one needs to clarify, where possible sources are located in this case. For this purpose, we separate our system into a background system with a trivial material distribution $\hat{\mathbb{P}}_{\mathrm{BG}}$ that should be free of resonant states, and a localized non-trivial variation $\Delta\hat{\mathbb{P}}$ that constitutes the resonator:

$$\hat{\mathbb{P}}(\mathbf{r};\omega) = \hat{\mathbb{P}}_{\mathrm{BG}}(\mathbf{r};\omega) + \Delta\hat{\mathbb{P}}(\mathbf{r};\omega). \tag{2.11}$$

Possible test sources for outgoing boundary conditions should be located in regions with $\Delta\hat{\mathbb{I}}\hat{\mathbb{P}} \neq 0$.

Still, there can be some ambiguity about the optimal set of resonant states. For instance, in planar periodic structures, Rayleigh-Wood anomalies [98–100] arise in the spectra. They occur spectrally, whenever a plane wave in the super- or substrate changes between propagating and decaying perpendicular to the planar system. In that case, the wavevector component perpendicular to the slab, which we denote here as k_z, approaches zero. As discussed later, this yields cuts in the complex frequency plane for the expansion of the Green's dyadic [109, 128]. The exact path of these cuts is not unique [106], but can be chosen in dependence of the selection of Riemann sheets in the square root function that relates k_z with the vacuum wavenumber $k = \omega/c$ via

$$k_z = \pm\sqrt{n^2k^2 - \mathbf{k}_{||}^2}, \tag{2.12}$$

where n is the refractive index in the super- or substrate and $\mathbf{k}_{||}$ is the projection of the wavevector parallel to the planar structure. A common selection for the Riemann sheet with outgoing plane waves, i.e., when to use the positive or negative sign in Eq. (2.12), is to warrant $\mathrm{Re}(k_z) + \mathrm{Im}(k_z) > 0$, but other definitions may be better suited. In some cases, it even turns out that a description of the optical response in terms of complex propagation constants k_z is favorable over an analytic continuation to complex frequencies [109, 128]. In that case, it is then possible to account for modes on both Riemann sheets simultaneously, while the related cut contribution is removed.

Finally, let us briefly address the question on how to obtain solutions of Eq. (2.8). In the cases of planar slabs, spherical particles, or infinitely long cylinders, we can derive the resonant states and their complex resonance frequencies by reducing Maxwell's equations to a transcendental equation that can be solved exactly up to machine precision. In very specific cases such as planar slabs consisting of homogeneous and isotropic non-dispersive materials, it is even possible to write down closed expressions for the resonance frequencies and fields [38, 109, 129]. In general, however, numerical methods are required to determine solutions of Eq. (2.8). This is probably the most important case in practice. Typical numerical methods that are commonly used in this context are the finite difference method, the finite-element method and the Fourier-modal method. In this thesis, we will make use of the latter two. An overview and benchmark of different numerical

schemes for determining resonant states can be found in Ref. [130]. It should be mentioned that as an alternative to the numerical approach, the resonant states of a complex system can also be calculated from simpler systems with known analytic solutions via a perturbative approach, known as the resonant-state expansion [35, 37], which will be explained in subsection 2.3.1.

2.2.2 *Pole expansion of the Green's dyadic*

In the following, we derive an expansion of the Green's dyadic in terms of the resonant states. For this purpose, we will make use of the Mittag-Leffler theorem [35, 37]. Let us briefly summarize this theorem: If $f(z)$ is a complex function that is analytic except for a countable number of poles a_n and exhibits the asymptotic behavior $\lim_{z\to\infty} f(z)/z^p = 0$, it can be expanded as [129, 131]

$$f(z) = f_p(z) + \sum_n \frac{b_n}{(z - a_n)}, \tag{2.13}$$

where b_n are the residues at the poles and

$$f_p(z) = \sum_{m=0}^{p-1} \left[\frac{f^{(m)}(0)}{m!} + \sum_n \frac{b_n}{a_n^{m+1}} \right] z^m \tag{2.14}$$

with $f_0(z) = 0$. That means the function $f(z)$ can be written as a pole contribution of the form $\sum_n b_n/(z - a_n)$, accompanied for $p > 0$ by a polynomial of order $p - 1$.

Let us now consider Eq. (2.3) with a particular source term chosen as $\mathbb{J}_n(\mathbf{r};\omega) = (\omega - \omega_n)\mathbb{S}_n(\mathbf{r})/c$, where $\mathbb{S}_n(\mathbf{r})$ represents an arbitrary vector function that is localized inside the resonator. This particular source term is selected, since it vanishes at the eigenfrequency ω_n. Equation (2.3) then reads:

$$\hat{\mathbb{M}}(\mathbf{r};\omega)\mathbb{F}(\mathbf{r};\omega) = \frac{\omega - \omega_n}{c}\mathbb{S}_n(\mathbf{r}). \tag{2.15}$$

We note that in the limit of $\omega \to \omega_n$, the right side vanishes and the above equation translates to the constitutive equation of resonant states. Therefore, the fields have to obey $\lim_{\omega\to\omega_n} \mathbb{F}(\mathbf{r};\omega) = \mathbb{F}_n$. Applying Eq. (2.5) to solve Eq.(2.15) for $\mathbb{F}(\mathbf{r};\omega)$ gives

$$\mathbb{F}(\mathbf{r};\omega) = \frac{\omega - \omega_n}{c} \int dV' \, \hat{\mathbb{G}}(\mathbf{r},\mathbf{r}';\omega)\mathbb{S}_n(\mathbf{r}'). \tag{2.16}$$

Utilizing the limiting behavior of the fields, assuming that $\hat{\mathbb{G}}$ is analytic except for a countable number of poles and that it has the asymptotic behavior $\lim_{\omega\to\infty}\hat{\mathbb{G}}=0$, and furthermore, using the Mittag-Leffler theorem, one can show that the Green's dyadic must be of the following form [37, 111]:

$$\hat{\mathbb{G}}(\mathbf{r},\mathbf{r}';\omega)=c\sum_n\frac{\mathbb{F}_n(\mathbf{r})\otimes\mathbb{X}_n(\mathbf{r}')}{\omega-\omega_n}, \tag{2.17}$$

where $\mathbb{X}_n$ are some yet unknown fields that we will determine in the following.

Let us now begin our journey to find an expression for $\mathbb{X}_n$. We will do the derivation in a very detailed manner, since on the way we will obtain some further relations that will be useful later in this thesis. Inspired by the generalization of the reciprocity theorem from Ref. [124], we define a transposed system (indicated by the superscript ‡)

$$\hat{\mathbb{M}}^{\ddagger}(\mathbf{r};\omega)\mathbb{F}^{\ddagger}(\mathbf{r};\omega)=\mathbb{J}^{\ddagger}(\mathbf{r};\omega). \tag{2.18}$$

Compared to the original system, the transposed system contains two differences: First, the material operator $\hat{\mathbb{P}}$ is replaced by its matrix-transposed counterpart $\hat{\mathbb{P}}^{\mathrm{T}}$, resulting in the Maxwell operator $\hat{\mathbb{M}}^{\ddagger}=\omega/c\,\hat{\mathbb{P}}^{\mathrm{T}}-\hat{\mathbb{D}}$. As a side note it should be mentioned that in the special case of reciprocal materials, this replacement does not make any change, since for reciprocal materials, one finds $\hat{\mathbb{P}}^{\mathrm{T}}=\hat{\mathbb{P}}$ [cf. explanation under Eq. (2.2)]. Second, if the original systems has external symmetry constraints on the solution space of Maxwell's equations that one is interested in, these symmetry constraints are supposed to be reversed. An example are systems with a planar periodic symmetry where one is interested at solutions of Maxwell's equations at fixed in-plane wavevectors $\mathbf{k}_{||}$. Here, reversing the symmetry constraint means going from $\mathbf{k}_{||}$ to $-\mathbf{k}_{||}$ [111]. Another example are rotationally symmetric systems where one is interested at solutions of Maxwell's equations with a fixed angular dependency of the form $\exp(im\varphi)$, where m is an integer number and φ denotes the azimuthal angle. In this case, reversing the symmetry constraint means going from m to $-m$. For completeness, we want to mention that in some literature works [45–47, 129, 132, 133], the reversal of the external symmetry constraints is referred to as "reciprocal conjugation" and denoted by a superscript R, because the considered systems therein are composed of purely reciprocal materials.

In the following, we want to find further relations between the fields of the original system and the fields of the transposed system. For this purpose,

we assume arbitrary sources $\mathbb{J}_1$ and $\mathbb{J}_2^\ddagger$ that are extended over a finite region in space and generate fields $\mathbb{F}_1$ and $\mathbb{F}_2^\ddagger$. Then, we multiply Eq. (2.3) and Eq. (2.18) from the left with $\mathbb{F}_2^\ddagger$ and $\mathbb{F}_1$, respectively, and subtract the results, which yields:

$$\mathbb{F}_1 \cdot \hat{\mathbb{D}}\mathbb{F}_2^\ddagger - \mathbb{F}_2^\ddagger \cdot \hat{\mathbb{D}}\mathbb{F}_1 = \mathbb{F}_2^\ddagger \cdot \mathbb{J}_1 - \mathbb{F}_1 \cdot \mathbb{J}_2^\ddagger. \tag{2.19}$$

Integrating this equation over a finite volume V and using the integral identity [45]

$$\int_V dV(\mathbb{F}_\mathrm{A}\cdot\hat{\mathbb{D}}\mathbb{F}_\mathrm{B} - \mathbb{F}_\mathrm{B}\cdot\hat{\mathbb{D}}\mathbb{F}_\mathrm{A}) = i\oint_{\partial V} d\mathbf{S}\cdot(\mathbf{E}_\mathrm{B}\times\mathbf{H}_\mathrm{A} - \mathbf{E}_\mathrm{A}\times\mathbf{H}_\mathrm{B}) \tag{2.20}$$

to transform the volume integral on the left side into a surface integral results in

$$i\oint_{\partial V} d\mathbf{S}\cdot(\mathbf{E}_2^\ddagger\times\mathbf{H}_1 - \mathbf{E}_1\times\mathbf{H}_2^\ddagger) = \int_V dV(\mathbb{F}_2^\ddagger\cdot\mathbb{J}_1 - \mathbb{F}_1\cdot\mathbb{J}_2^\ddagger). \tag{2.21}$$

In their tutorial [39], Kristensen et al. derived a suitable bi-orthogonal basis for the Green's dyadic expansion by using the condition that a similar surface integral as that on the left-hand side of Eq. (2.21) must vanish. We follow this idea, but approach it from a different direction. More specifically, we make use of generalized reciprocity relations: We note that in the special case of reciprocal systems, the Green's dyadic fulfills $\hat{\mathbb{G}}^\mathrm{T}(\mathbf{r},\mathbf{r}';\omega) = \hat{\mathbb{G}}(\mathbf{r}',\mathbf{r};\omega)$ [52, 124]. Using the Onsager-Casimir relation that is based on the work of Onsager and Casimir [134–136], one can generalize this relation to [124]:

$$\hat{\mathbb{G}}^\ddagger(\mathbf{r},\mathbf{r}';\omega) = \hat{\mathbb{G}}^\mathrm{T}(\mathbf{r}',\mathbf{r};\omega), \tag{2.22}$$

where $\hat{\mathbb{G}}^\ddagger$ is the Green's dyadic of the transposed system.

Taking the right-hand side of Eq. (2.21), expressing the fields $\mathbb{F}_1$ and $\mathbb{F}_2^\ddagger$ via Eq. (2.5) and its transposed counterpart, respectively, and using the relation in Eq. (2.22), we obtain zero:

$$\int_V dV \int_V dV'[(\hat{\mathbb{G}}^\ddagger\mathbb{J}_2^\ddagger)\cdot\mathbb{J}_1 - \mathbb{J}_2^\ddagger\cdot\hat{\mathbb{G}}\mathbb{J}_1] = 0. \tag{2.23}$$

In other words: The right-hand side of Eq. (2.21) vanishes. If the right-hand side vanishes, the left-hand side must vanish as well. Hence, we deduce:

$$\oint_{\partial V} d\mathbf{S} \cdot (\mathbf{E}_2^\ddagger \times \mathbf{H}_1 - \mathbf{E}_1 \times \mathbf{H}_2^\ddagger) = 0. \tag{2.24}$$

This is a necessary condition for pairs of fields that obey the prerequisites of the Onsager-Casimir relation [124] and are generated by sources that are completely localized inside the volume V. Since the above fields are generated by localized sources, they are inherently outgoing on the surface ∂V. Note that Eq. (2.24) also holds in the case that both sources $\mathbb{J}_1$ and $\mathbb{J}_2^\ddagger$ are located outside the volume V, in which case $\mathbb{F}_1$ and $\mathbb{F}_2^\ddagger$ are pairs of incoming fields; however, there are scenarios – such as the definition of the basis functions we will introduce in subsection 2.2.7 – where one wants to have a pair of fields $\mathbb{F}_1$ and $\mathbb{F}_2^\ddagger$ for which the above surface integral is nonzero. In this case, the solution is to combine an incoming with an outgoing field.

Finally, we can infer from Eq. (2.22) that $\hat{\mathbb{G}}$ and $\hat{\mathbb{G}}^\ddagger$ have the same poles, i.e., the operators $\hat{\mathbb{M}}$ and $\hat{\mathbb{M}}^\ddagger$ possess the same spectrum. The constitutive equation for the transposed resonant states is

$$\hat{\mathbb{M}}^\ddagger(\mathbf{r}; \omega_n)\mathbb{F}_n^\ddagger(\mathbf{r}) = 0. \tag{2.25}$$

Note that in general $\mathbb{F}_n \neq \mathbb{F}_n^\ddagger$. We may now follow the same steps as for deriving Eq. (2.17) to obtain the pole expansion of $\hat{\mathbb{G}}^\ddagger$, where $\mathbb{F}_n$ and $\mathbb{X}_n$ are replaced by $\mathbb{F}_n^\ddagger$ and an unknown field $\mathbb{X}_n^\ddagger$. Then, using Eq. (2.22), we obtain the analytic pole expansion of the Green's dyadic:

$$\hat{\mathbb{G}}(\mathbf{r}, \mathbf{r}'; \omega) = c \sum_n \frac{\mathbb{F}_n(\mathbf{r}) \otimes \mathbb{F}_n^\ddagger(\mathbf{r}')}{\omega - \omega_n}, \tag{2.26}$$

which represents the main result of this subsection.

For completeness, it should be mentioned that an alternative way of deriving this relation is to expand the operator $\hat{\mathbb{M}}$ in a suitable basis, in which Eq. (2.8) yields a nonlinear matrix-eigenvalue equation. In numerical calculations, this is done via a discretization of the computational domain, resulting in a finite-sized nonlinear eigenvalue problem [38, 137–139]. Then, using Keldysh theorem [140, 141], the expansion of the resolvent is straight-forward [137], with the representation of $\mathbb{F}_n^\ddagger$ being a left eigenvector of the nonlinear eigenvalue equation.

At the end of the subsection, let us use the pole expansion of the Green's dyadic to derive some further relations, which are of general usefulness. By inserting Eq. (2.26) into Eq. (2.4), we obtain the closure relation [37]

$$\sum_n \frac{\omega\hat{\mathbb{P}}(\mathbf{r};\omega)-\omega_n\hat{\mathbb{P}}(\mathbf{r};\omega_n)}{\omega-\omega_n}\mathbb{F}_n(\mathbf{r})\otimes\mathbb{F}_n^{\ddagger}(\mathbf{r}') = \hat{\mathbb{I}}\delta(\mathbf{r}-\mathbf{r}'). \tag{2.27}$$

Assuming material distributions of the form

$$\hat{\mathbb{P}}(\mathbf{r};\omega) = \hat{\mathbb{P}}(\mathbf{r}) + \sum_j \frac{\hat{\mathbb{Q}}_j}{\omega-\Omega_j}, \tag{2.28}$$

where Ω_j are complex poles of the material response with residues $\hat{\mathbb{Q}}_j$ [142], it is furthermore shown in Ref. [37] how to derive the following sum rules:

$$\hat{\mathbb{Q}}_j(\mathbf{r})\sum_n \frac{\mathbb{F}_n(\mathbf{r})\otimes\mathbb{F}_n^{\ddagger}(\mathbf{r}')}{\omega_n-\Omega_j} = 0. \tag{2.29}$$

Other forms of sum rules can be found in Refs. [41, 118], and a combination of the sum and closure relation yields [37]

$$\sum_n \hat{\mathbb{P}}(\mathbf{r};\omega_n)\mathbb{F}_n(\mathbf{r})\otimes\mathbb{F}_n^{\ddagger}(\mathbf{r}') = \hat{\mathbb{I}}\delta(\mathbf{r}-\mathbf{r}'). \tag{2.30}$$

The implications of the sum rules and closure relations are discussed later in the context of the completeness of the basis of resonant states. Furthermore, the sum rules can be used to obtain the connection between different formulations of the resonant expansion [129].

2.2.3 *Normalization of resonant states*

Equation (2.8) specifies the resonant field distributions $\mathbb{F}_n$ only up to a complex scalar factor. While we can infer from Eq. (2.7) that it should be possible to decompose arbitrary fields into their resonant contributions, such an expansion requires to fix the arbitrariness of this complex scalar factor. In other words: a unique normalization is needed.

For bound eigenstates ψ_n, as they appear, for instance, in quantum mechanics and lossless waveguides, defining a normalization is quite trivial: One can derive a simple orthogonality relation that reads as

$$\int dV\, \psi_n^* \psi_m = \delta_{nm}, \tag{2.31}$$

where the integral is meant to cover the whole space. Inserting $m = n$ provides the normalization condition: $\int dV\, \psi_n^* \psi_n = 1$.

For resonant states, the situation is, however, more sophisticated. The difference is that, as already indicated, resonant states are the eigenstates of non-Hermitian systems (recall that the absence of Hermiticity is caused by the occurrence of radiation leakage or absorption). In general, if a resonant state radiates to the far-field and experiences loss, it will exhibit fields that grow with distance to the resonator and diverge at infinity.[2] Consequently, a normalization similar to Eq. (2.31) is not possible, because the integral over the entire space will diverge.

To understand better why the fields grow with distance to the resonator, one can, for instance, have a look at the resonant states of spherical particles. Since the resonant states exhibit outgoing boundary conditions, their fields must scale as $\exp(i\omega_n r/c)/r$ for large distances to the particle (where r represents the radial distance to the center of the particle). From the considerations around Eq. (2.7), we recall that as soon as there is loss in the system, the time-dependent fields must exponentially decay over time, leading to resonant states with complex eigenfrequencies that exhibit a negative imaginary part. Hence, the eigenfrequencies can be written as $\omega_n = \Omega_n - i\Gamma_n$ with $\Gamma_n > 0$. Plugging this result in the above spatial dependence gives $\exp(i\Omega_n r/c + \Gamma_n r/c)/r$, i.e., the fields grow exponentially with r. Of course, one may ask if the growing character of resonant field distributions is unphysical. However, there is a simple physical explanation: The fields further away from the resonator have left the resonator at an earlier time at which more energy had been stored in it. The energy is then lost via radiative and non radiative processes. The radiative processes carry energy away with the speed of light, which is fully consistent with causality [143]. The divergent nature of the resonant states can be thus interpreted as if an infinite

2 For completeness, we want to mention that there is a theoretical scenario, where a resonant state can radiate to the far-field but does not exhibit growing fields. This is the case if the system contains active gain materials and if the gain is strong enough to overcompensate the loss, such that the eigenfrequency exhibits a positive imaginary part. In that case, the field intensities grow as a function of time.

amount of energy had been stored in the resonator at $t_0 \to -\infty$ and is now distributed over all space.

In early works related to first-order perturbation theories [122] and Purcell factors [144] of resonant states in open cavities, the divergence of resonant states was either ignored or overlooked, and the integration over the fields was restricted to a finite volume. While this may work out reasonably well for some cases, it has been noted already by Koenderink in 2010 [145] that the divergence of such integrals cannot provide accurate results in general. However, the simplicity of the incorrect theory and its good agreement with many expectations and observations has prevented the derivation of a more advanced theory for nanophotonics for more than a decade. In the following, let us now explain how one can define a rigorous and mathematically correct normalization of resonant states. We will distinguish two different approaches.

2.2.3.1 *Perfectly-matched layer normalization*

Solutions for a correct normalization of growing fields were available – either in quantum mechanics [102, 103, 146] or waveguide theory [104, 105]. Most common is to regularize the functions [102] or to make the system finite by a complex coordinate transformation [104, 105]. It is the merit of Sauvan and Lalanne to reinvent the latter method for applications in nanophotonics and to formalize it in the framework of the theory of perfectly-matched layers [36, 38]: An infinite system can be mapped via a complex coordinate transformation to an equivalent finite system, in which there is no divergence of fields at the boundaries if all parameters are chosen appropriately. This is equivalent to surrounding a given geometry by perfectly-matched layers [147], which is therefore the most common implementation of this normalization in numerical calculations. Mathematically, the resulting normalization can be written as[3]

$$\int_{\tilde{V}} dV\, \tilde{\mathbb{F}}_n^{\ddagger} \cdot (\omega\tilde{\mathbb{P}})'\tilde{\mathbb{F}}_n = 1, \tag{2.32}$$

where $\tilde{V}$ denotes a finite volume including the region of the perfectly-matched layers and the prime in $(\omega\tilde{\mathbb{P}})'$ was introduced as an abbreviation for the derivative with respected to ω evaluated at ω_n. While the above

3 For consistency with the rest of this thesis, we have generalized the original result from Refs. [36, 38] to systems containing nonreciprocal and bi-anisotropic materials.

approach is quite versatile, it is a bit problematic that the important fact that $\tilde{V}$ is not the entire infinite space often just shows up as a footnote. Hence, equation (2.32) makes the impression of a divergent integral. Moreover, the fields inside the region of perfectly-matched layers are related to the original fields in real space only by the corresponding complex coordinate transformation, and the original material parameters have to be replaced there by those artificial quantities of the perfectly-matched layers, see Supplementary Material of Ref. [36]. That is why we have added a tilde on top of the fields and the material operator in Eq. (2.32). Finally, note that the selection of appropriate parameters for the perfectly-matched layers can be rather delicate in some cases. Therefore, it has to be carefully checked that Eq. (2.32) has converged.

2.2.3.2 *Analytic normalization*

As an alternative to the perfectly-matched layer normalization, one can also formulate analytic normalization approaches that do not rely on the usage of these layers. One option is to consider the divergent integrals in a distribution sense [148]. Another possibility – the one that we will focus on here – is to introduce a surface term that compensates for the divergent nature of the volume integral. This approach is based on assigning the correct weight to the residues in the Mittag-Leffler expansion of the Green's dyadic provided in Eq. (2.26).

The starting point is Eq. (2.16). Inserting the Green's dyadic expansion from Eq. (2.26) gives

$$\mathbb{F}(\mathbf{r};\omega) = \sum_m \frac{\omega-\omega_n}{\omega-\omega_m}\mathbb{F}_m(\mathbf{r})\int dV'\mathbb{F}_m^{\ddagger}(\mathbf{r}')\cdot\mathbb{S}_n(\mathbf{r}'). \tag{2.33}$$

We recall that in the limit $\omega \to \omega_n$, $\mathbb{F}(\mathbf{r};\omega)$ should result in $\mathbb{F}_n$. The only way for this to make sense is that the function $\mathbb{S}_n(\mathbf{r})$, which was so far assumed to be arbitrary, is selected such that $\int_V dV\,\mathbb{F}_n^{\ddagger}\cdot\mathbb{S}_n = 1$. Using this condition and following the derivations in Ref. [37] and references therein, we obtain:

$$1 = \underbrace{\int_V dV\,\mathbb{F}_n^{\ddagger}\cdot(\omega\hat{\mathbb{P}})'\mathbb{F}_n}_{V_n} + \underbrace{ic\oint_{\partial V} d\mathbf{S}\cdot\left(\mathbf{E}_n^{\ddagger}\times\mathbf{H}_n' - \mathbf{E}_n'\times\mathbf{H}_n^{\ddagger}\right)}_{S_n}, \tag{2.34}$$

where the prime is again used as an abbreviation to indicate the derivative with respect to ω at ω_n (how exactly this is supposed to be interpreted for the case of $\mathbf{E}'_n$ and $\mathbf{H}'_n$ will be discussed further down). Equation (2.34) is the analytic normalization condition for resonant states. The right-hand side contains two terms: A volume integral V_n and a surface integral S_n. The former is supposed to be carried out over a volume V that surrounds the scattering geometry, while the latter one is meant to cover the surface ∂V of this volume. Note that, while V_n and S_n both depend on the exact choice of the integration volume V, it can be shown that their sum does not [110, 111]. Therefore, the choice of V is completely arbitrary, as long as it completely encompasses the scattering geometry. Note that the volume term V_n is formally identical to the volume term appearing in the perfectly-matched layer normalization from Eq. (2.32). There are, however, two differences: First, there is the aforementioned arbitrariness in the choice of the integration volume. Second, for the analytic normalization, no perfectly-matched layers are required. A visual comparison of the two approaches can be found in Fig. 2.4.

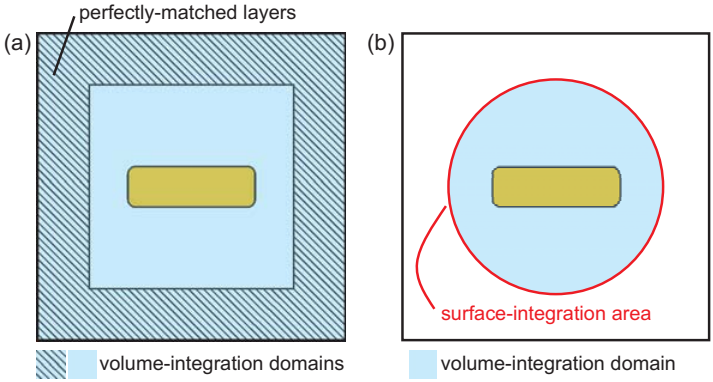

Figure 2.4. Visual comparison of the two normalization approaches. (a) Perfectly-matched layer normalization. The resonator (in our example a metallic nanoantenna) is surrounded by perfectly-matched layers. The volume integral of the normalization is evaluated over the whole calculation domain, including the region of perfectly-matched layers. (b) Analytic normalization. One chooses an arbitrary volume that contains the resonator. A volume integral is evaluated over this volume and additionally, a surface integral is evaluated over the surface of this volume.

Let us now have a closer look at the frequency derivatives $\mathbf{E}'_n$ and $\mathbf{H}'_n$ appearing in the surface term S_n from Eq. (2.34). These derivatives are meant to be understood as the electric and magnetic field components of the supervector $\mathbb{F}'_n = \partial \mathbb{F}_n(\omega)/\partial\omega|_{\omega=\omega_n}$, where $\mathbb{F}_n(\omega)$ represents an analytic continuation of the resonant state's field $\mathbb{F}_n$ in the complex frequency plane. How can one define this analytic continuation? One may be tempted to take $\mathbb{F}(\mathbf{r};\omega)$ from Eq. (2.33) and consider this quantity as an analytic continuation of $\mathbb{F}_n$ to the complex frequency plane. However, this approach is problematic for two reasons: First, it results in an expression that depends on all resonant states and on the specific form of $\mathbb{S}_n$. Second, as it will be discussed later (cf. subsection 2.2.6), it is questionable if Eq. (2.33) is valid everywhere in the exterior of the resonator. To resolve the issues, we will present two methods for defining the analytic continuation and evaluating the field derivative $\mathbb{F}'_n$ that do not suffer from the above problems. Method 1 is well-known from literature [35, 37, 41, 52, 111] and relatively easy to implement, but restricted to the special case of resonators that are embedded in a rather simple surrounding where one can analytically write down a complete set of basis functions that allow us to decompose the resonant field. Method 2 is a bit more sophisticated, but – in principle – applicable to any type of surrounding without any back reflection from outside the resonator. The prerequisite is that the Green's dyadic of the background system is known.

METHOD 1: DECOMPOSITION INTO BASIS FUNCTIONS.

If the surrounding is rather trivial with a known set of basis functions, any field distribution generated by sources inside the resonator can be expanded in terms of outgoing basis functions $\mathbb{O}_{\mathbf{N}}$ of the surrounding system [45]. Here, $\mathbf{N}$ is a vector that summarizes all labels to distinguish the outgoing basis functions. Consequently, one can define the analytic continuation of $\mathbb{F}_n$ as [45]:

$$\mathbb{F}_n(\mathbf{r};\omega) = \sum_{\mathbf{N}} \alpha_{\mathbf{N}}^{(n)}(\omega)\mathbb{O}_{\mathbf{N}}(\mathbf{r};\omega), \tag{2.35}$$

where $\alpha_{\mathbf{N}}^{(n)}(\omega)$ represent frequency-dependent expansion coefficients. Differentiating this expression with respect to ω at ω_n gives $\mathbb{F}'_n(\mathbf{r}) = \sum_{\mathbf{N}}(\alpha_{\mathbf{N}}^{(n)})'\mathbb{O}_{\mathbf{N}}(\mathbf{r};\omega_n) + \sum_{\mathbf{N}} \alpha_{\mathbf{N}}^{(n)}(\omega_n)\mathbb{O}'_{\mathbf{N}}(\mathbf{r})$. The first sum does not contribute to the surface integral S_n from Eq. (2.34). This follows from facts that both $\mathbb{F}_n^{\ddagger}$ and the first sum do only contain outgoing fields at the

frequency ω_n and that the integral between such fields vanishes, as shown by Eq. (2.24). Therefore, we can ignore the first sum, and may define

$$\mathbb{F}'_n(\mathbf{r}) = \sum_{\mathrm{N}} \alpha_{\mathrm{N}}^{(n)}(\omega_n)\mathbb{O}'_{\mathrm{N}}(\mathbf{r}). \tag{2.36}$$

where $\mathbb{O}'_{\mathrm{N}}$ is the frequency derivative of $\mathbb{O}_{\mathrm{N}}$ at ω_n, which can be expressed analytically. This approach for calculating $\mathbb{F}'_n$ has been used, e.g., for normalizing resonant states in planar periodic systems [52, 111]. For isolated nanostructures in a homogeneous and isotropic surrounding, it is possible to convert the frequency derivative into a spatial derivative [35, 37, 41], which simplifies the calculation of $\mathbb{F}'_n$ significantly.

METHOD 2: USING THE GREEN'S DYADIC OF THE BACKGROUND SYSTEM

We start with Eq. (2.15) and separate the material distribution $\hat{\mathbb{P}}$ that occurs in $\hat{\mathbb{M}}$ into a background system $\hat{\mathbb{P}}_{\mathrm{BG}}$ and a resonator contribution $\Delta\hat{\mathbb{P}}$. This gives

$$\hat{\mathbb{M}}_{\mathrm{BG}}\mathbb{F} = -\frac{\omega}{c}\Delta\hat{\mathbb{P}}\mathbb{F} + \frac{\omega-\omega_n}{c}\mathbb{S}_n, \tag{2.37}$$

where we have introduced the Maxwell operator of the background system as

$$\hat{\mathbb{M}}_{\mathrm{BG}} = \frac{\omega}{c}\hat{\mathbb{P}}_{\mathrm{BG}} - \hat{\mathbb{D}}. \tag{2.38}$$

Let us assume that we know the Green's dyadic $\hat{\mathbb{G}}_0$ of the background system. This allows us to reformulate Eq. (2.37) via Eq. (2.5) as

$$\mathbb{F} = \int_V dV\hat{\mathbb{G}}_0\left(-\frac{\omega}{c}\Delta\hat{\mathbb{P}}\mathbb{F} + \frac{\omega-\omega_n}{c}\mathbb{S}_n\right). \tag{2.39}$$

For the interested reader, we want to remark that for $\mathbb{S}_n = 0$, this formulation is equivalent to the regularized resonant fields in Ref. [149].

Differentiating Eq. 2.39 with respect to ω at ω_n provides:

$$\mathbb{F}' = -\frac{\omega_n}{c}\int_V dV\hat{\mathbb{G}}_0'\Delta\hat{\mathbb{P}}(\omega_n)\mathbb{F}_n + \frac{1}{c}\int_V dV\hat{\mathbb{G}}_0\left[\mathbb{S}_n - (\omega\Delta\hat{\mathbb{P}})'\mathbb{F}_n - \omega_n\Delta\hat{\mathbb{P}}(\omega_n)\mathbb{F}'\right]. \tag{2.40}$$

The second part contains only sources located inside the resonator, so that it yields purely outgoing fields outside the resonator. Hence, we infer from

the condition given by Eq. (2.24) that the fields generated by this source do not contribute to the surface integral in Eq. (2.34). The first part, however, contains the derivative $\hat{\mathbb{G}}_0'$ instead of the Green's dyadic, so that we must assume that this results in a nonvanishing contribution to Eq. (2.34). Therefore, we may define $\mathbb{F}_n'$ via

$$\mathbb{F}_n' = -\frac{\omega_n}{c} \int_V dV \hat{\mathbb{G}}_0' \Delta\hat{\mathbb{P}}(\omega_n) \mathbb{F}_n, \tag{2.41}$$

which is solely given by the underlying differential equation and the corresponding resonant field distribution $\mathbb{F}_n$. This method is expected to work for any kind of background system, as long as its Green's dyadic $\hat{\mathbb{G}}_0$ is known and warrants outgoing boundary conditions outside the resonator.

2.2.3.3 *Further remarks on the normalization*

It should be mentioned that in earlier works on analytic normalizations with surface terms, the starting point was the wave equation instead of the curl Maxwell's equations [35, 41, 50, 52, 109–111]. It has been shown that for nonmagnetic materials, these normalizations are equivalent to Eq. (2.34), except for an artificial factor of $\sqrt{2}$ [37]. However, they cannot be used for magnetic, bi-isotropic, and bi-anisotropic materials.

Comparing the normalization via perfectly-matched layers with the analytic normalization, the advantage of the perfectly-matched layers is that this approach can be used for any sort of resonator geometry. However, care has to be taken regarding the proper definition of the perfectly-matched layers. If they do not suppress back-reflection sufficiently or their discretization is not selected appropriately, the normalization via perfectly-matched layers will provide inaccurate results. Furthermore, as noted above, in systems such as planar slabs, the definition of incoming and outgoing fields may be not straight-forward on the complex frequency plane in the vicinity of Rayleigh-Wood anomalies. It may then happen that certain resonant states cannot be found numerically. Finally, not all numerical methods include perfectly-matched layers. In the case of the analytic normalization, the advantage is that we can obtain fully analytic equations in some cases such as slabs [109] or spheres [50]. Furthermore, it is possible to restrict the computational domain to a minimal volume surrounding the resonator. The main requirement is that the fields are calculated accurately enough at the surface and in the interior. The disadvantage of the analytic normalization is, however, that there is only a limited number of systems with known

surface integrals. Most importantly, the practically relevant case of a single resonator on top of a substrate is yet not solved analytically.

At the end, it should be mentioned that an alternative numerical normalization procedure is described in Refs. [112, 150]. In this approach, the system is driven by a source that oscillates at a complex frequency in the vicinity of the pole ω_n. Then, it is assumed that the resulting field distribution resembles the correctly normalized resonant state $\mathbb{F}_n$ multiplied by some proportionality factor, which can be deduced easily. In some sense, this can be considered as a numerical variant of assigning the correct weight to the residues of the Green's dyadic.

2.2.4 *Orthogonality relation*

Let us now derive an orthogonality relation for resonant states. When considering Eq. (2.8) for a resonant state with index n and Eq. (2.25) for a resonant state with index m, we may multiply Eq. (2.8) with $\mathbb{F}_m^\ddagger$ and Eq. (2.25) with $\mathbb{F}_n$ to obtain:

$$\mathbb{F}_m^\ddagger \cdot \left[\frac{\omega_n}{c}\hat{\mathbb{P}}(\omega_n) - \frac{\omega_m}{c}\hat{\mathbb{P}}(\omega_m)\right] \mathbb{F}_n - \mathbb{F}_m^\ddagger \cdot \hat{\mathbb{D}}\mathbb{F}_n + \mathbb{F}_n \cdot \hat{\mathbb{D}}\mathbb{F}_m^\ddagger = 0. \quad (2.42)$$

Integrating over a volume V and using the vector identities in Eq. (2.20) results in the following orthogonality relation:

$$\int_V dV \mathbb{F}_m^\ddagger \cdot \left[\omega_n \hat{\mathbb{P}}(\omega_n) - \omega_m \hat{\mathbb{P}}(\omega_m)\right] \mathbb{F}_n + ic \oint_{\partial V} d\mathbf{S} \cdot (\mathbf{E}_m^\ddagger \times \mathbf{H}_n - \mathbf{E}_n \times \mathbf{H}_m^\ddagger) = 0. \quad (2.43)$$

Similar expressions are given in Ref. [50] for non-dispersive and non-magnetic systems. In the case that we enclose the system by perfectly-matched layers, one may argue that the surface integral vanishes at the outermost interfaces of the perfectly-matched layers, resulting in the following orthogonality relation [38]:

$$\int_{\tilde{V}} dV \tilde{\mathbb{F}}_m^\ddagger \cdot \left[\omega_n \tilde{\mathbb{P}}(\omega_n) - \omega_m \tilde{\mathbb{P}}(\omega_m)\right] \tilde{\mathbb{F}}_n = 0. \quad (2.44)$$

2.2.5 *Near-field expansion*

In the following, we will discuss how the fields inside the resonator can be expanded in terms of the resonant states. Using the Green's dyadic expansion from Eq. (2.26) in Eq. (2.5), it is possible to write the fields $\mathbb{F}$ that are generated by an internal source $\mathbb{J}$ in the resonator as

$$\mathbb{F}(\mathbf{r};\omega) = c\sum_n \frac{\mathbb{F}_n(\mathbf{r})}{\omega-\omega_n}\int dV' \mathbb{F}_n^{\ddagger}(\mathbf{r}')\cdot\mathbb{J}(\mathbf{r}';\omega). \tag{2.45}$$

This yields a suitable near-field expansion for local sources that can be used in many practical applications [36, 38, 41]. Often, one is not interested in the fields that are generated by a local source $\mathbb{J}$, but in the scattered field that is generated by a given incident field. Following the derivations of Ref. [129], we now derive an expression for this scattered field.

Let us consider a region in space that is free of sources, i.e., the right-hand side of Eq. (2.3) is zero. In that case, the electromagnetic fields usually consist of incoming and outgoing parts. As described in Ref. [38, 45], we first separate the total system into a background system with material distribution $\hat{\mathbb{P}}_{\mathrm{BG}}$ and a local scattering part $\Delta\hat{\mathbb{P}} = \hat{\mathbb{P}} - \hat{\mathbb{P}}_{\mathrm{BG}}$ for the resonator, see Eq. (2.11). Then an arbitrary incoming field $\mathbb{I}_{\mathrm{BG}}$ may be regarded as the incoming part of a background field $\mathbb{F}_{\mathrm{BG}} = \mathbb{I}_{\mathrm{BG}} + \mathbb{O}_{\mathrm{BG}}$, where $\mathbb{O}_{\mathrm{BG}}$ is the corresponding outgoing field. The background field $\mathbb{F}_{\mathrm{BG}}$ is a solution of the following Maxwell's equations:

$$\hat{\mathbb{M}}_{\mathrm{BG}}(\mathbf{r};\omega)\mathbb{F}_{\mathrm{BG}}(\mathbf{r};\omega) = 0. \tag{2.46}$$

Here, $\hat{\mathbb{M}}_{\mathrm{BG}}$ is the Maxwell operator of the background system, see Eq. (2.38). Thus, the total field supervector can be expressed as a superposition of the background and a scattered field as $\mathbb{F}_{\mathrm{tot}} = \mathbb{F}_{\mathrm{BG}} + \mathbb{F}_{\mathrm{scat}}$. Although it is common to consider homogeneous and isotropic background material distributions $\hat{\mathbb{P}}_{\mathrm{BG}}$, it is as well possible to introduce more complex background systems such as planar interfaces between two materials to account, e.g., for the presence of substrates. After some algebra, we obtain [38, 45]:

$$\hat{\mathbb{M}}(\mathbf{r};\omega)\mathbb{F}_{\mathrm{scat}}(\mathbf{r};\omega) = -\frac{\omega}{c}\Delta\hat{\mathbb{P}}(\mathbf{r};\omega)\mathbb{F}_{\mathrm{BG}}(\mathbf{r};\omega). \tag{2.47}$$

The right-hand side can be interpreted as an internal source for the scattered field, which allows us to construct the total field via Eq. (2.45) as [129]

$$\mathbb{F}_{\mathrm{tot}}(\mathbf{r};\omega) = \mathbb{F}_{\mathrm{BG}}(\mathbf{r};\omega) - \sum_n \frac{I_n(\omega)}{\omega - \omega_n}\mathbb{F}_n(\mathbf{r}), \tag{2.48}$$

where we have introduced the overlap integral

$$I_n(\omega) = \omega \int dV \mathbb{F}_n^{\ddagger}(\mathbf{r}) \cdot \Delta\hat{\mathbb{P}}(\mathbf{r};\omega)\mathbb{F}_{\mathrm{BG}}(\mathbf{r};\omega). \tag{2.49}$$

Equation (2.48) defines a pole expansion of the total field. This approach is broadly used as a semi-analytical method to expand the near fields for a given resonator system [38, 45, 112]. However, it has been noted that such an expansion is not unique [38, 129, 139, 151, 152]. For instance, several formulations are benchmarked numerically for Lorentz-dispersive materials [152], and a whole family of possible expansions with different frequency-dependent weight functions is discussed in Ref. [139]. Unger and coworkers suggest an independent expansion of electric and magnetic fields [151], which provides more degrees of freedom and can be applied efficiently for certain geometries and materials with $\zeta = \xi = 0$.

While Eq. (2.47) and most other formulations contain weight functions of the poles that depend on frequency, Ref. [129] provides an alternative formulation with constant weight functions. The idea is to consider Eq. (2.47) as a function that is analytic except for a countable number of poles and to apply the Mittag-Leffler theorem once more. However, care has to be taken because the asymptotic behavior is usually more sophisticated than that of the Green's dyadic. This means that one has to check if the prerequisites for the Mittag-Leffler theorem are fulfilled. Often, higher-order versions of the Mittag-Leffler theorem have to be applied, i.e., $p > 0$ in Eq. (2.13). If the background field is free of poles, such as in the case of a homogeneous and isotropic background material, the p^{th}-order Mittag-Leffler expansion of the total field yields

$$\mathbb{F}_{\mathrm{tot}}(\mathbf{r};\omega) = \mathbb{F}_p(\mathbf{r};\omega) - \sum_n \frac{I_n(\omega_n)}{(\omega - \omega_n)}\mathbb{F}_n(\mathbf{r}), \tag{2.50}$$

where $\mathbb{F}_0 = 0$, while $\mathbb{F}_p$ is a polynomial of order $p-1$:

$$\mathbb{F}_p(\mathbf{r};\omega) = \sum_{m=0}^{p-1} a_m \omega^m, \tag{2.51}$$

$$a_m = \frac{\mathbb{F}_{\text{tot}}^{(m)}(\mathbf{r};0)}{m!} - \sum_n \frac{I_n(\omega_n)}{\omega_n^{m+1}} \mathbb{F}_n(\mathbf{r}). \tag{2.52}$$

Here, $\mathbb{F}_{\text{tot}}^{(m)}$ denotes the m^{th} derivative of $\mathbb{F}$ with respect to ω. Evidently, the pole contribution in Eq. (2.50) is much simpler than that in Eq. (2.48), since it requires calculating the overlap integral in Eq. (2.49) only once at the complex frequencies ω_n of the poles. The drawback is that we need to account for a more complex background. A comparison of Eq. (2.48) with the zeroth- and first-order version of Eq. (2.50) is displayed in Fig. 2.5 for the example of a planar dielectric slab. It can be seen that the zeroth-order version fails at the top interface, because the asymptotic behavior of the total field at the top interface prevents the application of the zeroth-order Mittag-Leffler expansion [129].

At the end of this subsection, we would like to sketch an alternative derivation for the pole contribution in Eq. (2.50) from Eq. (2.47) that does not require the pole expansion of the Green's dyadic and yields directly the correct normalization. First, we multiply Eq. (2.47) from the left with $\mathbb{F}_n^\ddagger$. Then, we subtract a zero in the form $\mathbb{F}_{\text{scat}} \cdot \hat{\mathbb{M}}^\ddagger(\omega_n)\mathbb{F}_n^\ddagger$, which yields:

$$\begin{aligned} &\mathbb{F}_n^\ddagger \cdot \left[\frac{\omega}{c}\hat{\mathbb{P}}(\omega) - \frac{\omega_n}{c}\hat{\mathbb{P}}(\omega_n)\right] \mathbb{F}_{\text{scat}} \\ -\mathbb{F}_n^\ddagger \cdot \hat{\mathbb{D}}\mathbb{F}_{\text{scat}} &+ \mathbb{F}_{\text{scat}} \cdot \hat{\mathbb{D}}\mathbb{F}_n^\ddagger = -\frac{\omega}{c}\mathbb{F}_n^\ddagger \cdot \Delta\hat{\mathbb{P}}(\omega)\mathbb{F}_{\text{BG}}. \end{aligned} \tag{2.53}$$

The expression in the first line vanishes at ω_n. In order to obtain finite results for the scattered field, we therefore assume that the scattered field can be expanded as[4]

$$\mathbb{F}_{\text{scat}} = -c \sum_n \frac{b_n(\omega)}{\omega - \omega_n} \mathbb{F}_n. \tag{2.54}$$

4 The factor $-c$ has been introduced for the sake of consistency with an expressions for the far field that we will provide in subsection 2.2.7.

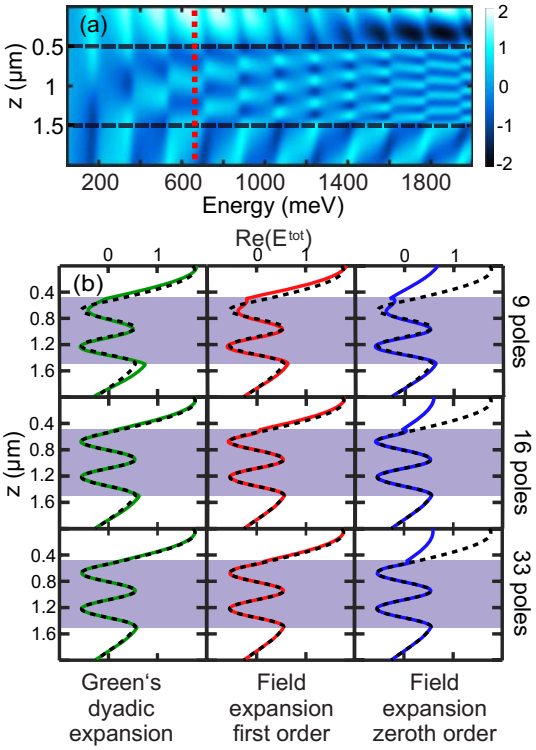

Figure 2.5. Near field in a dielectric slab with refractive index $n = 3.5$ and thickness 1 μm in air. Panel (a) displays the analytic near field as a function of photon energy. In panel (b), the comparison of different formulations for the pole expansion of the near field is shown at a photon energy of 650 meV [red dashed line in (a)]: The results on the left have been calculated via Eq. (2.48). The other results have been obtained using Eq. (2.50) in its first- (middle) and zeroth-order (right) formulation. From top to bottom, the number of poles is increased from 9 over 17 to 33. The dotted lines denote the analytic results. All approaches converge to the analytic result, except for the zeroth-order formulation, which cannot be applied at the top interface. Reprinted with permission from Ref. [129], copyright 2020, Optica.

By integrating over Eq. (2.53) and using the orthogonality relation in Eq. (2.43), we then obtain in the limit $\omega \to \omega_n$:

$$b_n(\omega_n) = \frac{1}{c}\frac{I_n(\omega_n)}{V_n + S_n}. \tag{2.55}$$

The expressions V_n and S_n in the denominator are defined in Eq. (2.34). In the case that the resonant field distributions are normalized, their sum equals unity, see Eq. (2.34).

This derivation is closely related to that of the so-called orthogonality decomposition [38]. Here, the starting point is to perform the calculations in a system that is surrounded by perfectly-matched layers. In this case, the scattered field can be decomposed everywhere in the calculation domain in terms of the resonant states $\tilde{\mathbb{F}}_n$ of this system. Then, the modal expansion is introduced as $\mathbb{F}_{\text{scat}} = \sum_n a_n(\omega)\tilde{\mathbb{F}}_n$, and an integral over Eq. (2.53) is carried out that spans over the entire calculation domain $\tilde{V}$, including the perfectly-matched layers, so that any occurring surface integrals vanish in that limit. Then, one obtains a matrix operator that needs to be regularized for dispersive media and inverted in order to calculate the coefficients a_n [36]. However, it is important to note that this expansion is only appropriate if one adds numerical solutions to the set of resonant states that are predominantly localized in the region of perfectly-matched layer (often referred to as perfectly-matched-layer modes) and do not have any physical counterpart in a system without these layers [153].

2.2.6 *Completeness*

The question arises if any of the aforementioned modal expansions converges properly and what are the limitations. Most importantly: Is the basis of resonant states actually complete? Regarding the spatial domain of completeness, it is obvious that Eq. (2.45) cannot be correct over the entire space. The reason is that fields generated by a local source at a real-valued frequency remain in general finite – particularly far away from the source. However, the resonant field distributions grow with distance to the resonator. The attempt of expressing a finite field by using only exponentially growing functions is condemned to fail. Therefore, strictly speaking, the pole expansion of the Green's dyadic in Eq. (2.26) is only valid inside the resonator and at its outermost interfaces. Nevertheless, Kristensen and coworkers identify a so-called region of consistency in the vicinity of the resonator, in which the expansion in terms of resonant states still gives reasonably accurate results [39]. When calculating in a system that is surrounded by perfectly-matched layers, the situation is slightly different: In this case, the modal expansion and therefore Eq. (2.26) can be assumed to be complete over the whole calculation domain. However, it is important to note that

this is only true if the non-physical modes that are localized in the regions of perfectly-matched layers are included [153].

Another question is the completeness in the interior. While the closure relation given by Eq. (2.27) yields the necessary condition for a complete basis, the sum rules in Eq. (2.29) indicate that the basis of resonant states can be overcomplete. This fact was already noted in the context of resonant states in quantum mechanics [118, 154]. An open question in this context is the completeness in the presence of exceptional points, where we find fewer linear independent resonant field distributions than eigenfrequencies.

It should be also mentioned that there is often another contribution to the pole expansion of the Green's dyadic. More specifically, the analytic continuation of the Green's dyadic to the complex frequency plane may contain cuts[5] that arise, e.g., due to selecting appropriate Riemann sheets in the case of complex square roots [106, 128]. In this general case, the Green's dyadic can be expanded as [49, 106, 111]

$$\hat{\mathbb{G}}(\mathbf{r},\mathbf{r}';\omega) = c\sum_n \frac{\mathbb{F}_n(\mathbf{r})\otimes\mathbb{F}_n^{\ddagger}(\mathbf{r}')}{\omega-\omega_n} + \sum_m \hat{\mathbb{G}}_m(\mathbf{r},\mathbf{r}';\omega), \tag{2.56}$$

where m labels the individual cut contributions with

$$\hat{\mathbb{G}}_m(\mathbf{r},\mathbf{r}';\omega) = \frac{1}{2\pi i}\int\limits_{C_m} d\omega' \frac{\Delta\hat{\mathbb{G}}(\mathbf{r},\mathbf{r}';\omega')}{\omega-\omega'}, \tag{2.57}$$

in which C_m denotes a path along the m^{th} cut and $\Delta\hat{\mathbb{G}}$ represents the difference between the Green's dyadic on the different Riemann sheets. In numerical calculations, these cut contributions can be discretized [49], and single cuts can be circumvented by using analytic continuations over other parameters than complex frequency [109, 128]. Furthermore, in systems surrounded by perfectly-matched layers, these cut contributions disappear and are replaced by a bunch of numerical modes [38, 153]. However, a general analytical treatment of arbitrary cut contributions is still to be developed.

Additionally, there is another issue arising due to the discontinuities of the electric and magnetic fields. Whenever it is required to expand quantities with discontinuities by basis functions that exhibit no appropriate discontinuities, the convergence of this expansion will suffer from the Gibbs

5 For the mathematically less experienced reader, it should be noted that a cut can be understood as a curve in the complex plane across which an (otherwise) analytic function is discontinuous.

phenomenon, which is well-understood in the framework of numerical calculations via the Fourier-modal method [155–158]. When using resonant states as basis, a possible solution is to include so-called static modes [120], which are not solutions of Maxwell's equations in a physical sense. This aspect will be discussed later in section 2.3.1. Finally, for the interested reader, it should be mentioned that a very recent review on the completeness of resonant state in different systems can be found in Ref. [159].

2.2.7 *Far-field expansion*

In the following, we show how the optical far-field response of a resonator can be calculated from its resonant states. Owing to its high practical relevance, we focus on the calculation of the optical scattering matrix [43–45, 125, 160]; however, it should be noted that the presented approach can be extended to other quantities, such as the radiation diagram of emitters that are located inside the resonator [161].

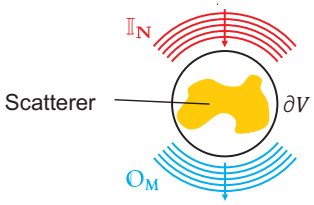

Figure 2.6. Illustration of the basis functions. We choose a surface ∂V that surrounds our resonator. On this surface, one can construct complete and orthogonal sets of incoming $\{\mathbb{I}_N\}$ and outgoing $\{\mathbb{O}_N\}$ basis functions that allow us to decompose any arbitrary field. Indicated is the case of a resonator that is made up of a single scatterer, for which it is convenient to select ∂V as a sphere and to use vector spherical harmonics as basis functions. Note that the above illustration is only meant symbolically, since in reality, vector spherical harmonics are defined over all solid angles instead of only a specific angular range.

Let us now assume we have a local inhomogeneity of materials that defines our resonator. We then choose a surface ∂V that surrounds the resonator. On this surface, one can construct complete and orthogonal sets of incoming $\{\mathbb{I}_N\}$ and outgoing $\{\mathbb{O}_N\}$ basis functions [45, 162] that allow us to decompose

an arbitrary field. For a visualization, see Fig. 2.6. The vector $\mathbf{N}$ is the same as introduced in section 2.2.3 and summarizes all labels needed to specify the basis functions (e.g., their polarization and propagation direction). Note that every incoming basis function $\mathbb{I}_\mathbf{N}$ has an outgoing counterpart $\mathbb{O}_\mathbf{N}$ that describes the same field patterns, but with a reversed propagation direction. The ideal choice of the basis functions depends on the geometry of interest [45]: For resonators consisting of single scatterers, it is convenient to take ∂V as a sphere around the resonator and to select vector spherical harmonics as basis functions. For planar periodic resonators, it is convenient, to take ∂V as two planes, one above and one below the resonator, and to choose plane waves as basis functions.

With the help of the basis functions, any arbitrary incoming field $\mathbb{F}_\text{in}(\mathbf{r};\omega)$ on the surface ∂V can be decomposed as

$$\mathbb{F}_\text{in}(\mathbf{r};\omega) = \sum_\mathbf{N} \alpha_\mathbf{N}^\text{in}(\omega)\mathbb{I}_\mathbf{N}(\mathbf{r};\omega). \tag{2.58}$$

where $\alpha_\mathbf{N}^\text{in}(\omega)$ are some frequency-dependent expansion coefficients. In an analogous manner, every arbitrary outgoing field $\mathbb{F}_\text{out}(\mathbf{r};\omega)$ on this surface can be decomposed as

$$\mathbb{F}_\text{out}(\mathbf{r};\omega) = \sum_\mathbf{N} \alpha_\mathbf{N}^\text{out}(\omega)\mathbb{O}_\mathbf{N}(\mathbf{r};\omega), \tag{2.59}$$

with expansion coefficients $\alpha_\mathbf{N}^\text{out}(\omega)$.

One can define the basis functions $\mathbb{I}_\mathbf{N}(\omega) = [\mathbf{E}_{\mathbb{I},\mathbf{N}}(\omega); i\mathbf{H}_{\mathbb{I},\mathbf{N}}(\omega)]^\mathrm{T}$ and $\mathbb{O}_\mathbf{N}(\omega) = [\mathbf{E}_{\mathbb{O},\mathbf{N}}(\omega); i\mathbf{H}_{\mathbb{O},\mathbf{N}}(\omega)]^\mathrm{T}$ such that they fulfill the following orthogonality relations [45]:

$$i\oint_{\partial V} d\mathbf{S}\cdot(\mathbf{E}_{\mathbb{I},\mathbf{N}}^\ddagger\times\mathbf{H}_{\mathbb{O},\mathbf{M}}-\mathbf{E}_{\mathbb{O},\mathbf{M}}\times\mathbf{H}_{\mathbb{I},\mathbf{N}}^\ddagger) = \delta_{\mathbf{N}\mathbf{M}}, \tag{2.60}$$

$$i\oint_{\partial V} d\mathbf{S}\cdot(\mathbf{E}_{\mathbb{I},\mathbf{N}}\times\mathbf{H}_{\mathbb{O},\mathbf{M}}^\ddagger-\mathbf{E}_{\mathbb{O},\mathbf{M}}^\ddagger\times\mathbf{H}_{\mathbb{I},\mathbf{N}}) = \delta_{\mathbf{N}\mathbf{M}}, \tag{2.61}$$

$$i\oint_{\partial V} d\mathbf{S}\cdot(\mathbf{E}_{\mathbb{I},\mathbf{N}}^\ddagger\times\mathbf{H}_{\mathbb{I},\mathbf{M}}-\mathbf{E}_{\mathbb{I},\mathbf{M}}\times\mathbf{H}_{\mathbb{I},\mathbf{N}}^\ddagger) = 0, \tag{2.62}$$

$$i\oint_{\partial V} d\mathbf{S}\cdot(\mathbf{E}_{\mathbb{O},\mathbf{N}}^\ddagger\times\mathbf{H}_{\mathbb{O},\mathbf{M}}-\mathbf{E}_{\mathbb{O},\mathbf{M}}\times\mathbf{H}_{\mathbb{O},\mathbf{N}}^\ddagger) = 0, \tag{2.63}$$

where we have suppressed the argument ω in the fields for reasons of compactness. In this case, the expansion coefficients from Eqs. (2.58) and (2.59) become:[6]

$$\alpha_{\mathbf{N}}^{\mathrm{in}}(\omega) = -i \oint_{\partial V} d\mathbf{S} \cdot \left[\mathbf{E}_{\mathbb{O},\mathbf{N}}^{\ddagger}(\omega) \times \mathbf{H}_{\mathrm{in}}(\omega) - \mathbf{E}_{\mathrm{in}}(\omega) \times \mathbf{H}_{\mathbb{O},\mathbf{N}}^{\ddagger}(\omega) \right] \tag{2.64}$$

$$\alpha_{\mathbf{N}}^{\mathrm{out}}(\omega) = i \oint_{\partial V} d\mathbf{S} \cdot \left[\mathbf{E}_{\mathbb{I},\mathbf{N}}^{\ddagger}(\omega) \times \mathbf{H}_{\mathrm{out}}(\omega) - \mathbf{E}_{\mathrm{out}}(\omega) \times \mathbf{H}_{\mathbb{I},\mathbf{N}}^{\ddagger}(\omega) \right], \tag{2.65}$$

We would like to mention that the normalized resonant field distributions $\mathbb{F}_n$ have units $\mathrm{m}^{-3/2}$, while Eqs. (2.60) and (2.61) imply that $\mathbb{I}_{\mathbf{N}}$ and $\mathbb{O}_{\mathbf{M}}$ have units m^{-1}. For the sake of consistency, we assume now that all fields except $\mathbb{F}_n$ are given in units m^{-1}. The results can be translated to any other units by multiplying the fields with an appropriate factor.

Let us now introduce the concept of the optical scattering matrix. A typical problem in nanophotonics is that one has a given incident field $\mathbb{F}_{\mathrm{in}}(\mathbf{r};\omega)$ that is impinging on a resonator, and is interested in the outgoing field $\mathbb{F}_{\mathrm{out}}(\mathbf{r};\omega)$ that the resonator is responding with. This interaction can be described via the optical scattering matrix: If the optical scattering matrix $S(\omega)$ of a resonator is known, and the resonator is excited by a particular incident field $\mathbb{F}_{\mathrm{in}}(\mathbf{r};\omega)$ [represented as a decomposition according to Eq. (2.58)], one can express the resulting output field $\mathbb{F}_{\mathrm{out}}(\mathbf{r};\omega)$ [represented as a decomposition according to Eq. (2.59)] via:

$$\alpha_{\mathbf{M}}^{\mathrm{out}}(\omega) = \sum_{\mathbf{N}} S_{\mathbf{MN}}(\omega) \alpha_{\mathbf{N}}^{\mathrm{in}}(\omega), \tag{2.66}$$

where $S_{\mathbf{MN}}(\omega)$ denote the corresponding elements of the scattering matrix. In other words: The optical scattering matrix is a formal way to summarize all possible far-field interactions of a resonator with the outside world. From now on – as it is often done in the context of the scattering matrix – we will refer to the indices **M** and **N** as channels.

In the following, we will show how the optical scattering matrix of a resonator can be calculated from its resonant states. Let us assume that the resonator is excited via the basis function $\mathbb{I}_{\mathbf{N}}(\omega)$. This generates the following fields in the resonator (cf. subsection 2.2.5):

$$\mathbb{F}_{\mathrm{tot},\mathbf{N}}(\omega) = \mathbb{F}_{\mathrm{BG},\mathbf{N}}(\omega) + \mathbb{F}_{\mathrm{scat},\mathbf{N}}(\omega). \tag{2.67}$$

6 Note that a missing minus sign from Ref. [45] is corrected for in Eq. (2.64.)

The subscript **N** is used to emphasize that the fields are the result of excitation via channel **N**. As in subsection 2.2.5, we assume that the background field is known (its exact relation to the basis function depends on the background system, but this relation is usually trivial [45, 125]), while the scattered field is unknown. By applying Eq. (2.65) for channel **M** to Eq. (2.67), the element $S_{\mathbf{MN}}$ of the scattering matrix can then be formally expressed as:

$$S_{\mathbf{MN}}(\omega) = S^{\mathrm{BG}}_{\mathbf{MN}}(\omega) + S^{\mathrm{scat}}_{\mathbf{MN}}(\omega), \tag{2.68}$$

with the scattering matrix of the background system

$$S^{\mathrm{BG}}_{\mathbf{MN}}(\omega) = i \oint_{\partial V} d\mathbf{S} \cdot \left[\mathbf{E}^{\ddagger}_{\mathbb{I},\mathbf{M}}(\omega) \times \mathbf{H}_{\mathrm{BG},\mathbf{N}}(\omega) - \mathbf{E}_{\mathrm{BG},\mathbf{N}}(\omega) \times \mathbf{H}^{\ddagger}_{\mathbb{I},\mathbf{M}}(\omega) \right], \tag{2.69}$$

which only contains known fields and can hence directly be calculated, and a contribution

$$S^{\mathrm{scat}}_{\mathbf{MN}}(\omega) = i \oint_{\partial V} d\mathbf{S} \cdot \left[\mathbf{E}^{\ddagger}_{\mathbb{I},\mathbf{M}}(\omega) \times \mathbf{H}_{\mathrm{scat},\mathbf{N}}(\omega) - \mathbf{E}_{\mathrm{scat},\mathbf{N}}(\omega) \times \mathbf{H}^{\ddagger}_{\mathbb{I},\mathbf{M}}(\omega) \right], \tag{2.70}$$

which contains the yet unknown scattered field and will be evaluated in the following. We will present two alternative approaches for this evaluation, resulting in two alternative representations of the scattering matrix.

2.2.7.1 *Asymmetric representation*

The first representation will be referred to as the asymmetric one. To obtain it, we take Eq. (2.70), then use the expansion of the scattered field given by Eq. (2.54), and insert the result back into Eq. (2.68). This yields the following scattering-matrix expansion [45]:

$$S_{\mathbf{MN}}(\omega) = S^{\mathrm{BG}}_{\mathbf{MN}}(\omega) - c \sum_n \frac{\alpha^{(n)}_{\mathbf{M}}(\omega) b^{(n)}_{\mathbf{N}}(\omega)}{\omega - \omega_n}, \tag{2.71}$$

with the quantities

$$\alpha^{(n)}_{\mathbf{M}}(\omega) = i \oint_{\partial V} d\mathbf{S} \cdot \left[\mathbf{E}^{\ddagger}_{\mathbb{I},\mathbf{M}}(\omega) \times \mathbf{H}_n - \mathbf{E}_n \times \mathbf{H}^{\ddagger}_{\mathbb{I},\mathbf{M}}(\omega) \right] \tag{2.72}$$

and

$$b_{\mathrm{N}}^{(n)}(\omega) = \frac{\omega}{c} \int_V dV \mathbb{F}_n^{\ddagger} \cdot \Delta\hat{\mathbb{P}}(\omega) \mathbb{F}_{\mathrm{BG,N}}(\omega), \tag{2.73}$$

which can be interpreted as the emission and excitation coefficients of resonant state $\mathbb{F}_n$, respectively. Note that these coefficients depend on the frequency ω. The Greek letter $\alpha_{\mathrm{M}}^{(n)}$ for the emission coefficient is used in contrast to the Latin letter $b_{\mathrm{N}}^{(n)}$ for the excitation coefficient, to emphasize that the former contains a surface integral, while the latter contains a volume integral. Owing to this asymmetry, we refer to Eq. (2.71) as the asymmetric representation.

2.2.7.2 *Symmetric representation*

We now come to the second representation, which will be referred to as the symmetric one. Note that, while the above derivation of the asymmetric representation is known from literature [45], the following derivation for the symmetric representation was specifically developed in the context of this thesis and is contained in publication [P6]. We will later, namely in chapters 4 and 5, use the derivation as a starting point to develop a perturbation theory for far-field quantities, which is then applied to understand the light-matter interaction in different nanophotonic sensors. Let us now start the derivation. As a first step, we take Eq. (2.70) and replace the basis function $\mathbb{I}_{\mathbf{M}}^{\ddagger}$ therein by the background field $\mathbb{F}_{\mathrm{BG,M}}^{\ddagger}$ that this basis function would generate when being launched into the resonator. One can easily verify that this replacement is possible by noting that on the surface ∂V, the scattered field $\mathbb{F}_{\mathrm{scat,N}}$ is a superposition of outgoing basis functions, while $\mathbb{F}_{\mathrm{BG,M}}^{\ddagger}$ is a superposition of the incoming basis function $\mathbb{I}_{\mathbf{M}}^{\ddagger}$ with some outgoing basis functions, and by further using the orthogonality relations from Eqs. (2.61) and (2.63). This gives

$$S_{\mathbf{MN}}^{\mathrm{scat}}(\omega) = i \oint_{\partial V} d\mathbf{S} \cdot \left[\mathbf{E}_{\mathrm{BG,M}}^{\ddagger}(\omega) \times \mathbf{H}_{\mathrm{scat,N}}(\omega) - \mathbf{E}_{\mathrm{scat,N}}(\omega) \times \mathbf{H}_{\mathrm{BG,M}}^{\ddagger}(\omega) \right], \tag{2.74}$$

For the second step, we take Eq. (2.74) and use Eq. (2.20) to convert the surface integral into two volume integrals containing the operator $\hat{\mathbb{D}}$. Furthermore, we insert $\hat{\mathbb{D}} = \omega/c\,\hat{\mathbb{P}}^{\ddagger} - \hat{\mathbb{M}}^{\ddagger}$ into the first volume integral and $\hat{\mathbb{D}} = \omega/c\,\hat{\mathbb{P}} - \hat{\mathbb{M}}$ into the second one, replace $\hat{\mathbb{M}}^{\ddagger} = \hat{\mathbb{M}}_{\mathrm{BG}}^{\ddagger} + \omega/c\Delta\hat{\mathbb{P}}^{\ddagger}$, use Eqs. (2.46) and (2.47) (the former in its transposed version), and utilize the identities $\hat{\mathbb{P}}^{\ddagger} = \hat{\mathbb{P}}^{\mathrm{T}}$ and $\Delta\hat{\mathbb{P}}^{\ddagger} = \Delta\hat{\mathbb{P}}^{\mathrm{T}}$, which allow us to invert the order of

the quantities under the integrals as $\mathbb{F}_{\mathrm{scat,N}} \cdot \hat{\mathbb{P}}^{\ddagger}\mathbb{F}^{\ddagger}_{\mathrm{BG,M}} = \mathbb{F}^{\ddagger}_{\mathrm{BG,M}} \cdot \hat{\mathbb{P}}\mathbb{F}_{\mathrm{scat,N}}$ and $\mathbb{F}_{\mathrm{scat,N}} \cdot \Delta\hat{\mathbb{P}}^{\ddagger}\mathbb{F}^{\ddagger}_{\mathrm{BG,M}} = \mathbb{F}^{\ddagger}_{\mathrm{BG,M}} \cdot \Delta\hat{\mathbb{P}}\mathbb{F}_{\mathrm{scat,N}}$. Altogether, this gives

$$\begin{aligned} S^{\mathrm{scat}}_{\mathbf{MN}}(\omega) = &-\frac{\omega}{c}\int_V dV \left[\mathbb{F}^{\ddagger}_{\mathrm{BG,M}}(\omega)\cdot\Delta\hat{\mathbb{P}}(\omega)\mathbb{F}_{\mathrm{BG,N}}(\omega)\right] \\ &-\frac{\omega}{c}\int_V dV \left[\mathbb{F}^{\ddagger}_{\mathrm{BG,M}}(\omega)\cdot\Delta\hat{\mathbb{P}}(\omega)\mathbb{F}_{\mathrm{scat,N}}(\omega)\right]. \end{aligned} \tag{2.75}$$

Finally, we take the above result, insert the expansion of the scattered field from Eq. (2.54), and plug everything into Eq. (2.68). Consequently, we end up with the following scattering-matrix representation:

$$S_{\mathbf{MN}}(\omega) = S^{\mathrm{BG}}_{\mathbf{MN}}(\omega) + S^{\mathrm{Born}}_{\mathbf{MN}}(\omega) + c\sum_n \frac{a^{(n)}_{\mathbf{M}}(\omega) b^{(n)}_{\mathbf{N}}(\omega)}{\omega - \omega_n}. \tag{2.76}$$

Comparing this representation with the asymmetric representation from Eq. (2.71), we note that there is an additional background term

$$S^{\mathrm{Born}}_{\mathbf{MN}}(\omega) = -\frac{\omega}{c}\int_V dV \mathbb{F}^{\ddagger}_{\mathrm{BG,M}}(\omega)\cdot\Delta\hat{\mathbb{P}}(\omega)\mathbb{F}_{\mathrm{BG,N}}(\omega), \tag{2.77}$$

and a modified numerator with the excitation coefficient $b^{(n)}_{\mathbf{M}}(\omega)$ known from Eq. (2.73) and an emission coefficient

$$a^{(n)}_{\mathbf{M}}(\omega) = \frac{\omega}{c}\int_V dV \mathbb{F}^{\ddagger}_{\mathrm{BG,M}}(\omega)\cdot\Delta\hat{\mathbb{P}}(\omega)\mathbb{F}_n. \tag{2.78}$$

Since Eq. (2.76) contains emission and excitation coefficients $a^{(n)}_{\mathbf{M}}$ and $b^{(n)}_{\mathbf{M}}$, respectively, that are both defined via volume integrals, we refer to it as the symmetric representation. To emphasize the symmetry, both the emission and excitation coefficients are written with Latin letters. In contrast to the asymmetric representation, the symmetric representation contains the additional term $S^{\mathrm{Born}}_{\mathbf{MN}}$, which comprises an overlap integral between the two background fields and can be interpreted as a Born-like scattering interaction [125]. Note that in Ref. [125], an alternative derivation of the symmetric representation is provided, which is based on the orthogonality-decomposition approach (for an explanation, see subsection 2.2.4). In this work, it is claimed that the asymmetric representation derived in Ref. [45] is incomplete. However, this appears to be a misinterpretation, since, as shown

above, both representations are equally valid and can be converted from one to the other. Furthermore, it should be mentioned that the two representations that were presented here, are not the only ones that are possible. For instance, instead of expanding only $\mathbb{F}_{\text{scat}}$ in terms of the resonant states while keeping $\mathbb{F}_{\text{BG}}$ as it is, one can also expand the total field $\mathbb{F}_{\text{tot}}$, which provides another valid scattering-matrix representation [44]. However, a detailed discussion of this latter representation is beyond the scope of this work.

2.2.7.3 *Simplified ω dependence*

All the scattering-matrix representations mentioned so far have the drawback that they contain ω-dependent overlap integrals. This may slow down practical computations, since the integrals have to be evaluated repeatedly. In analogy to the near-field case from subsection 2.2.5, it is possible to remove the ω dependence. The idea is to consider $S_{\text{MN}}(\omega)$ as a function that is analytic in ω, except for a countable number of poles, and applying the Mittag-Leffler theorem once more. Note that, as in the near-field case, the prerequisites have to be checked, especially regarding the asymptotic behavior of $S_{\text{MN}}(\omega)$ for $\omega \to \infty$.

We will now show the application of the Mittag-Leffer theorem for the example of the asymmetric representation from Eq. (2.71). An analogous procedure can be applied to the other representations (a detailed procedure for the case of the symmetric representation can be found in Ref. [125]). We start with Eq. (2.71) and apply the Mittag-Leffler theorem. Then, we replace the volume integral in Eq. (2.73) via simple algebra by a surface integral using [45]

$$b_{\text{N}}^{(n)}(\omega_n) = \beta_{\text{N}}^{(n)}(\omega_n), \tag{2.79}$$

with

$$\beta_{\text{N}}^{(n)}(\omega) = i \oint_{\partial V} d\mathbf{S} \cdot \left[\mathbf{E}_n^{\ddagger}(\omega) \times \mathbf{H}_{\mathbb{I},\text{N}} - \mathbf{E}_{\mathbb{I},\text{N}} \times \mathbf{H}_n^{\ddagger}(\omega) \right]. \tag{2.80}$$

Assuming a resonance-free background system, this gives [compare Eqs. (2.50) to (2.52) for the near-field case] [45]

$$S_{\text{MN}}(\omega) = S_{\text{MN}}^{p}(\omega) - c \sum_n \frac{\alpha_{\text{M}}^{(n)}(\omega_n) \beta_{\text{N}}^{(n)}(\omega_n)}{\omega - \omega_n}, \tag{2.81}$$

where $S^0_{\mathrm{MN}} = 0$, while S^p_{MN} is a polynomial of order $p-1$:

$$S^p_{\mathrm{MN}}(\omega) = \sum_{m=0}^{p-1} A^{(m)}_{\mathrm{MN}} \omega^m, \tag{2.82}$$

with matrix coefficients

$$A^{(m)}_{\mathrm{MN}} = \frac{S^{(m)}_{\mathrm{MN}}(0)}{m!} - c \sum_n \frac{\alpha^{(n)}_{\mathrm{M}}(\omega_n)\beta^{(n)}_{\mathrm{N}}(\omega_n)}{\omega_n^{m+1}}. \tag{2.83}$$

Here, $S^{(m)}_{\mathrm{MN}}$ denotes the m^{th} derivative of S_{MN} with respect to ω. The advantage of Eq. (2.81) compared to Eqs. (2.71) and (2.76) is a highly simplified ω dependence, where the excitation and emission coefficients have to be evaluated only once at the complex frequencies ω_n. The price to pay is, however, that one needs to deal with a more sophisticated background term S^p_{MN}.

Let us briefly discuss how to deal with such a background term. There are several possibilities: In analytically solvable systems (e.g., a dielectric slab resonator [45, 125]), the background term can be determined via its defining equation. However, in numerical calculations, this can be difficult, especially due to the occurrence of the ω derivatives. Here, a highly practical approach consists in including only a small number of poles in the scattering matrix expansion (enough to accurately resolve all relevant features within the spectral region of interest) and accounting for the background term S^p_{MN} as well as for the influence of all other poles by an additional polynomial, which can be fitted, e.g., from numerically exact calculations [45]. As an alternative to the fit, one can also establish symmetry constraints for the scattering matrix, and introduce a weighting of the coefficients that minimizes the error in the expansion [43]. This latter approach was recently refined by explicitely taking energy conservation into account [160]. For single resonant states, this regularization can be achieved even analytically, as shown already in 2005 by Gippius *et al.* [163]. Another alternative way to account for the influence of such a background as well as for that of remaining poles consists in the use of a Riesz-projection method [42, 161]. An important benefit of all of the above-mentioned approaches is that they allow one to accurately resolve resonant spectral features, while at the same time keeping the computational efforts very low compared to, e.g., full numerical calculations. An interesting open question to be answered is which method provides the best convergence performance for which kind of application.

An example calculation for the scattering-matrix expansion is shown in Fig. 2.7. The example is taken from Ref. [45]. Displayed are the transmittance, reflectance, and absorbance of a one-dimensional photonic crystal slab as a function of photon energy. The dots represent exact full-wave calculations (performed with the Fourier-modal method [164, 165]), while the lines denote the result of the pole expansion from Eq. (2.81). In the pole expansion, four resonant states, located at $2676.2 - 0.2i$ meV, $3180.0 - 92.7i$ meV, $3719.3 - 9.7i$ meV, and $3854.7 - 0.7i$ meV, have been considered together with a cubic fit for the background. It is evident that there is an excellent agreement between both calculation approaches. Note, however, that the predictions of the pole-expansion have been obtained with much less computational efforts than the results of the full-wave calculations, since the latter ones require one separate computation for each step on the energy axis.

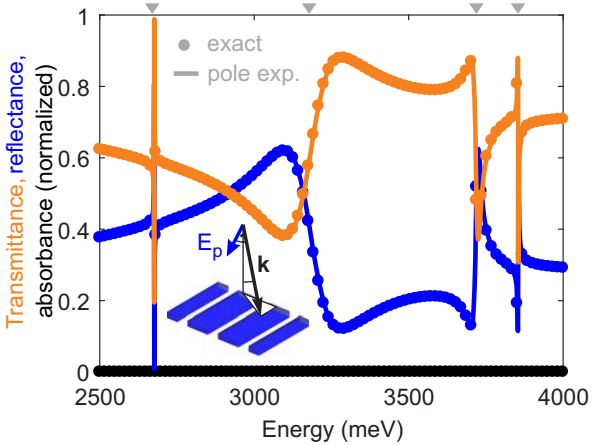

Figure 2.7. Pole expansion of the transmittance (orange), reflectance (blue), and absorbance (black) for p-polarized incidence at fixed in-plane wavevectors $k_x = k_y = 0.2\ \mu\text{m}^{-1}$ in the case of a one-dimensional photonic crystal slab. Numerically exact results are shown by dots, while the pole expansion with four resonant states and a cubic background fit is given by solid lines. The real part of the complex eigenfrequencies is indicated by the gray triangles at the top. Reprinted with permission from Ref. [45], copyright 2018, American Physical Society.

At the end of this subsection, let us use the insight of the pole expansion, to discuss some general deductions about the interplay between different resonances: When looking at the spectral lineshapes in Fig. 2.7, we can see that the resonant features not only differ in the resonant linewidths, but also in their shapes. Taking only a single pole contribution from Eq. (2.81), one would expect that each resonant state is manifested as a Lorentzian in the spectrum. However, the interplay between the various resonant states and the background results in the rich diversity of spectral lineshapes. A good overview of the classification of resonant lineshapes and their physical origin can be found in Ref. [166]. One prominent example is that of a Fano resonance [25, 167–170], which can be also observed in Fig. 2.7 with the typical asymmetry due to the interplay between the background and the resonant contribution. Fano lineshapes arise due to the coupling of a continuum with a single resonant state or the coupling of a broad optically active resonant state and a resonant state that is optically inactive [166]. A special case for Fano resonances is that of electromagnetically induced transparency, which occurs in the weak coupling regime between two resonant states with identical real parts of the eigenfrequencies [9, 166, 171, 172].

2.3 APPLICATIONS

Let us now discuss some applications of the theory of resonant states.

2.3.1 *Resonant-state expansion*

One of the first applications of the analytic mode normalization of resonant states was the resonant-state expansion as a perturbative method up to any orders of perturbation [35]. The starting point is a system with material distribution $\hat{\mathbb{P}}$ that exhibits a known set of resonant states with eigenfrequencies ω_n and field distributions $\mathbb{F}_n$, which will be used as basis functions. Then, we consider a perturbed system with material distribution $\hat{\mathbb{P}} + \delta\hat{\mathbb{P}}$, where $\delta\hat{\mathbb{P}}$ denotes the perturbation. In the most general case, $\delta\hat{\mathbb{P}}$ reads as

$$\delta\hat{\mathbb{P}}(\mathbf{r};\omega) = \begin{pmatrix} \delta\varepsilon(\mathbf{r};\omega) & -i\delta\xi(\mathbf{r};\omega) \\ i\delta\zeta(\mathbf{r};\omega) & \delta\mu(\mathbf{r};\omega) \end{pmatrix}, \tag{2.84}$$

where $\delta\varepsilon$, $\delta\mu$, $\delta\xi$, and $\delta\zeta$ denote the perturbations in the permittivity, permeability and bi-anisotropic parameters, respectively. Substituting the perturbed material distribution $\hat{\mathbb{P}} + \delta\hat{\mathbb{P}}$ into Eq. (2.8), we obtain for the new resonant states $\mathbb{F}_\nu$ of the perturbed system with eigenfrequencies ω_ν:

$$\hat{\mathbb{M}}(\mathbf{r};\omega_\nu)\mathbb{F}_\nu(\mathbf{r}) = -\frac{\omega_\nu}{c}\delta\hat{\mathbb{P}}(\mathbf{r};\omega_\nu)\mathbb{F}_\nu(\mathbf{r}). \tag{2.85}$$

Here, $\hat{\mathbb{M}} = \omega/c\hat{\mathbb{P}} - \hat{\mathbb{D}}$ is the Maxwell operator of the unperturbed system. Knowing the pole expansion of its Green's dyadic according to Eq. (2.26) and assuming that $\delta\hat{\mathbb{P}}$ is sufficiently localized to warrant the validity of this pole expansion, we can thus formally invert Eq. (2.85) and write [35, 37]:

$$\mathbb{F}_\nu(\mathbf{r}) = \sum_n \frac{-\omega_\nu \mathbb{F}_n(\mathbf{r})}{\omega_\nu - \omega_n} \int_V dV' \mathbb{F}_n^{\ddagger}(\mathbf{r}') \cdot \delta\hat{\mathbb{P}}(\mathbf{r}';\omega_\nu)\mathbb{F}_\nu(\mathbf{r}'). \tag{2.86}$$

Finally, we express $\mathbb{F}_\nu$ as $\mathbb{F}_\nu = \sum_n b_n \mathbb{F}_n$, where b_n are some expansion coefficients, and insert this on both sides of Eq. (2.86). Since the result must be valid at any position $\mathbf{r}$ and independently of $\delta\hat{\mathbb{P}}$, this yields

$$(\omega_\nu - \omega_n) b_n = -\omega_\nu \sum_m V_{nm}(\omega_\nu) b_m, \tag{2.87}$$

where

$$V_{nm}(\omega_\nu) = \int_V dV' \mathbb{F}_n^{\ddagger}(\mathbf{r}') \cdot \delta\hat{\mathbb{P}}(\mathbf{r}';\omega_\nu)\mathbb{F}_m(\mathbf{r}'). \tag{2.88}$$

If $\delta\hat{\mathbb{P}}$ is non-dispersive, i.e., it does not depend on ω, we thus obtain a general linear eigenvalue problem in the form of Eq. (2.87), which is the resonant-state expansion in its simplest form.

Assuming instead a perturbation of a general Drude-Lorentz from as in Eq. (2.28), with

$$\delta\hat{\mathbb{P}}(\mathbf{r};\omega) = \delta\hat{\mathbb{P}}_\infty(\mathbf{r}) + \sum_j \frac{\delta\hat{\mathbb{Q}}_j(\mathbf{r})}{\omega - \Omega_j}, \tag{2.89}$$

we can obtain after some algebra the dispersive formulation of the resonant-state expansion [37]:

$$(\omega_\nu - \omega_n) b_n = -\omega_\nu \sum_m V_{nm}(\infty) b_m + \omega_n \sum_m [V_{nm}(\infty) - V_{nm}(\omega_n)] b_m. \tag{2.90}$$

It should be noted that both the dispersive and the non-dispersive resonant-state expansion have been initially derived for non-magnetic systems [35, 110]. In that case, the perturbation is solely given by a change $\delta\varepsilon$ in the permittivity. It has been first demonstrated for perturbations of a dielectric slab and a microsphere [35, 48, 50]. Later, it has been extended to dielectric cylinders [49] and microcavities [173] as well as one- and two-dimensional periodic arrays [111]. The first dispersive formulation is given in Ref. [110], where the resonant states of a dielectric sphere have been used to calculate the resonant states of a gold sphere. This is highly beneficial, because calculating the resonant states of a dielectric sphere turns out to be much simpler than finding all relevant resonant states of a metallic sphere.

As discussed above in section 2.2.6, there is another possible contribution to the Green's dyadic, which are cuts in the complex frequency plane. In Ref. [109], these cut contributions are circumvented in a dielectric slab by considering the wavevector component k_z perpendicular to the slab as new variable for an analytic continuation to the complex plane instead of the frequency. In that case, the exact coefficients of transmission and reflection contain the frequency under a square root, see Eq. (2.12), which leads to the cut contributions, while the dependence on k_z is unambiguous and free of cuts. In other publications, the continuous frequency dependence of the cuts given in Eq. (2.57) is discretized in the form of a finite set of equivalent cut poles [49, 88, 89, 106]. For instance, the Muljarov group has shown recently that it is even possible to construct the resonant states of one-dimensional periodic arrays from the resonant states of a dielectric slab [88, 89], see Fig. 2.8. The discretized cuts are denoted by small dots. In the case that the cuts are far enough away from the spectral region of interest, they can be often ignored completely. Using this formalism, Neale and Muljarov investigated the occurrence of symmetry-protected and accidental bound states in the continuum and developed a criterion for distinguishing them: Symmetry-protected bound states in the continuum can be understood as a superposition of slab modes that do not radiate to the far field, while accidental bound states in the continuum arise as a superposition of several radiative slab modes such that the radiation to the far field is canceled out.

Another issue that has been mentioned in section 2.2.6 is that there exists a set of solutions of Eq. (2.8) at $\omega_n = 0$, which are not physical solutions of

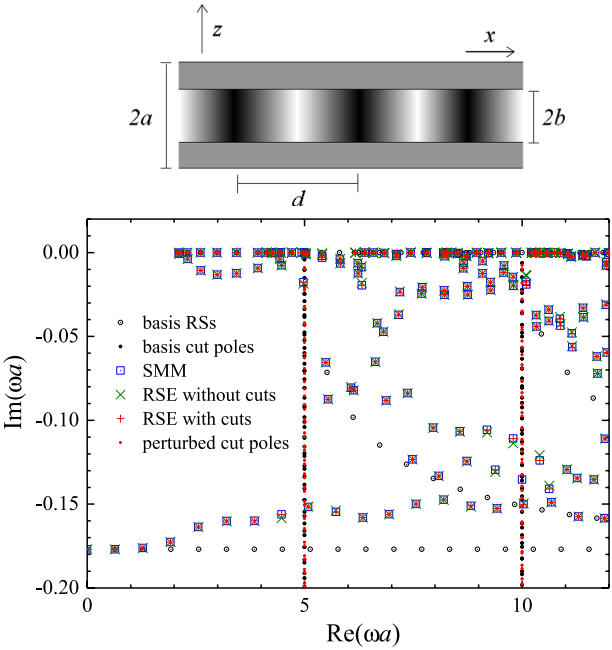

Figure 2.8. Resonant-state expansion for constructing the resonant states of a one-dimensional periodic modulated slab of thickness $2b = a$ and period $d = 2\pi a/5$ from those of a homogeneous and isotropic slab of thickness $2a$ in air. The permittivity modulation of the periodic system is sinusoidal with an amplitude of ± 1; the background permittivity is $\varepsilon = 6$. The top panel depicts a schematic of the system, while the bottom panel displays the complex eigenfrequencies of the perturbed and unperturbed system. Large and small black dots are the basis resonant states (RSs) and cut poles, respectively, while the blue squares denote the resonant states of the perturbed system. The results of resonant-state expansion with basis cut poles (red pluses) agrees better with the exact results of the perturbed system than those without cuts (green crosses) for the same number of Bragg harmonics ($M = 5$) and yields perturbed cut poles (red dots). Reprinted with permission from Ref. [89], copyright 2020, American Physical Society.

Maxwell's equations. These solutions are referred to as static modes and they obey [120, 174]:

$$\nabla \times \mathbf{E}_\lambda = 0, \tag{2.91}$$

$$\nabla \times \mathbf{H}_\lambda = 0. \tag{2.92}$$

The above equations are completely independent, so that we can derive two subclasses of static modes [174]:

$$\mathbf{E}_\lambda^{\mathrm{LE}} = -\nabla\psi_\lambda^{\mathrm{LE}}, \qquad \mathbf{H}_\lambda^{\mathrm{LE}} = 0, \tag{2.93}$$

$$\mathbf{H}_\lambda^{\mathrm{LM}} = -\nabla\psi_\lambda^{\mathrm{LM}}, \qquad \mathbf{E}_\lambda^{\mathrm{LM}} = 0. \tag{2.94}$$

Here, $\psi_\lambda^{\mathrm{LE}}$ and $\psi_\lambda^{\mathrm{LM}}$ are the potentials of longitudinal electric (LE) and longitudinal magnetic (LM) static modes. Since these modes are no solutions of the divergence equations

$$\nabla\cdot(\varepsilon\mathbf{E}+\xi\mathbf{H}) = 0, \tag{2.95}$$

$$\nabla\cdot(\zeta\mathbf{E}+\mu\mathbf{H}) = 0, \tag{2.96}$$

they do not necessarily obey Maxwell's boundary conditions for fields at interfaces between two materials. Therefore, adding the static modes as poles at $\omega = 0$ to the expansion of the Green's dyadic in Eq. (2.26) or Eq. (2.56) can result in a much better convergence of the resonant-state expansion in the case that the boundary conditions change between the initial and the perturbed system [120, 174]. For instance, it is shown in Ref. [120] how to derive the resonant states of a cylindrical disk from those of a spherical resonator. The static modes are normalized by the condition $V_n = 1$, where V_n is defined in Eq. (2.34) and the integration is taken over the entire space. Furthermore, it is shown in Ref. [174] how to eliminate static modes in the expansion of the Green's dyadic at the cost of an additional δ function. However, it should be noted that static modes have been considered so far only for dielectric systems.

2.3.2 *First-order perturbation theory and sensing*

Let us now discuss how the theory of resonant states is used in literature to describe the light-matter interaction in nanophotonic sensors. As explained in chapter 1, in many sensing applications, one is interested in detecting changes in a nanophotonic resonator that are associated with the presence of some analyte substance. Very often, the main effect of the analyte substance is to induce shifts of the resonator's resonance frequencies. In most scenarios, the presence of the analyte denotes only a weak perturbation to the resonators original material composition. In this case, as shown in Refs. [25, 50–52, 111, 173], the resulting shifts can be efficiently described via a simple first-order perturbation theory.

The corresponding equation can be deduced straightforwardly from the resonant state expansion: We start with Eqs. (2.87) and (2.88) and suppose that the perturbation δP denotes only a small change compared to the original material parameters. In this case, the perturbed eigenfrequencies can be written as $\omega_\nu = \omega_n + \delta\omega_n$, where $\delta\omega_n$ with $|\delta\omega_n| \ll |\omega_n|$ denotes the perturbation-induced change. Inserting this result into the above equations and assuming that the matrix V_{nm} is approximately diagonal (this is the case for weak perturbations), we end up with a simple-closed form expression:

$$\delta\omega_n = -\omega_n \int_V dV \mathbb{F}_n^\ddagger(\mathbf{r}) \cdot \delta\hat{\mathbb{P}}(\mathbf{r};\omega_n)\mathbb{F}_n(\mathbf{r}). \tag{2.97}$$

This equation allows us to predict the change of the eigenfrequencies under perturbations of the resonators material composition via a simple overlap integral over the resonant state's unperturbed electromagnetic fields. Note that in general, the change $\delta\omega_n$ is complex valued and contains two kinds of information: Its real part describes the shift of the resonance frequency, while its imaginary part is associated with a change in the resonance linewidth. It should be mentioned that Eq. (2.97) has the same prerequisites as the resonant state expansion: Strictly speaking, it is only applicable for perturbations $\delta\hat{\mathbb{P}}(\mathbf{r};\omega)$ that are localized inside the resonator. Nevertheless, it has been demonstrated that in practice, reasonably accurate predictions can also be obtained for perturbations that are localized in the close vicinity of the resonator [25, 51, 52, 111]. For perturbations of the surrounding medium, as they also often occur in sensing, the equation is, however, condemned to fail. We will later (in chapter 3) develop a generalized version of the theory that allows us to correctly account for this kind of perturbations.

Figure 2.9 displays an example, where the above perturbation theory is applied to a plasmonic refractive-index sensor [52]. The system consists of a periodic array of gold nanoantennas that sit on top of an infinitely thick glass substrate. The antennas are covered by a 650 nm thick layer of some analyte solution. Above the analyte, there is an infinitely extended layer of air. As a perturbation, the refractive index of the analyte is changed from its original value $n = 1.31$ (resembling pure water) to higher ones (corresponding to water with an added solute; for example glucose).

The plot depicts the resonance frequency (black) and resonance linewidth (blue) of the fundamental plasmonic mode as a function of the analyte refractive index. The lines denote the result of the first-order perturbation theory, while the dots and squares correspond to numerically exact calculations. It

is evident that there is an excellent agreement. Only for very high values of n, one can observe some deviations.

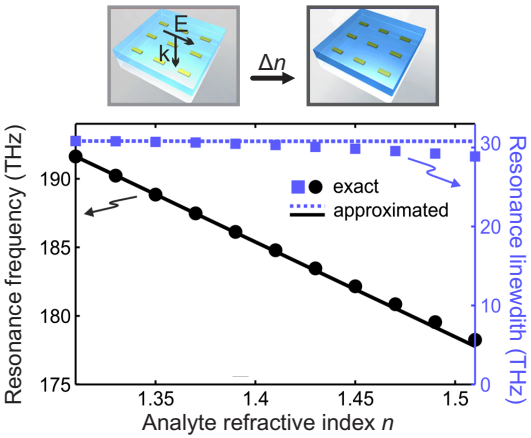

Figure 2.9. Perturbation theory applied to an array of plasmonic nanoantennas. The system consists of a glass substrate with the antennas on top. The antennas are covered by a layer of an analyte solution. As a perturbation, the refractive index n of the analyte is changed from its original value of 1.31 (resembling pure water) to higher ones (corresponding to water with an added solute). The plot displays the resonance frequency (black) and resonance linewidth (blue) as a function of the analyte refractive index. Lines denote the prediction of the first-order perturbation theory, while dots and squares represent numerically exact results. For not too large values of n, there is an excellent agreement. Adapted with permission from Ref. [52], copyright 2016, American Physical Society.

In sensor designs, it is often useful to quantify the sensing capability of an individual resonant state with respect to frequency shifts. For this purpose, it is very convenient to introduce the following figure of merit (FOM) [25]:

$$\mathrm{FOM} = \frac{[\text{sensitivity}] \times [\text{excitation strength}]}{[\text{resonance linewidth}]}. \tag{2.98}$$

The quantities in this equation can be derived from the resonant state: The sensitivity is usually defined around the eigenfrequency $\omega_n = \Omega_n - i\Gamma_n$ as $|\mathrm{Re}(\partial\omega_n/\partial \mathrm{X})|$, where X represents the material parameter that is varied in

the sensor. This expression can directly be calculated from Eq (2.97). The linewidth is known as $-2\Gamma_n$, and the excitation strength can be estimated as $|b_{\mathrm{N}}^{(n)}(\Omega_n)|$ from Eq. (2.73). In Ref. [25] it is demonstrated and experimentally verified how this FOM can be used to optimize the geometry of a complex sensor.

2.3.3 *Purcell enhancement*

Countless applications in micro- and nanophotonics [144, 175–182] (cf. also publication [P10]) exploit the interaction of dipole emitters with resonators. The heart of this interaction is the so-called Purcell effect, which describes the enhancement of the spontaneous emission rate that an emitter experiences when being coupled to a resonator. In his famous 1946 communication [183], Purcell stated that this enhancement is given as

$$F = \frac{6\pi c^3 Q_n}{\omega^3 V_n}, \tag{2.99}$$

which is nowadays known as the Purcell factor. Here, ω denotes the dipole's oscillation frequency, $Q_n = \Omega_n/2\Gamma_n$ is the quality factor of the optical mode, and V_n represents the mode volume. Initially, V_n was estimated as the effective volume of the resonator. Later, this definition was refined to (see for instance Refs. [41, 184, 185])

$$V_n = \frac{\int dV \varepsilon(\mathbf{r})|\mathbf{E}_n(\mathbf{r})|^2}{|\mathbf{e}_{\mathrm{d}} \cdot \mathbf{E}_n(\mathbf{r}_{\mathrm{d}})|^2}, \tag{2.100}$$

where $\mathbf{E}_n$ represents the modal field, $\mathbf{e}_{\mathrm{d}}$ describes the unit vector along the dipole orientation, $\mathbf{r}_{\mathrm{d}}$ represents the dipole position, and the integration is carried out over the volume occupied by the mode. Note that in consistency with Ref. [41], we reference the Purcell factor to the spontaneous emission rate in vacuum instead of a bulk medium, as it is also common in literature. The equations for a bulk medium can be obtained by simply including factors of $1/n^3$ and $1/n^2$ in the definition of F and V_n, respectively, where n represents the bulk's refractive index.

Although Eqs. (2.99) and (2.100) have been used for decades to describe light-matter interactions, it turns out that they are correct only in the limit of high quality factors and negligible energy leakage to the environment. The main reason is that – as discussed in subsection 2.2.3 – in the case of energy leakage, the modal field distributions become exponentially growing

with distance to the resonator and the integral in Eq. (2.100) is not applicable anymore. A first solution was suggested by Kristensen et al. in 2012 [113], where they introduced a generalized mode volume, based on an extension of a normalization scheme for open resonators that had been developed in the 1990s by Leung et al. [186–188]. However, while this approach was aiming in the right direction, it was later shown that the normalization used in Ref. [113] has a mathematical flaw (for details, see literature debate in Refs. [40, 41, 114–117]). Furthermore, this initial work focused on the case of an emitter interacting with only one single mode and being spectrally matched with this one. The first correct and rigorous theory was presented by Sauvan et al. in 2013 [36], based on the normalization via Eq. (2.32) using perfectly-matched layers and an orthogonality decomposition of the fields inside the resonator in terms of resonant states (for an explanation, see subsections 2.2.4). Shortly after, the first fully analytical treatment – similar to Sauvan's approach, but based on the analytic mode normalization and the analytic pole expansion of the Green's dyadic – was developed by Muljarov and Langbein [41]. In the following, we present the generalization of Purcell's theory to open systems, following mostly the derivation from this latter work. Note that we remain here in the weak-coupling regime between emitter and resonator, where the resonant states are still classical quantities. However, it has been shown by Franke et al. that it is possible to quantize the resonant states for describing the interaction of resonator and emitter on the few-photon level in a quantum-mechanical framework [189].

As shown in Refs. [36, 38, 40, 41, 113, 153, 190, 191], the correct Purcell factor for open electromagnetic resonators becomes

$$F(\omega) = \frac{3\pi c^3}{\omega} \sum_n \mathrm{Im} \frac{1}{V_n \omega_n (\omega_n - \omega)}, \tag{2.101}$$

with the generalized mode volume V_n defined as

$$V_n = \frac{1}{2[\mathbf{e}_\mathrm{d} \cdot \mathbf{E}_n^\ddagger(\mathbf{r}_\mathrm{d})][\mathbf{e}_\mathrm{d} \cdot \mathbf{E}_n(\mathbf{r}_\mathrm{d})]}, \tag{2.102}$$

where $\mathbf{E}_n$ and $\mathbf{E}_n^\ddagger$ are normalized according to Eqs. (2.34-2.34) or an equivalently applicable method [35, 36, 50, 112, 117]. Note that in comparison to Ref. [41], we have included a factor of 2 in order to be consistent with the normalization used in this thesis (which is defined via electric and magnetic fields instead of electric fields only), and furthermore generalized to the case where $\mathbf{E}_n^\ddagger \neq \mathbf{E}_n$.

It can be shown that the original Purcell factor of Eq. (2.99) is contained in Eq. (2.101) in the limit of high quality factors and negligible energy leakage. An important aspect of the generalized mode volume is that it can be complex [36, 38, 110, 113, 191], in contrast to its original definition, in which it is a real-valued positive number. This has two remarkable consequences (for a detailed discussion, see Refs. [36, 38]): First, modes with $\mathrm{Im}(V_n) \neq 0$ contribute with non-Lorentzian features to the spectral dependence of $F(\omega)$. Second, modes with $\mathrm{Re}(V_n) < 0$ provide a negative contribution to the overall enhancement.

Let us have a short excursion about the physical meaning of the Purcell factor. There are three different viewpoints [192], which can be summarized as:

$$F \overset{\text{(i)}}{=} \frac{\gamma}{\gamma_0} \overset{\text{(ii)}}{=} \frac{\rho}{\rho_0} \overset{\text{(iii)}}{=} \frac{P}{P_0}. \tag{2.103}$$

Viewpoint (i) resembles the definition mentioned at the beginning of this section, according to which F expresses the enhancement of the spontaneous emission rate γ of a dipole interacting with the resonator compared to its spontaneous emission rate γ_0 in vacuum. As stated by Fermi's golden rule [192], the spontaneous emission rate is proportional to the partial local density of states. Consequently, viewpoint (ii) denotes F as the increase of this density, where ρ represents the value in the presence of the resonator, and ρ_0 is the vacuum value. This concept is especially useful when dealing with systems that contain a multitude of emitters, as it is for example the case in Refs. [179, 180]. Concerning the physical interpretation of ρ in open resonators, one needs to be careful: In closed cavities, the density of states can be understood as the number of available electromagnetic modes per frequency interval $d\omega$, in analogy to the electronic density of states in solid-state physics. (The distinction between the density of states and the partial local density of states simply stems from the fact that the latter one contains an additional weighting factor that accounts for the coupling to the emitter [38].) In open resonators, the above interpretation breaks down. Intuitively, we can understand this from the fact that the modes of open resonators (i.e., the resonant states) have in general non-negligible linewidths and can spectrally interfere with each other. A detailed explanation of this matter is found in Ref. [38]. In this general case, the appropriate interpretation of ρ/ρ_0 is to associate it with the resonator-induced change of the local electric field generated by the emitter. Closely related is viewpoint (iii), which describes F as the enhancement of the power P that is radiated by a classical dipole in the presence of the resonator compared to the power P_0 that the same dipole would radiate in vacuum.

An example for the Purcell factor calculation in an open resonator is shown in Fig. 2.10, which is taken from Ref. [41]. Plotted is $F(\omega)$ for a dielectric sphere with radius a and the permittivity $\varepsilon = 4$, which is surrounded by air. The emitter is assumed to be located at a distance of $0.9a$ from the center. The Purcell factor is calculated via Eq. (2.101), taking into account modes with an angular quantum number of $l < 38$ and eigenfrequencies $|\omega_n| < 40c/a$, and is averaged over the polarization directions. The black line represents the full Purcell factor, while the blue line corresponds the partial Purcell factor, considering only transverse-electric (TE) modes.

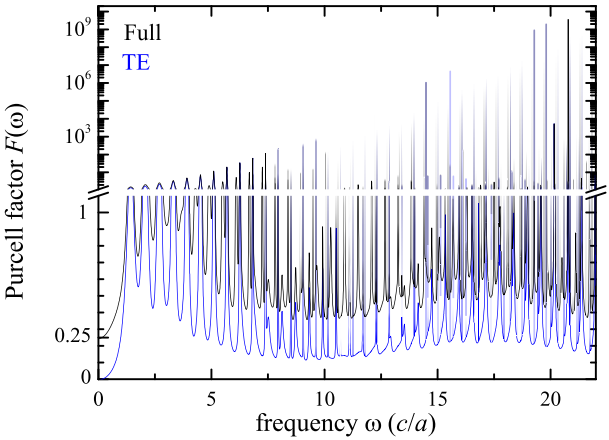

Figure 2.10. Purcell factor inside a dielectric sphere. The sphere has a radius of a and a permittivity of $\varepsilon = 4$. The emitter is placed at a distance of $0.9a$ from the center and the Purcell factor is averaged over the polarization directions. The black line displays the full Purcell factor, while the blue line denotes the partial Purcell factor, considering only transverse-electric (TE) modes. Reprinted with permission from Ref. [41], copyright 2016, American Physical Society.

It should be mentioned, that – due to the completeness issue discussed in subsection 2.2.6 – the decomposition of the Purcell factor in terms of the resonant state is strictly speaking only valid inside the resonator. Yet, in practise, reasonably accurate predictions are also obtained for dipoles placed outside in the vicinity of the resonator [36, 39, 40, 149]. Even at intermediate distances, the above decomposition might still deliver correct

results when the coupling to the free-space continuum is accounted for by adding an additional factor [36, 40, 149] (in the case of air this factor is 1). However, at long distances, namely when the exponential growth of the resonant states starts to dominate, even this extended approach is condemned to fail and will predict unphysically high-values of $F(\omega)$. The problem can be circumvented using one of the following two methods: The first option consists in calculating a mapped system, where the resonator and its surrounding are enclosed by perfectly-matched layers, and include the non-physical perfectly-matched-layer modes in the expansion [153]. This ensures completeness in the whole calculation domain. The second option is to use a regularization of the modal fields in the exterior of the resonator to remove the exponential growth [149, 193] (note, however, that Ref. [149] uses the same problematic normalization as Ref. [113], but can easily be extended to other normalization methods).

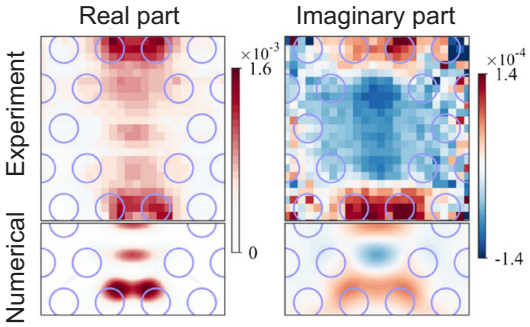

Figure 2.11. Complex mode volume in a photonic crystal cavity. Shown are the real (left) and the imaginary (right) parts of the inverse complex mode volume. The top plots contain experimental data, while the bottom plots correspond to numerical predictions. Evidently, there is a good agreement. Reprinted with permission from Ref. [194], copyright 2019, Optica.

At the end, let us have a closer look at the complex mode volume. One might think that this is purely an abstract mathematical definition, only meaningful because it appears in the Purcell factor calculation. However, it turns out that V_n itself is an observable quantity. It was predicted by Yang et al. [51] that when a tiny electrically polarizable object is placed inside (or nearby) an optical resonator, the complex eigenfrequency ω_n of the resonator's mode

experiences a change that is approximately proportional to the value of $1/V_n$ at the object's position. Hence, by probing the real and imaginary part of this eigenfrequency change (recall that they are measurable via the shift in the resonance frequency and the change in linewidth, respectively), one can experimentally access the complex nature of V_n. Such an experiment was completed by Cognée et al. [194] in 2019. By moving the electrically polarizable tip of a scanning near-field optical microscope over a photonic crystal cavity and simultaneously recording the peak frequency and the linewidth of the cavity's fluorescence spectrum, they were able to construct a spatially resolved map of the cavity's inverse complex mode volume. The results are displayed in Fig. 2.11. The left and right plots correspond to the real and imaginary part, respectively. It is evident that the experimental data (top) coincides very well with their numerical predictions (bottom). Recently, this approach was extended to magnetic mode volumes, i.e., the magnetic analog of Eq. (2.102) [195]. The experimental observation of complex mode volumes constitutes an important example where the theory of resonant states has led to the prediction and discovery of a new phenomenon. This clearly demonstrates that the theory is much more than only a computational tool.

2.4 RELATED TOPICS

At the end of the chapter, let us have a brief excursion about some related topics. The following subsections are not directly relevant for the rest of this thesis, however, they are included to give the reader some further impressions about what else the theory of resonant states and related approaches are useful for.

2.4.1 *Permittivity eigenmodes*

While the expansion of optical properties in terms of resonant states is based on an analytic continuation of this response to the complex frequency plane, other forms of analytic continuation are possible, too. One highly relevant case is that of an analytic continuation to a complex permittivity plane for a fixed real-valued frequency. The basic idea originates in electrostatics [196, 197] and has been later extended to electrodynamics [198, 199].

The starting point is the wave equation for non-magnetic materials ($\mu = 1$), which is

$$\nabla \times \nabla \times \mathbf{E} - \frac{\omega^2}{c^2}\varepsilon(\mathbf{r};\omega)\mathbf{E} = i\frac{4\pi\omega}{c^2}\mathbf{j}. \tag{2.104}$$

As in section 2.2.5, we separate the permittivity into a background part $\varepsilon_{\mathrm{BG}}$, which is now assumed to be homogeneous and isotropic, and the scattering geometry, which is given by $\Delta\varepsilon = (\varepsilon - \varepsilon_{\mathrm{BG}})\Theta(\mathbf{r})$, where Θ is a Heaviside function that is one inside and zero outside the scattering geometry. Using the well-known analytic form for the Green's dyadic $\hat{G}_0$ of the background material [200], which satisfies

$$\left(\nabla \times \nabla \times -\frac{\omega^2}{c^2}\varepsilon_{\mathrm{BG}}\right)\hat{G}_0(\mathbf{r},\mathbf{r}';\omega) = \hat{I}\delta(\mathbf{r}-\mathbf{r}'), \tag{2.105}$$

where $\hat{I}$ is a 3×3 unit matrix, it is possible to set up the following eigenvalue equation for $\mathbf{j} = 0$ [201]:

$$s_m\mathbf{E}_m(\mathbf{r}) = -\varepsilon_{\mathrm{BG}}\frac{\omega^2}{c^2}\int dV'\hat{G}_0(\mathbf{r},\mathbf{r}';\omega)\Theta(\mathbf{r}')\mathbf{E}_m(\mathbf{r}). \tag{2.106}$$

Here, s_m is the Bergman spectral parameter

$$s_m = \frac{\varepsilon_{\mathrm{BG}}}{\varepsilon_{\mathrm{BG}} - \varepsilon_m}, \tag{2.107}$$

with ε_m as the eigenpermittivity and $\mathbf{E}_m$ as the corresponding eigenfield. Then, all relevant quantities can be expanded in terms of these permittivity eigenmodes. A general description of such expansions can be found in Refs. [201–203].

The huge advantage of the permittivity eigenmodes is that they constitute a complete basis set, which holds not only inside the scattering geometry, but over the entire space, and the related eigenfields do not diverge in the exterior. Hence, there are no problems in field expansions outside the scattering geometry, e.g., in the case of an emitter in the exterior. There is also no need to find an analytic continuation of the material parameters to the complex frequency plane, because the method considers only real frequencies, where experimental data is available for material parameters such as the permittivity. Furthermore, it is possible to describe the coupling of two or more scattering geometries in a mode-hybridization theory [204], which yields a simple linear eigenvalue problem for the coupling of the individual resonators. Attempts of setting up a coupled-mode theory via resonant states either suffer from inaccuracies in the far-field coupling [205–

209] or involve a nonlinear eigenvalue problem [39, 210]. For the simple case of stacked gratings, however, an extended linear eigenvalue problem for the resonant states is developed in Ref. [211].

The downside of the permittivity eigenmodes is that an expansion of any optical properties in terms of these modes has to be repeated for each frequency of interest. Also, it is more difficult to grasp the physical meaning of the complex eigenpermittivity and the related eigenfields. Finally, the question arises about how to deal with several different materials, because the classical formulation only includes a background permittivity and the permittivity of the scattering geometry.

2.4.2 *Propagating modes*

In the case that the system of interest exhibits a certain translational symmetry, the complexity of that system can be mathematically reduced from a three-dimensional problem to a two-dimensional problem, see Ref. [212] and references therein. This can be achieved formally by carrying out a Fourier transform in the direction of translational symmetry. For instance, an ideal fiber or waveguide may be invariant under translations along the z direction. Then, we can apply the Fourier transform

$$\tilde{f}(x, y; \beta) = \frac{1}{2\pi} \int dz \, \mathrm{e}^{-i\beta z} f(x, y, z), \tag{2.108}$$

which transforms Maxwell's equations from Eq. (2.3) to

$$\tilde{\mathbb{M}}(x, y; \beta; \omega)\tilde{\mathbb{F}}(x, y; \beta; \omega) = \tilde{\mathbb{J}}(x, y; \beta; \omega), \tag{2.109}$$

where $\tilde{\mathbb{M}}$ originates from the Maxwell operator $\hat{\mathbb{M}}$ in Eq. (2.3) by the substitution $\partial z \to i\beta$ [46]. Historically, this Fourier transformation is mostly applied to the wave equation [213].

Fixing the frequency to a real value, we can then make an analytic continuation of Eq. (2.109) to the complex β plane. The related Green's dyadic $\tilde{\mathbb{G}}$ exhibits poles at complex β values, which we can relate to so-called propagating modes that obey the following constitutive equation with outgoing boundary conditions:

$$\tilde{\mathbb{M}}(x, y; \beta_n; \omega)\tilde{\mathbb{F}}_n(x, y; \omega) = 0. \tag{2.110}$$

As in the case of resonant states, it is then possible to expand the optical response in the basis of these propagating modes. From a physical perspective, propagating modes constitute solutions of Maxwell's equations in real space with a field distribution

$$\mathbb{F}_n(x, y, z; \omega) = \tilde{\mathbb{F}}_n(x, y; \omega) e^{i\beta_n z}, \tag{2.111}$$

which propagates along the z direction with only a change in phase that is governed by the real part of β_n and an exponential decay that stems from the imaginary part of β_n. In many cases, such as conventional step-index fibers [213], the dominant propagating modes exhibit a real-valued eigenvalue β_n, so that their fields are bound to a localized high-index region and decay perpendicular to the z axis with distance to this central region. These propagating modes are called "bound modes," with a normalization similar to Eq. (2.31). However, there are also solutions with a nonzero imaginary part of β_n that are called "leaky modes," because their fields grow perpendicular to the z axis with distance to the central region [104, 105, 213]. As discussed in section 2.2.3, similar normalization approaches as in Eq. (2.32) have been developed in the past [104, 105]. Only recently, the analytic normalization for resonant states from Ref. [37] has been adapted to these leaky modes and combined with the resonant-state expansion [46, 106].

2.4.3 *Application in nonlinear optics*

In most derivations, the theory of resonant states relies on the use of reciprocal materials, see Refs. [37, 38, 46] and references therein. Reciprocity is a very fundamental principle that can be broken only by a few possibilities [124]. One of them is based on nonlinearities. While we have shown here that the theory of resonant states can be extended to nonreciprocal materials, it still relies on the assumption of a linear material response. Hence, it might seem counterintuitive that it is possible to apply the theory of resonant states in nonlinear optics.

However, in the case of propagating modes, the description of nonlinear pulse propagation in optical fibers is mostly based on using a single or few bound modes as basis [214], resulting for a single mode with index m in the nonlinear Schödinger equation

$$\partial_z A_m \approx i\gamma |A_m|^2 A_m - i\frac{\overline{\beta}_m^{(2)}}{2}\partial_\tau^2 A_m - \overline{\alpha}_m^{(0)} A_m. \tag{2.112}$$

Here, A_m is the frequency-dependent amplitude of that modes, $\tau = t - \overline{\beta}_m^{(1)} z$, while $\overline{\beta}_m^{(n)}$ and $\overline{\alpha}_m^{(n)}$ are the n^{th} order frequency derivatives of the real and imaginary parts of the propagation constant β_m (see previous section) at a central frequency ω_0. Furthermore, γ is the Kerr nonlinearity parameter related to a third-order nonlinearity, which is typically calculated via an integral over expressions containing the correctly normalized modes [214].

The nonlinear Schrödinger equation is applicable, because the third-order nonlinearity is usually rather small, so that it is possible to treat it in a perturbative manner. In the case that we consider the propagation of leaky modes, it turns out that Eq. (2.112) remains valid, but the calculation of the Kerr nonlinearity parameter becomes more complicated due to the leakiness of the modes [132, 215–217]. Interestingly, γ is no longer real, but in general a complex number with the imaginary part resulting either in nonlinear loss or even nonlinear gain for the overall attenuating pulses [132]. The nonlinear gain results in optical pulses that are spectrally broader and more compressed temporally than expected from the simpler theory of bound modes. In addition to the Kerr nonlinearity, it is also possible to describe four-wave mixing of bound and leaky modes [133, 214].

While the nonlinear Schrödinger equation is a theoretical description of Kerr nonlinearities based on propagating modes, resonant states associated to poles of the Green's dyadic on the complex frequency plane have been used for approximating nonlinear responses, too. In the case of harmonic generation [218], the nonlinear susceptibility of order n generates fields at frequency $n\omega$. In the so-called undepleted-pump approximation [219–221], the energy transfer from the pump frequency to the harmonic is neglected, which allows one to first solve Maxwell's equations at the pump frequency and then to calculate the field emitted at the n^{th} harmonic by considering the nonlinear polarization as an equivalent source current. The fields at the fundamental harmonic can be expanded in terms of the resonant states as described in section 2.2.5. Using the pole expansion of the Green's dyadic in Eq. (2.26) at the harmonic frequency, it is then possible to derive also the emitted field in the basis of resonant states [222].

In the case of the Kerr nonlinearity, it is not possible to neglect the interplay of the linear fields and the contributions due to the nonlinear susceptibility. Still, it has been shown that one can use a modal description in terms of resonant states to approximate the Kerr nonlinearity in a ring resonator by appropriately accounting for the stored energy density [223].

2.5 CONCLUSION

In this chapter, we have given a thorough introduction into the theory of resonant states. We have explained that in optics, resonant states are defined as eigensolutions of Maxwell's equations that simultaneously satisfy outgoing boundary conditions. Apart from a few exceptions, this definition results in a discrete set of states at complex eigenfrequencies. These states can be interpreted as the rigorous mathematical definition of what is often intuitively understood as a mode or a resonance.

It was briefly summarized how resonant states can be calculated and it was discussed how they can be normalized. Subsequently, we have explained how the normalized resonant states can be used as a physically meaningful basis to expand the near and far fields of nanophotonic resonators. It was shown that in many cases, a small subset of relevant resonant states is sufficient to obtain reasonably accurate descriptions of these quantities with very low computational cost. However, it was also clarified that care has to be taken in some situations, because the expansion in terms of resonant states is not always complete. This is for example the case in the exterior of the resonator, as well as, in general, in systems that exhibit so-called branch cuts. Possible workarounds for this problem have been presented as well.

Based on the theoretical framework, several applications were discussed: First, it was demonstrated how the knowledge of a large set of resonant states of a reference system can be used to deduce the resonant states of a perturbed system via a simple eigenvalue equation. This method is known as the resonant-state expansion. Second, it was revealed how the first-order approximation of the above eigenvalue equation leads to a simple closed-form expression for resonance shifts and linewidth changes, which can be highly useful for describing nanophotonic substance sensors. Third, we included an overview of how to describe the Purcell effect in open resonators based on the theory of resonant states.

Finally, we have briefly discussed some related topics in order to give the reader some further impressions about the usefulness of the presented mathematical concepts. In particular, we have given a short introduction into permittivity eigenmodes and furthermore, we have revealed how the theory of resonant states can be applied to describe light propagation in fibers as well as nonlinear phenomena.

3

PERTURBATION THEORY FOR EXTERIOR MATERIAL CHANGES

In subsection 2.3.2, a simple expression from literature was presented that can describe resonance frequency shifts and linewidth changes in open resonators induced by small localized material changes in the resonator. It was briefly indicated how this expression is useful for modeling and designing nanophotonic sensors. It was, however, also emphasized that the expression is only valid for changes inside or in the close vicinity of the resonator, but in general fails for changes of the resonator's surrounding medium, as they are quite often relevant in sensing. Here, we solve this issue and derive a generalized version of the theory that is capable of including these kinds of exterior changes. Furthermore, we demonstrate its applicability on several example systems.

Most of this chapter is based on publication [P5]:

S. Both and T. Weiss: *First-order perturbation theory for changes in the surrounding of open optical resonators*. Optics Letters **44**, 5917–5920 (2019).
DOI 10.1364/OL.44.005917. Reprinted/adapted with permission. Copyright, 2019, Optica Publishing Group.

There are, however, two exceptions:

Section 3.2 contains a generalization of the derivation to nonreciprocal systems that is based on publication [P7]:

S. Both and T. Weiss: *Resonant states and their role in nanophotonics*. Semiconductor Science and Technology **1**, 013002 (2022).
DOI 10.1088/1361-6641/ac3290.
Reprinted/adapted with permission. Copyright 2021, The Authors.

Subsection 3.3.3 contains an example that is not included in the original publication [P5], but has been published beforehand in its preprint version, which is available under:

S. Both and T. Weiss: *First-order perturbation theory for material changes in the surrounding of open optical resonators*. arXiv:1902.08120 (2019).
Link https://arxiv.org/abs/1902.08120.

3.1 INTRODUCTION

Nanophotonic structures such as photonic crystals or plasmonic nanoparticles comprise optical resonances with strong electromagnetic near fields. Consequently, even tiny changes in the surrounding medium can have significant influence on their resonance frequencies. This is the key to various kinds of optical sensing applications [7, 11, 13, 25, 122, 123]. Figure 3.1 displays exemplarily a metallic sphere, around which the surrounding permittivity is changed from ε to $\varepsilon + \delta\varepsilon$, thus shifting the complex eigenfrequency of the fundamental plasmonic mode from ω_n to ω_ν.

The modeling of such interactions often relies on extensive numerical simulations, which can be rather inefficient, since in many practical cases, the variations in the material properties are extremely small. In contrast, perturbative theories are particularly suited for such cases. Besides providing intuitive insights into the underlying physics [11, 224], giving explicit expression for the sensitivities [11, 52, 122], and resulting in simple design rules [52, 122, 224], their most important benefit is drastically reduced calculation times [50–52, 111]. As shown in Ref. [25] and verified experimentally, by using the simple figure of merit from Eq. (2.98), it is possible to optimize a complex sensor design much faster than by conventional full-wave simulations.

The crucial part of almost any perturbation theory is an appropriate normalization of the eigenmodes. As explained in chapter 2, in nanophotonics, a difficulty arises from the fact that most systems are open resonators due to the presence of radiative losses. Consequently, their eigenmodes (i.e., the resonant states) correspond to field distributions that grow with distance to the resonator. Hence, conventional normalization schemes based on energy considerations fail and have to be replaced by one of the approaches from subsection 2.2.3.

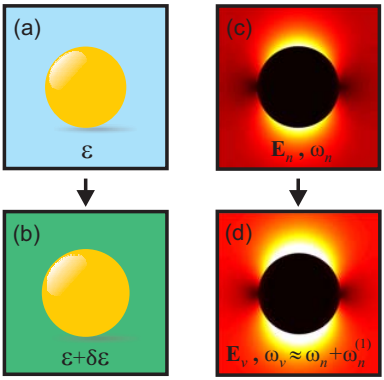

FIGURE 3.1. Influence of the surrounding medium on the resonant states of an open optical system. Depicted is a metallic nanosphere, which also serves as our test system (i). (a) In the unperturbed case, the sphere is surrounded by a medium with permittivity ε. (b) Exemplary resonant state of the unperturbed system, characterized by its electric field distribution $\mathbf{E}_n$ and its eigenfrequency ω_n. (c) Perturbed system with permittivity $\varepsilon + \delta\varepsilon$. (d) Resonant state of the perturbed system, characterized by a modified field distribution $\mathbf{E}_\nu$ and a modified eigenfrequency $\omega_\nu \approx \omega_n + \omega_n^{(1)}$.

As we have seen in subsection 2.3.2, equipped with the correct normalization, it is possible to deduce a simple closed-form expression for predicting frequency shifts and linewidth changes in such open optical resonators [cf. Eq (2.97)]. This expression has proven to be highly efficient for describing all kinds of perturbations inside or in close proximity to the resonator [25, 50–52, 111, 173]; however, as we have already emphasized, it fails for perturbations of the surrounding medium. The reason is very simple: In order to account for changes in the surrounding via Eq (2.97), one would need to carry out the corresponding integration over the whole space. Due to the growing fields of the resonant states in the exterior, this integral will, however, diverge (similar to conventional normalization integrals that also diverge, see subsection 2.2.3). In the following, we close the existing gap and derive a generalized theory that is capable of circumventing the problem and can correctly account for perturbations in the surrounding medium.

3.2 THEORY

We start with the resonant states of the unperturbed resonator, which are defined via Eq. (2.8) (repeated here for convenience):

$$\hat{\mathbb{M}}(\mathbf{r};\omega_n)\mathbb{F}_n = 0, \tag{3.1}$$

where $\mathbb{F}_n$ denotes the resonant field distributions and ω_n is the complex eigenfrequency. As a side note it should be mentioned that we do not require here that the field distributions are normalized. Instead, the analytical normalization condition of Eq. (2.34) will automatically come out as a byproduct of our derivations.

Now, similar to the resonant-state expansion (subsections 2.3.1) and the derivation of the first-order perturbation theory for interior changes (subsection 2.3.2), we introduce a perturbation $\delta\hat{\mathbb{P}}$ that alters the material distribution of the system from $\hat{\mathbb{P}}$ to $\hat{\mathbb{P}} + \delta\hat{\mathbb{P}}$. As in subsection 2.3.2, we assume that the perturbation is small, such that we can later use a first-order approximation. In contrast to the previous derivation, we do not require $\delta\hat{\mathbb{P}}$ to be localized inside the resonator. Instead, it can be nonzero in the surrounding. In order for being able to systematically deduce a first-order approximation later, we furthermore introduce a dimensionless parameter Λ that allows us to turn the perturbation on ($\Lambda = 1$) and off ($\Lambda = 0$). Consequently, the material distribution becomes $\hat{\mathbb{P}} + \Lambda\delta\hat{\mathbb{P}}$. Note that Λ is typically referred to as the perturbation parameter, and its usage is motivated by conventional perturbation theories (known from quantum mechanics [225]). The resonant states of the perturbed system obey

$$\left[\hat{\mathbb{M}}(\mathbf{r};\omega_v) + \Lambda\frac{\omega_v}{c}\delta\hat{\mathbb{P}}(\mathbf{r};\omega_v)\right]\mathbb{F}_v = 0, \tag{3.2}$$

where ω_v is the perturbed eigenfrequency and $\mathbb{F}_v$ are the corresponding field distributions.

Let us now derive an expression that connects the resonant states of the perturbed system with the ones of the unperturbed system. To obtain it, we multiply Eq. (3.2) with $\mathbb{F}_n^{\ddagger}$, subtract $\mathbb{F}_v$ times the transposed version of Eq. (3.2), integrate the result over a finite volume V that encloses all inhomogeneities, use $\hat{\mathbb{M}} = \omega/c\,\hat{\mathbb{P}} - \hat{\mathbb{D}}$, and apply Eq. (2.20) to convert the

two volume integrals that include the operator $\hat{\mathbb{D}}$ into a single surface integral. Consequently, we end up with:

$$\int_V dV \mathbb{F}_n^{\ddagger} \cdot \left[\omega_\nu \hat{\mathbb{P}}(\omega_\nu) - \omega_n \hat{\mathbb{P}}(\omega_n)\right] \mathbb{F}_\nu + \Lambda\omega_\nu \int_V dV \mathbb{F}_n^{\ddagger} \cdot \delta\hat{\mathbb{P}}(\omega_\nu)\mathbb{F}_\nu$$
$$-ic \oint_{\partial V} d\mathbf{S} \cdot (\mathbf{E}_n^{\ddagger} \times \mathbf{H}_\nu - \mathbf{E}_\nu \times \mathbf{H}_n^{\ddagger}) = 0. \tag{3.3}$$

In analogy to conventional perturbation theories, we expand the perturbed quantities $\mathbb{F}_\nu$ and ω_ν as perturbation series in powers of Λ:

$$\mathbb{F}_\nu = \mathbb{F}_n + \Lambda\mathbb{F}_n^{(1)} + \Lambda^2\mathbb{F}_n^{(2)} + \dots, \tag{3.4}$$
$$\omega_\nu = \omega_n + \Lambda\omega_n^{(1)} + \Lambda^2\omega_n^{(2)} + \dots. \tag{3.5}$$

Here, $\mathbb{F}_n^{(1)}, \mathbb{F}_n^{(2)}, \dots$ and $\omega_n^{(1)}, \omega_n^{(2)}, \dots$ are correction terms for the perturbed fields and the perturbed eigenfrequencies, respectively. Since our perturbation $\Lambda\delta\hat{\mathbb{P}}$ has been assumed as small, we can safely neglect all higher-order correction terms and only consider the first-order result. Furthermore, we are only interested in the shifts of the eigenfrequencies and not in the changes in the fields (since the former denote the relevant quantities in the kinds of sensing applications that are considered in this chapter). Consequently, our goal will be to determine $\omega_n^{(1)}$.

We insert the above relations into Eq. (3.3) and sort by powers of Λ. It turns out that the zeroth order is trivially fulfilled and hence does not contain any information. The first order, however, yields:

$$\omega_n^{(1)} V_n + \omega_n \int_V dV \mathbb{F}_n^{\ddagger} \cdot \delta\hat{\mathbb{P}}(\omega_n)\mathbb{F}_n = S_n^{(1)}. \tag{3.6}$$

Here, V_n is the volume term of the normalization defined in Eq. (2.34). For the sake of brevity of notations, we have furthermore introduced the abbreviation

$$S_n^{(1)} = ic \oint_{\partial V} d\mathbf{S} \cdot (\mathbf{E}_n^{\ddagger} \times \mathbf{H}_n^{(1)} - \mathbf{E}_n^{(1)} \times \mathbf{H}_n^{\ddagger}). \tag{3.7}$$

Equation (3.6) implicitly describes the first-order correction term of the eigenfrequency $\omega_n^{(1)}$. However, the problem is that the equation also contains the unknown first-order field correction terms $\mathbf{E}_n^{(1)}$ and $\mathbf{H}_n^{(1)}$. In the next

steps, we will show how to deal with these field-correction terms, in order to obtain an explicit expressions for $\omega_n^{(1)}$.

As it has been done in subsection 2.2.3, we define an analytic continuation $\mathbb{F}_n(\omega)$ of the unperturbed resonant state $\mathbb{F}_n$ in the complex ω plane around the point $\omega = \omega_n$. Additionally, we define an analytic continuation $\mathbb{F}_\nu(\omega;\Lambda)$ of the perturbed resonant state $\mathbb{F}_\nu(\Lambda)$ around the point $\omega = \omega_\nu$. The argument Λ is included, to emphasize that the perturbed resonant state also exhibits a Λ dependence. With the help of these analytic continuations, we can formally express the first-order field correction term $\mathbb{F}_n^{(1)}$ as

$$\mathbb{F}_n^{(1)} = \left.\frac{\mathrm{d}\mathbb{F}_\nu}{\mathrm{d}\Lambda}\right|_{\Lambda=0} = \left\{\frac{\partial\mathbb{F}_\nu}{\partial\Lambda} + \frac{\partial\mathbb{F}_\nu}{\partial\omega}\frac{\partial\omega}{\partial\Lambda}\right\}_{\Lambda=0} = \delta\mathbb{F}_n + \mathbb{F}_n'\omega_n^{(1)}, \tag{3.8}$$

where the first equal sign follows by definition from Eq. (3.4) and the second one from applying the chain rule. Note that furthermore, we have identified $\partial\omega_\nu/\partial\Lambda|_{\Lambda=0}$ as $\omega_n^{(1)}$, used the abbreviation $\mathbb{F}_n' = \partial\mathbb{F}_n(\omega)/\partial\omega|_{\omega=\omega_n}$ from subsection 2.2.3, and, for later convenience, introduced the definition

$$\delta\mathbb{F}_n = \left.\frac{\partial\mathbb{F}_\nu}{\partial\Lambda}\right|_{\Lambda=0}. \tag{3.9}$$

Plugging Eq. (3.8) into Eq. (3.7), we obtain

$$S_n^{(1)} = \delta S_n + S_n\omega_n^{(1)}, \tag{3.10}$$

where S_n denotes the surface term of the normalization from Eq. (2.34) and where we have introduced the abbreviation

$$\delta S_n = ic\oint_{\partial V} d\mathbf{S}\cdot(\mathbf{E}_n^\ddagger\times\delta\mathbf{H}_n - \delta\mathbf{E}_n\times\mathbf{H}_n^\ddagger). \tag{3.11}$$

Inserting the above $S_n^{(1)}$ into Eq. (3.6), we obtain the first-order correction of the eigenfrequency:

$$\omega_n^{(1)} = -\frac{\omega_n\int_V dV\mathbb{F}_n^\ddagger\cdot\delta\hat{\mathbb{P}}(\omega_n)\mathbb{F}_n + \delta S_n}{V_n + S_n}. \tag{3.12}$$

This is the same result as in Eq. (2.97), apart from two differences: First and most importantly, there is an additional surface term δS_n, which allows us to account for perturbations in the surrounding of the resonator. We

will later show that if the perturbation is completely localized inside the resonator, this surface term will vanish. Thus, one will recover the old formula for interior perturbations. Second, there is a denominator $V_n + S_n$, which resembles the analytic normalization condition from Eq. (2.34). It arises from the fact that we have not required (for our derivations) that the resonant field distributions $\mathbb{F}_n$ are normalized. For normalized field distributions, the denominator will simply become one. It is worth pointing out that this denominator automatically came out of the derivations, which means that the perturbation theory provides an alternative path for deriving the analytic normalization condition.

So far, Eq. (3.12) resembles only a formal solution to the problem of exterior perturbations, since the term δS_n is still not known explicitly. Therefore, let us now evaluate it. In order to do this, we will restrict our considerations to the special but highly important scenario, where the resonator's surrounding consists of a homogeneous and isotropic medium, characterized by spatially constant and scalar permittivity ε and permeability μ values, and the perturbation is associated with spatially constant and scalar changes $\delta\varepsilon$ and $\delta\mu$ of these quantities.

For the sake of generality, we allow ε, μ, $\delta\varepsilon$ and $\delta\mu$ to be dispersive. We want to emphasize that the restriction to homogeneous surroundings does not rule out the practically highly important case of periodic resonators that have different substrate and superstrate materials. The reason is that the substrate and superstrate can be considered as two separate exterior domains and can be treated independently.

Let us now come back to the evaluation of δS_n. Since this evaluation corresponds to a lengthy mathematical derivation, which does not provide too much relevant insight, we will here only briefly sketch the main idea, while the detailed steps are provided in Appendix A: The key is to notice that for a homogeneous surrounding, the fields in the exterior of the resonator can be written as a superposition of outgoing basis functions $\mathbb{O}_\mathrm{N}$ (for an explanation, see subsection 2.2.3 or Ref. [45]) and to explicitly make use of the properties of these basis functions. Consequently, one obtains:

$$\delta S_n = \frac{\eta\omega_n}{2}\left(\frac{\delta\varepsilon}{\varepsilon}+\frac{\delta\mu}{\mu}\right) S_n + \frac{i\eta\beta c}{2}\oint_{\partial V} d\mathrm{S}\cdot(\mathbf{E}_n^{+}\times\mathbf{H}_n), \tag{3.13}$$

where S_n is the surface term of the normalization and where we have introduced the abbreviations $\eta = \sqrt{\varepsilon\mu}/(\omega\sqrt{\varepsilon\mu})'$ and $\beta = \left[(\omega\mu)'\delta\varepsilon - (\omega\varepsilon)'\delta\mu\right]/\varepsilon\mu$. The prime denotes again the derivative with respect to ω at ω_n, as introduced

in subsection 2.2.3. For non-dispersive ε and μ, the above abbreviations simplify to $\eta = 1$ and $\beta = \delta\varepsilon/\varepsilon - \delta\mu/\mu$. Equations (3.12) and (3.13) constitute the main result of this chapter and allow us to predict the change of the eigenfrequencies $\omega_n^{(1)}$ under interior and exterior perturbations via a simple closed-form expression from the unperturbed resonant states.

3.3 EXAMPLES

In the following, we will investigate the applicability of the above equations on several example systems.

3.3.1 *Plasmonic nanosphere*

Let us start with a particularly simple geometry: As depicted in Fig. 3.1, we consider a metallic nanosphere and vary the permittivity of its surrounding medium. We deliberately chose this system, since its resonant states can be calculated analytically [50, 110], which allows a precise and easy to follow verification of our theory. For our example calculation, we take a gold sphere with a diameter of 400 nm, described by a Drude model ($\omega_\mathrm{p} = 13.8 \times 10^{15}$ s^{-1} and $\gamma = 1.075 \times 10^{14}$ s^{-1}). The unperturbed permittivity of the surrounding medium is chosen as $\varepsilon = 2$.

In Fig. 3.2(a-c), we display the normalized electric field distribution of exemplary resonant states of the unperturbed system. Panels (a) and (b) show the fundamental plasmonic dipole and quadrupole mode, which correspond to poles of the transverse-magnetic (TM) Mie coefficients for an angular momentum quantum number of $l = 1$ and $l = 2$, respectively, and occur at frequencies below the plasma frequency ω_p, where the gold is metallic. For frequencies larger than ω_p, the gold behaves as a dielectric, and whispering gallery modes inside the sphere are possible. Panel (c) shows a transverse-electric (TE) higher-order whispering gallery mode with an angular momentum quantum number of $l = 3$ and three radial antinodes inside the sphere. Fig. 3.2(d-f) depict the resonance energies and linewidths of the three modes as a function of the permittivity ε of the surrounding medium. The solid lines indicate the results of the perturbation theory, while the squares have been derived from exact analytical calculations [50]. For not too big variations in ε, we find a good agreement between the perturbation theory and the exact calculations. Only at the edge of the plotted ε range, some deviations become visible.

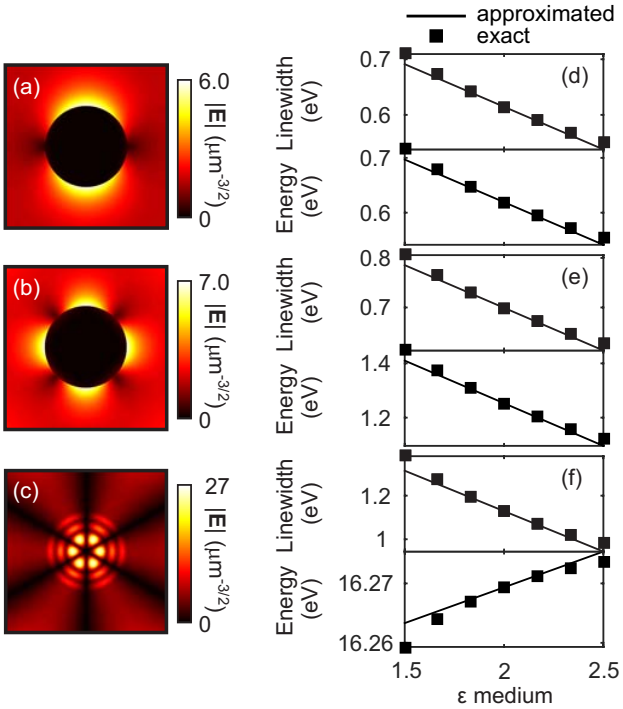

Figure 3.2. Results for test system (i). As illustrated in Fig. 3.1, we consider a gold nanosphere (diameter 400 nm) and vary the permittivity ε of its surrounding. (a-c) Normalized electric field distribution of exemplary resonant states of the unperturbed system ($\varepsilon = 2$). Panels (a) and (b) depict the fundamental plasmonic dipole and quadrupole mode, while (c) displays a transverse-electric Mie resonance. (d-f) Resonance energy and linewidth as a function of ε, with solid lines as the results of the perturbation theory and squares derived by exact analytical calculations.

3.3.2 *Plasmonic nanoslits*

While test system (i) has been particularly chosen to demonstrate the validity of our theory, its full power becomes obvious when changing to a system without any known analytical solution. For this reason, we now switch to a second, more practically relevant example: We consider a periodic array of plasmonic nanoslits as depicted in Fig. 3.3(a). The structure consists of a gold layer (yellow) with the slits etched into it. The gold sits on top of a glass substrate (dark gray) with refractive index 1.5 and is covered by an

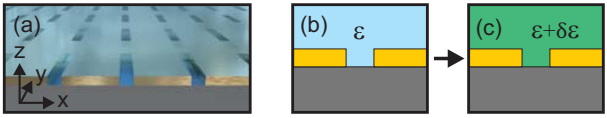

Figure 3.3. Schematic of test system (ii). We consider a two-dimensional periodic array of plasmonic nanoslits. (a) Geometry: The structure consists of a gold layer with the nanoslits etched into it. The gold sits on top of a glass substrate (dark gray) with refractive index 1.5 and is covered by an analyte solution (light blue) with permittivity ε (unperturbed case: $\varepsilon = 1.71$, which is the value of water). (b,c) We introduce a perturbation by changing ε to $\varepsilon + \delta\varepsilon$.

analyte solution (light blue) with permittivity ε (unperturbed case: $\varepsilon = 1.71$, which is the value of water). As indicated in Fig. 3.3(b,c), we change the permittivity of the analyte solution from ε to $\varepsilon + \delta\varepsilon$. This is a typical example of a plasmonic refractive index sensor. The slits have a width of 60 nm (x direction) and a length of 400 nm (y direction). The system is periodic in both x and y directions with periods of 300 nm and 700 nm, respectively. The height of the gold layer is 40 nm, while the heights of the substrate and the analyte solution are taken as infinite. Of course, infinite heights are not possible in reality, but since the substrate and analyte are typically orders of magnitude thicker than the gold, this is a justified approximation. Furthermore, large finite heights with perfectly flat interfaces would result in fast oscillations due to spectrally dense Fabry-Perot resonances [52]. In order to keep the calculations as realistic as possible, the gold is modeled according to Ref. [226].

The field distribution of the resonant state in the unperturbed system, as well as the exact eigenfrequencies in the perturbed case, have been calculated using the Fourier modal method [52, 164, 165, 227]. Exploiting the periodicity, the calculation domain and the integration volume V in Eqs. (3.12) and (3.13) can be reduced to a volume that spans over one unit cell within the xy plane and covers the inhomogeneity in the z direction.

Fig. 3.4(a) shows the normalized electric field distribution of the fundamental plasmonic resonance, plotted within the xz plane at a y position that corresponds to half the slit length. Panel (b) depicts the resonance energy and linewidth as a function of ε. Solid lines represent the result of the first-order perturbation theory, while the squares have been derived from exact numerical calculations. As in the other example, there is a good agreement between perturbation theory and exact results, as long as the change in ε is not too big.

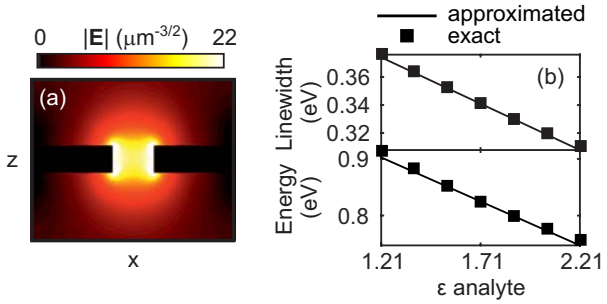

Figure 3.4. Results for test system (ii). (a) Normalized electric field distribution of the fundamental plasmonic resonance within the unperturbed system ($\varepsilon = 1.71$), plotted in the xz plane at half the slit length in the y direction. (b) Corresponding resonance energy and linewidth as a function of the permittivity ε of the analyte solution. Solid lines represent the first-order perturbation theory, while the squares have been derived by numerically exact calculations.

3.3.3 *Photonic crystal*

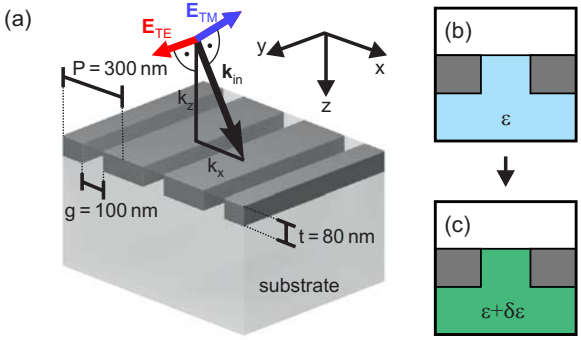

Figure 3.5. Schematic of test system (iii). We consider a one-dimensional photonic crystal slab that is known from Ref. [111, 128], where it is investigated in different contexts. (a) Structure geometry with parameters as specified in the above references. The structure consists of a periodic grating (dark gray) of a material with refractive index 2.5, embedded into a substrate with permittivity ε (unperturbed case: $\varepsilon = 2.25$), and air on top. Reprinted with permission from Ref. [111], copyright 2017, American Physical Society. (b,c) We introduce a perturbation by changing ε to $\varepsilon + \delta\varepsilon$.

As a third example, we consider a one-dimensional photonic crystal slab. The system is known from Refs. [111, 128], where it has been used to validate the perturbation theory from Eq. (2.97) for interior material changes and to investigate the description of optical Fano resonances in periodic structures near Rayleigh anomalies [99], respectively. The geometry is depicted in Fig. 3.5(a). The system is periodic in the x direction, translationally symmetric in the y direction, and remains finite within the z direction. It consists of a 80 nm thick periodically modulated layer (period $P = 300$ nm) with a 200 nm wide region of ZnO (dark gray, $n = 2.5$) per unit cell, embedded into a quartz substrate (light gray) with a permittivity value ε, where $\varepsilon = 2.25$ in the unperturbed case, and an air cover layer. As indicated in Fig. 3.5(b,c), we change the permittivity of the quartz from ε to $\varepsilon + \delta\varepsilon$.

The resonant states of the system correspond to quasiguided TE and TM waveguide modes [111, 228]. Due to the periodicity, the resonant states can be written as Bloch waves, which are characterized by their in-plane momentum k_x. As for test system (ii), the field distribution of the resonant states in the unperturbed system, as well as the exact eigenfrequencies in the perturbed case, have been calculated using the Fourier modal method [52, 164, 165, 227]. Exploiting the periodicity and the translational symmetry [111], the calculation domain and the integration volume V appearing in Eq. (3.12) can be reduced to a two-dimensional rectangle within the xz plane that spans over one unit cell in the x direction and covers the inhomogeneity in the z direction.

Figure 3.6(a,b) show the normalized electric field distribution of exemplary resonant states in the unperturbed system. The example uses exactly the same modes as discussed in Ref. [111], which are a TE resonance at $k_x = \pi/(2P) = 5.236\ \mu\text{m}^{-1}$ (a), and a TM resonance at $k_x = 0.2\ \mu\text{m}^{-1}$ (b). Panels (c) and (d) depict the corresponding resonance energy and linewidth as a function of ε. The solid lines represent the result of the first-order perturbation theory, while the squares have been derived from exact numerical calculations. For both modes, perturbation theory and exact results exhibit a good agreement over the depicted ε range. For the TE mode, the first-order perturbation theory works over a much larger range of ε than for the TM mode (note that the ε ranges are different in both plots). The reason is that the TM resonance depicted here is coincidentally very close to a Rayleigh anomaly [99, 111] that strongly effects the far field coupling, which in turn significantly depends on the substrate index that is changed here as the perturbation parameter.

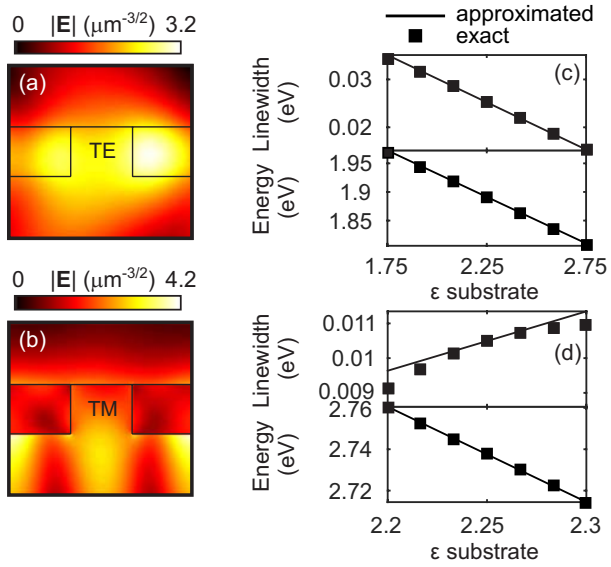

Figure 3.6. Results for test system (iii). (a,b) Normalized electric field distributions of exemplary resonant states within the unperturbed system ($\varepsilon = 2.25$). Reprinted with permission from Ref. [111], copyright 2017, American Physical Society. (a) Transverse-electric (TE) mode at $k_x = \pi/(2P) = 5.236\ \mu\text{m}^{-1}$, (b) Transverse-magnetic (TM) mode at $k_x = 0.2\ \mu\text{m}^{-1}$. (c,d) Corresponding resonance energy and linewidth as a function of the permittivity ε of the substrate. Solid lines represent the results of the first-order perturbation theory, while the squares have been derived by numerically exact calculations. Note that (c) and (d) are plotted for different ranges of ε.

3.4 LIMITATIONS

Let us have a short discussion about the limitations of our first-order perturbation theory. It should be noted that we have applied it to several other test systems, including slits and spheres (metallic and nonmetallic) of different sizes, as well as to a plasmonic rod antenna array. In general, we found that the theory typically works over quite large ranges of ε values, as long as there is only one single resonant state around the frequency of interest. However, as soon as there are two or more resonant states in close spectral proximity, the first-order approximation starts to deviate relatively fast from the exact results with increasing $\delta\varepsilon$. This finding completely coincides with what one would expect from conventional perturbation theories as

well as with the observations from Ref. [111] for interior perturbations. The narrow applicability range that was observed for test system (iii) around the Rayleigh anomaly can also be explained in this context, since the Rayleigh anomaly effectively acts as a large ensemble of modes [89, 229]. In the end, we want to emphasize that even if, in a particular system, the first-order approximation has a limited applicability range, this is often not a problem, since in the majority of sensing applications, the material changes of interest are extremely small anyway.

3.5 CONCLUSION AND OUTLOOK

In conclusion, we have presented a first-order perturbation theory that can predict frequency shifts and linewidth variations under material changes in the exterior of open optical resonators. Our theory denotes a generalization of a well-known literature expression for interior material changes. The key for the generalization is to include an additional surface term that accounts for the exterior changes. We have demonstrated the applicability of the theory on several example systems.

At the end, it should be mentioned that our approach was recently extended by Upendar et al. to propagating modes in leaky optical fibers [47]. In this context, the exterior perturbation theory is not only useful for describing the influence of exterior material changes, but additionally, it also allows for predicting the group velocity of a mode from the pure knowledge of its resonant field distribution. A further recent follow-up work was presented by Almousa and Muljarov [230]. Therein, it is shown how one can go beyond the first-order approximation and treat exterior changes up to arbitrary orders of perturbation, as long as they are homogeneous and isotropic.

4

PERTURBATION THEORY FOR FAR-FIELD QUANTITIES

So far, only the impact of material variations on the eigenfrequencies of resonators was considered. In this chapter, we go one step further and present a more general perturbation theory that allows us to describe the effect of material variations on the resonators' far-field properties, such as their transmission and reflection spectra. We will see that besides resonance frequency shifts and linewidth changes, there exist further perturbation-induced effects that can lead to observable signals. The main goal of this chapter is to present the derivation of the theory. Additionally, we will investigate a simple exemplary system from the field of dielectric sensing. Later, in chapter 5, the theory will then extensively be used to describe and understand the mechanisms that occur in a very specific application: nanophotonic chiral sensing.

The chapter is based on publications [P6] (where the initial theory is derived) and [P7] (where a generalization to nonreciprocal systems is presented):

S. Both, M. Schäferling, F. Sterl, E. A. Muljarov, H. Giessen, and T. Weiss: *Nanophotonic chiral sensing: How does it actually work?* ACS Nano **16**, 2822–2832 (2022).
DOI 10.1021/acsnano.1c09796.

S. Both and T. Weiss: *Resonant states and their role in nanophotonics.* Semiconductor Science and Technology **1**, 013002 (2022).
DOI 10.1088/1361-6641/ac3290.

4.1 INTRODUCTION

As it was already explained, a huge number of nanophotonic sensing schemes are based around the idea of detecting the presence of an analyte medium via the changes that it can induce in the eigenfrequencies of a nanophotonic system. Consequently, in subsection 2.3.2 and chapter 3 a thorough theoretical description of the underlying interaction was provided. However, it turns out that such eigenfrequency shifts are not the only effect that can be relevant in nanophotonic sensing.

The reason is that typical experimental sensing approaches rely on probing the resonator's far-field response [cf. Fig. 1.1]. Let us have a look at a simple example, which is shown in Fig. 4.1. As indicated in panel (a), the starting point is a nanophotonic resonator, to which the analyte medium is added. In the depicted example, the resonator consists of an array of plasmonic rod antennas, and the analyte medium is added via cubic patches at the end of the antennas. Panel (b) displays the resulting far-field response. Depicted is the transmittance (T) of the array, without (gray) and with (red) the analyte medium, as a function of energy. To highlight the change, we also plot the difference (ΔT) of the two curves. Comparing the two transmittance curves, one finds that in the above example, the most obvious change is a shift of the transmittance dip to higher photon energies. This effect can be well described with the eigenfrequency-perturbation theories from subsection 2.3.2 and chapter 3. However, a closer look reveals that there is an additional difference: The depth of the dip changes. This change cannot be described within the above-mentioned eigenfrequency-perturbation theory. Moreover, the eigenfrequency-perturbation theory cannot predict the lineshape of the curves and the absolute transmittance values. There exist, however, many sensing schemes where this information becomes relevant: For example, instead of recording a spectrum, in some applications it is enough to take a light source with a fixed photon energy and track the absolute transmittance change at this energy.

The above considerations clearly show that in addition to the eigenfrequency-perturbation theory, it is highly useful to have a more general theory that allows one to describe the impact of material changes on the resonator's far-field response. In the following, we will derive such a theory. The derivation is closely related to the derivation of the symmetric representation for the resonant-state expansion of the optical scattering matrix that we have provided in subsection 2.2.7.

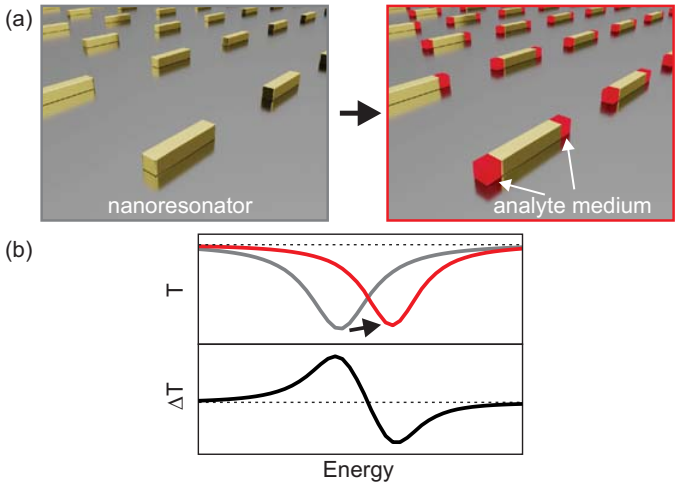

FIGURE 4.1. Typical principle of nanophotonic substance sensing via probing a resonator's far-field response. (a) The starting point is a nanophotonic resonator, which is brought in contact with the analyte medium. In this example, the resonator consists of an array of plasmonic rod antennas, and the analyte medium is added in cubic patches at the ends of the antennas. (b) The optical far-field response of the resonator (as an example, we take the transmittance T) is measured without (gray) and with the analyte medium (red). The change in the response (in our case, the transmittance change ΔT) contains information about the analyte medium.

4.2 THEORY

To start our derivation, we recall from subsection 2.2.5 that the total field $\mathbb{F}_{\text{tot}}$ in the unperturbed resonator satisfies the relation

$$\hat{\mathbb{M}}(\mathbf{r};\omega)\mathbb{F}_{\text{tot}}(\omega) = 0. \tag{4.1}$$

Here, $\hat{\mathbb{M}}(\mathbf{r};\omega) = \omega/c\hat{\mathbb{P}}(\mathbf{r};\omega) - \hat{\mathbb{D}}$ is the Maxwell operator of the unperturbed resonator, which contains the unperturbed material distribution $\hat{\mathbb{P}}(\mathbf{r};\omega)$. Furthermore, we recall that the total field can be split into a background field and a scattered field: $\mathbb{F}_{\text{tot}} = \mathbb{F}_{\text{BG}} + \mathbb{F}_{\text{scat}}$.

As before in several other parts of this thesis, we introduce a perturbation $\delta\hat{\mathbb{P}}$ that alters the material distribution from $\hat{\mathbb{P}}$ to $\hat{\mathbb{P}} + \delta\hat{\mathbb{P}}$. A visualization is provided in Fig. 4.2. We make the same assumptions as in subsection 2.3.2 and

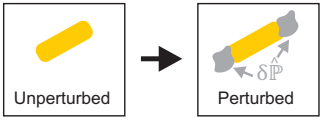

FIGURE 4.2. Visualization of the perturbation. The left-hand side denotes the unperturbed system, associated with a material distribution $\hat{\mathbb{P}}$, while the right-hand side denotes the perturbed system, associated with a material disribution $\hat{\mathbb{P}} + \delta\hat{\mathbb{P}}$.

in chapter 3: The perturbation is small, such that one can later apply a first-order approximation. In contrast to chapter 3, we restrict our considerations, however, again to a perturbation that is localized inside or in the vicinity of the resonator. As in chapter 3, we furthermore introduce a perturbation parameter Λ that allows us to switch the perturbation on ($\Lambda = 1$) and off ($\Lambda = 0$). Consequently, the material distribution becomes $\hat{\mathbb{P}} + \Lambda\delta\hat{\mathbb{P}}$.

Let $\mathbb{F}_{\text{tot}}^{\text{pert}}$ now denote the total field in the perturbed resonator. It obeys

$$\left[\hat{\mathbb{M}}(\mathbf{r};\omega) + \Lambda\frac{\omega}{c}\delta\hat{\mathbb{P}}(\mathbf{r};\omega)\right]\mathbb{F}_{\text{tot}}^{\text{pert}}(\omega) = 0. \tag{4.2}$$

We write $\mathbb{F}_{\text{tot}}^{\text{pert}}$ as a perturbation series in Λ and note that only the scattered field is affected by the perturbation, while the background field remains unaffected since the background material distribution $\hat{\mathbb{P}}_{\text{BG}}$ does not change. This yields:

$$\mathbb{F}_{\text{tot}}^{\text{pert}} = \mathbb{F}_{\text{BG}} + \mathbb{F}_{\text{scat}} + \Lambda\mathbb{F}_{\text{scat}}^{(1)} + \Lambda^2\mathbb{F}_{\text{scat}}^{(2)} + \ldots, \tag{4.3}$$

where $\mathbb{F}_{\text{BG}}$ and $\mathbb{F}_{\text{scat}}$ denote the unperturbed background and scattered field, respectively, and $\mathbb{F}_{\text{scat}}^{(1)}$, $\mathbb{F}_{\text{scat}}^{(2)}$, ... are correction terms. Inserting Eq. (4.3) into Eq. (4.2) and comparing the coefficients for every power of Λ provides:

$$\hat{\mathbb{M}}\mathbb{F}_{\text{scat}} = -\hat{\mathbb{M}}\mathbb{F}_{\text{BG}} \tag{4.4}$$

$$\hat{\mathbb{M}}\mathbb{F}_{\text{scat}}^{(1)} = -\frac{\omega}{c}\delta\hat{\mathbb{P}}\mathbb{F}_{\text{BG}} - \frac{\omega}{c}\delta\hat{\mathbb{P}}\mathbb{F}_{\text{scat}} \tag{4.5}$$

$$\ldots$$

This set of equations implicitly describes the scattered field and all its correction terms. The first equation defines the unperturbed scattered field $\mathbb{F}_{\text{scat}}$ and translates into the already known Eq. (2.47). The second equation defines the first-order correction term $\mathbb{F}_{\text{scat}}^{(1)}$. We can solve it with the help of

the Green's dyadic of the unperturbed system, which is given in Eq. (2.26). This yields:

$$\mathbb{F}^{(1)}_{\mathrm{scat}}(\omega) = -\sum_n \mathbb{F}_n \frac{\omega \int dV \mathbb{F}^{\ddagger}_n \cdot \delta\hat{\mathbb{P}}(\omega)\mathbb{F}_{\mathrm{BG}}(\omega)}{\omega - \omega_n} - \sum_n \mathbb{F}_n \frac{\omega \int dV \mathbb{F}^{\ddagger}_n \cdot \delta\hat{\mathbb{P}}(\omega)\mathbb{F}_{\mathrm{scat}}(\omega)}{\omega - \omega_n}. \tag{4.6}$$

Note that for the brevity of notations, the argument $\mathbf{r}$ in the fields and in the perturbation operator was suppressed. Successively applying the above method would allow for deriving expressions for all higher-order correction terms $\mathbb{F}^{(2)}_{\mathrm{scat}}, \ldots$; however, since the perturbation is assumed to be small, we only need to consider the first correction order. Consequently, we can write $\mathbb{F}^{\mathrm{pert}}_{\mathrm{tot}} \approx \mathbb{F}_{\mathrm{BG}} + \mathbb{F}_{\mathrm{scat}} + \mathbb{F}^{(1)}_{\mathrm{scat}}$.

Let us now evaluate the scattering matrix of the perturbed system. Similar as it was done for the evaluation of the unperturbed scattering matrix [cf. Eqs.(2.67) and (2.68)], we suppose that the system gets excited via the basis function $\mathbb{I}_{\mathbf{N}}(\omega)$. This results in the total field $\mathbb{F}^{\mathrm{pert}}_{\mathrm{tot},\mathbf{N}} \approx \mathbb{F}_{\mathrm{BG},\mathbf{N}} + \mathbb{F}_{\mathrm{scat}} + \mathbb{F}^{(1)}_{\mathrm{scat},\mathbf{N}}$. Here, the subscript $\mathbf{N}$ is used to indicate where the excitation is coming from. The scattering matrix of the perturbed system is then obtained by projecting this total field $\mathbb{F}^{\mathrm{pert}}_{\mathrm{tot},\mathbf{N}}$ onto the probe function $\mathbb{I}^{\ddagger}_{\mathbf{M}}(\omega)$ via Eq. (2.65). This gives

$$S^{\mathrm{pert}}_{\mathbf{MN}}(\omega) = S_{\mathbf{MN}}(\omega) + \delta S_{\mathbf{MN}}(\omega), \tag{4.7}$$

where $S_{\mathbf{MN}}$ denotes the scattering matrix of the unperturbed system, and $\delta S_{\mathbf{MN}}$ describes the perturbation-induced change, which reads as

$$\delta S_{\mathbf{MN}}(\omega) = i \oint_{\partial V} d\mathbf{S} \cdot \left[\mathbf{E}^{\ddagger}_{\mathbb{I},\mathbf{M}}(\omega) \times \mathbf{H}^{(1)}_{\mathrm{scat},\mathbf{N}}(\omega) - \mathbf{E}^{(1)}_{\mathrm{scat},\mathbf{N}}(\omega) \times \mathbf{H}^{\ddagger}_{\mathbb{I},\mathbf{M}}(\omega) \right]. \tag{4.8}$$

To evaluate $\delta S_{\mathbf{MN}}$, we apply a similar procedure as we have applied to $S^{\mathrm{scat}}_{\mathbf{MN}}$ from Eq. (2.70) to derive the symmetric representation of the unperturbed scattering matrix in Eq. (2.76). There are three steps: The first one consists in replacing the probe function $\mathbb{I}^{\ddagger}_{\mathbf{M}}$ by the background field $\mathbb{F}^{\ddagger}_{\mathrm{BG},\mathbf{M}}$ that it would create when being launched into the resonator. This step is analogous to the conversion from Eq. (2.70) to Eq. (2.74). One can easily verify that the replacement is possible by noting that on the integration surface ∂V, the field $\mathbb{F}^{(1)}_{\mathrm{scat},\mathbf{N}}$ must be some superposition of outgoing basis function and by using

the same arguments that where used to obtain Eq. (2.74). The replacement gives

$$\delta S_{\mathrm{MN}}(\omega) = i \oint_{\partial V} d\mathbf{S}\cdot\left[\mathbf{E}^{\ddagger}_{\mathrm{BG,M}}(\omega)\times\mathbf{H}^{(1)}_{\mathrm{scat,N}}(\omega) - \mathbf{E}^{(1)}_{\mathrm{scat,N}}(\omega)\times\mathbf{H}^{\ddagger}_{\mathrm{BG,M}}(\omega)\right]. \tag{4.9}$$

The second step is similar to the conversion from Eq.(2.74) to Eq. (2.75). We use Eq. (2.20) to convert the surface integral into two volume integrals containing the operator $\hat{\mathbb{D}}$. Then, we insert $\hat{\mathbb{D}} = \omega/c\,\hat{\mathbb{P}}^{\ddagger} - \hat{\mathbb{M}}^{\ddagger}$ into the first volume integral and $\hat{\mathbb{D}} = \omega/c\,\hat{\mathbb{P}} - \hat{\mathbb{M}}$ into the second one, replace $\hat{\mathbb{M}}^{\ddagger} = \hat{\mathbb{M}}^{\ddagger}_{\mathrm{BG}} + \omega/c\Delta\hat{\mathbb{P}}^{\ddagger}$, use Eqs. (2.46) and (4.5) (the former in its transposed version) as well as the identities $\hat{\mathbb{P}}^{\ddagger} = \hat{\mathbb{P}}^{\mathrm{T}}$, $\Delta\hat{\mathbb{P}}^{\ddagger} = \Delta\hat{\mathbb{P}}^{\mathrm{T}}$, and $\delta\hat{\mathbb{P}}^{\ddagger} = \delta\hat{\mathbb{P}}^{\mathrm{T}}$ to switch the order of the quantities under the integrals. Consequently, we get

$$\begin{aligned}\delta S_{\mathrm{MN}}(\omega) = &-\frac{\omega}{c}\int dV \mathbb{F}^{\ddagger}_{\mathrm{BG,M}}(\omega)\cdot\delta\hat{\mathbb{P}}(\omega)\mathbb{F}_{\mathrm{BG,N}}(\omega)\\ &-\frac{\omega}{c}\int dV \mathbb{F}^{\ddagger}_{\mathrm{BG,M}}(\omega)\cdot\delta\hat{\mathbb{P}}(\omega)\mathbb{F}_{\mathrm{scat,N}}(\omega)\\ &-\frac{\omega}{c}\int dV \mathbb{F}^{\ddagger}_{\mathrm{BG,M}}(\omega)\cdot\Delta\hat{\mathbb{P}}(\omega)\mathbb{F}^{(1)}_{\mathrm{scat,N}}(\omega).\end{aligned} \tag{4.10}$$

As the third step, we insert the expansions of $\mathbb{F}_{\mathrm{scat}}$ and $\mathbb{F}^{(1)}_{\mathrm{scat}}$ from Eqs. (2.54) and (4.6), respectively, and utilize the definitions of $a^{(n)}_{\mathrm{M}}$ and $b^{(n)}_{\mathrm{N}}$ from Eqs. (2.78) and (2.73), respectively. Consequently, we obtain the change of the scattering matrix as

$$\delta S_{\mathrm{MN}} = \delta S^{\mathrm{nr}}_{\mathrm{MN}} + \delta S^{\mathrm{ex}}_{\mathrm{MN}} + \delta S^{\mathrm{em}}_{\mathrm{MN}} + \delta S^{\mathrm{shift}}_{\mathrm{MN}} + \delta S^{\mathrm{cross}}_{\mathrm{MN}}, \tag{4.11}$$

which contains the following five contributions:

$$\delta S^{\mathrm{nr}}_{\mathrm{MN}}(\omega) = -\frac{\omega}{c}\int dV \mathbb{F}^{\ddagger}_{\mathrm{BG,M}}(\omega)\cdot\delta\hat{\mathbb{P}}(\omega)\mathbb{F}_{\mathrm{BG,N}}(\omega) \tag{4.12}$$

$$\delta S^{\mathrm{ex}}_{\mathrm{MN}}(\omega) = \omega\sum_n \frac{a^{(n)}_{\mathrm{M}}(\omega)\int dV \mathbb{F}^{\ddagger}_{n}\cdot\delta\hat{\mathbb{P}}(\omega)\mathbb{F}_{\mathrm{BG,N}}(\omega)}{\omega-\omega_n} \tag{4.13}$$

$$\delta S^{\mathrm{em}}_{\mathrm{MN}}(\omega) = \omega\sum_n \frac{b^{(n)}_{\mathrm{N}}(\omega)\int dV \mathbb{F}^{\ddagger}_{\mathrm{BG,M}}(\omega)\cdot\delta\hat{\mathbb{P}}(\omega)\mathbb{F}_{n}}{\omega-\omega_n} \tag{4.14}$$

$$\delta S^{\mathrm{shift}}_{\mathrm{MN}}(\omega) = -\omega c\sum_n \frac{a^{(n)}_{\mathrm{M}}(\omega)b^{(n)}_{\mathrm{N}}(\omega)\int dV \mathbb{F}^{\ddagger}_{n}\cdot\delta\hat{\mathbb{P}}(\omega)\mathbb{F}_{n}}{(\omega-\omega_n)^2} \tag{4.15}$$

$$\delta S_{\mathrm{MN}}^{\mathrm{cross}}(\omega) = -\omega c \sum_{n \neq m} \frac{a_{\mathrm{M}}^{(n)}(\omega) b_{\mathrm{N}}^{(m)}(\omega) \int dV \mathbb{F}_n^{\ddagger} \cdot \delta\hat{\mathbb{P}}(\omega) \mathbb{F}_m}{(\omega - \omega_n)(\omega - \omega_m)}. \tag{4.16}$$

Equations (4.11) to (4.16) are the main result of this chapter. They allow us to predict the change of the scattering matrix via simple overlap integrals over the unperturbed fields. Each of the five contributions describes the effect of a different perturbation-induced process onto the scattering matrix. The first one, $\delta S_{\mathrm{MN}}^{\mathrm{nr}}$, contains an overlap integral between the incoming and outgoing background fields and can be interpreted as a nonresonant interaction. The second and third one, $\delta S_{\mathrm{MN}}^{\mathrm{ex}}$ and $\delta S_{\mathrm{MN}}^{\mathrm{em}}$, respectively, encompass overlap integrals between the background fields and the resonant states and denote changes in the excitation and emission efficiencies, respectively. The fourth one, $\delta S_{\mathrm{MN}}^{\mathrm{shift}}$, contains overlap integrals of the resonant states with themselves, which can be associated with the eigenfrequency shift given by Eq. (2.97). The fifth one, $\delta S_{\mathrm{MN}}^{\mathrm{cross}}$, involves overlap integrals between different resonant states and can be interpreted as perturbation-induced crosstalk.

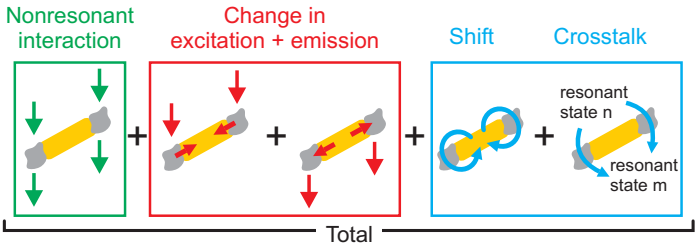

Figure 4.3. Visualization of the five contributions that constitute the perturbation-induced change of the scattering matrix: Nonresonant interaction, changes in excitation and emission efficiencies of the resonant states, shifts of the resonant states' eigenfrequencies, and crosstalk between different resonant states. The gray structures indicate the perturbation $\delta\hat{\mathbb{P}}$, as introduced in Fig. 4.2. Note that the changes in the excitation and emission efficiencies are mathematically very similar and are hence categorized into a common group. The same applies to the shift and the crosstalk contribution.

A visualization of the five contributions is displayed in Fig. 4.3. The gray structures indicate the perturbation $\delta\hat{\mathbb{P}}$, as introduced in Fig. 4.2. Note that the change in the excitation and emission are mathematically very similar.

This is why both are categorized into a common group of effects. The same applies to the shift and the crosstalk contribution.

We will later, in subsection 4.3 as well as in chapter 5, investigate the significance of these contributions in different sensing applications. However, from the above equations, one can already make some general deductions: The nonresonant interaction is independent of the resonant states and thereby independent of any resonant near-field enhancement. Therefore, it can be expected to be weak, as long as the volume of the perturbation is not significantly large. Furthermore, in many resonators, the resonant states are spectrally well separated [mathematically speaking, the difference between $\mathrm{Re}(\omega_n)$ and $\mathrm{Re}(\omega_m)$ of neighboring resonant states is larger than their linewidths]. In this case, the crosstalk will be weak as well [*cf.* denominator of Eq. (4.16)].

4.3 EXAMPLE: DIELECTRIC PERTURBATION

Let us now apply our theory to a simple example. We choose the scenario that is depicted in Fig. 4.1: An array of rod antennas gets perturbed by placing patches of an analyte medium at their ends. We consider that the effect of the analyte medium is to induce a local change of the permittivity by a value of $\delta\varepsilon = 1 \times 10^{-4}$. We consider gold antennas that are surrounded by water. The geometry parameters are selected such that the system exhibits a resonance in the near-infrared spectral range. The length of the antennas is 200 nm and their width and height are 40 nm. They are periodically arranged in a square lattice with a period of 600 nm. The analyte medium is placed in cubic patches $40 \times 40 \times 40$ nm^3 at both antenna ends.

For the calculations, we use the commercially available finite-element solver COMSOL Multiphysics.[1] The calculation domain consists of a single unit cell of the antenna array. The periodicity is accounted for by applying periodic boundary conditions in lateral directions. At the top and bottom, the calculation domain is terminated with perfectly-matched layers. The gold dielectric function is described by a Drude model with plasma frequency $\omega_\mathrm{p} = 1.37 \times 10^{16}$ rad/s and a damping constant $\gamma = 1.22 \times 10^{14}$ rad/s (adopted from Ref. [231]), while the water is accounted for with a constant refractive index of 1.33. To calculate the resonant state of the system, we apply the method from Ref. [153]. For the normalization, we use the perfectly-matched layer approach from Eq. (2.32).

1 See https://www.comsol.com.

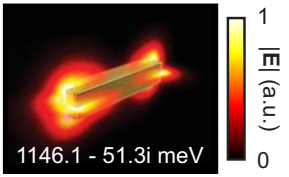

FIGURE 4.4. Fundamental resonant state of the unperturbed rod antennas. Details on how this three-dimensional plot was created can be found in Appendix B.

Before we calculate the impact of the perturbation, let us first have a look at the optical properties of the unperturbed system. Figure 4.4 displays its fundamental resonant state, which is found at an energy eigenvalue of 1146.1 − 51.3 meV. Details on how this three-dimensional plot was created can be found in Appendix B. By applying the far-field expansion approach from subsection 2.2.7, we can predict the transmittance of the system in the energy range around this resonant state. The result is compared with full-wave calculations in Fig. 4.5. We define the transmittance as $T = |S_{\mathbf{M}_\mathrm{b}\mathbf{N}_\mathrm{t}}|^2$, where the channels $\mathbf{N}_\mathrm{t}$ and $\mathbf{M}_\mathrm{b}$ correspond to plane waves that are propagating towards the antenna array from the top and away from it to the bottom, respectively. The waves are linearly polarized along the long antenna axes. Note that there is no polarization conversion and diffraction, which is why the expression for the transmittance is so simple. For the calculation of $S_{\mathbf{M}_\mathrm{b}\mathbf{N}_\mathrm{t}}$, we have used the symmetric scattering-matrix representations from Eq. (2.76) and included the fundamental resonant state. The influence of higher-order resonant states was accounted for by adding a cubic fit as background, which had been obtained from exact full-wave calculations that were evaluated at four energy points, equidistantly distributed over the considered spectral range. The line denotes the result of the above approximation, while the dots correspond to the full-wave calculations. Evidently, there is an excellent agreement. Note that the transmittance curve exhibits a Lorentzian lineshape with its minimum value located at the resonance energy of the resonant state, which is indicated by a vertical dashed line.

Let us now investigate the impact of the perturbation. As already mentioned, we consider an analyte medium that changes the local permittivity by a value of $\delta\varepsilon = 1 \times 10^{-4}$ [cf. illustration in Fig. 4.6(a)]. Using Eq. (4.11), we can predict the resulting change $\delta S_{\mathbf{MN}}$ of the scattering matrix and, consequently, the resulting transmittance change. Note that we define the change in the transmittance as $\Delta T = T_\mathrm{pert} - T$, where $T_\mathrm{pert} = |S_{\mathbf{M}_\mathrm{b}\mathbf{N}_\mathrm{t}} + \delta S_{\mathbf{M}_\mathrm{b}\mathbf{N}_\mathrm{t}}|^2$ is the transmittance of the perturbed system and $T = |S_{\mathbf{M}_\mathrm{b}\mathbf{N}_\mathrm{t}}|^2$ is the transmittance

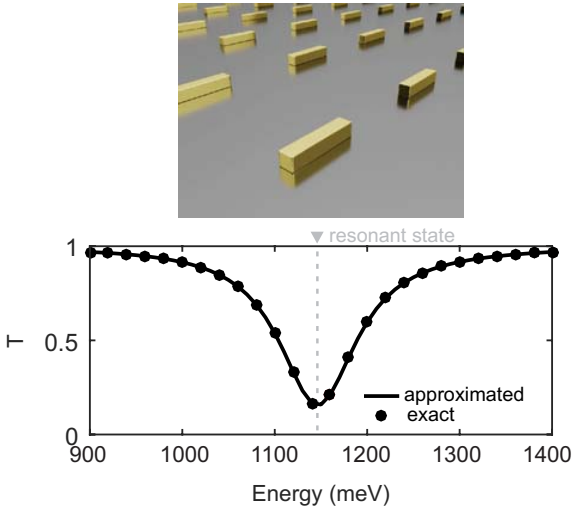

FIGURE 4.5. Optical response of the unperturbed rod antennas. Depicted is the transmittance T as a function of energy. The line represents the prediction of the resonant-state theory, which was obtained by using the scattering-matrix expansion from Eq. (2.76) for the fundamental resonant state together with a cubic background fit, while the dots correspond to exact full-wave calculations and are plotted for comparison. It can be seen that there is an excellent agreement.

of the unperturbed system. The total transmittance change is depicted by the top plot in Fig. 4.6(b). The line denotes the prediction of the perturbation theory [i.e., Eq. (4.11)], while the dots correspond to exact full-wave calculations and are shown for comparison. Clearly, both agree very well. Note that in contrast to the unperturbed scattering matrix S_{MN}, the change δS_{MN} has been calculated by only considering the fundamental resonant state, without relying any additional fitted background term.

The lower plots in panel (b) depict the individual contributions to the total transmittance change. Note that we have defined the contributions ΔT_{x} of the transmittance change as $\Delta T_{\mathrm{x}} = \Delta T\big|_{\delta S_{\mathrm{M_b N_t}} = \delta S^{\mathrm{x}}_{\mathrm{M_b N_t}}}$, where $\delta S^{\mathrm{x}}_{\mathrm{M_b N_t}}$ with $\mathrm{x} = \{\mathrm{nr}, \mathrm{ex}, \mathrm{em}, \mathrm{shift}, \mathrm{cross}\}$ denotes the contributions of the scattering matrix change. For compactness, we have summed up the change in the excitation and emission efficiency contributions to one curve. Furthermore, there is no crosstalk curve, since only one resonant state is considered. The results are very clear: The contribution of the nonresonant interaction is extremely close to zero and appears to be completely negligible. The changes

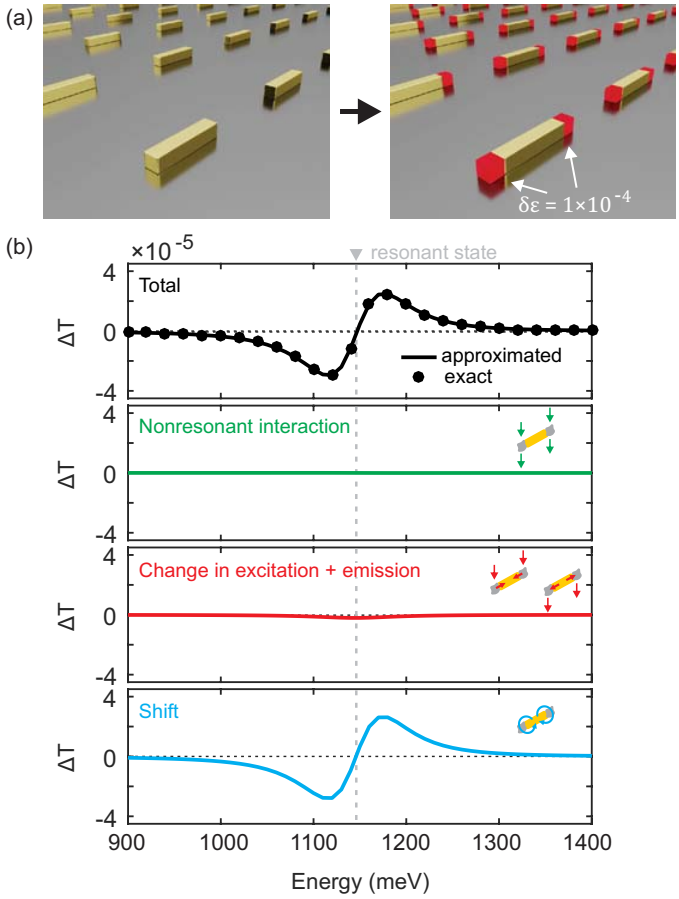

FIGURE 4.6. Optical response of the rod antenna array to the perturbation. (a) As perturbation, we consider a permittivity change by the value $\delta\varepsilon = 1 \times 10^{-4}$. (b) Resulting transmittance change ΔT. The top plot denotes the total signal (line: calculated with the perturbation theory; dots: exact full-wave calculations). The individual contributions are depicted in the plots below. It can be seen that in the above scenario, the transmittance change is dominated by the shift contribution, while all other contributions are virtually negligible.

in the excitation and emission efficiencies are very weak and practically negligible as well. Basically, the whole transmittance change is associated with the perturbation-induced eigenfrequency shift of the resonant state. This finding fully agrees with the expectation from literature [7, 11, 13, 25, 51,

52, 122, 123, 224] that resonance shifts are the dominating effect in resonant nanophotonic sensing of dielectric material properties. We will later, in chapter 5, see that for the sensing of chiral material properties, the situation is vastly different.

4.4 CONCLUSION

In this chapter, we have presented a first-order perturbation theory that allows for predicting the impact of local material variations inside a resonator onto any of its far-field quantities via evaluating simple overlap integrals over the unperturbed electromagnetic fields. The far-field quantities were represented via the optical scattering matrix. We have shown that the change in this matrix is originating from exactly five different contributions: a nonresonant interaction, changes in the excitation and emission efficiencies of the resonant states, resonance shifts, and crosstalk between different resonant states. To verify the applicability of the theory, we have investigated a simple example from the field of dielectric sensing. We have found that here – in full accordance with the literature expectation – resonance shifts are the dominating effect that basically makes up all of the observable sensor signal.

5

CHIRAL SENSING

In chapter 4, we have provided a first-order perturbation theory for the changes of optical far-field quantities under local material variations in open optical resonators. Here, we will apply this theory to understand the mechanisms that occur in a very specific application: nanophotonic chiral sensing.

This chapter is based on publication [P6]:

S. Both, M. Schäferling, F. Sterl, E. A. Muljarov, H. Giessen, and T. Weiss: *Nanophotonic chiral sensing: How does it actually work?* ACS Nano **16**, 2822–2832 (2022).
DOI 10.1021/acsnano.1c09796.

5.1 INTRODUCTION

The term "chirality" refers to objects that cannot be superimposed with their mirror image [232]. These two so-called enantiomorphs (or, in case of molecules, enantiomers) differ only in their handedness, which can be left or right. What sounds like a purely mathematical concept has in fact a huge impact, as life itself is chiral [233, 234]. The outcome of most biochemical interactions, where chiral biomolecules shake hands, strongly depends on the mutual handedness of the reactants. In extreme examples, the handedness of a molecule makes the difference between a drug and a toxin [235, 236]. Therefore, detecting the handedness of molecules is of crucial interest for countless applications in life science and chemistry, as well as for the pharmaceutical industry [237].

Conventional detection schemes rely on the fact that the interaction of chiral media with light can differ among the two circular polarizations and depends on the handedness of the enantiomers. Assuming a homogeneous and isotropic medium, this interaction is governed by the chiral constitutive equations (provided in Gaussian units, in accordance with the rest of this thesis) [238, 239]:

$$\begin{aligned} \mathbf{D} &= \varepsilon \mathbf{E} - i\kappa \mathbf{H}, \\ \mathbf{B} &= \mu \mathbf{H} + i\kappa \mathbf{E}. \end{aligned} \tag{5.1}$$

Here, the permittivity ε and the permeability μ represent the "nonchiral" properties of the medium, and the Pasteur parameter κ quantifies its chirality. Opposite handedness of the medium results in an opposite sign of κ. A nonzero real part of κ induces a difference in the phase velocities of left- and right-handed circularly polarized light, i.e., circular birefringence, while a nonzero imaginary part induces a difference in their absorption. Measuring this absorption difference – denoted as the circular-dichroism (CD) signal – is the standard method for optically characterizing the chirality of a medium.

Since chiral light-matter interactions are typically extremely weak (at optical frequencies, natural materials have $\kappa \ll 1$), this detection can be very challenging, especially when only tiny amounts of substances are involved. Overcoming this limitation would be highly attractive for numerous applications. A promising approach consists in the use of nanophotonic resonators to boost the chiral light-matter interactions. For the sensing of "nonchiral" material properties, this is already a well-established technique. Applications include the ultra-sensitive detection of biomolecules [7, 9–13, 17], gases [P9],[21], and much more [23–25]. In the past decade, a lot of work, both experimental [26–29, 240–248] and theoretical [245, 249–273], has been carried out to utilize the benefits of this technique for the detection of chiral substances. Different resonator designs have been investigated, ranging from plasmonic antennas [26–28, 240–244, 253, 257] to dielectric nanostructures [29, 264, 267, 269, 270] or combinations [265] to so-called "helicity-preserving" cavities [268, 271–273]. Another promising route is using structures that exhibit resonances in the ultraviolet region [246–248], where natural molecules have particularly large κ values. Comprehensive overviews can be found in corresponding review articles [30, 274–280].

The basic principle of nanophotonic chiral sensing is illustrated in Fig. 5.1: The starting point is a nanophotonic resonator that can be brought into contact with the chiral medium. The resonator itself may also be chiral (e.g., due to its shape), but does not have to be. As an example, we depict an

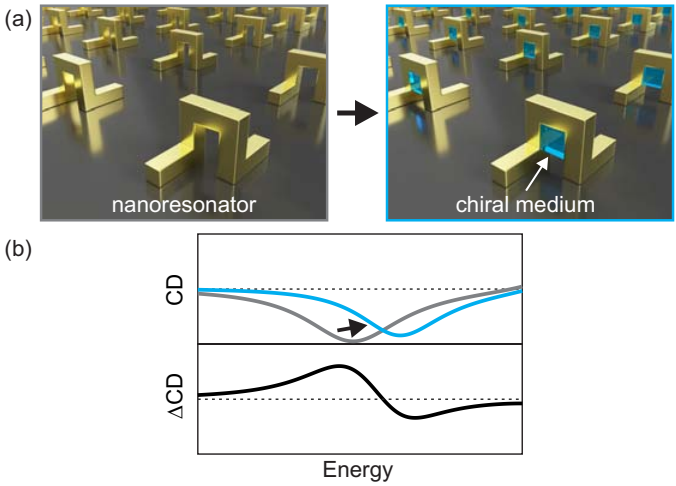

FIGURE 5.1. Principle of nanophotonic chiral sensing. (a) The starting point is a nanophotonic resonator that can be brought in contact with the chiral medium. The example depicts an array of Ω-shaped plasmonic antennas, where the chiral medium is added to their centers. (b) The circular-dichroism (CD) spectrum is measured without (gray) and with (light blue) chiral medium. The change in the spectrum (ΔCD) contains information about the chirality of the medium. Due to the enhanced light-matter interaction taking place in the resonator, the ΔCD signal is typically orders of magnitude larger than the signal that would be obtained from the chiral medium alone.

array of Ω-shaped plasmonic nanoantennas [281–284]. The chiral medium is assumed to be added in their centers. First, the CD spectrum of the resonator without the chiral medium is measured (gray), to serve as a reference. Then, the resonator is brought into contact with the chiral medium and the CD spectrum is measured again (light blue). Note that for visualization, the spectral changes in the plot are dramatically exaggerated. The difference between both spectra (we denote it as ΔCD) contains information about the handedness of the medium. Due to the enhanced light-matter interaction taking place in nanophotonic resonators, the ΔCD signal is typically orders of magnitude larger than the signal that would be obtained from the chiral medium alone.

An important experimental detail in the above procedure is not to use the plain resonator as reference, but rather the resonator covered with a so-called racemic mixture [28, 29] (1:1 mixture of left-handed and right-handed enantiomers, which is optically achiral) at the positions where the

chiral medium is supposed to be placed later. This ensures that only κ varies between both measurements, while the other material parameters are constant. Note that there also exist variations of the procedure that work without the need to use a racemic mixture [26, 261]; however, also in these cases, the key lies in tracing the change of an optical signal induced by the interaction of the resonator with the chiral medium.

For the case of a single chiral molecules, the above interaction is well understood [251, 252]; however, in practice, one typically does not deal with single chiral molecules, but with chiral media (i.e., a solution or a layer of many molecules). In this case, describing the interaction with a resonator is more sophisticated. The description relies on either simple approximations or on purely numerical approaches: The intuitive method [26, 245, 254, 256, 259, 262, 263] consists in evaluating the optical chirality [250]

$$C = -\frac{\omega}{8\pi c} \operatorname{Im}\left(\mathbf{E}^* \cdot \mathbf{B}\right), \tag{5.2}$$

of the resonator's near field (the superscript $*$ indicates the complex conjugate). The optical chirality allows for predicting the power P_{abs} that is absorbed in the chiral medium via[1] $P_{\text{abs}} \propto \int_{V_c} dV \operatorname{Im}(\kappa) C$ [238], where V_c represents the volume that is occupied by the medium. However, while being very illustrative, this approach has severe limitations [29, 30, 285]: First, it neglects any influence of the real part of κ, which – although it would not contribute to the CD of the chiral medium located outside a resonator – is known to strongly contribute to the CD of the combined system [29, 285]. Second, it neglects the back action from the chiral medium onto the fields of the resonator, known as induced CD [252, 279, 285, 286]. The rigorous method [29, 244, 261, 266, 272, 285–289] consists in directly including the chiral medium into numerical calculations via Eq. (5.1). However, while this approach accounts for all electromagnetic effects, it provides rather limited insights into the interaction. As an alternative to numerical calculations, in some cases, the interaction can be described analytically via Mie theory [290], or semianalytically via a simple closed-form expression [264]. The former is, however, only applicable for systems with spherical or ellipsoidal symmetry, while the latter only works for resonators that can be treated as an effective medium.

Based on the theoretical framework from chapter 4, we close the existing gap and present a theory of chiral light-matter interactions in arbitrary

1 For simplicity, we have assumed here that the chiral medium exhibits $\operatorname{Im}(\varepsilon) = \operatorname{Im}(\mu) = 0$. The expression for the absorbed power in the general case can be found in Ref. [238]

resonators. This approach retains the rigorousness of the numerical calculations, while at the same time providing a deep intuitive insight. We show that the *entire chiral light-matter interaction* can be explained as a combination of the five different contributions that have been defined in chapter 4. We quantify the impact of these contributions in different sensor geometries. Furthermore, we show that – contrary to common expectation – resonance shifts are often not the dominating sources of signal changes.

5.2 THEORY

In chapter 4, we have presented a first-order perturbation theory that allows us to predict changes in the far-field quantities of an optical resonator under local material variations inside the resonator. The resonator was described with a material operator $\hat{\mathbb{P}}$ and the material variations were incorporated via a perturbation operator $\delta\hat{\mathbb{P}}$. Let us now apply this approach for the special case of chiral sensing. We assume that we start with an unperturbed resonator with $\kappa = 0$ and as a perturbation, a chiral medium is locally inserted. Consequently, the perturbation operator reads as

$$\delta\hat{\mathbb{P}} = \begin{cases} -\kappa \begin{pmatrix} 0 & \hat{I} \\ \hat{I} & 0 \end{pmatrix} & \text{inside volume } V_\mathrm{c}, \\ 0 & \text{outside.} \end{cases} \tag{5.3}$$

Here, $\hat{I}$ denotes 3×3 unit matrix, V_c represents the volume in which the chiral medium is inserted, and κ is the Pasteur parameter of the chiral medium. The above $\delta\hat{\mathbb{P}}$ corresponds to the most relevant scenario, where one transitions from a racemic mixture to a chiral medium, such that only κ varies and the "nonchiral" material parameters ε and μ stay constant. In the following, we will focus on this scenario. Note, however, that, as shown in chapter 4, it is straightforward to account for changes in ε and μ as well. Furthermore, instead of considering a scalar κ, it is also possible to include bi-anisotropic contributions, originating, e.g., from molecular alignment effects [244, 289].

As a consequence of the perturbation, the scattering matrix changes from S_{MN} to $S_{\mathrm{MN}} + \delta S_{\mathrm{MN}}$. As we have seen in chapter 4, the resulting scattering-matrix change δS_{MN} (in first-order perturbation theory) is given by

$$\delta S_{\mathrm{MN}} = \delta S_{\mathrm{MN}}^{\mathrm{nr}} + \delta S_{\mathrm{MN}}^{\mathrm{ex}} + \delta S_{\mathrm{MN}}^{\mathrm{em}} + \delta S_{\mathrm{MN}}^{\mathrm{shift}} + \delta S_{\mathrm{MN}}^{\mathrm{cross}}, \tag{5.4}$$

where the five contributions on the right-hand side are defined by Eqs. (4.12) to (4.16). For convenience, let us write out the equations for the special case of the above $\delta\hat{\mathbb{P}}$ in Eq. (5.3):

$$\delta S^{\mathrm{nr}}_{\mathrm{MN}}(\omega) = \frac{\omega}{c}\int\limits_{V_\mathrm{c}} dV i\kappa \left[\mathbf{E}^{\ddagger}_{\mathrm{BG,M}}(\omega)\cdot\mathbf{H}_{\mathrm{BG,N}}(\omega) + \mathbf{H}^{\ddagger}_{\mathrm{BG,M}}(\omega)\cdot\mathbf{E}_{\mathrm{BG,N}}(\omega)\right], \quad (5.5)$$

$$\delta S^{\mathrm{ex}}_{\mathrm{MN}}(\omega) = -\omega\sum_n \frac{a^{(n)}_{\mathrm{M}}(\omega)}{\omega-\omega_n}\int\limits_{V_\mathrm{c}} dV i\kappa \left[\mathbf{E}^{\ddagger}_{n}\cdot\mathbf{H}_{\mathrm{BG,N}}(\omega) + \mathbf{H}^{\ddagger}_{n}\cdot\mathbf{E}_{\mathrm{BG,N}}(\omega)\right], \quad (5.6)$$

$$\delta S^{\mathrm{em}}_{\mathrm{MN}}(\omega) = -\omega\sum_n \frac{b^{(n)}_{\mathrm{N}}(\omega)}{\omega-\omega_n}\int\limits_{V_\mathrm{c}} dV i\kappa \left[\mathbf{E}^{\ddagger}_{\mathrm{BG,M}}(\omega)\cdot\mathbf{H}_{n} + \mathbf{H}^{\ddagger}_{\mathrm{BG,M}}(\omega)\cdot\mathbf{E}_{n}\right], \quad (5.7)$$

$$\delta S^{\mathrm{shift}}_{\mathrm{MN}}(\omega) = \omega c\sum_n \frac{a^{(n)}_{\mathrm{M}}(\omega)b^{(n)}_{\mathrm{N}}(\omega)}{(\omega-\omega_n)^2}\int\limits_{V_\mathrm{c}} dV i\kappa \left(\mathbf{E}^{\ddagger}_{n}\cdot\mathbf{H}_{n} + \mathbf{H}^{\ddagger}_{n}\cdot\mathbf{E}_{n}\right), \quad (5.8)$$

$$\delta S^{\mathrm{cross}}_{\mathrm{MN}}(\omega) = \omega c\sum_{n\neq m} \frac{a^{(n)}_{\mathrm{M}}(\omega)b^{(n)}_{\mathrm{N}}(\omega)}{(\omega-\omega_n)(\omega-\omega_m)}\int\limits_{V_\mathrm{c}} dV i\kappa \left(\mathbf{E}^{\ddagger}_{n}\cdot\mathbf{H}_{m} + \mathbf{H}^{\ddagger}_{n}\cdot\mathbf{E}_{m}\right). \quad (5.9)$$

This set of equations allows us to predict the response of a resonator to chiral perturbations via simple overlap integrals of the unperturbed fields over the region of the perturbation. As a reminder, we recall that the five contributions $\delta S^{\mathrm{nr}}_{\mathrm{MN}}$, $\delta S^{\mathrm{ex}}_{\mathrm{MN}}$, $\delta S^{\mathrm{em}}_{\mathrm{MN}}$, $\delta S^{\mathrm{shift}}_{\mathrm{MN}}$, $\delta S^{\mathrm{cross}}_{\mathrm{MN}}$ have clear physical interpretations: They are associated with a nonresonant interaction, changes in the excitation efficiencies of the resonant states, changes in the emission efficiencies, shifts in the resonant states' eigenfrequencies, and crosstalk between different resonant states, respectively.

In the following, we will investigate the significance of these contributions in different chiral-sensing examples. However, before we continue, let us now have a closer look at the shift contribution. As already indicated, $\delta S^{\mathrm{shift}}$ denotes the response of the scattering matrix to resonance shifts. As we have seen in subsection 2.3.2, the shift of the eigenfrequency of an individual resonant state under any kind of local material perturbations $\delta\hat{\mathbb{P}}$ is given by Eq. (2.97). Plugging in the special $\delta\hat{\mathbb{P}}$ from above, we obtain an explicit expression for the eigenfrequency shift under chiral perturbations:

$$\delta\omega_n = \omega_n\int\limits_{V_\mathrm{c}} dV \underbrace{i\kappa\left(\mathbf{E}^{\ddagger}_{n}\cdot\mathbf{H}_{n} + \mathbf{H}^{\ddagger}_{n}\cdot\mathbf{E}_{n}\right)}_{\text{“}\delta\omega_n\text{ per volume”}}. \quad (5.10)$$

For later convenience, we will refer to the term under the integral as the "shift per volume" density. Note that as explained in subsection 2.3.2, in general, $\delta\omega_n$ is complex, with $\mathrm{Re}(\delta\omega_n)$ corresponding to a change in the resonance frequency and $\mathrm{Im}(\delta\omega_n)$ to a change in the linewidth, respectively.

The above equation reveals an interesting connection to the optical chirality from Eq. (5.2): Let us assume a typical chiral medium with $|\mathrm{Re}(\kappa)| \gg |\mathrm{Im}(\kappa)|$, a resonator with low losses, i.e., $|\mathrm{Re}(\omega_n)| \gg |\mathrm{Im}(\omega_n)|$, and furthermore restrict the considerations to a scenario where $\mathbf{E}_n^{\ddagger}=\mathbf{E}_n$ and $\mathbf{H}_n^{\ddagger}=\mathbf{H}_n$. In this case, one finds that the change of the resonance frequency $\mathrm{Re}(\delta\omega_n)$ is proportional to the integral over $\mathrm{Im}(\mathbf{E}_n \cdot \mathbf{H}_n)$. This quantity is closely related to the optical chirality. Therefore, as a rule of thumb, one can deduce that systems optimized for strong chiral resonant states are also sensitive for resonance frequency changes.

5.3 RESULTS

Let us now investigate some example systems.

5.3.1 *Example 1: Rod antennas.*

For the first example, we again consider the rod antenna array that has been discussed in section 4.3 in the context of dielectric sensing. This example is selected, since it represents one of the most frequently used kind of structures in nanophotonic sensing. The dimensions as well as the unperturbed material parameters are the same as in section 4.3. The only difference is that instead of a perturbation by a dielectric medium, we now consider a perturbation by a chiral medium, represented by a Pasteur parameter of $\kappa = (1 + 0.01i) \times 10^{-4}$. As in the dielectric example, the medium is placed in cubic patches of size $40 \times 40 \times 40\ \mathrm{nm}^3$ at the ends of the antennas, i.e., in the regions where the strongest near fields are known to occur. A visualization is provided in Fig. 5.2(a). The value of κ is deliberately chosen such that it exhibits a large but still realistic magnitude [29, 291] and contains a typical ratio between real and imaginary part [29, 286].

Figure 5.2(b) shows the spectral response of the antennas around the fundamental plasmonic resonant state (cf. Fig. 4.4). As a representative quantity, we plot the ΔCD signal. The corresponding matrices S_{MN} and δS_{MN} with all their components can be found in Figs. C.1 and C.2 of Appendix C.1.

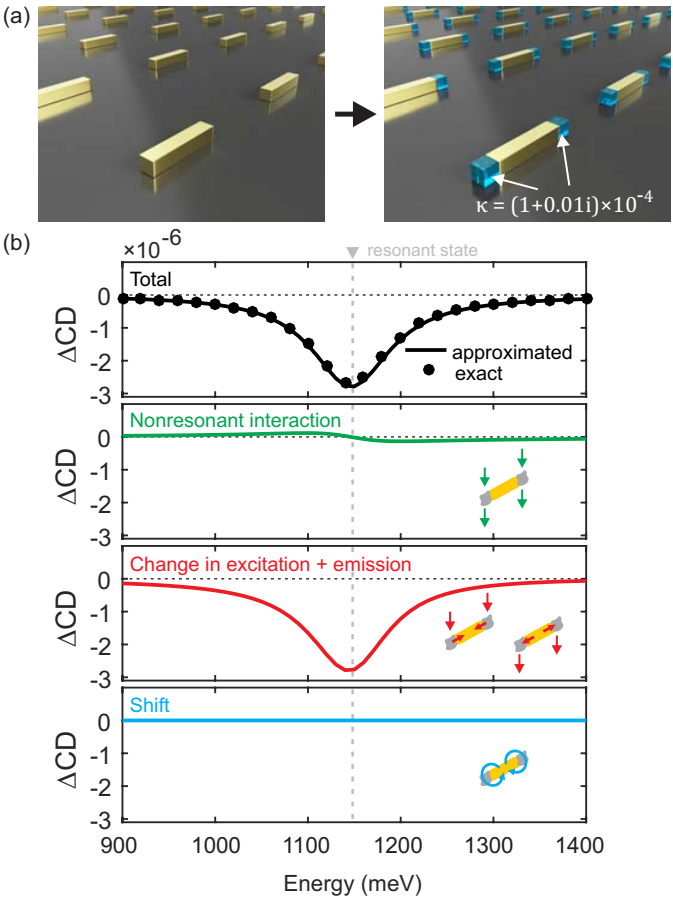

Figure 5.2. Optical response of the plasmonic rod antennas. (a) We consider an array of rod antennas with chiral media placed at each end as a perturbation. The antenna dimensions as well as the unperturbed materials are the same as in the dielectric-sensing example from section 4.3. (b) Resulting ΔCD spectrum. The top plot denotes the total signal (line: approximated with our perturbation theory; dots: exact full-wave calculations). The individual contributions are depicted below. The system is dominated by the changes in the excitation and emission efficiencies, while the shift contribution is exactly zero.

Details on how the ΔCD signal is obtained from S_{MN} and δS_{MN} are provided in Appendix C.2. In analogy to section 4.3, the matrices were calculated from inserting the fundamental resonant state into Eqs. (2.76) and (5.4). To

improve the accuracy of S_{MN}, the same cubic background fit as before was used, to account for the influence of higher-order resonant states. The calculations were again performed with COMSOL Multiphysics[2] by using the same approaches as before.

The top panel in Fig. 5.2(b) depicts the total ΔCD signal. The line denotes the result of the perturbation theory, while the dots have been obtained by exact full-wave calculations and are plotted for comparison. It should be mentioned that the rod antennas are geometrically achiral and hence do not produce any CD signal in the absence of the chiral medium [249]. Therefore, the ΔCD signal is identical to the CD signal of the perturbed system.

Note that for the full-wave calculations, it was necessary to implement the chiral constitutive relations in COMSOL. This has been done by following the method described in Ref. [286].

It can be seen that there is an excellent agreement. The total ΔCD signal exhibits a Lorentzian lineshape, with its highest absolute value being located at the resonance energy of the resonant state (indicated by a vertical dashed line). The lower panels display the different contributions. For compactness, we have summed up the change in the excitation and emission efficiency contributions to one curve. Furthermore, there is no crosstalk curve, since only one resonant state is considered. Note that the curve for the nonresonant interaction shows a zero crossing at exactly the resonance energy of the resonant state. This might strike as a mistake, since $\delta S_{\mathrm{MN}}^{\mathrm{nr}}$ does not contain any dependence on the resonant states [cf. Eq.(5.5)]. There is, however, a trivial explanation: As already mentioned, we do not look at the contributions of δS_{MN}, but at their impacts on the ΔCD signal. These impacts contain an additional modulation by the unperturbed scattering matrix S_{MN} (for details, see derivation of ΔCD in Appendix C.2), and this matrix depends on the resonant states.

The results in Fig. 5.2(b) paint a very clear picture: The system is dominated by the change in the excitation and emission efficiencies of the resonant state. The nonresonant interaction contribution is very small and practically irrelevant. The shift contribution is not only small but turns out to be strictly zero. This result is quite surprising, since resonance shifts are widely believed to be the driving mechanism behind nanophotonic chiral sensing [26, 242, 244, 253].

In order to understand why the shift contribution is zero, it is instructive to have a closer look at the resonant state. Its electric field can be found in

2 See https://www.comsol.com.

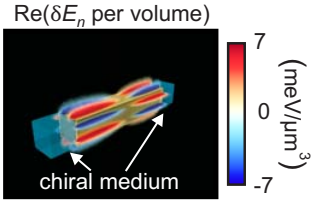

FIGURE 5.3. Details on the resonance shift in the rod antennas. Depicted is the "shift per volume" density of the fundamental plasmonic resonant state (cf. Fig. 4.4). From the plot, it is obvious that inside the volume of the chiral media patches (displayed as bluish cubes), the "shift per volume" is very weak, and furthermore, positive and negative contributions cancel out each other. Details on how this three-dimensional plot was created can be found in Appendix B.

Fig. 4.4 from the previous chapter. By applying Eq. (5.10), one can derive the corresponding "shift per volume" density. The result is plotted in Fig. 5.3. Note that for consistency with the spectra, we use units of energy ("δE_n per volume") instead units of frequency ("$\delta\omega_n$ per volume"). The shift of the energy eigenvalue δE_n ($=\hbar\delta\omega_n$) is obtained by integrating the "shift per volume" density over the volume of the perturbation (the chiral media patches are displayed in Fig. 5.3 as bluish cubes). From the plot, it is obvious that the integral vanishes: First of all, the "shift per volume" is very weak inside the region of the patches. Second, and more importantly, positive (red) and negative (blue) contributions are occurring symmetrically such that they cancel out each other. It can be easily deduced from the plot that this symmetry argument does not only apply when the chiral medium is positioned at the ends of the antenna, but also holds for other distributions, e.g., when the medium would completely surround the antenna.

In fact, it is straightforward to prove that *any geometrically achiral sensor* will experience zero resonance shift in first-order perturbation theory. The argument is as follows: The electric field classifies as a vector (it flips its direction under parity inversion), while the magnetic field classifies as a pseudovector (it does not flip its direction under parity inversion) [200]. This makes the shift δE_n defined by Eq. (5.10) a pseudoscalar (it does change its sign under parity inversion). Now let us suppose that the considered sensor is geometrically achiral. Since geometrically achiral sensors are by definition invariant under parity inversion, one will obtain $\delta E_n = -\delta E_n$. The only solution is that $\delta E_n = 0$. Hence, geometrically achiral sensors cannot exhibit a resonance shift within the limits of first-order perturbation theory.

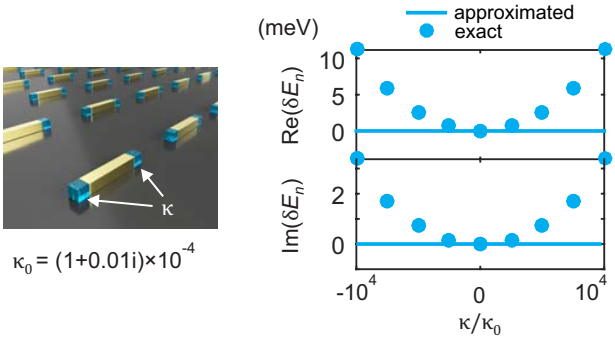

Figure 5.4. Resonance shift in the rod antenna for extremely large $|\kappa|$ values. We plot the change in the energy eigenvalue of the fundamental resonant state as a function of κ. On the x axis, κ is varied as a multiple of $\kappa_0 = (1 + 0.01i) \times 10^{-4}$. The lines denote the prediction of the theory [i.e, the first-order approximation from Eq. (5.10)], while the dots represent exact full-wave calculations. We see that for large $|\kappa|$ values, the first-order approximation (which predicts that the eigenvalue is constant) breaks down and a shift appears. Note, however, that the corresponding $|\kappa|$ values are extremely large (the edge of the x axis corresponds to $|\kappa|$ values in the order of one) and are far beyond what is known for any natural material. Furthermore, the shift is symmetric with respect to $+\kappa$ and $-\kappa$.

Since this statement only concerns the first perturbation order, one may wonder if there can appear a shift in higher orders of perturbation. To investigate this, we have calculated the eigenvalues of the rod antenna system as a function of κ, for the case that $|\kappa|$ becomes extremely large. The results are displayed in Fig. 5.4. We find that, indeed, for very large $|\kappa|$, the eigenvalues start to noticeably change, even in this achiral sensor. Thus, there does exist a higher-order shift. However, it turns out that this higher-order shift is useless for sensing: First, it only occurs at extremely large $|\kappa|$ values, which are far beyond what is known for any natural material. Second, and more importantly, for achiral sensors, it is always symmetric with respect to $+\kappa$ and $-\kappa$. To prove this, one simply needs to consider two facts: 1) Replacing $+\kappa$ by $-\kappa$ in an achiral sensor is equivalent to a parity inversion of the perturbed Maxwell operator. 2) Energy eigenvalues must be invariant under parity inversion. In other words: Only even orders of perturbation in κ can yield nonzero resonance shifts, but these are insensitive with respect to the sign of κ. Therefore, the higher-order shift cannot distinguish between the two enantiomers of a chiral molecule.

However, the above considerations suggest that it can be possible to enforce a first-order resonance shift in the rod antennas by breaking the achiral symmetry of the patch arrangement. An obvious choice consists in placing the chiral medium only in regions with a uniform sign of the "shift per volume" density [255]. To verify this, we have considered the rod antenna with the chiral medium distributed over the positive regions (red spots in Fig. 5.3). The results (see Figs. C.3 and C.4 of the Appendix) confirm that this arrangement indeed provides a nonzero shift contribution. However, interestingly, it can only be observed in the channels of δS_{MN}, but not in the ΔCD spectrum, since the signals from different channels cancel out each other. Furthermore, it is quite obvious that such a three-dimensional patch arrangement would be rather difficult to realize in practice.

5.3.2 *Example 2: Ω antennas*

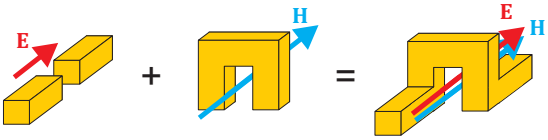

Figure 5.5. Example for a geometry that promises a large resonant shift: The textbook example for a nanostructure that supports strong resonant electric fields is the plasmonic gap antenna (left). The textbook example for a nanostructure that supports strong resonant magnetic fields is the split ring resonator (middle). An easy way to combine both, is to take an upright standing split-ring resonator and attach two rod antennas to its feet. The result (right) is a structure that looks like the Greek letter Ω. The particular arrangement of the building blocks promises collinearity of the electric and magnetic fields within the center of the Ω.

Let us now use the insights of our theory to find a system that is particularly designed to feature a strong resonance shift. According to Eq. (5.10), there are two requirements: On the one hand, the system needs to support a resonant state with strong collinear electric and magnetic fields in some region of space. On the other hand, the product between both fields should exhibit one predominant sign. Nanophotonics provides a rich pallet of building blocks that can be used to achieve this. In fact, many systems discussed in the literature on chiral sensing [26, 253, 254, 257, 259, 261] are already

optimized for strong optical chirality and – due to the connection discussed under Eq. (5.10) – should intrinsically meet these requirements. However, as a very intuitive example, let us consider the following: The textbook example for a nanostructure that supports strong resonant electric fields is the plasmonic gap antenna. The textbook example for a nanostructure that supports strong resonant magnetic fields is the split ring resonator. An easy way to combine both, is to take an upright standing split-ring resonator and attach two rod antennas to its feet. A visualization is provided in Fig. 5.5. As it can be seen, the result is a structure that looks like the Greek letter Ω. The particular arrangement of the building blocks promises collinearity of the electric and magnetic fields within the center of the Ω. Although they have never been utilized in the context of sensing so far, such Ω antennas are known to exhibit a strong chiroptical far-field response [281–284].

We consider again a periodic array of antennas, as depicted in Fig. 5.1(a). The materials are the same as in the rod antenna example, and the dimensions are chosen comparably: The Ωs have a total length of 240 nm, a total width of 140 nm, and a total height of 140 nm. They are wound of a quadratic wire with a lateral extension of 40 nm. The chiral medium is assumed to be inserted into their centers, within patches that are 40 nm in length, 60 nm in width, and 60 nm in height. The period is 500 nm. It should, however, be mentioned that the fabrication of such three-dimensional structures is in general not an easy challenge (although there are approaches [283, 284, 292, 293]).

Figure 5.6(a) displays the "shift per volume" density of the energetically lowest two excitable plasmonic resonant states. The results confirm what was intuitively expected: There is a hotspot with high uniform values in the center of the antenna. Note that for the given configuration, resonant state 1 exhibits a negative sign, while resonant state 2 exhibits a positive one. Let us now assume that a patch of chiral medium is inserted into the hotspot [for visualization, see Fig. 5.1(a)]. Figure 5.6(b) displays the resulting energy eigenvalue shifts δE_n (both the real and imaginary parts) as a function of κ. On the x axis, κ is varied as a multiple of $\kappa_0 = (1 + 0.01i) \times 10^{-4}$. The lines show the prediction of the perturbation theory, while the dots have been derived from exact full-wave calculations and are depicted for comparison. It is evident that there is an excellent agreement. As expected from the "shift per volume" plots, the energy eigenvalues are very sensitive to κ changes. In agreement with the sign of the "shift per volume" density in the hotspot, resonant state 1 shows a negative slope in the $\mathrm{Re}(\delta E_n)$ plot, while resonant state 2 exhibits a positive one.

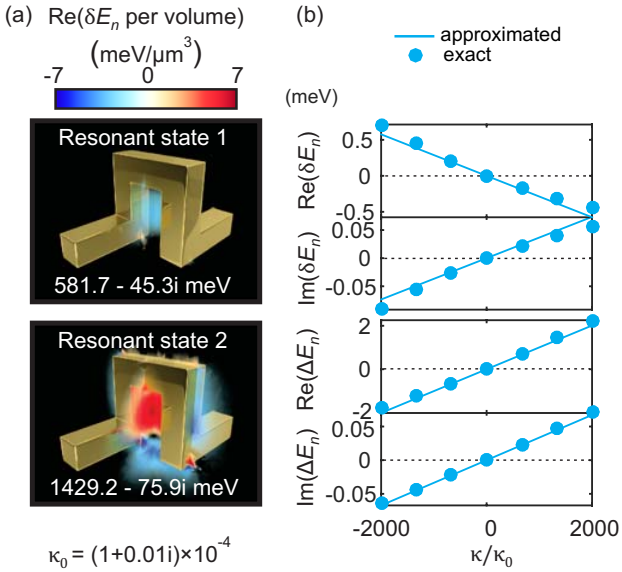

Figure 5.6. Resonance shift in the Ω antennas. The Ω antennas are expected to have a collinear electric and magnetic field at their centers, which results in a nonzero resonance shift. (a) "Shift per volume" of two plasmonic resonant states. Both resonant states exhibit hotspots with high values and a uniform sign in the center of the antenna. Details on how this three-dimensional plot was created can be found in Appendix B. (b) Changes in the energy eigenvalues (lines: approximation via the perturbation theory; dots: exact full-wave calculations) of the resonant states as a function of κ for a chiral medium inserted into the center of the antenna as shown in Fig. 5.1. The top and bottom plots of each subpanel correspond to the change in the real and imaginary part, respectively. Note that at the edges of the depicted $|\kappa|$ range, one can observe small deviations between the results predicted by the perturbation theory and the exact calculations, resembling the slow onset of the breakdown of the validity range of the first-order approximation.

To investigate the impact of the δE_n shifts, we evaluate again the spectral response of the system. In order to improve the accuracy, we include one further resonant state in the calculation. This resonant state is found at an energy eigenvalue of $1750.1 - 25.4i$ meV and (as we will see further below) contributes to the ΔCD signal via crosstalk.

As in the rod antenna example, we depict only the chiral response, while the matrices S_{MN} and δS_{MN} are provided in Figs. C.5 and C.6, respectively, of the Appendix. The calculations of the matrices are analogous to the case

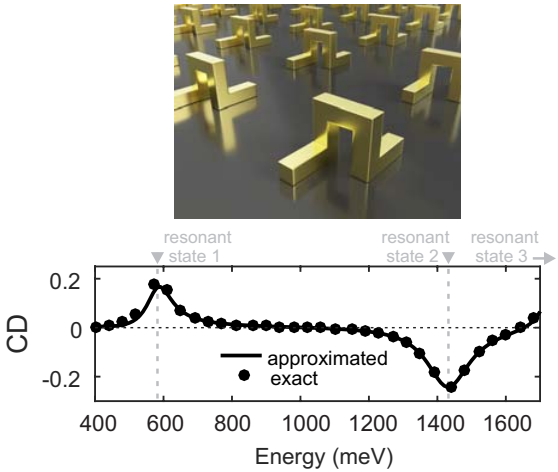

Figure 5.7. CD spectrum of the unperturbed Ω antennas. There are two features: a positive positive peak at resonant state 1 and a negative one at resonant state 2.

of the rod antennas, with the only difference that three resonant states are considered instead of one. As in the rod antenna case, the influence of higher-order resonant state in $S_{\mathbf{MN}}$ is accounted for with a cubic fit. The fit is evaluated at four energy points, equidistantly distributed over the calculated spectral range.

Figure 5.7 shows the CD spectrum of the unperturbed resonator. The line denotes the prediction of the resonant-state theory, while the dots correspond to full-wave calculations and are shown for comparison. The spectrum contains two pronounced features: a positive peak at resonant state 1 and a negative one at resonant state 2. Note that resonant state 3 lies outside the depicted spectral range.

Let us now investigate the response to a chiral medium. As for the rod antennas, we take a fixed value of $\kappa = (1 + 0.01i) \times 10^{-4}$ [cf. Fig. 5.8(a)] and calculate the ΔCD signal. The total ΔCD signal is displayed in Fig. 5.8(b) (top panel). One can again observe an excellent agreement between the prediction of the perturbation theory (line) and exact full-wave calculations (dots). Two distinct features can be identified: A peak at the resonance energy of resonant state 1, and a zero crossing surrounded by large absolute values at the resonance energy of resonant state 2. (Note that for a deeper analysis of resonant state 3, the interested reader may find the calculation

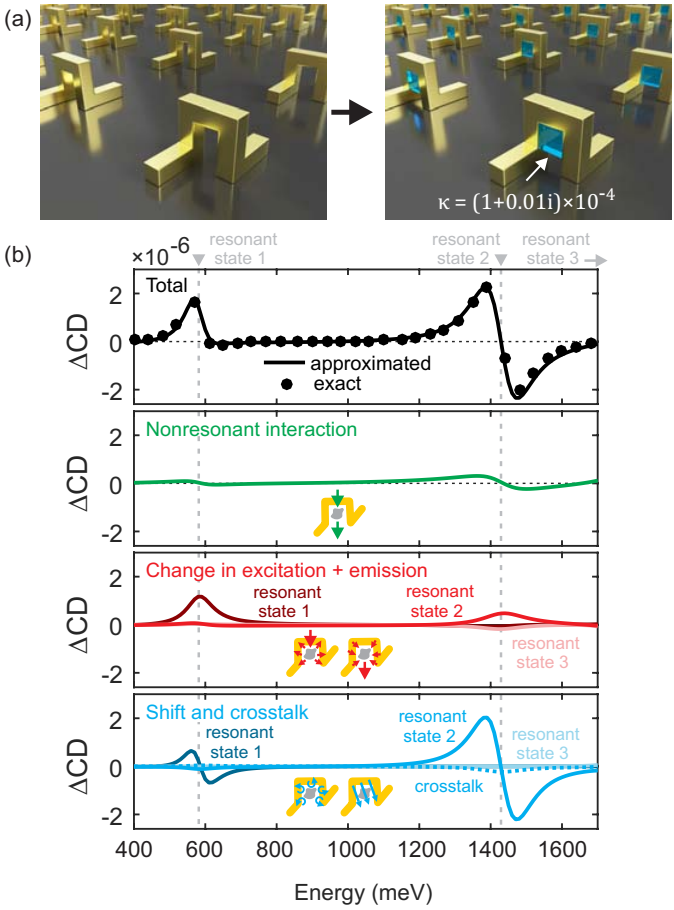

Figure 5.8. Optical response of the Ω antennas. (a) An array of antennas with chiral media patches in their center. (b) Resulting ΔCD spectrum. The top plot denotes the total signal (line: calculated with our perturbation theory; dots: exact full-wave calculations). The individual contributions are depicted below. As it can be seen, in this system, the change in the excitation and emission efficiencies as well as the shift are all relevant. Around resonant state 2, the shift is dominant.

results with the energy range extended to this resonant state in Fig. C.7 of the Appendix.)

The lower panels depict the individual contributions, subdivided into their modal origin. As it can be seen, in this system, the shift contribution plays an

important role for the total signal. However, in addition, also the changes in the excitation and emission efficiencies are quite strong. One can quantify the importance of the individual contributions for each resonant state separately: For resonant state 1, the change in the emission efficiencies is dominating over the shift. This combination leads to the peak shape in the ΔCD spectrum. For resonant state 2, the shift is dominating over the efficiency changes, leading to the zero-crossing behavior. The contributions associated with resonant state 3 only play a minor role. The nonresonant interaction is weak as well.

A careful reader may have noticed that resonant states 1 and 2 show opposite signs of the "shift per volume" density and their resonance energies are shifted in opposite directions by the perturbation (cf. Fig. 5.6), but nevertheless, both provide shift contributions of the same sign to the ΔCD signal. This seems to be a paradox. However, there is a simple explanation: We look at the ΔCD signal, i.e., the change of the CD signal. As it is shown in Fig. 5.7, the CD signal of the unperturbed Ω has a positive peak at resonant state 1, but a negative peak at resonant state 2 (cf. Fig. 5.7). Shifting a positive CD peak along one specific direction on the energy axis provides a contribution to ΔCD that has the opposite sign compared to shifting a negative peak along the same direction. Since both peaks are shifted in different directions, the sign of their contribution to ΔCD is the same.

To summarize the findings of the Ω example: This example demonstrates that it is indeed possible to design a sensor with large resonance shifts. However, interestingly, even in this sensor, the relevance of the changes in the excitation and emission efficiencies should not be underestimated. We do not see any reason that this should be different for other structures optimized for strong chiral near fields. Thus, while an analysis of optical chirality can yield promising nanostructure designs for sensing applications, all contributions must be taken into account for sensor optimization.

5.3.3 *Discussions*

After considering these two example systems, one might wonder which one has the better overall performance. Therefore, we evaluated their CD enhancement factors [286] (defined as $|\Delta\text{CD}|$ of the system normalized to the $|\text{CD}|$ of the chiral patches without the antennas). The results are depicted in Fig. 5.9. The answer might appear rather surprising: The rod antennas exhibit a maximum value of 325 and thereby outperform the Ω antennas, which only provide a maximum value of 250. Another advantage of the rod

antennas is that, since they are geometrically achiral, they do not provide any CD signal in the absence of the chiral medium [249].

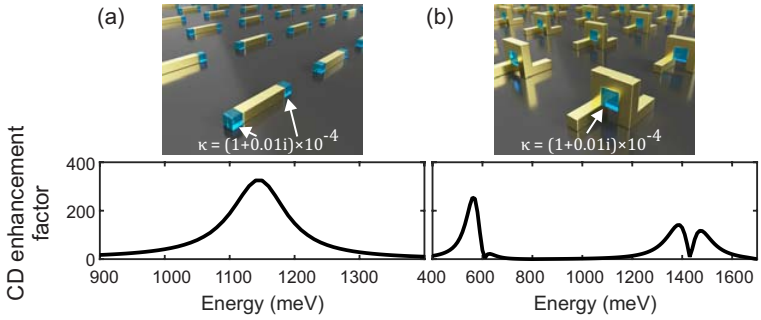

Figure 5.9. Calculated CD enhancement factors. (a) Rod antennas. (b) Ω antennas. The CD enhancement factor was calculated following Ref. [286] as the ratio between the $|\Delta\mathrm{CD}|$ spectrum of the chiral patches with antennas and the $|\mathrm{CD}|$ spectrum of the chiral patches alone.

In accordance with a previous numerical study [286], our results suggest that changes in the excitation and emission efficiencies (related to strong overlap of the incident fields with the resonant states) have to be considered as a relevant mechanism for nanophotonic chiral sensing rather than resonance shifts (related to strong overlap between the resonant states' electric and magnetic fields). Furthermore, our derivations reveal that in general, stronger near fields – regardless of with or without high optical chirality – lead to larger signals. There is no need for designing systems such that they exhibit a strong optical chirality with simultaneously weak electric fields, as suggested in early works [250, 294]. The difference is that these early works focused on optimizing a quantity known as "enantioselectivity", which is defined as the chiral asymmetry in the rate of excitation of two enantiomers of a chiral molecule. However, in the majority of optical sensors, the relevant factor that defines the signal-to-noise ratio and consequently the detection thresholds is the absolute signal strength [P9] and not the enantioselectivity.

Concerning the detection thresholds, one should be aware that the absolute values of the $\Delta\mathrm{CD}$ signal reported here are quite low and roughly one order of magnitude below the detection limit of most commercial CD spectrometers [249, 286]. The low $\Delta\mathrm{CD}$ values stem from the small amount of

chiral medium per unit volume of the periodic system that was used in our examples, in order to keep them simple. Comparable systems, but with a larger amount of chiral medium inserted, have shown to provide absolute signal strengths well above the detection limit [28, 29]. In our case, a larger amount of chiral medium per unit volume can be achieved by using either a higher density of antennas or by covering the antennas completely with the chiral medium instead of only their ends or centers, respectively.

5.4 LIMITATIONS OF THE APPROACH

All considerations made in this chapter are based on a first-order approximation in κ. Therefore, it is quite natural to ask what the limitations of this approach are. To systematically investigate the validity range of the theory, we have varied κ over many orders of magnitude and compared the predicted ΔCD spectra to exact full-wave calculations. Negative signs were considered as well. The results are depicted in Fig. 5.10. They reveal that the first-order approximation is accurate over a surprisingly huge range of values. Only when the order of $|\kappa|$ approaches unity, the deviations become relevant. Such values would, however, be far beyond what is known for any natural material.

Additionally, let us add some further remarks on the overall applicability of our method: In systems that have a lot of resonant states within (or around) the energy range of interest, the approach may become impractical. The reason is that in general, all those resonant states have to be considered in the calculation, in order to obtain accurate results. Furthermore, in periodic systems, energies around the Rayleigh anomalies [99] are problematic, since these anomalies also effectively act as an ensemble of resonant states [89, 229].

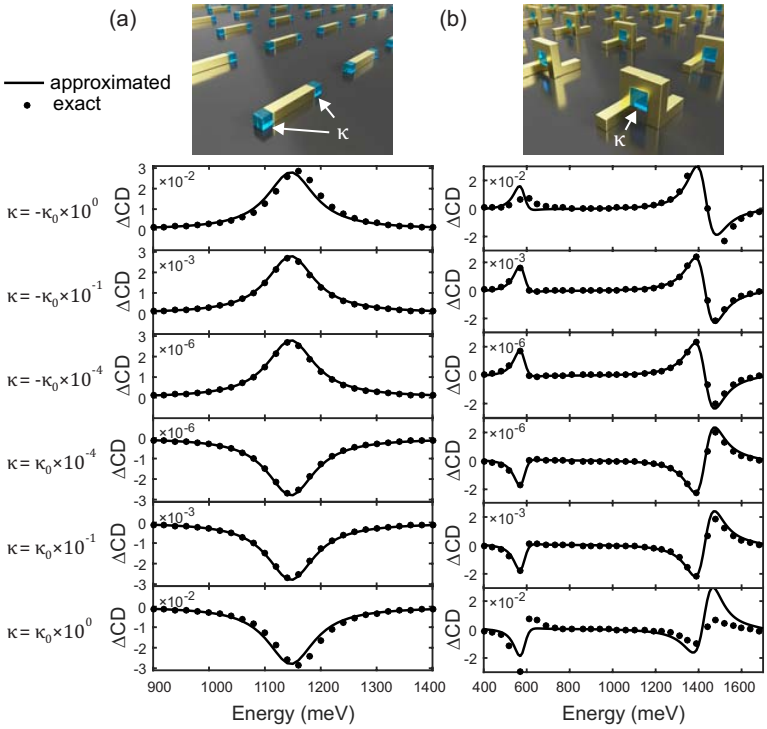

Figure 5.10. Validity range of the first-order approximation. (a) Rod antennas. (b) Ω antennas. The Pasteur parameter κ was varied over many orders of magnitude. Negative signs were considered as well. As it can be seen, our approach works well over a huge range of values. Only when the order of $|\kappa|$ starts to approach unity, the deviations become clearly visible. However, such values would be far beyond what is known for any natural material.

5.5 ADDITIONAL ADVANTAGES

In the end, we want to point out a benefit of the perturbative approach that was not mentioned so far and becomes relevant when calculating spectra for different κ values: While conventional full-wave simulations have to be repeated multiple times, the perturbative approach allows one to predict the output over the whole range of κ values with one single calculation. This is possible, because κ appears as a linear factor in the integrals of δS_{MN} [see Eqs. (5.4) to (5.9)]. Therefore, one only has to evaluate the integrals

with κ factored out and can multiply the result with any complex value of interest, to directly obtain the desired spectra. This even works when κ is not constant, but dispersive. There are at least two applications in sensor modeling: First, one is often interested in the sensor response to different analyte media. Second, even for one particular chiral analyte, one is typically interested in the response to both of its enantiomers (i.e., to both values $\pm\kappa$). Related to sensor modeling, there is a further benefit of the perturbative approach: It should not be forgotten that realistic κ values are typically extremely small. In full-wave calculations, this sets high standards for the accuracy of the simulations, so that the relevant signals do not vanish within numerical noise [266, 286]. The smaller the value of κ gets, the more computationally expensive the numerical simulation becomes. In sharp contrast, the perturbative approach can effortlessly predict spectral changes for *arbitrarily* small values of κ.

5.6 CONCLUSION AND OUTLOOK

In this chapter, we have presented a detailed theory of chiral light-matter interactions in nanophotonic resonators. Our theory reveals the mechanisms behind nanophotonic chiral sensing. There are exactly five contributions: a nonresonant interaction, changes in the excitation and emission efficiencies of the resonant states, resonance shifts, and crosstalk between resonant states. We have investigated the impact of these contributions in different sensor geometries. We have demonstrated that – contrary to common expectations – resonance shifts are often not the dominating source of the signal. In the case of achiral sensors, they are even strictly zero. Instead, it turns out that the changes in the excitation and emission efficiencies can be the driving mechanism for enhancing circular dichroism spectroscopy. Besides enabling deep intuitive insights for the understanding and tailoring of nanophotonic chiral light-matter interactions, our theory also constitutes a highly efficient computational tool, with clear advantages over conventional approaches in terms of calculation time and efforts.

A highly appealing future application of the theory would be to employ it for analyzing the chiral light-matter interactions in more sophisticated resonator geometries, such as achiral dual systems [256] as well as the "helicity-preserving" cavities from Refs. [268, 271–273].

6

EMITTER-NANOPARTICLE INTERACTION

So far in this thesis, we have focused on passive light-mater interactions in the context of sensing. In this chapter, we will now switch to active interactions, namely the interplay between light emitters and nanostructures. We will present a detailed theoretical model of the underlying interactions and show that they – if well understood – can be utilized as a tool to track movements on the nanoscale. In particular, our model will be applied to describe observations from experiments on DNA-based molecular nanodevices that were carried out in a theory-experiment collaboration.

This chapter is based on publications [P1], [P2], and [P3]:

M. J. Urban, S. Both, C. Zhou, A. Kuzyk, K. Lindfors, T. Weiss, and N. Liu: *Gold nanocrystal-mediated sliding of doublet DNA origami filaments.* Nature Communications **9**, 1454 (2018).
DOI 10.1038/s41467-018-03882-w.
Reprinted/adapted with permission. Copyright 2018, The Authors.

L. Xin, M. Lu, S. Both, M. Pfeiffer, M. J. Urban, C. Zhou, H. Yan, T. Weiss, N. Liu, and K. Lindfors: *Watching a single fluorophore molecule walk into a plasmonic hotspot.* ACS Photonics **6**, 985-993 (2019).
DOI 10.1021/acsphotonics.8b01737.
Reprinted/adapted with permission. Copyright 2019, American Chemical Society.

P. Zhan, M. J. Urban, S. Both, X. Duan, A. Kuzyk, T. Weiss, and N. Liu: *DNA-assembled nanoarchitectures with multiple components in regulated and coordinated motion.* Science Advances **5**, eaax6023 (2019).
DOI 10.1126/sciadv.aax6023.
Reprinted/adapted with permission. Copyright 2019, The Authors.

Note that there are further example systems from the field of DNA nanotechoonology that were investigated in the context of this thesis, but are not discussed in detail. They can be found in publications [P4] and [P8].

6.1 INTRODUCTION

6.1.1 *Emitter-nanostructure interaction*

Shortly after the rise in popularity of modern nano-optics in the first decade of the 2000s, a great interest of the scientific community started to emerge, concerning the exploration of the interaction between quantum emitters and optically resonant nanostructures. Successively, it has been demonstrated that this kind of interaction can be utilized for enhancing the emission strength of emitters [295–297], shaping their emission spectra [298], tailoring their directionality [177], or even for experimentally realizing quantum phenomena at room temperature [299].

While the above applications are very well-known, there exists another application that is less popular: the utilization of the interaction between emitter and nanostructure as a physical probe for tracking movements on the nanoscale. The basic principle is illustrated in Fig. 6.1. (a) A quantum emitter is placed in the vicinity of an optically resonant nanostructure (the example depicts a metallic nanoparticle). (b) Due to the Purcell effect (cf. 2.3.3), the fluorescence intensity may change depending on the distance between the emitter and the particle. Thus, by experimentally tracking the intensity, one can obtain information about a possible movement of the emitter with respect to the nanoparticle (as well as about the movement of the structures to which they may be attached).

In order to exploit the above approach in practice, it is of crucial relevance to have a thorough theoretical description of the underlying light-matter interactions. This is the goal of this chapter. We will first recap from literature the basic theory of how quantum emitters interact with resonant nanophotonic structures. Then, we will discuss several refinements that allow for accounting for specific experimental complications. The extended theory will be applied to describe and elucidate observations from experiments on DNA-based molecular nanodevices. We will also discuss how the theoretical approach outlined above can be combined with a kinetic model of chemical reaction dynamics in order to obtain insights into the dynamics of such

nanosystems. Furthermore, we will show how one can include another effect into the equations, known as Förster resonance energy transfer.

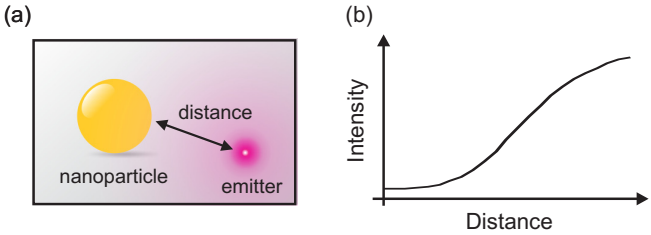

FIGURE 6.1. Principle of nanoscale movement sensing based on emitter-nanostructure interactions. (a) Depicted is a quantum emitter that is placed in the vicinity of an optically resonant nanoparticle. (b) The fluorescence intensity may change depending on the distance between the emitter and the nanoparticle. Thus, by experimentally tracking the intensity, one can obtain information about a possible movement of the emitter with respect to the nanoparticle (as well as about the movement of the structures to which they may be attached).

6.1.2 *DNA nanotechnology*

As already mentioned, the theory that we present in the following will be used to describe and elucidate observations in DNA-based nanomachines and nanodevices. Therefore, before we start discussing the light-matter interaction modeling, let us briefly introduce the concept of DNA nanotechnology: In a groundbreaking work from 2006, Paul Rothemund demonstrated that DNA can be programmed such that it folds itself into arbitrary two-dimensional nanoscale patterns via a self-assembly process [300] and termed this technique DNA origami. In 2009, shortly after Rothemund's initial work, it was shown that the approach can be extended to create structures in three dimensions [301]. Since DNA constitutes a very stable and easy-to-handle molecule, the possibility of using it as a building block for creating arbitrary three-dimensional nanostructures immediately started to attract a lot of attention [302]. Particularly interesting is the possibility of attaching other nanoobjects, such as metallic nanoparticles or quantum

emitters, to the DNA structures. This, e.g., allows for the realization of complex nanophotonic systems via this bottom-up fabrication technique [303]. Over the years, the DNA nanotechnology became more and more advanced. Nowadays, it is possible to realize molecular machines that can perform controllable motions and exercise specific tasks, with steadily increasing complexity [304, 305]. Later in this chapter, we will explore the light-matter interaction to study movements in such nanodevices.

6.2 BASIC THEORY

In the following, we will recap from literature [306] the basic theory of how a quantum emitter interacts with a resonant nanostructure. Note that instead of quantum emitter, we will use the term dye, since in this chapter, we are interested in describing fluorescent dye molecules. However, it is worth to emphasize that the presented approach is also valid for other kinds of emitters, such as quantum dots or defect centers, as long as they can be associated with an oscillating electric dipole moment.

First of all, a free dye is considered (i.e., a dye in the absence of any resonant nanostructure). Its fluorescence rate $\gamma_{\mathrm{fl},0}$ (i.e., the number of emitted photons per second, which is proportional to the fluorescence intensity) can be written as

$$\gamma_{\mathrm{fl},0} = q_0 \gamma_{\mathrm{exc},0}, \tag{6.1}$$

where q_0 denotes the so-called quantum yield and $\gamma_{\mathrm{exc},0}$ is the excitation rate (i.e., the number of absorbed photons per second). Note that the subscript 0 indicates quantities that belong to the free dye.

The quantum yield of a free dye is defined as the ratio of its radiative decay rate $\gamma_{\mathrm{r},0}$ and its total decay rate $\gamma_{\mathrm{tot},0}$. The total decay rate $\gamma_{\mathrm{tot},0}$ summarizes all decay channels of the dye and can be written as $\gamma_{\mathrm{tot},0} = \gamma_{\mathrm{r},0} + \gamma_{\mathrm{nr},0}$, where $\gamma_{\mathrm{nr},0}$ is the internal nonradiative decay rate, which accounts for nonradiative processes inside the dye molecule. Consequently, the quantum yield becomes

$$q_0 = \frac{\gamma_{\mathrm{r},0}}{\gamma_{\mathrm{r},0} + \gamma_{\mathrm{nr},0}}. \tag{6.2}$$

We now assume that the dye is placed in the vicinity of some resonant nanostructure. The interaction with the nanostructure gives rise to a modified fluorescence rate γ_{fl}, which, in analogy to Eq. (6.1), can be expressed as

$$\gamma_{\mathrm{fl}} = q \gamma_{\mathrm{exc}}, \tag{6.3}$$

where q and γ_{exc} are the modified quantum yield and modified excitation rate, respectively.

The modified quantum yield is defined as the ratio of the radiative decay rate γ_{r} in the presence of the nanostructure and the total decay rate γ_{tot} in the presence of the nanostructure. Here, $\gamma_{\mathrm{tot}} = \gamma_{\mathrm{r}} + \gamma_{\mathrm{abs}} + \gamma_{\mathrm{nr}}$, where γ_{nr} again accounts for nonradiative processes inside the dye and γ_{abs} denotes the rate of photon absorption in the nanostructure. Consequently, the modified quantum yield reads as

$$q = \frac{\gamma_{\mathrm{r}}}{\gamma_{\mathrm{r}} + \gamma_{\mathrm{abs}} + \gamma_{\mathrm{nr}}}. \tag{6.4}$$

Multiplying the right side with $\gamma_{\mathrm{r},0}/\gamma_{\mathrm{r},0}$, assuming that the presence of the nanostructure does not influence the internal decay processes (i.e., $\gamma_{\mathrm{nr}} = \gamma_{\mathrm{nr},0}$), and using $\gamma_{\mathrm{nr},0}/\gamma_{\mathrm{r},0} = (1 - q_0)/q_0$ [this follows from Eq. (6.2)] allows us to rewrite the quantum yield as

$$q = \frac{\frac{\gamma_{\mathrm{r}}}{\gamma_{\mathrm{r},0}}}{\frac{\gamma_{\mathrm{r}}}{\gamma_{\mathrm{r},0}} + \frac{\gamma_{\mathrm{abs}}}{\gamma_{\mathrm{r},0}} + \frac{1-q_0}{q_0}}. \tag{6.5}$$

Dividing Eq. (6.3) by (6.1), we can express the modification of the fluorescence rate as

$$\frac{\gamma_{\mathrm{fl}}}{\gamma_{\mathrm{fl},0}} = \frac{q}{q_0}\frac{\gamma_{\mathrm{exc}}}{\gamma_{\mathrm{exc},0}}, \tag{6.6}$$

where the factor $\gamma_{\mathrm{exc}}/\gamma_{\mathrm{exc},0}$ represents the modification of the excitation rate.

Equations (6.5) and (6.6) allow for formally describing how the presence of a nanostructure modifies the fluorescence rate of a dye. Note that we can interpret the modification of the fluorescence rate as a combination of three different effects, which are visualized in Fig. 6.2: First, the nanostructure may act as an antenna and influence the efficiency with which the dye is excited by incident light. This effect is contained in the factor $\gamma_{\mathrm{exc}}/\gamma_{\mathrm{exc},0}$. Second, in a similar way, the nanostructure may influence the efficiency with which the dye can radiate photons to the far field. This effect is described by the factor $\gamma_{\mathrm{r}}/\gamma_{\mathrm{r},0}$. Third, the nanostructure can absorb photons, which is accounted for via the term $\gamma_{\mathrm{abs}}/\gamma_{\mathrm{r},0}$.

Let us now have a look at the corresponding modification of the fluorescence lifetime. In general, the fluorescence lifetime τ of a dye is given as the inverse of its total decay rate γ_{tot} [307]. Since the total decay rate and the radiative decay rate are connected via $\gamma_{\mathrm{r}} = q\gamma_{\mathrm{tot}}$ [cf. Eq. (6.4)], we can write $\tau = q/\gamma_{\mathrm{r}}$ for the lifetime in the presence of the nanostructure and $\tau_0 = q_0/\gamma_{\mathrm{r},0}$ for the

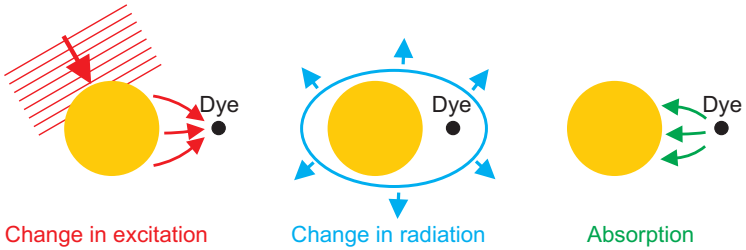

FIGURE 6.2. Illustration of the dye-nanostructure interaction. There are three effects: First, the presence of the nanostructure can change the excitation rate of the dye. Second, it can alter the efficiency with which the dye radiates photons to the far field. Third, if the nanostructure is lossy, it can absorb photons.

intrinsic lifetime of the free dye. Using this result together with Eq. (6.5) allows for expressing the lifetime as

$$\tau = \frac{\frac{\tau_0}{q_0}}{\frac{\gamma_r}{\gamma_{r,0}} + \frac{\gamma_{abs}}{\gamma_{r,0}} + \frac{1-q_0}{q_0}}. \tag{6.7}$$

In summary, Eqs. (6.5), (6.6), and (6.7) allow for predicting the modification of the fluorescence rate (which is equal to the modification of the fluorescence intensity) and the modification of the lifetime in the presence of a nanostructure. The intrinsic quantum yield q_0 and the intrinsic lifetime τ_0 that are appearing in these equations denote properties of the dye molecule, while the factors $\gamma_{exc}/\gamma_{exc,0}$, $\gamma_r/\gamma_{r,0}$, and $\gamma_{abs}/\gamma_{r,0}$ can be obtained from electromagnetic field calculations.

6.2.1 *How to calculate the rate modifications*

In the following, we will briefly discuss how the factors $\gamma_{exc}/\gamma_{exc,0}$, $\gamma_r/\gamma_{r,0}$, and $\gamma_{abs}/\gamma_{r,0}$ can be calculated. We will follow the basic idea from Ref. [306]. The key assumption is to associate the dye with a classical point dipole that can be excited at a frequency ω_{exc} (determined by the experiment) and can emit light at a frequency ω_{em} (determined by the dye). In accordance with Ref. [306], we will assume that we remain in the so-called weak-excitation regime (i.e., that the intensity of the excitation wave remains low enough to

not saturate the dye molecule) and furthermore that there is no coherence between the excitation and the emission process.

Let us start with the excitation process. One finds $\gamma_{\mathrm{exc}} \propto |\mathbf{e}_{\mathrm{d}} \cdot \mathbf{E}_{\mathrm{exc}}|^2$ and $\gamma_{\mathrm{exc},0} \propto |\mathbf{e}_{\mathrm{d}} \cdot \mathbf{E}_{\mathrm{exc},0}|^2$, where $\mathbf{E}_{\mathrm{exc}}$ and $\mathbf{E}_{\mathrm{exc},0}$ are the electric fields of the excitation wave at frequency ω_{exct}, evaluated at the position of the dye with and without the presence of the nanostructure, respectively, while $\mathbf{e}_{\mathrm{d}}$ represents a unit vector in the direction of the dye's dipole moment. Consequently, the modification of the excitation rate becomes

$$\frac{\gamma_{\mathrm{exc}}}{\gamma_{\mathrm{exc},0}} = \frac{|\mathbf{e}_{\mathrm{d}} \cdot \mathbf{E}_{\mathrm{exc}}|^2}{|\mathbf{e}_{\mathrm{d}} \cdot \mathbf{E}_{\mathrm{exc},0}|^2}, \tag{6.8}$$

which can be easily deduced from numerical calculations. Note that the exact shape of the excitation wave depends on the experiment, but typically (as it will be the case in all examples discussed in this chapter), one can assume a simple plane wave.

Let us now have a look at the quantities $\gamma_{\mathrm{r}}/\gamma_{\mathrm{r},0}$, and $\gamma_{\mathrm{abs}}/\gamma_{\mathrm{r},0}$. They can be obtained by considering an oscillating dipole at frequency ω_{em} and using $\gamma_{\mathrm{r}}/\gamma_{\mathrm{r},0} = P_{\mathrm{r}}/P_{\mathrm{r},0}$ and $\gamma_{\mathrm{abs}}/\gamma_{\mathrm{r},0} = P_{\mathrm{abs}}/P_{\mathrm{r},0}$, where P_{r} is the power that is radiated to the far field when the nanostructure is present, P_{abs} is the power that is absorbed in the nanostructure, and $P_{\mathrm{r},0}$ is the power that the same dipole would radiate in the absence of the nanostructure. Following the approach in Ref. [308], the above powers can be deduced straightforwardly from full numerical calculations.

As an alternative to full numerical calculations, the quantities $\gamma_{\mathrm{r}}/\gamma_{\mathrm{r},0}$, and $\gamma_{\mathrm{abs}}/\gamma_{\mathrm{r},0}$ can also be calculated via the resonant-state approach. The key is to realize that the quantities $\gamma_{\mathrm{r}}/\gamma_{\mathrm{r},0}$, and $\gamma_{\mathrm{abs}}/\gamma_{\mathrm{r},0}$ are closely related to the Purcell factor form subsection 2.3.3: The terms $\gamma_{\mathrm{r}} + \gamma_{\mathrm{abs}}$ and $\gamma_{\mathrm{r},0}$ represent the spontaneous emission rates of the dipole with and without the nanostructure, respectively. Therefore, one can associate them with γ and γ_0 from Eq. (2.103) via $\gamma_{\mathrm{r}} + \gamma_{\mathrm{abs}} = \gamma$ and $\gamma_{\mathrm{r},0} = n\gamma_0$, where n is the refractive index in which the dipole is embedded.[1] This allows for relating $\gamma_{\mathrm{r}}/\gamma_{\mathrm{r},0} + \gamma_{\mathrm{abs}}/\gamma_{\mathrm{r},0} = F/n$, where F is the Purcell factor, which can be directly calculated from the resonant states via Eq. (2.101). Note, however, that for modeling the emission process according to Eqs. (6.5) and (6.7), it is not only important to know the sum

1 One might wonder why the refractive index n is needed here. This simply comes form the fact that γ_0 represents the spontaneous emission rate in free-space vacuum, while for convenience with the definitions that are typically used in experiments, $\gamma_{\mathrm{r},0}$ is taken as the spontaneous emission rate in free space that is filled with the same medium in which the emitter-nanostructure combination is embedded when deducing $\gamma_{\mathrm{r}} + \gamma_{\mathrm{abs}}$.

$\gamma_r/\gamma_{r,0} + \gamma_{abs}/\gamma_{r,0}$, but also, to split this sum into its two contributions $\gamma_r/\gamma_{r,0}$ and $\gamma_{abs}/\gamma_{r,0}$. This can be achieved by separately calculating $\gamma_{abs}/\gamma_{r,0}$ via an overlap integral over the resonant states, as shown in Ref. [36].

For the calculations that will be discussed in this chapter, we consistently use the full-wave approach instead of the resonant-state approach. There are two reasons: 1) The examples that we are investigating in the following include situations where the emitters are quite far away from the nanostructure, at distances where the resonant-states may not form a complete basis anymore. To properly account for this (cf. subsection 2.3.3), one would either need to include perfectly-matched-layer modes in the expansion or have to exploit a regularization of the resonant fields, which both reduces the computational efficiency of the resonant-state approach. 2) The examples also include the opposite case that the emitters are extremely close to the surface of metallic nanoparticles. In this case, there is no completeness issue; however, in order to obtain accurate predictions, it is often necessary to consider a large number of resonant states due to the involvement of high-k surface plasmon polaritons [153].

6.3 REFINEMENTS

In the following, we will discuss several refinements of the theory that are relevant in order to account for experimental complications.

6.3.1 *Accounting for emission spectra*

So far, it was assumed that the emission process happens at a single fixed frequency ω_{em}. However, in reality, dye molecules very often have a broad spectrum of frequencies over which they emit. To account for this, we adopt a method that was proposed in Ref. [298]. The idea is to evaluate the factors $\gamma_{abs}/\gamma_{r,0}$ and $\gamma_{abs}/\gamma_{r,0}$ that are appearing in Eqs. (6.5) and (6.7) not at a single fixed frequency, but instead, to replace them by their spectral average:

$$\frac{\gamma_r}{\gamma_{r,0}} = \int d\omega \left[\frac{\gamma_r}{\gamma_{r,0}}\right](\omega) f_0(\omega) \tag{6.9}$$

$$\frac{\gamma_{abs}}{\gamma_{r,0}} = \int d\omega \left[\frac{\gamma_{abs}}{\gamma_{r,0}}\right](\omega) f_0(\omega) \tag{6.10}$$

where $f_0(\omega)$ is the intrinsic emission spectrum of the free dye molecule (which is typically determined experimentally), normalized such that $\int d\omega f_0(\omega) = 1$, and $[\gamma_r/\gamma_{r,0}](\omega)$ as well as $[\gamma_{abs}/\gamma_{r,0}](\omega)$ represent the frequency-dependent versions of the above factors. In the following, when $\gamma_r/\gamma_{r,0}$ and $\gamma_{abs}/\gamma_{r,0}$ (without frequency argument) appear, we will always imply that their spectral average is meant, as defined above.

6.3.2 *Accounting for dye rotation*

In general, the rates γ_r, γ_{abs}, γ_{exc}, $\gamma_{exc,0}$ appearing in the above equations depend on the orientation $\mathbf{e}_d$ of the dye's dipole moment. So far, it was assumed that this orientation is fixed. However, in reality, this is often not the case. Especially dye molecules that are attached to DNA linkers, as they appear in the systems that will be presented later in this chapter, have been demonstrated to exhibit the ability to freely rotate at their attachment position [309, 310]. Therefore, we will now show how to account for dye rotation in the equations.

To start, let us consider an arbitrary quantity Γ that depends on the orientation of the dye's dipole moment, i.e, $\Gamma = \Gamma(\mathbf{e}_d)$. Writing $\mathbf{e}_d$ in spherical coordinates, i.e., $\mathbf{e}_d(\theta,\varphi) = [\cos(\varphi)\sin(\theta), \sin(\varphi)\sin(\theta), \cos(\varphi)]^T$, and assuming a uniform probability distribution in all spatial directions, we can calculate an orientation average $\langle\Gamma(\mathbf{e}_d)\rangle$ of $\Gamma(\mathbf{e}_d)$ as

$$\langle\Gamma(\mathbf{e}_d)\rangle = \frac{1}{4\pi}\int_0^{2\pi} d\varphi \int_0^{\pi} \Gamma(\mathbf{e}_d)\sin\theta d\theta. \tag{6.11}$$

This equation will be used as the starting point to incorporate dye rotation in the model. We will distinguish two cases: fast rotation and slow rotation.

6.3.2.1 *Fast rotation*

By fast rotation, we mean that the rotation takes place on a timescale that is much faster than the excited state lifetime of the dye. In this case, the emission dipole moment samples all possible spatial orientations during the emission process and the dye can hence be considered as an effectively isotropic emitter [311, 312]. Consequently, the quantum yield q_{fast} and the lifetime τ_{fast} of the fast-rotating dye are obtained by replacing γ_r and γ_{abs} in

Eqs. (6.5) and (6.7) by their orientation-averaged values $\langle\gamma_\mathrm{r}\rangle$ and $\langle\gamma_\mathrm{abs}\rangle$. This results in:

$$q_\mathrm{fast} = \frac{\frac{\langle\gamma_\mathrm{r}\rangle}{\gamma_{\mathrm{r},0}}}{\frac{\langle\gamma_\mathrm{r}\rangle}{\gamma_{\mathrm{r},0}} + \frac{\langle\gamma_\mathrm{abs}\rangle}{\gamma_{\mathrm{r},0}} + \frac{1-q_0}{q_0}} \tag{6.12}$$

and

$$\tau_\mathrm{fast} = \frac{\frac{\tau_0}{q_0}}{\frac{\langle\gamma_\mathrm{r}\rangle}{\gamma_{\mathrm{r},0}} + \frac{\langle\gamma_\mathrm{abs}\rangle}{\gamma_{\mathrm{r},0}} + \frac{1-q_0}{q_0}}. \tag{6.13}$$

Note that the radiative decay rate $\gamma_{\mathrm{r},0}$ of the dye in the absence of the nanostructure (and consequently, also its intrinsic quantum yield q_0 and its intrinsic lifetime τ_0) are independent of the dye's orientation and therefore independent of the rotation.

Let us now tackle the excitation process. In a similar spirit as for the emission process, we assume that the dipole moment of the dye is able to scramble all spatial directions during the time it takes to absorb a photon. Therefore, the excitation rates γ_exc and $\gamma_{\mathrm{exc},0}$ have to be replaced by their orientation-averaged values $\langle\gamma_\mathrm{exc}\rangle$ and $\langle\gamma_{\mathrm{exc},0}\rangle$, respectively. Note that in contrast to the radiative decay rate $\gamma_{\mathrm{r},0}$ of the dye without nanostructure, the excitation rate $\gamma_{\mathrm{exc},0}$ without nanostructure is not independent of the dye orientation.

Altogether, the fluorescence rates of the fast-rotating dye with and without the nanostructure are given as $\gamma_\mathrm{fl,fast} = q_\mathrm{fast}\langle\gamma_\mathrm{exc}\rangle$ and $\gamma_\mathrm{fl,fast,o} = q_0\langle\gamma_{\mathrm{exc},0}\rangle$, respectively. Dividing these equations by each other provides the corresponding fluorescence rate modification:

$$\frac{\gamma_\mathrm{fl,fast}}{\gamma_\mathrm{fl,fast,0}} = \frac{q_\mathrm{fast}}{q_0}\frac{\langle\gamma_\mathrm{exc}\rangle}{\langle\gamma_{\mathrm{exc},0}\rangle}. \tag{6.14}$$

The factor $\langle\gamma_\mathrm{exc}\rangle/\langle\gamma_{\mathrm{exc},0}\rangle$ can be deduced by using $\langle\gamma_\mathrm{exc}\rangle \propto \langle|\mathbf{e}_\mathrm{d}\cdot\mathbf{E}_\mathrm{exc}|^2\rangle$ and $\langle\gamma_{\mathrm{exc},0}\rangle \propto \langle|\mathbf{e}_\mathrm{d}\cdot\mathbf{E}_{\mathrm{exc},0}|^2\rangle$ and applying Eq. (6.11). This gives

$$\frac{\langle\gamma_\mathrm{exc}\rangle}{\langle\gamma_{\mathrm{exc},0}\rangle} = \frac{|\mathbf{E}_\mathrm{exc}|^2}{|\mathbf{E}_{\mathrm{exc},0}|^2}. \tag{6.15}$$

As already emphasized, the above equations have been derived for the case that the dye is rotating on a timescale that is larger than its excited state lifetime. It should already be mentioned here that this case resembles the situation that – at least approximately – applies in the systems that will be investigated in this chapter (cf. experimentally observed rotational correlation times of dyes that are attached to DNA linkers in Ref. [309]).

Nevertheless, for reasons of completeness, we will also discuss the opposite case.

6.3.2.2 *Slow rotation*

Let us now discuss the case of slow rotation. In particular, we assume that the dye is rotating on a timescale that is much smaller than its excited state lifetime, but still faster than the integration time of the detector. Then, the (time-averaged) fluorescence rates can then be calculated by averaging over an ensemble of fixed dipoles that are equally distributed over all orientations. Consequently, the (time-averaged) fluorescence rates with and without nanostructure read as $\langle \gamma_{\mathrm{fl}} \rangle = \langle q(\mathbf{e}_{\mathrm{d}}) \gamma_{\mathrm{exc}}(\mathbf{e}_{\mathrm{d}}) \rangle$ and $\langle \gamma_{\mathrm{fl},0} \rangle = \langle q_0 \gamma_{\mathrm{exc},0}(\mathbf{e}_{\mathrm{d}}) \rangle$, respectively, where $\langle \dots \rangle$ denotes the orientation average as defined in Eq. (6.11) and $q(\mathbf{e}_{\mathrm{d}})$ is the orientation-dependent quantum yield:

$$q(\mathbf{e}_{\mathrm{d}}) = \frac{\frac{\gamma_{\mathrm{r}}(\mathbf{e}_{\mathrm{d}})}{\gamma_{\mathrm{r},0}}}{\frac{\gamma_{\mathrm{r}}(\mathbf{e}_{\mathrm{d}})}{\gamma_{\mathrm{r},0}} + \frac{\gamma_{\mathrm{abs}}(\mathbf{e}_{\mathrm{d}})}{\gamma_{\mathrm{r},0}} + \frac{1-q_0}{q_0}}. \tag{6.16}$$

Dividing $\langle \gamma_{\mathrm{fl}} \rangle$ by $\langle \gamma_{\mathrm{fl},0} \rangle$, using $\gamma_{\mathrm{exc}}(\mathbf{e}_{\mathrm{d}}) \propto |\mathbf{e}_{\mathrm{d}} \cdot \mathbf{E}_{\mathrm{exc}}|^2$ as well as $\gamma_{\mathrm{exc},0}(\mathbf{e}_{\mathrm{d}}) \propto |\mathbf{e}_{\mathrm{d}} \cdot \mathbf{E}_{\mathrm{exc},0}|^2$, and applying Eq. (6.11), we can express the modification of the fluorescence rate for the slowly-rotating dye as

$$\frac{\langle \gamma_{\mathrm{fl}} \rangle}{\langle \gamma_{\mathrm{fl},0} \rangle} = \frac{3 \langle q(\mathbf{e}_{\mathrm{d}}) |\mathbf{e}_{\mathrm{d}} \cdot \mathbf{E}_{\mathrm{exc}}|^2 \rangle}{q_0 |\mathbf{E}_{\mathrm{exc},0}|^2}. \tag{6.17}$$

It should, however, be mentioned that a similar approach for defining the lifetime of the slowly-rotating dye is not possible, due to the simple fact that in the ensemble case, every dipole orientation has its own lifetime and there is no unambiguously defined and physically meaningful average lifetime.

6.3.3 *Speeding up calculations of orientation dependence*

In section 6.3, we have revealed how the rotation of the dye molecules can be accounted for in the theoretical description. It was explained that in order to model the emission process of a fast-rotating dye, it is necessary to know the orientation-averaged rates $\langle \gamma_{\mathrm{r}} \rangle$ and $\langle \gamma_{\mathrm{abs}} \rangle$. Furthermore, it was revealed that for modeling the emission process of a slowly-rotating dye, it is crucial to know the full orientation dependence of $\gamma_{\mathrm{r}}(\mathbf{e}_{\mathrm{d}})$ and $\gamma_{\mathrm{abs}}(\mathbf{e}_{\mathrm{d}})$.

In general, both the orientation dependence as well as the orientation average can be deduced from simply numerically calculating the above rates for a number of different dipole orientations. However, this brute-force ansatz can become quite inefficient from a computational point of view, since without further insight, one has to perform the calculation for a large number of different dipole orientations. Therefore, in the following, we will discuss how some additional analytical insight can be used to keep the number of computations to a minimum. The approach is based on Ref. [313]. In this work, it is shown that the knowledge of γ_r and γ_abs for three orthogonal dipole orientations is sufficient to semi-analytically express their full orientation dependence. This orientation dependence reads as[2]

$$\gamma_\mathrm{r}(\mathbf{e}_\mathrm{d}) = \gamma_\mathrm{r}^\mathrm{x} c_\mathrm{x}(\mathbf{e}_\mathrm{d}) + \gamma_\mathrm{r}^\mathrm{y} c_\mathrm{y}(\mathbf{e}_\mathrm{d}) + \gamma_\mathrm{r}^\mathrm{z} c_\mathrm{z}(\mathbf{e}_\mathrm{d}), \tag{6.18}$$

$$\gamma_\mathrm{abs}(\mathbf{e}_\mathrm{d}) = \gamma_\mathrm{abs}^\mathrm{x} c_\mathrm{x}(\mathbf{e}_\mathrm{d}) + \gamma_\mathrm{abs}^\mathrm{y} c_\mathrm{y}(\mathbf{e}_\mathrm{d}) + \gamma_\mathrm{abs}^\mathrm{z} c_\mathrm{z}(\mathbf{e}_\mathrm{d}), \tag{6.19}$$

where $\gamma_\mathrm{r}^\mathrm{x}$, $\gamma_\mathrm{r}^\mathrm{y}$,$\gamma_\mathrm{r}^\mathrm{z}$, $\gamma_\mathrm{abs}^\mathrm{x}$, $\gamma_\mathrm{abs}^\mathrm{y}$, and $\gamma_\mathrm{r}^\mathrm{z}$ are the respective rates for the dipole moment pointing along the three orthogonal axes x, y, and z. Note that the choice of the axes is not arbitrary, but they have to be aligned along with the principal axes of the system (i.e, one of the three axes has to coincide with the emitter orientation under which the rates exhibit a maximum, and another one has to coincide with the direction under which the rates exhibit a minimum). In simple geometries, one can deduce the principal axes from the symmetry of the system. A recipe for the general case is provided in Ref. [313]. The coefficients c_x, c_y, and c_z in the above equations are given as:

$$c_\mathrm{x}(\mathbf{e}_\mathrm{d}) = |\mathbf{e}_\mathrm{x} \cdot \mathbf{e}_\mathrm{d}|^2 = \cos^2(\varphi)\sin^2(\theta), \tag{6.20}$$

$$c_\mathrm{y}(\mathbf{e}_\mathrm{d}) = |\mathbf{e}_\mathrm{y} \cdot \mathbf{e}_\mathrm{d}|^2 = \sin^2(\varphi)\sin^2(\theta), \tag{6.21}$$

$$c_\mathrm{z}(\mathbf{e}_\mathrm{d}) = |\mathbf{e}_\mathrm{z} \cdot \mathbf{e}_\mathrm{d}|^2 = \cos^2(\theta), \tag{6.22}$$

where $\mathbf{e}_\mathrm{x}$, $\mathbf{e}_\mathrm{y}$, and $\mathbf{e}_\mathrm{z}$ represent unit vectors along the x, y, and z axis, respectively, and $\mathbf{e}_\mathrm{d}$ is again assumed to be provided in spherical coordinates, i.e., $\mathbf{e}_\mathrm{d}(\theta, \varphi) = [\cos(\varphi)\sin(\theta), \sin(\varphi)\sin(\theta), \cos(\varphi)]^\mathrm{T}$.

2 Strictly speaking, the relation is only proven for the total spontaneous decay rate, i.e, for the sum $\gamma_\mathrm{r} + \gamma_\mathrm{abs}$, and not for the two terms separately. However, the authors of Ref. [313] state that there is no reason to expect that the relation should not hold for both rates γ_r and γ_abs individually, and furthermore, they have numerically verified this in all their example systems. In all example systems where we have used the above relations, we have confirmed this as well.

For the slowly-rotating dye, one can plug Eqs. (6.18) and (6.19) into Eqs. (6.16) and (6.17), and evaluate the remaining integral numerically. For the fast-rotating dye, one needs the orientation-averaged values $\langle\gamma_\mathrm{r}\rangle$ and $\langle\gamma_\mathrm{abs}\rangle$. Exploiting the above orientation dependence, they become [313]

$$\langle\gamma_\mathrm{r}\rangle = \frac{1}{3}\left(\gamma_\mathrm{r}^\mathrm{x} + \gamma_\mathrm{r}^\mathrm{y} + \gamma_\mathrm{r}^\mathrm{z}\right), \tag{6.23}$$

$$\langle\gamma_\mathrm{abs}\rangle = \frac{1}{3}\left(\gamma_\mathrm{abs}^\mathrm{x} + \gamma_\mathrm{abs}^\mathrm{y} + \gamma_\mathrm{abs}^\mathrm{z}\right). \tag{6.24}$$

As a side note, it should be mentioned that, if one is only interested in the average values and not in the full orientation dependence, it is actually not necessary to choose x, y, and z as the principal axes of the system. In this particular case, any set of three orthogonal axes can be selected.

6.3.4 *Accounting for random structure orientation*

So far, it has been assumed that the dye-nanoparticle complex exhibits a fixed orientation with respect to the excitation wave. However, in many experimental situations, this is not the case. Very often, one is dealing with an ensemble of randomly oriented dye-nanoparticle complexes (this scenario occurs, for instance, when the DNA structures are dissolved in a solution).

The random orientation can be accounted for in the following way: Let $\boldsymbol{\rho}_\mathrm{inc} = \{\theta_\mathrm{inc}, \varphi_\mathrm{inc}, \alpha_\mathrm{inc}\}$ denote a set of angles that characterize the orientation of the dye-nanoparticle complex with respect to the incident excitation wave (θ_inc: elevation, φ_inc: azimuth, α_inc: tilt). Then, assuming a uniform distribution, we can define an ensemble average over any $\boldsymbol{\rho}$-dependent quantity $\Gamma(\boldsymbol{\rho}_\mathrm{inc})$ as

$$\left\langle\Gamma(\boldsymbol{\rho}_\mathrm{inc})\right\rangle_\mathrm{inc} = \frac{1}{8\pi^2}\int_0^{2\pi} d\alpha_\mathrm{inc}\int_0^{2\pi} d\varphi_\mathrm{inc}\int_0^{\pi}\Gamma(\boldsymbol{\rho}_\mathrm{inc})\sin\theta_\mathrm{inc}\,d\theta_\mathrm{inc}. \tag{6.25}$$

With this definition, we can formally write the fluorescence rate of an ensemble of randomly oriented dye-nanoparticle complexes under the fast-rotating dye assumption as $\left\langle\gamma_\mathrm{fl,fast}(\boldsymbol{\rho}_\mathrm{inc})\right\rangle_\mathrm{inc} = q_\mathrm{fast}\left\langle\langle\gamma_\mathrm{exc}(\boldsymbol{\rho}_\mathrm{inc})\rangle\right\rangle_\mathrm{inc}$ (note that q_fast is independent of $\boldsymbol{\rho}_\mathrm{inc}$), with $\left\langle\langle\gamma_\mathrm{exc}(\boldsymbol{\rho}_\mathrm{inc})\rangle\right\rangle_\mathrm{inc} \propto \left\langle\langle|\mathbf{e}_\mathrm{d}\cdot\mathbf{E}_\mathrm{exc}(\boldsymbol{\rho}_\mathrm{inc})|^2\rangle\right\rangle_\mathrm{inc}$. Here, $\mathbf{E}_\mathrm{exc}(\boldsymbol{\rho}_\mathrm{inc})$ denotes the electric field of the excitation wave at the position of the dye as a function of the orientation $\boldsymbol{\rho}_\mathrm{inc}$ of the dye-nanoparticle complex. Dividing the above fluorescence rate by the fluorescence rate of the

fast-rotating dye without nanoparticle (which is independent of $\boldsymbol{\rho}_{\mathrm{inc}}$), allow us to express the modification of the fluorescence rate as

$$\frac{\left\langle \gamma_{\mathrm{fl,fast}} \right\rangle_{\mathrm{inc}}}{\gamma_{\mathrm{fl,fast},0}} = \frac{q_{\mathrm{fast}}}{q_0} \frac{\left\langle \left\langle \gamma_{\mathrm{exc}} \right\rangle \right\rangle_{\mathrm{inc}}}{\left\langle \gamma_{\mathrm{exc},0} \right\rangle}, \tag{6.26}$$

with $\left\langle \left\langle \gamma_{\mathrm{exc}} \right\rangle \right\rangle_{\mathrm{inc}} / \left\langle \gamma_{\mathrm{exc},0} \right\rangle = \left\langle |\mathbf{E}_{\mathrm{exc}}(\boldsymbol{\rho}_{\mathrm{inc}})|^2 \right\rangle_{\mathrm{inc}} / |\mathbf{E}_{\mathrm{exc},0}|^2$.

Similar considerations for the slow-rotating dye provide the corresponding fluorescence modification as

$$\frac{\left\langle \left\langle \gamma_{\mathrm{fl}} \right\rangle \right\rangle_{\mathrm{inc}}}{\left\langle \gamma_{\mathrm{fl},0} \right\rangle} = \frac{\left\langle 3 \langle q(\mathbf{e}_{\mathrm{d}}) | \mathbf{e}_{\mathrm{d}}(\mathbf{e}_{\mathrm{d}}) \cdot \mathbf{E}_{\mathrm{exc}}(\boldsymbol{\rho}_{\mathrm{inc}})|^2 \rangle \right\rangle_{\mathrm{inc}}}{q_0 |\mathbf{E}_{\mathrm{exc},0}|^2}. \tag{6.27}$$

Note, however, that this equation is not used anywhere within this thesis, and only provided for the sake of completeness.

In order to calculate the modification of the fluorescence rate according to Eq. (6.26), it is necessary to evaluate the ensemble average $\left\langle |\mathbf{E}_{\mathrm{exc}}(\boldsymbol{\rho}_{\mathrm{inc}})|^2 \right\rangle_{\mathrm{inc}}$. One might expect that this evaluation needs many computations steps due to the three degrees of freedom that are contained within $\boldsymbol{\rho}_{\mathrm{inc}}$. However, it turns out that the evaluation is actually extremely simple in most practical cases. The reason is that in most cases, the involved nanoparticles are highly symmetric. In particular, all nanoparticles that will be discussed in this chapter exhibit either spherically or cylindrical symmetry. The symmetry can be used to drastically reduce the degrees of freedom that need to be considered when calculating the above ensemble average. For instance, in the case of a spherical particle, one can deduce the value of $\left\langle |\mathbf{E}_{\mathrm{exc}}(\boldsymbol{\rho}_{\mathrm{inc}})|^2 \right\rangle_{\mathrm{inc}}$ by performing one single numerical simulation to obtain the electric near field that the excitation wave generates around the nanoparticle and then spatially averaging the magnitude of the near field over a spherical surface with a fixed radius around the particle.

6.4 EXAMPLES

In the context of this thesis, the theory from the previous section was applied to describe and understand the light-matter interaction in a large number of different experimentally-realized DNA nanosystems (cf. publications [P2], [P3], [P4], and [P8]). In the following, we will present two selected examples.

6.4.1 *Watching a dye molecule walk into a plasmonic hotspot*

As the first example, we investigate the situation that a dye molecule dynamically moves into a plasmonic hotspot. The example is based on publication [P2].

The system that will be discussed is depicted in Fig. 6.3(a). It contains two spherical gold nanoparticles (diameter: 60 nm) that are attached to a template of DNA bundles (gray). It is known for such kinds of nanoparticle-dimer configurations that in the gap between the two nanoparticles, there exists a hotspot, in which strong light-matter interactions can occur. On top of the DNA template is a track made out of DNA strands, along which a dye molecule (red sphere) can autonomously walk from outside the gap to the hotspot in the center. This walking process can be initiated by a chemical trigger. Panel (b) shows a transmission-electron microscopy image of fabricated structures. The inset contains the enlarged view of one exemplary structure (scale bar: 50 nm).

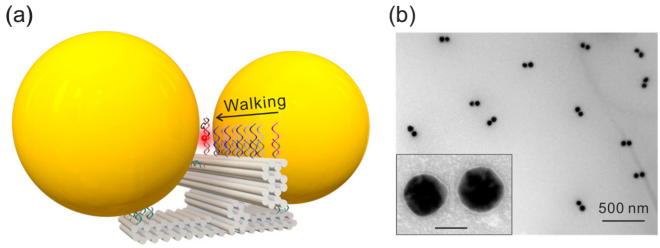

FIGURE 6.3. Dynamic DNA nanodevice. (a) Sketch of the system. The device consists of two gold nanoparticles (diameter: 60 nm) that are connected by a platform made out of DNA bundles (gray). On top of this platform is a track along which a single dye molecule (red sphere) can autonomously walk from the outside to the center of the gap between the two nanoparticles. The walking process can be initiated by a chemical trigger. (b) Transmission-electron microscopy image of assembled structures. The inset shows the enlarged view of one exemplary structure (scale bar: 50 nm).

Figure 6.4(a) depicts the top view of the structure, with a schematic illustration of the track (black line). Let us now use the theory from the previous

section to investigate what happens when the dye molecule walks along this track.

The calculations in the following are based on finite-element simulations, performed with COMSOL Multiphysics.[3] The gold nanoparticles were modeled as spheres of diameter 60 nm with a gap of 21 nm. Note that, although the fabricated target gap size of the device is 15 nm, it can be estimated from the DNA design, considering the softness of the structure, that the actual gap lies between 15 nm and 21 nm. It was found that the simulation results for 21 nm better explain the experimental observations, so this value was chosen. One should be aware that, in the transmission-electron microscopy images from Fig 6.3, the gap is distorted due to drying of the structure, which makes it impossible to determine the exact value. In the calculations, the gold dielectric function was described according to Ref. [314]. As in the experiment, the surrounding medium was considered to be water (accounted for via its refractive index of 1.332).

Figure 6.4(b) displays the calculated field distribution of the excitation wave at a wavelength of 635 nm in the vicinity of the structure. In accordance with the experimental situation, it was assumed that the system is illuminated with a plane wave that is circularly polarized within the depicted plane and propagating along the out-of-plane direction. The simulations confirm that there is a hotspot with a strong field enhancement inside the gap.

In the experiment, the dye Atto 647N was used. To account for this dye in the calculations, its intrinsic quantum yield, intrinsic lifetime and intrinsic emission spectrum were needed. The intrinsic quantum yield $q_0 = 0.65$ was taken from the specifications provided by the supplier[4], while the intrinsic lifetime $\tau_0 = 4.09$ ns and the intrinsic emission spectrum were determined from reference measurements. It is known from literature that Atto 647N attached to similar DNA linkers as the ones that are used in our system exhibits a rotational correlation time of 0.8 ns [309]. Therefore, the situation can – at least approximately – described via the fast-rotating dye approach that was presented in the previous section (a more detailed discussion will be provided at the end of the section).

The top plot in panel (c) depicts the calculated fluorescence lifetimes at different positions along the track. The blue curves denote the results for fixed dipole orientations [the orientations with respect to the nanoparticle dimer from panel (a) are indicated next to the curves], which were obtained

3 See https://www.comsol.com.

4 Available under http://www.atto-tec.com.

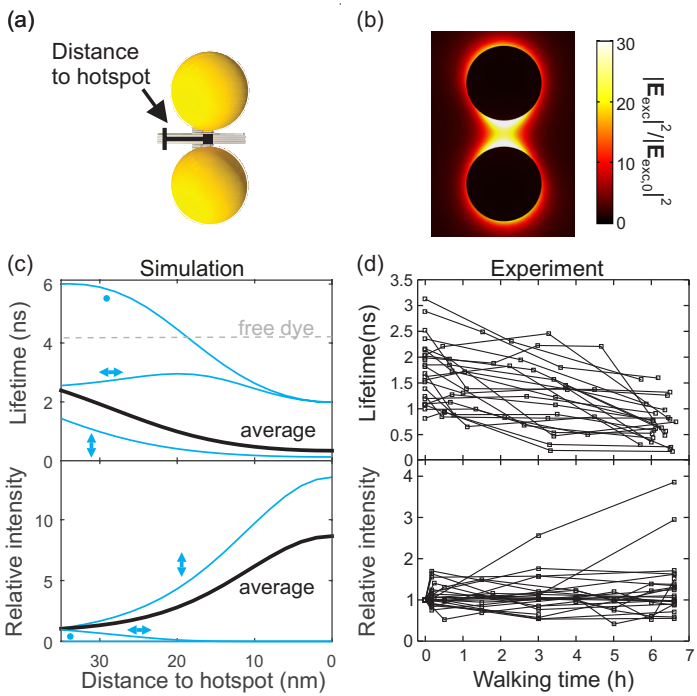

Figure 6.4. Light-matter interaction in the nanodevice. (a) Top view of the structure, with the walking track indicated by a black line. (b) Calculated near-field enhancement of the excitation wave at 635 nm. The wave is propagating in the out-of-plane direction and circularly polarized within the depicted plane. (c) Calculated lifetime and relative intensity as a function of the dye position. The blue curves denote the result for fixed dipole orientations, while the black curve represents the orientation average, calculated under the assumption of a fast rotating dye. The arrows and the dots specify the orientation of the dipole moment with respect to the structure in panel (a) (arrows: in-plane directions, dots: out-of-plane direction). In the top plot, the lifetime of the free dye without nanoparticles is indicated by a gray dashed line. (d) Experimentally tracked lifetimes and intensities as a function of the walking time. Each curve represents one single device. The squares denote actual measurement values, while the connectors in between have been inserted to serve as a guide for the eye.

via Eq. (6.7). The black curve represents the orientation average, calculated via Eq. (6.13). For reference, the intrinsic lifetime of the free dye is indicated by a gray dashed line. According to the calculations, the lifetime drastically

decreases when the dye approaches the hotspot. This can be explained by an increase of the spontaneous decay rate $\gamma_r + \gamma_{abs}$, attributed to the strong light-matter interaction between the dye and the nanoparticles taking place within the gap.

The bottom plot shows the calculation results for fluorescence intensity of the dye, normalized to the value at the start of the track (which is located 35 nm away from the hotspot). The blue curves denote the result for fixed dipole orientations, calculated via Eq. (6.6). Note that the curve for the out-of-plane orientation is set to zero, since this orientation cannot be excited by the incident wave. The black curve represents the orientation average, calculated from Eq. (6.6). It can be seen that the calculations predict an increase of the fluorescence intensity when the dye approaches the hotspot. This increase can be mostly attributed to the increase of the excitation rate γ_{exc}, which is caused by the strong near-field enhancement of the excitation wave [cf. panel (b)]. Note that the maximum intensity enhancement is about a factor of nine.

Let us now compare our theoretical predictions to experimental results, which are provided in panel (d). Depicted are the experimentally observed lifetimes and fluorescence intensities for 24 individual dye-nanoparticle assemblies. Every curve represents one single device. The squares correspond to actual measurement points, while the connector lines in between are inserted as a guide for the eye. Note that the x axis, in contrast to the theory plots from panel (c), represents the walking time (i.e., the time that passed by since the walking process was initiated). At time zero, the dye is located at the start of the track, while at the end of the timescale, it is expected that the dye has reached the hotspot.

The lifetime measurements reveal that for most of the dyes, the fluorescence lifetime monotonously decreases with the walking time. The average reduction in lifetime is approximately a factor of three. These findings clearly confirm the trend that was predicted by the simulations. It is, however, noteworthy, that the experimentally observed lifetimes are scattered over a quite large range of values. The intensity measurements reveal a maximum enhancement of four. It is worth to point out, however, that many devices only show a very weak enhancement and in some cases, there is even a decrease in intensity. We speculate that the large spread in the observed values is due to sample imperfections resulting from missing particles, inhomogeneous and nonspherical shapes, and defective assemblies. In these cases, the presence of the nanoparticles might result in partial quenching of the emission. We note that the observed changes in the fluorescence lifetime

and intensity are very similar to what has been previously reported in static plasmonic DNA nanodevices [315–317].

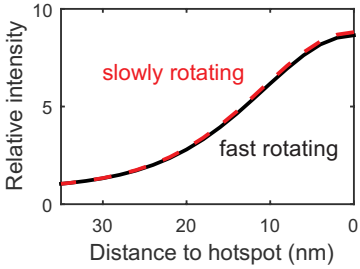

FIGURE 6.5. Comparison of the calculated intensities under the fast-rotating and the slowly-rotating dye assumption. The results for fast rotation are indicated by the black solid line, while the results for slow rotation are represented by the red dashed line. Remarkably, they are almost identical.

One of the core assumptions of our theoretical considerations was that the dye can be considered as fast-rotating. This assumption is appropriate when the rotational correlation time is much shorter than the fluorescence lifetime of the dye. As we have already mentioned, the rotational correlation time of Atto 647N attached to a DNA has been reported to be in the order of 0.8 ns. While this time is indeed more than a factor of five smaller than the dye's intrinsic lifetime $\tau_0 = 4.1$ ns, the situation drastically changes when the dye approaches the hotspot. In this case, our theoretically predicted average lifetime is even slightly smaller than the 0.8 ns [cf. Fig. 6.4(a)]. Hence, in this case, the prerequisites of the fast-rotating dye assumption are – at best – only fulfilled approximately. Consequently, one might wonder if the possible error that might follow from the above assumption could explain the relatively large discrepancy between the theoretically predicted and the experimentally observed intensity enhancements. To investigate this, we have performed the same calculations under the assumption of a slowly-rotating dye [cf. Eq. (6.17)]. The comparison of both calculations is depicted in Fig. 6.5. Remarkably, it turns out that the results for both cases are almost identical. Therefore, we deduce that, as long as the Atto647N molecule is able to freely rotate, our approach of assuming fast rotation is a suitable approximation.

6.4.2 *Tracking movements in DNA nanogears*

Let us now discuss an example where dye-nanoparticle interactions are exploited to track movements in a DNA-based gear system. The example is taken from publication [P3].

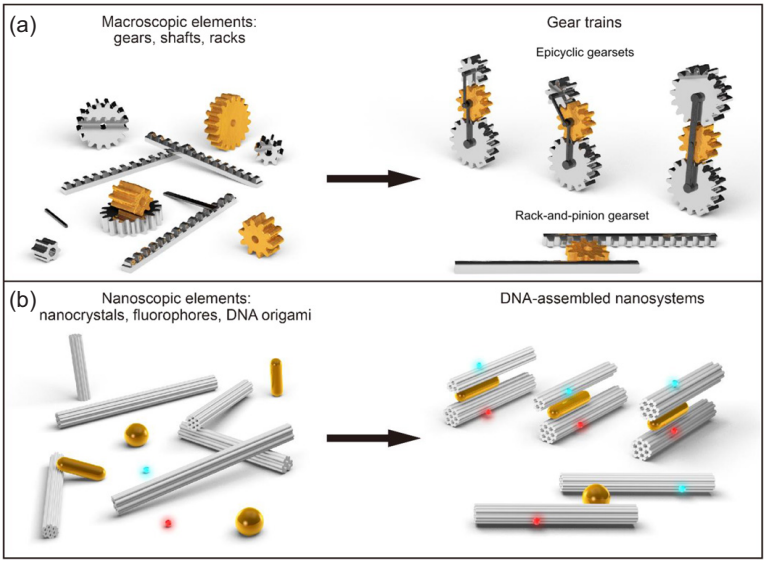

Figure 6.6. Functional DNA nanodevices. (a) In our macroscopic world, we can combine building blocks, such as gears, shafts and racks, to construct devices with complex mechanical functionalities, such as gear trains. (b) By assembling together nanoscopic elements, such as DNA origami filaments and metallic nanoparticles, it is possible to realize analog apparatuses in the nanoworld.

In our macroscopic world, we can combine building blocks, such as gears, shafts and racks, to construct devices with complex mechanical functionalities, such as gear trains [cf. Fig. 6.6(a)]. These devices are then used as components in order to build machines that can be programmed to perform all sorts of specific tasks and facilitate our everyday live. Ever since the rise of nanotechnology, people have started wondering if it is possible to realize similar apparatuses in the nanoworld. One can fantasize about all sorts

of applications, including advanced medical diagnostic systems, specialized therapies, targeted drug delivery, as well as a large number of sensing schemes, to only name a few [304]. In analogy to macroscopic machines, the basic step for the realization of nanomachines is to construct individual components that can perform specific mechanical movements. Figure 6.6(b) shows how such components can be built using the DNA nanotechnology. The starting point are different nanoscopic elements, such as DNA origami filaments and metallic nanoparticles. These elements are then assembled to form functional components.

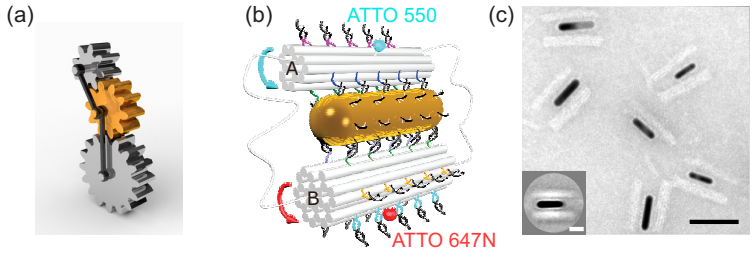

Figure 6.7. DNA nanogear device. (a) Sketch of the concept: Depicted is a mechanical gearset that consists of two so-called planet gears (gray) that can independently revolve around a so-called sun gear (brown). (b) Corresponding DNA design. The two planet gears are realized as differently-sized DNA origami filaments (labeled as A and B), while the sun gear consists of a gold nanorod. Note that the system is equipped with two dye molecules (ATTO 550 and ATTO 647N), which will later be used to track the movements. (c) Transmission-electron microscopy image of actual structures (scale bar: 50 nm). The inset depicts an averaged image of several devices (scale bar: 20 nm).

In the following, we will discuss one specific gear device. The idea is sketched in Fig. 6.7(a). The system consists two so-called planet gears (gray) that can independently revolve around a so-called sun gear (brown). Note that the two planet gears have different sizes. Panel (b) shows the corresponding DNA design. The two planet gears are realized as differently-sized DNA origami filaments (labeled as A and B), while the sun gear consists of a gold nanorod. The origami filaments and the gold nanorod are connected at predefined docking sites via DNA strands. Using chemically triggered DNA reactions, one can open and close specific docking sites and thereby

induce controlled revolutions of the origami filaments. Panel (c) shows a transmission-electron microscopy image of fabricated structures (scale bar: 50 nm). The inset depicts an averaged image of several devices (scale bar: 20 nm).

As shown in panel (b), the two outer gears are equipped with dye molecules (ATTO 550 and ATTO 647N), which allow for in-situ optical monitoring of the movements. If one of the two gears revolves, the corresponding dye changes its distance to the nanorod. Consequently, its fluorescence intensity will be altered, thus, providing optical feedback about the movement. Both dyes emit light at different wavelengths, which allows for an independent monitoring of the two outer gears.

In order to utilize the above effect for movement tracking, it is crucial to have a good understanding of the underlying light-matter interaction. So, we now apply our theory to calculate the impact of the distance change on the fluorescence intensities. As in the example from subsection 6.4.1, we rely on finite-element simulations, performed with COMSOL Multiphysics.[5] The gold nanorod is modeled as a cylinder with a diameter of 10 nm and a length of 35 nm. To approximate the shapes that are visible in the transmission-electron microscopy images, the ends of the cylinder were not taken as flat surfaces, but instead constructed as half spheres with a radius of 5 nm. The surrounding medium is water. The permittivity of the gold and the refractive index of the water are described the same way as in the previous example. The intrinsic quantum yield of the two dyes (ATTO 550, $q_0 = 0.8$; ATTO 647N, $q_0 = 0.65$) and their intrinsic emission spectra are taken from the specifications of the supplier, which is the same as in the other example. As in the previous case, the dyes are assumed to be fast-rotating. In accordance with the experimental setup, the excitation wavelengths are taken as ATTO 550 nm and 647 nm for ATTO 550 and ATTO 647N, respectively. In contrast to the previous example, the experiments are, however, not carried out on single devices with a fixed orientation towards the incident wave; instead, they are performed on an ensemble of structures that are dissolved in solution and hence exhibit random orientations towards the incident wave. To account for this, we apply the ensemble average from subsection 6.3.4.

Figure 6.8(a) depicts the configuration that was simulated. Due to the rotational symmetry of the nanorod, it is sufficient to consider the movement of the dyes on a radial axis perpendicular to the nanorod. Note that due to the way the DNA structure is designed, this axis is not located at exactly half of

5 See https://www.comsol.com.

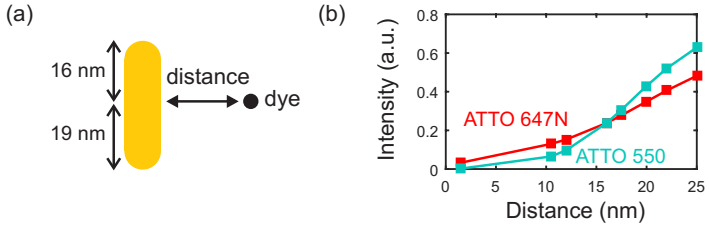

Figure 6.8. Interaction between the dyes and the nanorod. (a) Due to the rotational symmetry of the nanorod, it is sufficient to consider the movement of the dyes on a radial axis perpendicular to the nanorod. Note that due to the way the DNA structure is built, this axis is not located at exactly half of the nanorods length, but instead, 16 nm away from the top end and 19 nm away from the bottom end. (b) Calculated fluorescence intensities as a function of distance between the dyes and the nanorod. The squares denote the calculated values, while the connectors in between have been added as a guide for the eye. For short distances, the intensities drastically decrease, due to an increase of the strong absorption that is taking place in the rod.

the nanorods length, but instead, 16 nm away from the top end and 19 nm away from the bottom end. Panel (b) shows the calculation results. Plotted are the fluorescence intensities of the two dyes as a function of the distance between the dyes and the surface of the nanorod. The intensities have been calculated via Eq. (6.26). The squares denote the calculated values, while the connectors in between have been added as a guide for the eye. It can be seen that the fluorescence intensities drastically decrease when the dyes approach the nanorod. This can be attributed to fluorescence quenching that occurs due to a high increase of the absorption rate γ_{abs}. Intuitively, the effect can be understood from the fact that compared to the nanoparticle-dimer from subsection 6.4.1, the rod has much smaller dimensions and therefore, it acts as a very inefficient antenna, which mostly absorbs the light instead of radiating it to the far field. The closer the dyes get to the surface, the stronger becomes the interaction and hence the absorption.

Next, let us compare the prediction of our calculations to an actual experiment. Figure 6.9(a) shows a series of consecutive revolution states (I to IX) that can be induced in the gearset. The origami filaments A and B are represented by a triangle and a hexagon, respectively. These shapes are chosen since they resemble the corresponding distributions of the DNA docking site arrangements. The gold nanorod is indicated by a gray disk. For each revolution state, the corresponding distances between the dyes and the

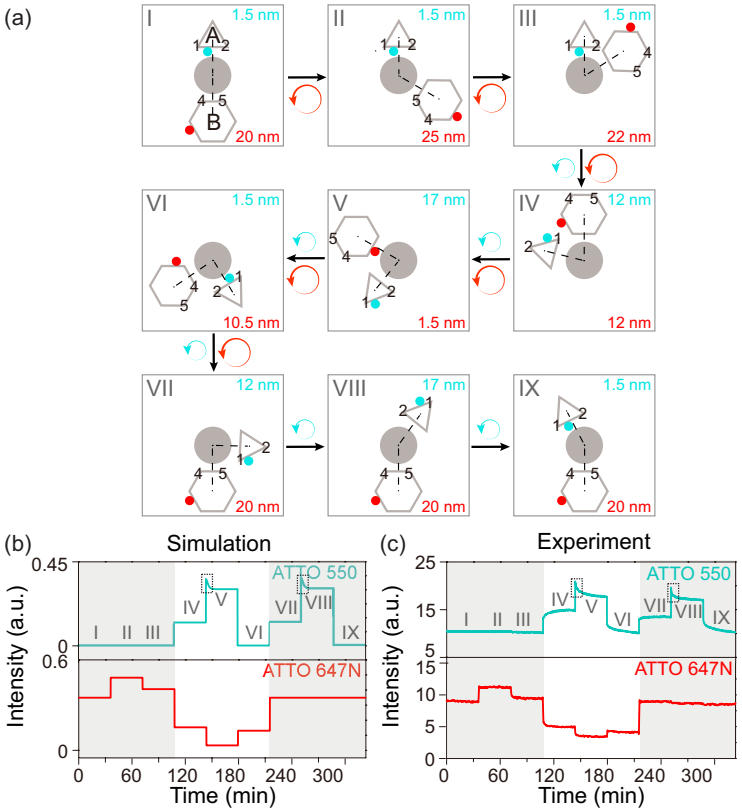

Figure 6.9. Revolution experiment. (a) Series of consecutive revolution states (I to IX). The origami filaments A and B are represented by a triangle and a hexagon, respectively, while the gold nanorod is symbolized via the gray disk. For each revolution state, the corresponding distances between the dyes and the nanorod's surface are written next to the illustration. (b) Calculated fluorescence intensities. (c) Experimental results. It can be seen that there is a good qualitative agreement. Note that there are some kinks appearing in both the calculated and in the experimental curves (see black dashed frames), which will be explained later in section 6.5.

nanorod's surface are given. The series contains the following movements: From state I to III, filament A is kept at a fixed position and only filament B is revolving. From state III to VII, both filaments are revolving. From state VII to IX, filament A is revolving, while filament B remains stationary.

Panel (b) shows the results of our calculations. Plotted are the intensities of the two dyes as a function of time, assuming that the system successively goes through the above revolution states. The times at which the state transitions are assumed to occur are taken as the times at which the corresponding chemical triggers for each step are added during the experiment. Note that the fluorescence-intensity curve of ATTO 550 contains two kinks (see the black dashed frames). Those will be explained later.

The experimental results are displayed in panel (c). It can be seen that there is a good qualitative agreement with the simulations. It is, however, worth to point out that there are some quantitative differences: For instance, during states in which a dye is very close to the nanorod's surface (as it is, e.g., the case for ATTO 550 during states I to III), the theoretically predicted intensity is almost identical to zero, while the experimentally obtained values are clearly not. This can be explained by the fact that not all gear devices from the solution are properly functioning; instead, a fraction of the devices may be stuck in some random state and thereby induce a background signal. Additionally, the experimental intensities exhibit a slow drift, which is also not covered by the simulations. Possible reasons for the drift could be mechanical instabilities of the DNA structures as well as photobleaching of the dyes.

Note that the experimental signal of ATTO 550 exhibits the same kind of kinks (see black dashed frames) that already had been mentioned above. These kinks occur when filament A transits from state IV to V and from state VII to VIII. They arise due to the fact that during these particular transitions, there exists a moment in time when the dye is farther away from the nanorod than at the beginning and at the end of the transition. A deeper discussion of this effect (as well as how it can be modeled) will be provided in section 6.5.

It should be mentioned that the same theoretical approach that was used in this section was applied to describe the dye-nanoparticle interactions in several other functional DNA nanodevices. In particular, the examples include other kinds of nanogears [P3], two multilayer sliding systems [P4], as well as several arrangements of rotating DNA rings [P8].

6.5 REACTION DYNAMICS

In the following, we provide a detailed discussion of the kinks that had been observed in the nanogear experiment [cf. Fig. 6.9(c)] and present a kinetic

model for their description. We discuss this effect on purpose in a detailed manner, since it allows us to gain interesting insights into the dynamics of such DNA nanosystems. Note that this section is based on publication [P3].

6.5.1 *Origin of the kinks*

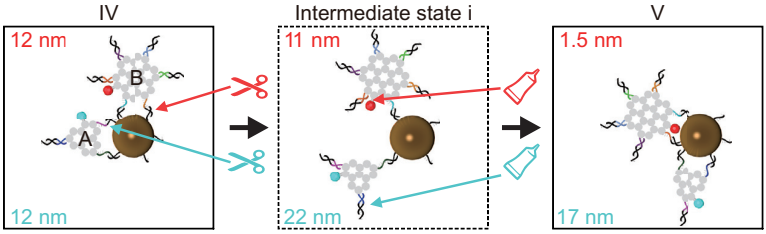

Figure 6.10. Transition from state IV to state V. In state IV, the two DNA origami filaments are each attached via two DNA docking sites to the gold nanorod. The transition to state V is induced the following way: Four kinds of DNA compounds are added to the solution: Two sorts of so-called blocking strands (symbolized via the red and blueish scissors), which open specific docking sites, and two sorts of so-called removal strands (symbolized via the red and blueish glue tubes), which activate a new docking site for each filament. Consequently, the filaments can bond via these new docking sites to the nanorod and thereby finish the revolution movement. In between IV and V, there exists an intermediate state i, where the filaments are only attached to the nanorod via one docking site each. For filament A, the distance between the dye and the nanorod is drastically enlarged during this intermediate state (cf. distance values given in the figure). Consequently, the corresponding dye experiences an increase in its fluorescence intensity.

To understand the origin of the kinks, it is necessary to have a closer look at the underlying DNA reactions that allow the gearset to transit from one state to another. Note that in the following, we try to keep the explanations as simply as possible, such that a reader without a chemistry related background is able to follow them. A more detailed description of the chemical processes may be found in the original publication [P3].

Figure 6.10 depicts exemplarily the transition from state IV to V. In state IV, the two DNA origami filaments are each attached via two DNA docking sites

to the gold nanorod. In order to induce the transition to state V, four kinds of DNA compounds have to be added to the solution: Two sorts of so-called blocking strands (symbolized via the red and blueish scissors), which open specific docking sites, and two sorts of so-called removal strands (symbolized via the red and blueish glue tubes), which activate a new docking site for each filament.[6] Consequently, the filaments can bond via these new docking sites to the nanorod and thereby finish the revolution movement.

In the experiment, all of the four components are added nearly simultaneously to the solution. However, during the course of the chemical reactions, there has to be a moment in time, when the filaments are only attached via one docking site to the nanorod. This can be associated with an intermediate state i. For filament A, the distance between the dye and the nanorod is increased during this intermediate state, while for filament B, it does not change much (cf. distance values provided in the figure). Therefore the dye that is attached to filament A (ATTO 550) exhibits an increased intensity in this intermediate state. Inserting the estimated distances for ATTO 550 into our numerical simulations predicts the following intensities (normalized on the free dye molecule): $I_{\mathrm{IV,simulated}} = 0.10$, $I_{\mathrm{i,simulated}} = 0.44$, and $I_{\mathrm{V,simulated}} = 0.24$.

All transitions that occur during the experiment from Fig. 6.9 do exhibit such an intermediate state; however, due to the geometry of the DNA design, only for the transitions IV to V and VII to VIII, and only for filament A, there is an increased distance between dye and nanoparticle during the intermediate state. This explains why only in these cases, kinks can be observed in the fluorescence intensities.

Figure 6.11 contains a control experiment that was carried out to directly probe the intermediate states. Panel (a) depicts the underlying series of revolution states, labeled as I to IV [note that two steps are skipped, compared to the sequence in Fig. 6.9(a), and thus, the labeling here is different]. The special point about this experiment is that for the transition from state II

6 One might wonder about the fact that the strands that open connections are called blocking strands and the strands that close connections are referred to as removal strands. Intuitively, one would probably expect the opposite naming convention. The names of the strands are derived from the chemical task that they perform: The blocking strands bind to docking sites and *block* them such that the sites are deactivated and cannot bind to the nanorod anymore (since the binding between the blocking strands and the docking sites is energetically preferred to the binding between the nanorod and the docking sites, the above reaction also allows for opening existing nanorod-docking-site bindings). The removal strands get their name from the fact that they can *remove* blocking strands from blocked docking sites and thereby activate the sites again.

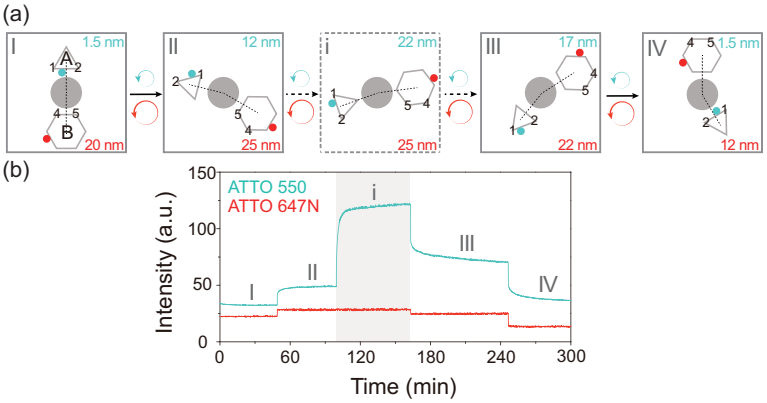

Figure 6.11. Control experiment to directly probe the intermediate states. Instead of adding both blocking and removal strands for the transition II to III in a single step, first, only the blocking strands were added, to drive the filaments from state II to state i, and after waiting for approximately on hour, the removal strands were added, to complete the transition to state III. (a) Sequence of states and corresponding distances [note that two states are skipped, compared to the sequence in Fig. 6.9(a), and thus, the labeling here is different]. (b) Measured fluorescence signal, which proves the existence of the intermediate state.

to III, the triggering DNA compounds are not simultaneously added to the solution; instead, they are added in two steps: First, at time $t \approx 100$ min, only the blocking strands are added to induce a transition to the intermediate state. Then, approximately one hour later, the removal strands are added to complete the transition to state III. It can be seen that the intensity that corresponds to filament A is increased during the time interval of the intermediate state, while the intensity that corresponds to filament B remains constant, as expected.

6.5.2 *Kinetic model*

While the above considerations can explain why the kinks are occurring in the experiment from Fig. 6.9, they do not explain the shape of the kinks. So let us now have a closer look at the dynamics of the system, in order to understand the observed shape. The dynamics can be described by employing a simple kinetic model. The transition from one state (for reasons of

generality denoted as X) to another state (for reasons of generality denoted as Y) via the intermediate state i can be divided into two processes:

$$\mathrm{X} \longrightarrow \mathrm{i}, \tag{6.28}$$

$$\mathrm{i} \longrightarrow \mathrm{Y}, \tag{6.29}$$

where the first process [Eq. (6.28)] summarizes the reaction of the nanogear devices with the blocking strands and an orientation change of the filaments, while the second process [Eq. (6.29)] summarizes the reaction of the nanogear devices with the removal strands, another conformation change, and the bonding reaction between the activated docking sites and the nanorod. In the simplest approximation, $\mathrm{X} \longrightarrow \mathrm{i}$ and $\mathrm{i} \longrightarrow \mathrm{Y}$ can be modeled as first-order chemical processes, which translates into the following differential equations:

$$\frac{d[\mathrm{X}]}{dt} = -\alpha[\mathrm{X}], \tag{6.30}$$

$$\frac{d[\mathrm{i}]}{dt} = \alpha[\mathrm{X}] - \beta[\mathrm{i}], \tag{6.31}$$

$$\frac{d[\mathrm{Y}]}{dt} = \beta[\mathrm{i}], \tag{6.32}$$

where the square brackets denote the concentration of the respective state, and α as well as β are two unknown rate constants. For the sake of completeness, it should be mentioned, that in general, the reactions of the nanogear devices with the blocking and the removal strands are actually second-order chemical reactions [318], since in each case, two reactants are involved (namely the nanogear devices and the blocking strands, and the nanogear devices and the removal strands, respectively). However, in the experiments, the concentrations of blocking and removal strands are three orders of magnitude higher than the concentrations of the nanogear devices, and in this limit, the concentrations of the exceeding species can be assumed as constant, which gives rise to an effective dynamic represented by a first-order process [319].

6.5.2.1 *Fit of the rate constants*

The rate constants α and β were fitted from the control experiment (Fig. 6.11). The fact that in this experiment the two processes $\mathrm{X} \longrightarrow \mathrm{i}$ and $\mathrm{i} \longrightarrow \mathrm{Y}$ are well separated in time allows one to independently extract the values for α and β. The corresponding model functions were obtained by solving the

differential equations Eqs. (6.30), (6.31), and (6.32) with the respective initial conditions that will be described in the following.

First, let us consider the process X → i. Initially, all nanogears are in state X. At the time t_0, the blocking strands are added to trigger the transition to state i. From Eqs. (6.30), and (6.31), the time-dependent concentrations for times $t \geq t_0$ follow as

$$[\mathrm{X}](t) = [\mathrm{N}]e^{-\alpha(t-t_0)}, \tag{6.33}$$

$$[\mathrm{i}](t) = [\mathrm{N}]\left(1 - e^{-\alpha(t-t_0)}\right), \tag{6.34}$$

where [N] denotes the total concentration of the nanogear devices in the system. Let I_X and I_i be the intensities for the case when all nanogears are in state X and i, respectively. Then, the total intensity as a function of time is given by

$$I(t) = I_\mathrm{X}e^{-\alpha(t-t_0)} + I_\mathrm{i}\left(1 - e^{-\alpha(t-t_0)}\right). \tag{6.35}$$

Now, let us consider the process i → Y. The process starts at the time t_1, when the removal strands are added. Since in the control experiment, the times t_0 and t_1 are well separated [i.e. $(t_1 - t_0)\alpha \gg 1$], we can assume that at time t_1, all nanogears are in state i. From Eqs. (6.31), and (6.32), the time-dependent concentrations for times $t \geq t_1$ follow as

$$[\mathrm{i}](t) = [\mathrm{N}]e^{-\beta(t-t_1)}, \tag{6.36}$$

$$[\mathrm{Y}](t) = [\mathrm{N}]\left(1 - e^{-\beta(t-t_1)}\right). \tag{6.37}$$

The corresponding time-dependent intensity is then given by

$$I(t) = I_\mathrm{i}e^{-\beta(t-t_1)} + I_\mathrm{Y}\left(1 - e^{-\beta(t-t_1)}\right), \tag{6.38}$$

where I_Y represents the intensity for the case when all nanogears are in state Y. Fitting Eqs. (6.35) and (6.38) to the rising and the decaying slopes of the control experiment (Fig. 6.11), respectively, yields $\alpha \approx 1.2 \cdot 10^{-2}$ s^{-1} and $\beta \approx 1.3 \cdot 10^{-2}$ s^{-1} (Fig. 6.12). Note that the curves were only fitted to the first 300 s of the slopes, in order to reduce the influence of an additional slow linear drift of the fluorescence signal that is occurring on a larger time scale.

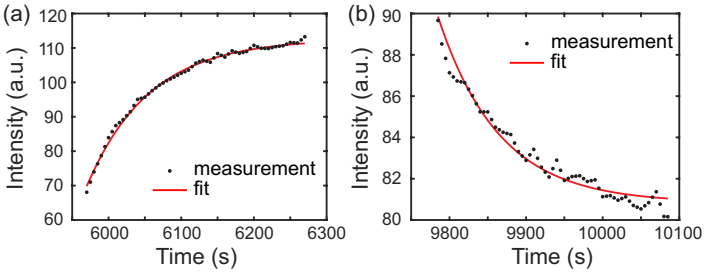

FIGURE 6.12. Fit of rate constants from the control experiment (Fig. 6.11). (a) Fitting the rising slope yields $\alpha \approx 1.2 \cdot 10^{-2}$ s^{-1}. (b) Fitting the decaying slope yields $\beta \approx 1.3 \cdot 10^{-2}$ s^{-1}.

6.5.2.2 *Modeling of the kinks*

As already mentioned, in the revolution experiment (cf. Fig. 6.9), the blocking and the removal strands are added at once (only separated by the small time delay it takes to mix the solution and prepare the pipettes). This means that both processes X $\longrightarrow$ i and i $\longrightarrow$ Y are happening simultaneously. Assuming that the blocking strands are again added at a time t_0 and the removal strands at a time t_1, but that this time the condition $(t_1 - t_0)\alpha \gg 1$ does not apply, and solving Eqs. (6.30), (6.31), and (6.32), results in the following time-dependent concentrations for $t \geq t_0$:

$$[\mathrm{X}](t) = [\mathrm{N}]e^{-\alpha(t-t_0)}; \tag{6.39}$$

$$[\mathrm{i}](t) = \begin{cases} [\mathrm{N}]\left(1 - e^{-\alpha(t-t_0)}\right), & t < t_1; \\ [\mathrm{X}]_1 \alpha \frac{e^{-\beta(t-t_1)} - e^{-\alpha(t-t_1)}}{\alpha - \beta} + [\mathrm{i}]_1 e^{-\beta(t-t_1)}, & t \geq t_1; \end{cases} \tag{6.40}$$

$$[\mathrm{Y}](t) = \begin{cases} 0, & t < t_1; \\ [\mathrm{X}]_1 \left(1 - \frac{\alpha e^{-\beta(t-t_1)} - \beta e^{-\alpha(t-t_1)}}{\alpha - \beta}\right) + [\mathrm{i}]_1 \left(1 - e^{-\beta(t-t_1)}\right), & t \geq t_1; \end{cases} \tag{6.41}$$

with $[\mathrm{X}]_1 = [\mathrm{N}]e^{-\alpha(t_1-t_0)}$ and $[\mathrm{i}]_1 = [\mathrm{N}](1 - e^{-\alpha(t_1-t_0)})$. Consequently, the time-dependent intensity is given by

$$I(t) = I_{\mathrm{X}} \frac{[\mathrm{X}](t)}{[\mathrm{N}]} + I_{\mathrm{i}} \frac{[\mathrm{i}](t)}{[\mathrm{N}]} + I_{\mathrm{Y}} \frac{[\mathrm{Y}](t)}{[\mathrm{N}]}. \tag{6.42}$$

In the revolution experiment, adding the blocking and removal strands had been done by executing the following procedure: 1) Taking the sample out of the measurement chamber, adding the blocking strands for filament A, and mixing the solution. 2) Adding the blocking strands for filament B, and mixing the solution. 3) Adding the removal strands for filament A, and mixing the solution. 4) Adding the removal strands for filament B, mixing the solution, and putting the sample back. Each of these steps takes approximately 30 s, which gives a total time of approximately 2 min. During this period, the intensity recording had to be paused, and afterwards the experimental curves were stitched together at the pausing point.

In order to resemble the experimental conditions as accurately as possible, the above procedure was considered in the modeling. It was estimated that, when taking the sample out and starting the process at a time $t = 0$ s, the blocking strands and the removal strand for the triangular filament (filament A) come in contact with the nanogears at a time $t_0 = 30$ s and at a time $t_1 = 90$ s, respectively.

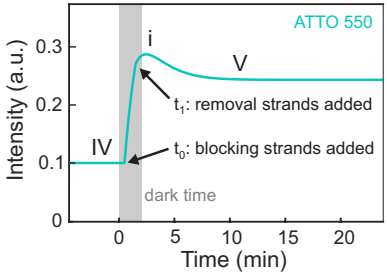

Figure 6.13. Calculated time-dependent fluorescence intensity for the transition from state IV to state V via the intermediate state i. The gray insert marks the time interval that is not recorded in the experiments (dark time). This curve (dark time removed, in order to be comparable with the experimental data) is depicted in Fig. 6.9(b).

Inserting these values into our model, together with the fitted rate constants α and β, and using the above given simulated values for $I_{\mathrm{IV,simulated}}$, $I_{\mathrm{i,simulated}}$, and $I_{\mathrm{V,simulated}}$, provides the time-dependent intensity that is plotted in Fig. 6.13. The gray insert marks the period, during which the intensity was not recorded in the experiment (denoted as dark time). This curve (dark

time removed, in order to be comparable with the experimental data) is depicted in Fig. 6.9(b). Note that due to the stitching, the rising slopes of the kinks in Fig. 6.9(b) and Fig. 6.9(c) appear to be steeper than they actually are. It can be seen that, apart from an additional slow linear drift in the measured signals, our kinetic model allows us to qualitatively reproduce the experimental observations.

6.5.2.3 *Limitations of the model*

For the sake of completeness, it should be mentioned that our kinetic model, although being able of providing a qualitative insight into the dynamics of the system, still has some clear limitations and should hence only be seen as a rough approximation: First, the concentrations of blocking and removal strands in the experiment are actually not truly constant throughout the reactions, since in each step, a surplus of the new blocking and removal strands has to be added, in order to deactivate unreacted blocking and removing strands that remaining from the previous step (for more details, cf. the explanation of the chemical procedures in publication [P3]). Second, our model neglects the possibility that the removal strands can also react with the respective docking sites of the nanogears while those are still in state X. Third, as already mentioned earlier, it appears that there are some additional slow linear drifts in the experimental fluorescence intensities, which cannot be reproduced by our model.

6.6 INCLUSION OF FÖRSTER RESONANCE ENERGY TRANSFER

So far, we have considered the electromagnetic interaction between dyes and nanoparticles; however, there is another electromagnetic interaction that can be used for optically tracking distance changes on the nanoscale: The interaction of a dye with another dye, which is known as Förster resonance energy transfer (FRET). In the following, we will show how FRET can be included in the dye-nanoparticle interaction model and we will discuss an example, where the combined interaction is utilized to monitor movements in a DNA nanodevice. This section is based on publication [P1]. Note that chronologically, this publication was actually the first of all DNA-related works that had been published in the context of this thesis. However, for didactic reasons, we have on purpose saved its discussion for last.

6.6.1 *Theory*

In the following, we will start with explaining the basic equations of FRET. Then, we will show how FRET can be included in the dye-nanoparticle interaction model.

6.6.1.1 *Basics*

In general, FRET describes the phenomenon that one dye (from now on referred to as the donor) can transfer energy to another dye (from now on referred to as the acceptor) via electromagnetic near-field interaction. The prerequisites are that both dyes are physically close to each other (typical distances are a few nm) and that there exists a spectral overlap between the emission spectrum of the donor and the absorption spectrum of the acceptor.

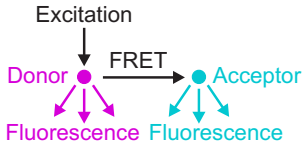

Figure 6.14. Illustration of the underlying mechanisms of Förster resonance energy transfer (FRET). Two dyes are involved (denoted as donor and acceptor). The prerequisites are that the donor's emission frequency spectrum exhibits an overlap with the acceptor's absorption spectrum and that both dyes are spatially close to each other (typical distances are in the order of a few nm). When the donor is excited, it may transfer energy to the acceptor via near-field interaction. This transfer is denoted as FRET. Consequently, the donor's fluorescence intensity will get weaker and furthermore, the acceptor will start to fluoresce as well. The rate of the energy transfer and thus the fluorescence intensities of the two dyes strongly depend on the relative distance.

The underlying mechanisms are illustrated in Fig, 6.14. The donor is excited by light at its excitation frequency. As a result, it will fluoresce at its emission frequencies. If now an acceptor comes close to the donor, it is possible that energy may be transferred via FRET. This has two consequences: First, the emission intensity of the donor will get weaker, since a part of the excitation

energy is lost to the acceptor. Second, and more importantly, the acceptor will start to fluoresce as well, at its own emission frequency. It is critical to note that the rate of the energy transfer strongly depends on the distance between the two dyes (the closer the dyes are, the higher is the energy transfer rate). Thus, by monitoring the fluorescence intensity of one of the two dyes (typically the intensity of the acceptor), one obtains feedback about their relative distance.

Following Ref. [192], the rate of the energy transfer γ_{FRET} (from now on referred to as the FRET rate) can be calculated via:[7]

$$\frac{\gamma_{\mathrm{FRET}}}{\gamma_{\mathrm{r,o}}^{\mathrm{D}}} = 18\pi \int d\omega \left| \frac{c}{\omega\mu} \right|^2 f_0^{\mathrm{D}}(\omega)\sigma_{\mathrm{A}}(\omega) \left| \mathbf{e}_{\mathrm{A}} \cdot \hat{\mathbf{G}}_{\mathbf{EE}}(\mathbf{r}_{\mathrm{A}}, \mathbf{r}_{\mathrm{D}}; \omega) \cdot \mathbf{e}_{\mathrm{D}} \right|^2 . \quad (6.43)$$

Here, $\gamma_{\mathrm{r,o}}^{\mathrm{D}}$ denotes the intrinsic radiative decay rate of the donor, $f_0^{\mathrm{D}}(\omega)$ represents the donor's normalized intrinsic emission spectrum, and $\sigma_{\mathrm{A}}(\omega)$ is the frequency-dependent absorption cross section of the acceptor. Furthermore, $\mathbf{r}_{\mathrm{D}}$ and $\mathbf{r}_{\mathrm{A}}$ represent the position of the donor and the acceptor, respectively, and $\mathbf{e}_{\mathrm{D}}$ as well as $\mathbf{e}_{\mathrm{A}}$ are unit vectors that point in the directions of their dipole moments. The quantity $\hat{\mathbf{G}}_{\mathbf{EE}}$ denotes the 3×3 dimensional electric-electric part of the 6×6 dimensional Green's dyadic $\hat{\mathbb{G}} = [\hat{\mathbf{G}}_{\mathbf{EE}}, \hat{\mathbf{G}}_{\mathbf{EH}}; i\hat{\mathbf{G}}_{\mathbf{HE}}, i\hat{\mathbf{G}}_{\mathbf{HH}}]$ of the Maxwell operator that is used throughout this thesis. One might wonder why only the electric-electric part of the Green's dyadic enters the equation. This simply comes from the fact that FRET describes the interaction of one electric dipole with another electric dipole.

Note that equation (6.43) is valid for any kind of electromagnetic environment. For the special case of a homogeneous and isotropic surrounding, the Green's dyadic can be expressed analytically. By inserting the corresponding expression, the FRET-rate expression simplifies to [192]:

$$\frac{\gamma_{\mathrm{FRET}}}{\gamma_{\mathrm{r,o}}^{\mathrm{D}}} = \left(\frac{R_0}{R} \right)^6 . \quad (6.44)$$

Here, $R = |\mathbf{r}_{\mathrm{A}} - \mathbf{r}_{\mathrm{D}}|$ represents the distance between the two dyes and R_0 denotes the so-called Förster radius, which will be provided in the following. The above equation is very instructive since it reveals that in the above scenario, the FRET rate is proportional to the sixth power of the inverse of

7 The factor $|c/(\omega\mu)|^2$ appears due to the fact that in consistency with the rest of this thesis, we have written the equation in terms of the Green's dyadic of the Maxwell operator instead of the Green's dyadic of the wave equation, which is used in Ref. [192]. Furthermore, note that we are assuming Gaussian units here, as in the rest of the thesis.

the distance between the two dyes, and therefore, that the effect is extremely sensitive to distance changes. The Förster radius is defined via

$$R_0^6 = \frac{9c^4\varkappa^2}{8\pi}\int \frac{f_0^{\mathrm{D}}(\omega)\sigma_{\mathrm{A}}(\omega)}{n^4\omega^4}d\omega, \tag{6.45}$$

where n is the refractive index of the surrounding medium and the factor $\varkappa^2 = [\mathbf{e}_{\mathrm{A}}\cdot\mathbf{e}_{\mathrm{D}} - 3(\mathbf{e}_{\mathrm{R}}\cdot\mathbf{e}_{\mathrm{D}})(\mathbf{e}_{\mathrm{R}}\cdot\mathbf{e}_{\mathrm{A}})]^2$, with $\mathbf{e}_{\mathrm{R}}$ being a unit vector in the direction of $\mathbf{r}_{\mathrm{A}} - \mathbf{r}_{\mathrm{D}}$, accounts for the relative orientation of the two dipoles. It should be mentioned that for random orientations of both dipoles, and assuming fast rotation, one can replace $\varkappa^2$ by its orientation-averaged value $\langle\varkappa^2\rangle = 2/3$ [192].

6.6.1.2 *How to combine FRET and dye-nanostructure interactions*

Let us now consider a system where the donor and the acceptor are not only interacting with each other via FRET, but simultaneously with a nanostructure. Note that the considerations that we provide in the following can be seen as a generalization of a model from literature [320] (which is valid for emitters with high quantum yields) to emitters with arbitrary quantum yields.

In general, the fluorescence rates of the donor and acceptor in the presence of a nanostructure can be written as (cf. section 6.2)

$$\gamma_{\mathrm{fl}}^{\mathrm{D}} = q^{\mathrm{D}}\gamma_{\mathrm{exc}}^{\mathrm{D}} \tag{6.46}$$

and

$$\gamma_{\mathrm{fl}}^{\mathrm{A}} = q^{\mathrm{A}}\gamma_{\mathrm{exc}}^{\mathrm{A}}, \tag{6.47}$$

respectively, where q^{D} as well as q^{A} denote the quantum yields of the two dyes and $\gamma_{\mathrm{exc}}^{\mathrm{D}}$ and $\gamma_{\mathrm{exc}}^{\mathrm{D}}$ represent their excitation rates. Note that in the following, we will consistently use the superscripts D and A in order to label quantities that belong to the donor and acceptor, respectively.

We now show how FRET can be incorporated in these equations. The quantum yield of the donor under the influence of FRET is obtained by taking the quantum-yield expression from Eq. (6.5) and including the term $\gamma_{\mathrm{FRET}}/\gamma_{\mathrm{r,o}}^{\mathrm{D}}$

in the denominator, in order to account for the energy loss to the acceptor. This gives:

$$q^{\mathrm{D}} = \frac{\frac{\gamma_{\mathrm{r}}^{\mathrm{D}}}{\gamma_{\mathrm{r,0}}^{\mathrm{D}}}}{\frac{\gamma_{\mathrm{r}}^{\mathrm{D}}}{\gamma_{\mathrm{r,0}}^{\mathrm{D}}} + \frac{\gamma_{\mathrm{abs}}^{\mathrm{D}}}{\gamma_{\mathrm{r,0}}^{\mathrm{D}}} + \frac{\gamma_{\mathrm{FRET}}}{\gamma_{\mathrm{r,o}}^{\mathrm{D}}} + \frac{1-q_0^{\mathrm{D}}}{q_0^{\mathrm{D}}}}. \tag{6.48}$$

The quantum yield of the acceptor is not influenced by the FRET process and directly follows from Eq. (6.5) as

$$q^{\mathrm{A}} = \frac{\frac{\gamma_{\mathrm{r}}^{\mathrm{A}}}{\gamma_{\mathrm{r,0}}^{\mathrm{A}}}}{\frac{\gamma_{\mathrm{r}}^{\mathrm{A}}}{\gamma_{\mathrm{r,0}}^{\mathrm{A}}} + \frac{\gamma_{\mathrm{abs}}^{\mathrm{A}}}{\gamma_{\mathrm{r,0}}^{\mathrm{A}}} + \frac{1-q_0^{\mathrm{A}}}{q_0^{\mathrm{A}}}}. \tag{6.49}$$

Since the acceptor obtains all its excitation photons from the donor, its excitation rate reads as

$$\gamma_{\mathrm{exc}}^{\mathrm{A}} = q_{\mathrm{FRET}} \gamma_{\mathrm{exc}}^{\mathrm{D}}, \tag{6.50}$$

where $\gamma_{\mathrm{exc}}^{\mathrm{D}}$ represents the excitation rate of the donor and q_{FRET} denotes the so-called FRET efficiency [192], which is, in our case, given by

$$q_{\mathrm{FRET}} = \frac{\frac{\gamma_{\mathrm{FRET}}^{\mathrm{D}}}{\gamma_{\mathrm{r,0}}^{\mathrm{D}}}}{\frac{\gamma_{\mathrm{r}}^{\mathrm{D}}}{\gamma_{\mathrm{r,0}}^{\mathrm{D}}} + \frac{\gamma_{\mathrm{abs}}^{\mathrm{D}}}{\gamma_{\mathrm{r,0}}^{\mathrm{D}}} + \frac{\gamma_{\mathrm{FRET}}}{\gamma_{\mathrm{r,o}}^{\mathrm{D}}} + \frac{1-q_0^{\mathrm{D}}}{q_0^{\mathrm{D}}}}. \tag{6.51}$$

Intuitively, the FRET efficiency can be understood as the ratio between the number of photons that are transferred to the acceptor via FRET and the number of photons that are absorbed by the donor.

As a side note, we want to mention that, in principle, our model also can account for another effect between two dye molecules, which is known as contact quenching [321]. This effect has been observed in cases when two dye molecules are extremely close to each other. Its impact can be considered by adding a term $\gamma_{\mathrm{con}}/\gamma_{\mathrm{r,o}}^{\mathrm{D}}$ to the denominators of Eqs. (6.48) and (6.51) as well as a term $\gamma_{\mathrm{con}}/\gamma_{\mathrm{r,o}}^{\mathrm{A}}$ to the denominator of Eq. (6.49), where γ_{con} denotes the rate of photon loss due to the contact quenching. It should, however, be noted that so far, there is no general ab-initio theory of the underlying mechanisms and thus, the rate γ_{con} as well as its distance dependence typically have to be estimated from experiments.

Now, let us come back to our FRET model. It is practical, to normalize the modified fluorescence rates of the donor and the acceptor to the donor's intrinsic fluorescence rate $\gamma_{\mathrm{fl},0}^{\mathrm{D}} = q_0^{\mathrm{D}} \gamma_{\mathrm{exc},0}^{\mathrm{D}}$. This gives:

$$\frac{\gamma_{\mathrm{fl}}^{\mathrm{D}}}{\gamma_{\mathrm{fl},0}^{\mathrm{D}}} = \frac{q^{\mathrm{D}}}{q_0^{\mathrm{D}}} \frac{\gamma_{\mathrm{exc}}^{\mathrm{D}}}{\gamma_{\mathrm{exc},0}^{\mathrm{D}}}, \tag{6.52}$$

$$\frac{\gamma_{\mathrm{fl}}^{\mathrm{A}}}{\gamma_{\mathrm{fl},0}^{\mathrm{D}}} = \frac{q^{\mathrm{A}} q_{\mathrm{FRET}}}{q_0^{\mathrm{D}}} \frac{\gamma_{\mathrm{exc}}^{\mathrm{D}}}{\gamma_{\mathrm{exc},0}^{\mathrm{D}}}. \tag{6.53}$$

These two equations together with the above expressions for q^{D}, q^{A} and q_{FRET} allow for describing a system where FRET and dye-nanostructure interactions are occurring simultaneously. It should be noted that one can now again account for all sorts of orientation averages (fast and slow dye rotation according to subsection 6.3.2; random structure orientation according to subsection 6.3.4) by simply applying the respective procedures to the numerators and denominators of Eqs. (6.52) and (6.53).

6.6.2 *Results*

Let us now investigate the system that was mentioned at the beginning of the section. The device is depicted in Fig. 6.15(a). It consists of two DNA origami filaments (gray) that are attached to a pair of spherical gold nanoparticles (yellow) with diameters of 10 nm. Two dyes (donor: ATTO 550, acceptor: Atto 647N) are tethered to the ends of the DNA filaments, which will be later used for optical monitoring. Note that these two dyes are well-known to exhibit a strong FRET when they are close to each other. Each DNA filament is equipped with ten rows of DNA binding sites (labeled 1 to 10). By exploiting similar chemical mechanisms as explained in subsection 6.4.2, it is possible to activate and deactivate specific binding sites and thereby, to enforce a sliding movement of the filaments, as illustrated in panel (b).

During the sliding, the distance between the two dyes changes. The displacement can be optically tracked via FRET. For this purpose, the donor is excited at its excitation wavelength of 530 nm and the emission intensities of the donor and the acceptor are recorded at their emission wavelengths of 578 nm and 663 nm, respectively. A difficulty arises from the presence of the two gold nanoparticles. The reason is that simultaneously to interacting with each other via FRET, the dyes can interact with the nanoparticles, which

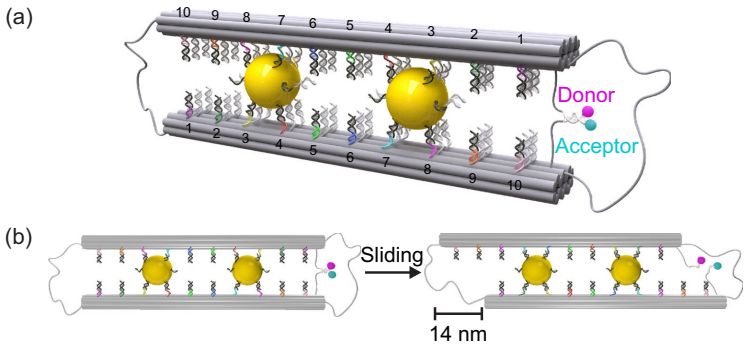

FIGURE 6.15. Sketch of the DNA slider. (a) The device consists of two DNA filaments (gray) that are attached to a pair of gold nanoparticles (yellow; diameter: 10 nm). Two dye molecules (donor and acceptor) are tethered to the ends of the filaments. (b) By exploiting similar chemical mechanisms as in the nanogear system from subsection 6.4.2, it is possible to activate and deactivate specific binding sites, and thereby to enforce a sliding movement of the filaments. During the sliding, the distance between the dyes changes. This distance change and thus the displacement of the two filaments can be optically monitored via FRET.

complicates the optical signals. In the following, we will use our theory from the previous subsection to understand this effect.

Before we continue, it should be noted that at first glance, the above approach for the optical tracking of the movements might appear very similar to the one that was employed for the nanogear device from subsection 6.4.2 (especially, since the same dyes are used). However, there is a fundamental difference: In the experiment for the gear system, both dyes were independently excited at their own excitation wavelengths and both dyes were well separated in space. Therefore, FRET did not play a role.[8] Here, both dyes

8 The careful reader may have noticed that in the revolution sequence from Fig. 6.9(a), there are a few rare situations where the two dyes accidentally come very close to each other. Hence, one might speculate if FRET might be relevant there. However, it turns out that this is not the case: First of all, it is actually not necessarily always provided that both DNA filaments start in state I at exactly opposite sites of the nanorod (although, this might be suggested by the illustration). The reason is that the exact positioning of the two DNA filaments in the gear device is very hard to experimentally control during the assembly process. Therefore, while the distances between the dyes and the nanorod can be assumed to be fixed and are well-known with high accuracy, the relative distance between the two dyes varies across different gear devices. Second, it had been experimentally confirmed that there are no noticeable FRET contributions in the system.

are quite close to each other and only the donor is excited. Therefore, the acceptor obtains all its energy via FRET.

Let us now apply our theory from the previous subsection to understand the light-matter interaction in the slider device.

First, let us discuss the modeling of the dye-nanoparticle interaction. As in the other systems, we rely on finite-element simulations, performed with COMSOL Multiphysics.[9] The gold nanoparticles were described as spheres of diameter 10 nm (permittivity taken from Ref. [322]), surrounded by water (refractive index: 1.332). The actual slider contains two nanoparticles, which are placed at a center-to-center distance of 28 nm. In the simulations, it was found that the influence of the second nanoparticle on all rates of the dyes is negligible and hence, only the nanoparticle close to the dye is relevant. Therefore, in order to keep the final model simple, only this nanoparticle was included. The intrinsic quantum yields $q_0^{\mathrm{D}} = 0.8$ and $q_0^{\mathrm{A}} = 0.65$ of the two dyes were taken as in subsection 6.4.2, while the intrinsic emission spectra f_0^{D} and f_0^{A} were determined from reference measurements.

The calculations reveal that the main effect of the nanoparticle is to act as a quencher: The closer the dyes come to the nanoparticle's surface, the weaker are their fluorescence intensities. The reason is that – similar to the case for the nanorod in subsection 6.4.2 – the nanoparticle is very small in size and thus, it functions as a highly inefficient antenna that mostly absorbs the light.

Now, let us discuss the modeling of the FRET process. For the calculations, it is necessary to know the frequency-dependent absorption cross section $\sigma_{\mathrm{A}}(\omega)$ of the acceptor. The cross section was obtained via the following method: First, the excitation spectrum of the acceptor was measured, which yielded the spectral shape of the absorption cross section, but not the absolute values. Then, in order to get the absolute values, the spectrum was scaled using the maximum molar attenuation coefficient that is given by the supplier[10] as $1.5 \times 10^5\,\mathrm{M^{-1}cm^{-1}}$. Furthermore, for describing the FRET effect, it is necessary, to calculate the quantity $\gamma_{\mathrm{FRET}}/\gamma_{\mathrm{r,o}}^{\mathrm{D}}$. To determine it, we have compared two approaches: 1) calculating it via Eq. (6.43), which constitutes the rigorous way and explicitly takes into account the presence of the nanoparticle, and 2) calculating it via Eq. (6.44), which is technically only valid for a homogeneous surrounding and completely neglects the presence of the nanoparticle. For Eq. (6.44), we have used the measured dye properties

9 See https://www.comsol.com.
10 Available under http://www.atto-tec.com.

to calculate the Förster radius, which yields a value of $R_0 = 6.65$ nm (for $\varkappa^2 = 2/3$).[11] For Eq. (6.43), we have used the measured dye properties as well; however, instead of calculating the Förster radius, we used the local electric field obtained from finite element calculations in order to construct the Green's dyadic. Interestingly, it was found that for all donor-acceptor configurations that are relevant in the system, both equations provide extremely similar values for $\gamma_{\mathrm{FRET}}/\gamma_{\mathrm{r,o}}^{\mathrm{D}}$ (practically indistinguishable within the range of the numerical precision of the finite-element calculations). At first glance, this might appear as a surprise; however, it can be explained by the fact that in the vicinity of the donor, the magnitude of the initial electric field caused by the donor dipole is much stronger than the magnitude of the scattered field generated by the nanoparticle, so that the scattered field of the nanoparticle can be neglected. Only in cases where both donor and acceptor are very close to the nanoparticle's surface (in the order of 5 nm), the scattered field becomes relevant and the results start to differ. This agrees very well with results reported in Ref. [320]. In order to keep the final model simple, we have decided to use Eq. (6.44) and thereby, neglected the direct influence of the nanoparticle on the FRET rate.

Let us briefly comment on the orientation averaging. As in the nanogear system from subsection 6.4.2, both dyes were assumed to be able to freely rotate at their attachment position, and furthermore, the experiment had been carried out in a solution, containing a large number of randomly oriented DNA devices. The dye rotation was accounted for by averaging the fluorescence rates in Eqs. (6.52) and (6.53) simultaneously over all donor and all acceptor orientations. In contrast to the nanogear system, the averaging was, however, performed under the assumption of slow rotation. The reason is that – as already indicated – chronologically, the slider system had been the first DNA nanosystem that was investigated in the context of this thesis. At the time, it was not well-known that the actual rotation speeds of dyes attached to DNA can be quite high and hence, slow rotation had been considered more plausible. The random orientations of the devices were accounted for via applying the ensemble average from Eq. (6.25) to the donor's excitation-rate modification $\gamma_{\mathrm{exc}}^{\mathrm{D}}/\gamma_{\mathrm{exc,0}}^{\mathrm{D}}$. For more details on the orientation-averaging in this system, the interested reader may refer to the Supplementary Information of publication [P1].

11 To avoid confusion, it should be mentioned that in publication [P1], a different value for the Förster radius is provided, namely $R_0 = 6.41$ nm. This is not a mistake, but stems from the fact that in the publication, an alternative definition had been used, where factors of $1/q_0^{\mathrm{D}}$ and q_0^{D} are included in Eq. (6.44) and Eq. (6.45), respectively. For consistency with Ref. [192], we have changed the definition.

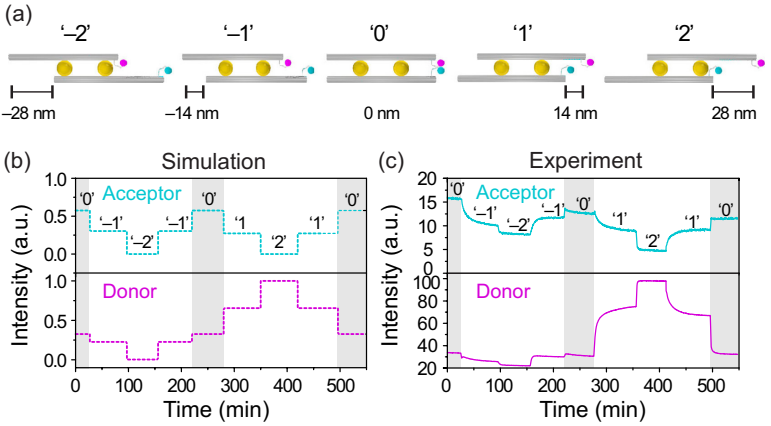

Figure 6.16. Results of the optical distance tracking via FRET. (a) Set of sliding states that can be induced in the system. Details on the dye positions are provided in Appendix D. (b) Theoretically predicted time-dependent fluorescence intensities of donor and acceptor. (c) Corresponding experimental results. One can observe that there is an excellent qualitative agreement.

We now have a look at the calculation results. Figure 6.16(a) depicts a set of sliding states ('–2' to '2') that can be experimentally induced in the device. The displacement between two consecutive states is 14 nm. During the sliding, the distances between the two dyes as well as the distances between the dyes and the nanoparticles change. The corresponding dye positions can be found in Appendix D. Note that – as already indicated – the DNA slider was chronologically the first of all DNA devices that were realized in the works that are discussed in this chapter. Between the different generations of DNA systems, the design of the linker structure that connects the dyes with the DNA filaments had been optimized in order to minimize the position uncertainty of the dyes. Compared to the nanogear system, where the estimated position uncertainty is less than 2 nm, the dye positions in the slider system exhibit a quite large uncertainty. To account for this, some additional assumptions had to be made, in order to estimate the dye positions in the most plausible way. The details are explained in Appendix D as well.

Panel (b) provides the calculated intensities of donor and acceptor for the case that the system is driven over time through a predefined sequence of sliding states. The sequence starts with state '0', where the distance between

donor and acceptor is minimal. Consequently, the calculation predicts a high intensity for the acceptor, due to the strong FRET. Next, the system transits to state '−1', followed by state '−2'. With each of the two steps, the predicted acceptor intensity gets weaker. This can be explained by the distance increase between the two dyes and the resulting reduced strengths of the FRET. The donor intensity becomes weaker as well, since with each step the dye comes closer to the nanoparticle. Afterwards, the sliding direction is reversed and the system is first driven back to '0' (where the initial intensities are restored) and then to states '1' and '2'. During the latter two steps, the acceptor intensity decreases again, due to the increase of the distance between the two dyes. The donor intensity, however, gets stronger, due to the increase of its distance to the nanoparticle. Afterwards, the system is driven back to state'0', where the initial intensities are restored again.

Panel (c) shows the corresponding experimental results. It turns out that there is an excellent qualitative agreement. Each of the predicted intensity steps is clearly visible in the experimental data. Nevertheless, it is worth mentioning that – as in the case of the nanogear system from Fig. 6.9 – there are a few quantitative differences: First, in contrast to the calculated intensities, the experimental ones never truly reach a value of zero. This can again be explained by the fact that there is a fraction of ill-functioning devices present in the solution. Second, the absolute heights of the predicted and the measured intensity steps are not identical. This can be explained by the high uncertainty in the dye positions as well as by inhomogeneities in the nanoparticles' shapes and sizes. Third, the acceptor intensity curves drift to lower values during the time the experiment is running. This is most likely caused by the fact that the number of broken devices increases over time.

6.7 CONCLUSION AND OUTLOOK

In this chapter, we have presented a detailed theoretical model of the light-matter interaction between quantum emitters and optically resonant nanostructures. We have applied the model to describe and elucidate experimental observations in different example systems from the field of DNA nanotechnology. Special care was devoted to accounting for experimental complications, such as emitter rotation and random structure orientation. We have demonstrated that when understanding the above light-matter interaction very well, one can employ it as a highly useful tool to track all sorts of movements on the nanoscale. Particularly interesting is also that,

while applications that exploit the emitter-nanostructure interaction for enhancing the fluorescence properties of emitters [295–297, 299] are often hampered by the high intrinsic loss of plasmonic nanosystems, the sensing application actually utilizes this loss as a benefit: The higher is the loss, the stronger becomes the quenching, and the more sensitive is the fluorescence intensity with respect to the emitter position.

We have also demonstrated that by combining the modeling of the light-matter interactions with a kinetic model for the chemical reactions, one can obtain interesting insights into the dynamics of such DNA nanosystems. Furthermore, we have shown how to include Förster resonance energy transfer in the emitter-nanostructure interaction equations and demonstrated that also this effect can be used for movement sensing.

The models that were presented in this chapter can provide the basis for many future works. Most likely, more complex functional nanosystems will be designed and investigated in the near future. In this context, it also appears quite intriguing to perform additional experiments on single devices and – equipped with the above theoretical approaches – use the results to gain a deeper understanding of the reaction dynamics. Finally, it is worth emphasizing again that the presented models are quite universal in the sense that they are not only applicable for dye molecules, but also virtually for any kind of emitter that can be associated with an oscillating electric dipole, which includes many kinds of quantum dots and defect centers.

7

CONCLUSIONS AND OUTLOOK

In this thesis, we have presented a detailed theoretical description of resonant light-matter interactions in nanophotonic sensing. We have started by introducing the reader to the theory of resonant states, which are defined as eigensolutions of Maxwell's equations in open optical resonators at discrete complex frequencies. We have explained that these states constitute a physically meaningful basis to describe resonant optical phenomena. We have given a broad overview of the current state of the art from literature and discussed how resonant states can be utilized to expand the near and far field of optical resonators and how they are useful for modeling light-matter interactions.

While the main purpose of that part of the thesis was to make the reader familiar with the basics of the theory of resonant states, it is worth noting that the part also contains some new results: First, the presented approaches from literature are formulated in a consistent framework that allows for incorporating nonreciprocal materials. Second, a new analytic normalization scheme for resonant states is derived, which is based on the Green's dyadic of the background system and – in contrast to the state-of-the-art analytic approach – is expected to hold for more complex geometrical surroundings (cf. subsection 2.2.3.2). Third, a rigorous pole-expansion based derivation of the so-called symmetric representation of the optical scattering matrix is provided (cf. subsection 2.2.7.2).

Afterwards, we have in detail discussed the light-matter interactions that occur in nanophotonic substance sensing. Since this kind of sensing is typically associated with small material changes, perturbation theory is a natural approach for the theoretical description. We have first focused on eigenfrequency changes, as they are relevant in many sensing schemes. Here, literature provides a highly useful first-order perturbation theory that allows

for predicting frequency shifts and linewidth changes under material perturbations in the resonator. We have explained that the literature expression is, however, limited to localized perturbations inside or in the vicinity of a given resonator geometry. Motivated by the fact that many applications in sensing are associated with changes of the resonator's surrounding medium, we have developed a generalization that allows one to incorporate these exterior material changes. We have demonstrated the applicability of the theory at several example systems.

Furthermore, we also have explained that frequency shifts and linewidth changes are not the only effects that can be relevant in substance sensing. In order to have a more general description available, we have derived a perturbation theory that allows for predicting the changes in optical far-field quantities under local perturbations. In our approach, the changes can be calculated via simple closed-form expressions from the unperturbed electromagnetic fields inside the resonator. We have shown that our theory provides deep insights into the underlying physics. In particular, we were able to demonstrate that all observable far-field changes originate from exactly five contributions: a nonresonant interaction, changes in the excitation and emission efficiencies of the resonant states, resonance shifts, and crosstalk between different resonant states. We have employed the theory to study a simple example from the field of dielectric sensing and found that – in full accordance with the literature expectation – in this sensing scheme, resonance shifts are the dominating effect.

Afterwards, we have applied the theory to a highly special sensing scheme, which is experiencing increasing interest in recent times: nanophotonic chiral sensing. We have shown that also here, the whole light matter interaction is composed of exactly the above five contributions. We have studied the influence of these contributions in different example systems and we have demonstrated that – in contrast to common expectation – here, resonance shifts are often not the dominating effect. In geometrically achiral sensors, they can even be strictly zero. Instead, changes in the excitation and emission efficiencies were found to play a crucial role. Furthermore we have explained that besides allowing for deep insights into the physics, the perturbative approach exhibits many practical benefits for sensor modeling in terms of computational efficiency.

In the end, we have switched from passive to active light-matter interactions. We have provided a detailed theoretical model of the interaction between quantum emitters and optically resonant nanostructures. The model was applied to describe and elucidate experimental observations in different

example systems from the field of DNA nanotechnology. Particular efforts were devoted to correctly accounting for experimental complications, such as emitter rotation and random structure orientations. It was also discussed how one can reduce the computational efforts by relying on semi-analytical expressions for the orientation dependence in the emission process as well as by exploiting symmetries of the nanostructures. Furthermore, it was demonstrated how one can incorporate other effects into the equations, such as the Förster resonance energy transfer between two emitters. In addition to the light-matter interaction model, a simple kinetic model was provided for describing the time-dependence of DNA reactions. It was shown that the combination of both models can provide interesting insights into the dynamics of such DNA nanosystems.

The theoretical framework that was presented in this thesis can provide the basis for many future studies related to sensor modeling and design as well as for understanding resonant light-matter interactions on a more fundamental level. Here, we want to take the opportunity to suggest some concrete ideas:

First, as already indicated, one can employ the resonant-state framework to understand the light-matter interactions in more sophisticated systems. Examples that appear particularly interesting are advanced resonator designs for chiral sensing [256, 268, 271–273] as well as nonreciprocal resonators and reciprocal resonators with nonreciprocal perturbations.

Second, it would be highly intriguing to apply the far-field perturbation theory to the case of dispersive analyte media where the dispersion is associated with the occurrence of molecular resonances. This situation is relevant in sensing schemes that rely on the nanophotonic enhancement of molecular vibrations [5, 17, 18, 323]. Although this technique has started to attract a lot of popularity due to its many benefits (it allows for the unambiguous identification of target substances, it can detect multiple substances simultaneously, and it can, in some cases, even be used to monitor molecular configuration changes), the involved mechanisms are still not fully understood. In some case, elaborate post-processing of the optical signals is used to extract relevant information from the measured data [324]. Clarifying the signal contributions could reveal deep new insights.

Third, from our current far-field perturbation theory, one could extract an alternative version that is based on full-wave calculations instead of the resonant states. To derive it, one would just need to choose a different separation of the unperturbed material distribution $\hat{\mathbb{P}}$ into a background system $\hat{\mathbb{P}}_{\mathrm{BG}}$ and a scattering part $\Delta\hat{\mathbb{P}}$ than the one that was employed so far

(cf. 2.2.5). In particular, one should choose $\Delta\hat{\mathbb{P}} = 0$ and $\hat{\mathbb{P}}_{\mathrm{BG}} = \hat{\mathbb{P}}$. This would give $\mathbb{F}_{\mathrm{scat}} = 0$ and $\mathbb{F}_{\mathrm{tot}} = \mathbb{F}_{\mathrm{BG}}$. One can then numerically solve Maxwell's equations for the total field $\mathbb{F}_{\mathrm{tot}}$ in the unperturbed system and plug this one – without applying any expansion in terms of the resonant states – as background field into the far-field perturbation equations [Eqs. (4.11) to (4.16)]. Due to the choice $\Delta\hat{\mathbb{P}} = 0$, the coefficients $a_{\mathrm{N}}^{(n)}$ and $b_{\mathrm{N}}^{(n)}$ are zero. Consequently, all contributions vanish except for the nonresonant interaction. Thus, one ends up with a single equation that allows for predicting the change in the resonator's optical far-field quantities under arbitrary perturbations $\delta\hat{\mathbb{P}}$ from the (numerically calculated) unperturbed total electromagnetic near fields in the resonator. The disadvantage of this full-wave based approach is that it does not provide as much insight into the physics as the resonant-state based version; however, there are several interesting benefits: (i) The approach should be very easy to implement in almost any numerical solver since no eigenmode analysis is required. (ii) Similar as the resonant-state based approach (cf. discussion in section 5.5), it should be able to predict the sensor response to different $\delta\hat{\mathbb{P}}$ with a minimum of computational efforts in one single evaluation step, and it should be capable of dealing with arbitrarily small $\delta\hat{\mathbb{P}}$. (iii) This new approach could provide interesting new quantitative insights, for instance, concerning the exact relation between the local near fields and the strength of the sensor response.

A

DERIVATION OF THE SURFACE TERM FOR EXTERIOR PERTURBATIONS

In the following, we provide the evaluation of the surface term δS_n from Eq. (3.11) (repeated here for convenience):

$$\delta S_n = ic \oint_{\partial V} d\mathbf{S} \cdot (\mathbf{E}_n^{\ddagger} \times \delta\mathbf{H}_n - \delta\mathbf{E}_n \times \mathbf{H}_n^{\ddagger}), \tag{A.1}$$

with $\delta\mathbb{F}_n = \partial\mathbb{F}_\nu/\partial\Lambda|_{\Lambda=0}$.

We note that in a homogeneous surrounding with permittivity ε_S and permeability μ_S, any outgoing field can be expanded in a set of outgoing basis functions $\mathbb{O}_\mathrm{N}$ as defined in Ref. [45]. These basis functions can be factorized as

$$\mathbb{O}_\mathrm{N}(\varepsilon_\mathrm{S}, \mu_\mathrm{S}; \omega) = A_\mathrm{N}(\varepsilon_\mathrm{S}, \mu_\mathrm{S}; \omega) \begin{pmatrix} \sqrt{\mu_\mathrm{S}}\mathcal{E}_\mathrm{N}(n_\mathrm{S}\omega; \mathbf{r}) \\ i\sqrt{\varepsilon_\mathrm{S}}\mathcal{H}_\mathrm{N}(n_\mathrm{S}\omega; \mathbf{r}) \end{pmatrix}, \tag{A.2}$$

where $A_\mathrm{N}(\varepsilon_\mathrm{S}, \mu_\mathrm{S}; \omega)$ represents a scalar, $n_\mathrm{S} = \sqrt{\varepsilon_\mathrm{S}\mu_\mathrm{S}}$ denotes the refractive index, and $\mathcal{E}_\mathrm{N}(n_\mathrm{S}\omega; \mathbf{r})$ as well as $\mathcal{H}_\mathrm{N}(n_\mathrm{S}\omega; \mathbf{r})$ are vectors. It is important to notice that these vectors depend on the product of n_S and ω, as this will be relevant later.

Let ε_S and μ_S represent the permittivity and permeability, respectively, in the perturbed surrounding. They read as:

$$\varepsilon_\mathrm{S}(\omega; \Lambda) = \varepsilon(\omega) + \Lambda\delta\varepsilon(\omega) \tag{A.3}$$

$$\mu_\mathrm{S}(\omega; \Lambda) = \mu(\omega) + \Lambda\delta\mu(\omega). \tag{A.4}$$

Consequently, we identify the perturbed refractive index to be $n_\mathrm{S}(\omega; \Lambda) = \sqrt{\varepsilon_\mathrm{S}(\omega; \Lambda)\mu_\mathrm{S}(\omega; \Lambda)}$. For $\Lambda = 0$, the above quantities become their unperturbed counterparts $\varepsilon(\omega)$, $\mu(\omega)$, and $n(\omega) = \sqrt{\varepsilon(\omega)\mu(\omega)}$.

With the help of Eqs. (A.2), (A.3), and (A.4), we can express the analytic continuations $\mathbb{F}_\nu(\omega;\Lambda)$ and $\mathbb{F}_n(\omega)$ [note that the latter is identical to $\mathbb{F}_\nu(\omega;0)$] as

$$\mathbb{F}_\nu(\omega;\Lambda) = \sum_{\mathrm{N}} \alpha_{\mathrm{N}}^{(n)}(\omega;\Lambda)\mathbb{O}_{\mathrm{N}}[\varepsilon_{\mathrm{S}}(\omega;\Lambda),\mu_{\mathrm{S}}(\omega;\Lambda);\omega], \tag{A.5}$$

$$\mathbb{F}_n(\omega) = \sum_{\mathrm{N}} \alpha_{\mathrm{N}}^{(n)}(\omega;0)\mathbb{O}_{\mathrm{N}}[\varepsilon(\omega),\mu(\omega);\omega], \tag{A.6}$$

where $\alpha_N^{(n)}(\omega;\Lambda)$ are perturbation-dependent expansion coefficients.

EVALUATION OF $\delta\mathbb{F}_n$

Let us now evaluate $\delta\mathbb{F}_n$. We recall that it is defined as $\delta\mathbb{F}_n = \partial\mathbb{F}_\nu/\partial\Lambda|_{\Lambda=0}$ $= \partial\mathbb{F}_\nu(\omega_n;\Lambda)/\partial\Lambda|_{\Lambda=0}$. Using Eq. (A.5) and applying the product rule gives

$$\delta\mathbb{F}_n = \delta\mathbb{X}_n + \delta\mathbb{Y}_n + \delta\mathbb{Z}_n, \tag{A.7}$$

with

$$\delta\mathbb{X}_n = \sum_{\mathrm{N}} \frac{\partial}{\partial\Lambda}\left\{\alpha_{\mathrm{N}}^{(n)}(\omega_n;\Lambda)A_{\mathrm{N}}[\varepsilon_{\mathrm{S}}(\omega_n;\Lambda),\mu_{\mathrm{S}}(\omega_n;\Lambda);\omega_n]\right\}_{\Lambda=0}\begin{pmatrix}\sqrt{\mu}\mathcal{E}_{\mathrm{N}}(n\omega_n;\mathbf{r})\\ i\sqrt{\varepsilon}\mathcal{H}_{\mathrm{N}}(n\omega_n;\mathbf{r})\end{pmatrix}, \tag{A.8}$$

$$\delta\mathbb{Y}_n = \sum_{\mathrm{N}} \alpha_{\mathrm{N}}^{(n)}(\omega_n;0)A_{\mathrm{N}}(\varepsilon,\mu;\omega_n)\begin{pmatrix}\frac{\partial}{\partial\Lambda}\left\{\sqrt{\mu_{\mathrm{S}}(\omega_n;\Lambda)}\right\}_{\Lambda=0}\mathcal{E}_{\mathrm{N}}(n\omega_n;\mathbf{r})\\ i\frac{\partial}{\partial\Lambda}\left\{\sqrt{\varepsilon_{\mathrm{S}}(\omega_n;\Lambda)}\right\}_{\Lambda=0}\mathcal{H}_{\mathrm{N}}(n\omega_n;\mathbf{r})\end{pmatrix}, \tag{A.9}$$

$$\delta\mathbb{Z}_n = \sum_{\mathrm{N}} \alpha_{\mathrm{N}}^{(n)}(\omega_n;0)A_{\mathrm{N}}(\varepsilon,\mu;\omega_n)\begin{pmatrix}\sqrt{\mu}\frac{\partial}{\partial\Lambda}\left\{\mathcal{E}_{\mathrm{N}}[n_{\mathrm{S}}(\omega_n;\Lambda)\omega_n;\mathbf{r}]\right\}_{\Lambda=0}\\ i\sqrt{\varepsilon}\frac{\partial}{\partial\Lambda}\left\{\mathcal{H}_{\mathrm{N}}[n_{\mathrm{S}}(\omega_n;\Lambda)\omega_n;\mathbf{r}]\right\}_{\Lambda=0}\end{pmatrix}, \tag{A.10}$$

where the material parameters ε, μ, and n are meant to be evaluated at ω_n if no explicit frequency argument is given. To avoid confusion regarding the double meaning of n: throughout this thesis, n in the subscript or superscript is consistently used for the mode index, while the refractive index is represented in normal script.

We will now tackle each of the three terms $\delta\mathbb{X}_n$, $\delta\mathbb{Y}_n$, and $\delta\mathbb{Z}_n$ individually and bring them into particular shapes that shall be useful later. Let us start

with $\delta\mathbb{X}_n$. By comparing Eqs. (A.8) and (A.2), one finds that this term can be identified as a superposition of outgoing basis functions of the unperturbed surrounding:

$$\delta\mathbb{X}_n = \sum_{\mathrm{N}} \beta_{\mathrm{N}}^{(n)} \mathbb{O}_{\mathrm{N}}(\varepsilon, \mu, \omega_n), \tag{A.11}$$

with expansion coefficients $\beta_{\mathrm{N}}^{(n)}$. For later, it is actually not important how these expansion coefficients look like; however, for the sake of completeness, let us mention that they read as $\beta_{\mathrm{N}}^{(n)} = \partial/\partial\Lambda\{\dots\}_{\Lambda=0}/A_{\mathrm{N}}(\epsilon, \mu; \omega_n)$, where $\{\dots\}_{\Lambda=0}$ denotes the expression with the curly braces in Eq. (A.8), while A_{N} is the same as in Eq. (A.2).

Next, we examine $\delta\mathbb{Y}_{\mathrm{N}}$. By explicitly writing out the Λ derivatives and comparing the expression to Eq. (A.6), one can associate this term with the unperturbed resonant state multiplied by a simple matrix:

$$\delta\mathbb{Y}_n = \frac{1}{2}\begin{pmatrix} \delta\mu/\mu & 0 \\ 0 & \delta\varepsilon/\varepsilon \end{pmatrix} \mathbb{F}_n. \tag{A.12}$$

As for the other material parameters, $\delta\varepsilon$ and $\delta\mu$ without frequency argument are meant to be evaluated at ω_n.

Now, let us deal with $\delta\mathbb{Z}_{\mathrm{N}}$. By noting that $\mathcal{E}_{\mathrm{N}}$ and $\mathcal{H}_{\mathrm{N}}$ depend on the product $n_{\mathrm{S}}\omega_n$ and by applying the chain rule $\partial/\partial\Lambda = \partial\rho/\partial\Lambda \cdot \partial/\partial\rho$ with $\rho = n_{\mathrm{S}}\omega_n$, we get

$$\delta\mathbb{Z}_n = \sum_{\mathrm{N}} \alpha_{\mathrm{N}}^{(n)}(\omega_n; 0) A_{\mathrm{N}}(\varepsilon, \mu; \omega_n) \frac{n\omega}{2}\begin{pmatrix} \frac{\delta\varepsilon}{\varepsilon} + \frac{\delta\mu}{\mu} \end{pmatrix} \begin{pmatrix} \sqrt{\mu}\frac{\partial}{\partial x}\left\{\mathcal{E}_{\mathrm{N}}(\rho; \mathbf{r})\right\}_{\rho=n\omega_n} \\ i\sqrt{\varepsilon}\frac{\partial}{\partial x}\left\{\mathcal{H}_{\mathrm{N}}(\rho; \mathbf{r})\right\}_{\rho=n\omega_n} \end{pmatrix}. \tag{A.13}$$

EVALUATION OF $\mathbb{F}'_n$

In a similar way as it was done for $\delta\mathbb{F}_n$, let us now evaluate $\mathbb{F}'_n$. We recall that $\mathbb{F}'_n = \partial\mathbb{F}_n(\omega)/\partial\omega|_{\omega=\omega_n}$. Using Eq. (A.6) and applying the product rule gives

$$\mathbb{F}'_n = \mathbb{X}_n + \mathbb{Y}_n + \mathbb{Z}_n, \tag{A.14}$$

with

$$\mathbb{X}_n = \sum_{\mathrm{N}} \frac{\partial}{\partial\omega}\left\{\alpha_{\mathrm{N}}^{(n)}(\omega;0)A_{\mathrm{N}}[\varepsilon(\omega),\mu(\omega);\omega]\right\}_{\omega=\omega_n}\begin{pmatrix}\sqrt{\mu}\mathcal{E}_{\mathrm{N}}(n\omega_n;\mathbf{r})\\ i\sqrt{\varepsilon}\mathcal{H}_{\mathrm{N}}(n\omega_n;\mathbf{r})\end{pmatrix}, \tag{A.15}$$

$$\mathbb{Y}_n = \sum_{\mathrm{N}} \alpha_{\mathrm{N}}^{(n)}(\omega_n;0)A_{\mathrm{N}}(\varepsilon,\mu;\omega_n)\begin{pmatrix}\frac{\partial}{\partial\omega}\left\{\sqrt{\mu(\omega)}\right\}_{\omega=\omega_n}\mathcal{E}_{\mathrm{N}}(n\omega_n;\mathbf{r})\\ i\frac{\partial}{\partial\omega}\left\{\sqrt{\varepsilon(\omega)}\right\}_{\omega=\omega_n}\mathcal{H}_{\mathrm{N}}(n\omega_n;\mathbf{r})\end{pmatrix}, \tag{A.16}$$

$$\mathbb{Z}_n = \sum_{\mathrm{N}} \alpha_{\mathrm{N}}^{(n)}(\omega_n;0)A_{\mathrm{N}}(\varepsilon,\mu;\omega_n)\begin{pmatrix}\sqrt{\mu}\frac{\partial}{\partial\omega}\left\{\mathcal{E}_{\mathrm{N}}[n(\omega)\omega_n;\mathbf{r}]\right\}_{\omega=\omega_n}\\ i\sqrt{\varepsilon}\frac{\partial}{\partial\omega}\left\{\mathcal{H}_{\mathrm{N}}[n(\omega)\omega_n;\mathbf{r}]\right\}_{\omega=\omega_n}\end{pmatrix}. \tag{A.17}$$

We again examine the three terms individually. In analogy to $\delta\mathbb{X}_n$ from Eq. (A.11), we find that $\mathbb{X}_n$ can be identified as a superposition of outgoing basis functions of the unperturbed surrounding:

$$\mathbb{X}_n = \sum_{\mathrm{N}} \gamma_{\mathrm{N}}^{(n)}\mathrm{O}_{\mathrm{N}}(\varepsilon,\mu,\omega_n), \tag{A.18}$$

with $\gamma_{\mathrm{N}}^{(n)} = \partial/\partial\omega\{\dots\}_{\omega=\omega_n}/A_{\mathrm{N}}(\epsilon,\mu;\omega_n)$.

Similarly as for $\delta\mathbb{Y}_n$ from Eq. (A.12), we can reformulate

$$\mathbb{Y}_n = \frac{1}{2}\begin{pmatrix}\mu'/\mu & 0\\ 0 & \varepsilon'/\varepsilon\end{pmatrix}\mathbb{F}_n, \tag{A.19}$$

where the prime in $\delta\varepsilon'$ and $\delta\mu'$ denotes the derivative with respect to ω at ω_n.

Following an analogous procedure as the one that had been applied above to $\delta\mathbb{Z}_n$ when deducing Eq. (A.12), but now with the ω derivative instead of the Λ derivative, we get:

$$\mathbb{Z}_n = \sum_{\mathrm{N}} \alpha_{\mathrm{N}}^{(n)}(\omega_n;0)A_{\mathrm{N}}(\varepsilon,\mu;\omega_n)(n\omega)'\begin{pmatrix}\sqrt{\mu}\frac{\partial}{\partial x}\left\{\mathcal{E}_{\mathrm{N}}(\rho;\mathbf{r})\right\}_{\rho=n\omega_n}\\ i\sqrt{\varepsilon}\frac{\partial}{\partial x}\left\{\mathcal{H}_{\mathrm{N}}(\rho;\mathbf{r})\right\}_{\rho=n\omega_n}\end{pmatrix}, \tag{A.20}$$

where the prime in $(n\omega)'$ is again used to indicate the ω derivative at ω_n.

COMBINING THE RESULTS

Let us now combine the above results. Comparing Eqs. (A.13) and (A.20) gives

$$\delta\mathbb{Z}_n = \frac{\eta\omega_n}{2}\left(\frac{\delta\varepsilon}{\varepsilon}+\frac{\delta\mu}{\mu}\right)\mathbb{Z}_n, \tag{A.21}$$

where we have defined $\eta = n/(n\omega)'$ for reasons of compactness.

Plugging the above expression into Eq. (A.7) and replacing $\mathbb{Z}_n$ via Eq. (A.14) results in

$$\delta\mathbb{F}_n = \delta\mathbb{X}_n + \delta\mathbb{Y}_n + \frac{\eta\omega_n}{2}\left(\frac{\delta\varepsilon}{\varepsilon}+\frac{\delta\mu}{\mu}\right)\left(\mathbb{F}'_n - \mathbb{X}_n - \mathbb{Y}_n\right). \tag{A.22}$$

Inserting this $\delta\mathbb{F}_n$ into δS_n from Eq. (A.1) provides

$$\delta S_n = \delta S_n|_{\delta\mathbb{X}_n} + \delta S_n|_{\delta\mathbb{Y}_n} + \frac{\eta\omega_n}{2}\left(\frac{\delta\varepsilon}{\varepsilon}+\frac{\delta\mu}{\mu}\right)\left(\delta S_n|_{\mathbb{F}'_n} - \delta S_n|_{\mathbb{X}_n} - \delta S_n|_{\mathbb{Y}_n}\right), \tag{A.23}$$

where $\delta S_n|_{\mathbb{F}}$ is used to symbolically represent the overlap integral on the right side of Eq. (A.1), but with $\delta\mathbb{F}_n$ replaced by the quantity $\mathbb{F}$.

It turns out that $\delta S_n|_{\delta\mathbb{X}_n} = \delta S_n|_{\mathbb{X}_n} = 0$. This becomes obvious when writing $\delta\mathbb{X}_n$ and $\mathbb{X}_n$ as a superposition of $\mathbb{O}_{\mathrm{N}}(\varepsilon,\mu,\omega_n)$ via Eqs. (A.11) and (A.18), respectively, expressing $\mathbb{F}_n^{\ddagger}$ as a superposition of $\mathbb{O}_{\mathrm{N}}^{\ddagger}(\varepsilon,\mu,\omega_n)$ via the transposed version of Eq. (A.6), and applying the orthogonality condition from Eq. (2.63). We also note that $\delta S_n|_{\mathbb{F}'_n} = S_n$, where S_n is the surface term of the analytical normalization, defined in Eq. (2.34). Finally, we express $\delta\mathbb{Y}_n$ and $\mathbb{Y}_n$ via Eqs. (A.12) and (A.19), respectively, explicitly write out the integrals $\delta S_n|_{\delta\mathbb{Y}_n}$ and $\delta S_n|_{\mathbb{Y}_n}$, and use $\oint_{\partial V} d\mathbf{S}\cdot(\mathbf{E}_n^{\ddagger}\times\mathbf{H}_n) = \oint_{\partial V} d\mathbf{S}\cdot(\mathbf{E}_n\times\mathbf{H}_n^{\ddagger})$ [this follows from Eq. (2.24)] to simplify the result. Altogether, we end up with:

$$\delta S_n = \frac{\eta\omega_n}{2}\left(\frac{\delta\varepsilon}{\varepsilon}+\frac{\delta\mu}{\mu}\right)S_n + \frac{i\eta\beta c}{2}\oint_{\partial V} d\mathrm{S}\cdot(\mathbf{E}_n^{\ddagger}\times\mathbf{H}_n), \tag{A.24}$$

where we have introduced the abbreviation $\beta = \left[(\omega\mu)'\delta\varepsilon - (\omega\varepsilon)'\delta\mu\right]/\varepsilon\mu$.

B

DETAILS ABOUT THE VISUALIZATIONS

Here, we provide details on how the three-dimensional visualizations from Figs. 4.4, 5.3 and 5.6 were created.

The fields and the "shift per volume" densities were displayed on selectively chosen slices through the antennas. The slice plots were generated from simulation data and then incorporated into a three-dimensional model of the structure, which had been created with the open-source graphics suite Blender[1] . The transparency (i.e., the alpha channel of the RGBA color space that is used here) of each slice plot is proportional to the magnitude of the displayed value. The slice positions were selected such that all relevant features are visible: For the field plot of the rod antenna, the slices are at half of the antenna's width and height; for the corresponding "shift per volume" plot, they are at one quarter and three quarters of the antenna's width and height; for the plots of the Ω antenna, they are at half the Ω's width and length.

1 See https://www.blender.org.

C

DETAILS ABOUT THE CHIRAL-SENSING EXAMPLES

C.1 ADDITIONAL FIGURES

This section contains additional figures, supporting the claims in Chapter 5.

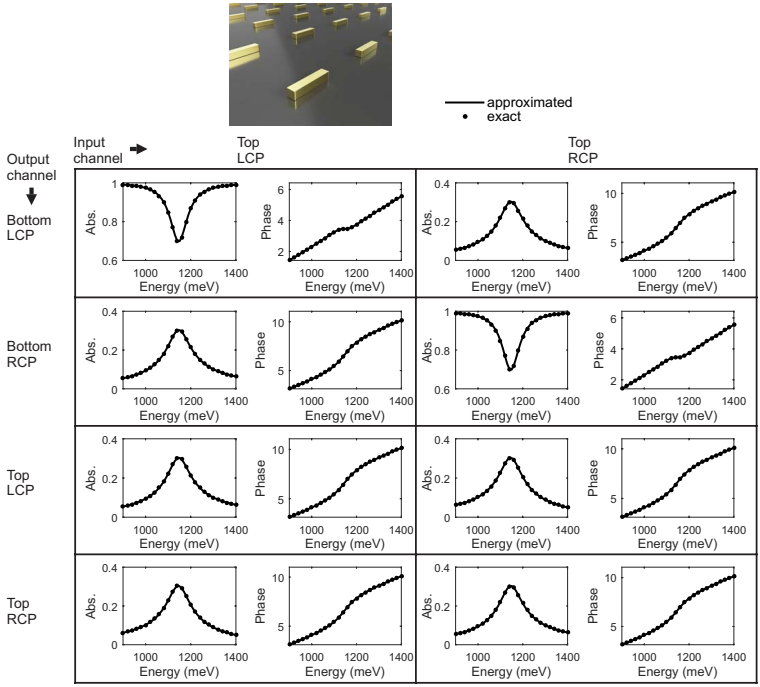

Figure C.1. Unperturbed elements of the scattering matrix S_{MN} of the rod antennas. Each element is represented by its absolute value and its phase. For comparison, we plot both the approximation via the resonant state theory [i.e., Eq. 2.76] and the results of exact full-wave calculations. We consider two input channels: A left-handed circularly polarized (LCP) plane wave and a right-handed circularly polarized (RCP) plane wave, which impinge from the top onto the periodic array of antennas. The propagation angle is normal to the plane of periodicity. This scenario reflects the typical experimental situation. As output channels, we consider left- and right-handed circularly polarized plane waves that leave the system in top and bottom direction, again with a normal propagation angle. One might wonder why the periodic system has only four output channels to the far field. This comes from the fact that the system is operated in an energy range below the opening of the first diffraction orders. At higher energies, the opening of diffraction orders will provide additional energy-carrying output channels, which correspond to plane waves that leave the system under discrete oblique propagation angles [45].

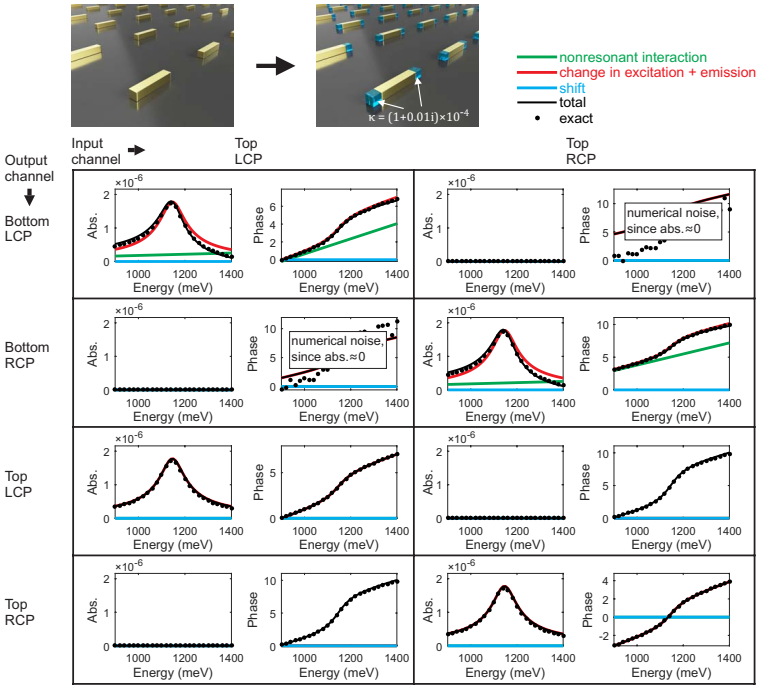

FIGURE C.2. Change of the scattering-matrix elements δS_{MN} of the rod antennas with top incidence due to chiral media patches at each end. As in Fig. 5.2(b), the lines depict the results of our perturbation theory (total signal, as well as the separation into individual contributions), while the dots have been obtained from exact full-wave calculations. Note that the (1,2) and the (2,1) matrix components have an absolute value close to zero and hence their phase term is governed by numerical noise. As it can be seen, the shift contribution is zero in all components.

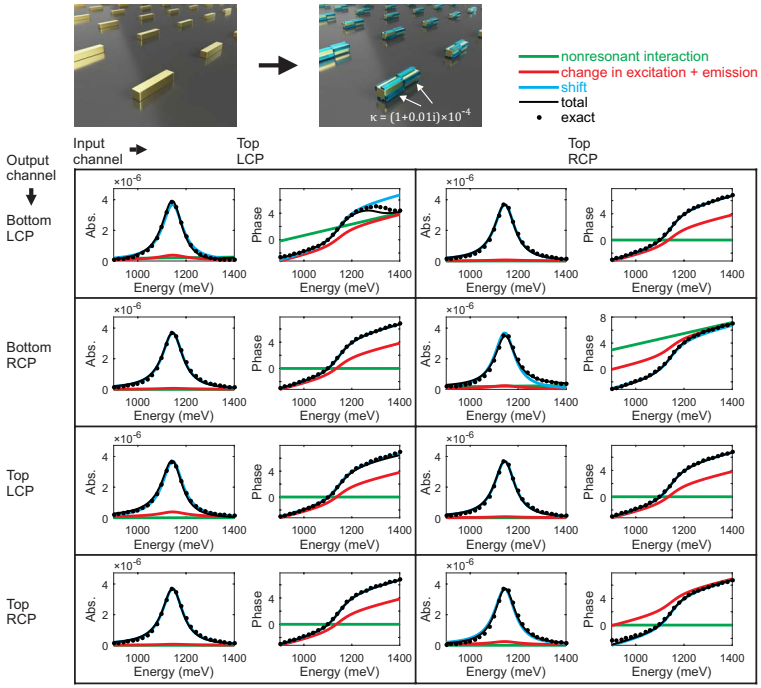

Figure C.3. Change of the scattering-matrix elements δS_{MN} of the rod antennas with top incidence due to chiral media patches distributed over chiral hotspots. In order to enforce a resonance shift in the rod antennas, we take the chiral medium from the end of the antennas [cf. Fig 5.3(b) and Fig. C.2] and redistribute it over the regions with positive "shift per volume" values [red spots in Fig. 5.3(b)]. As it can be seen, this configuration results in a nonzero shift contribution in all matrix elements.

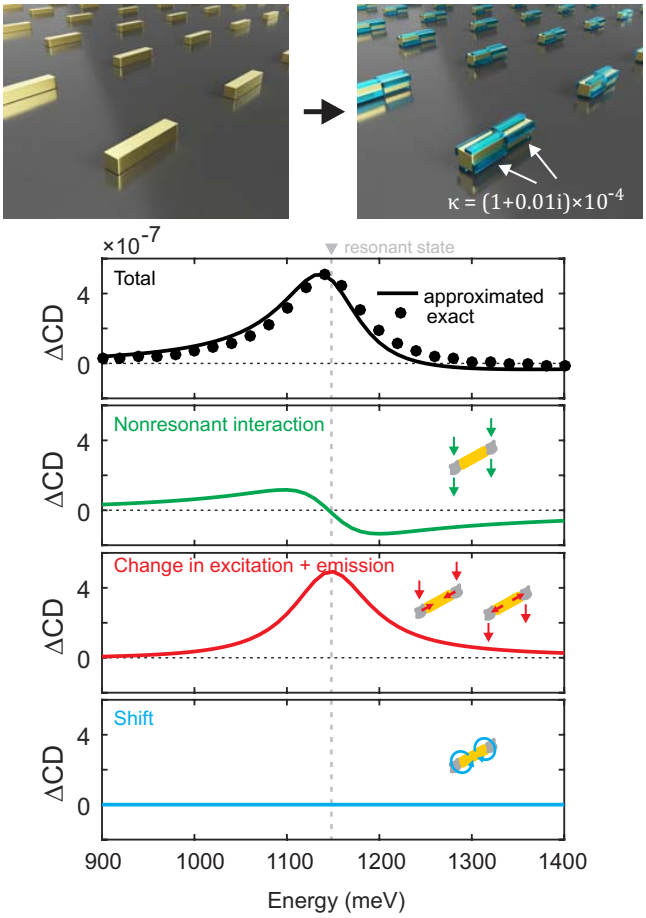

FIGURE C.4. Optical ΔCD response of the rod antennas with top incidence in the case that the chiral medium is distributed over chiral hotspots. Remarkably, although all matrix elements in Fig. C.3 exhibit a nonzero shift contribution, the shift contribution in the ΔCD spectrum remains zero. At first glance this might seem surprising; however, it can be understood by noting that the shift contributions in the matrix are symmetric such that they affect left-handed and right-handed circularly polarized input the same way and hence cancel out each other in the ΔCD signal.

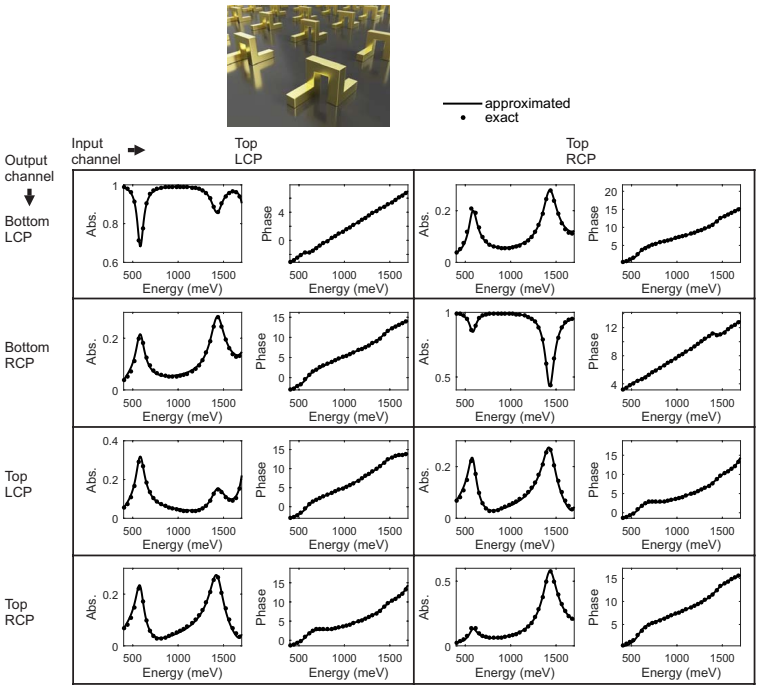

Figure C.5. Unperturbed scattering-matrix elements S_{MN} of the Ω antennas with top incidence.

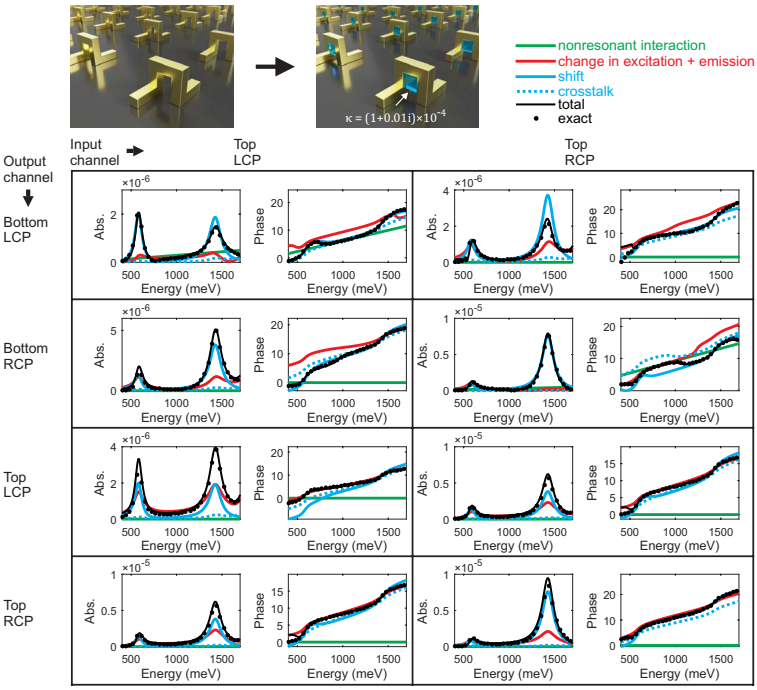

FIGURE C.6. Change of the scattering-matrix elements δS_{MN} of the Ω antennas with top incidence due to chiral media patches in their centers.

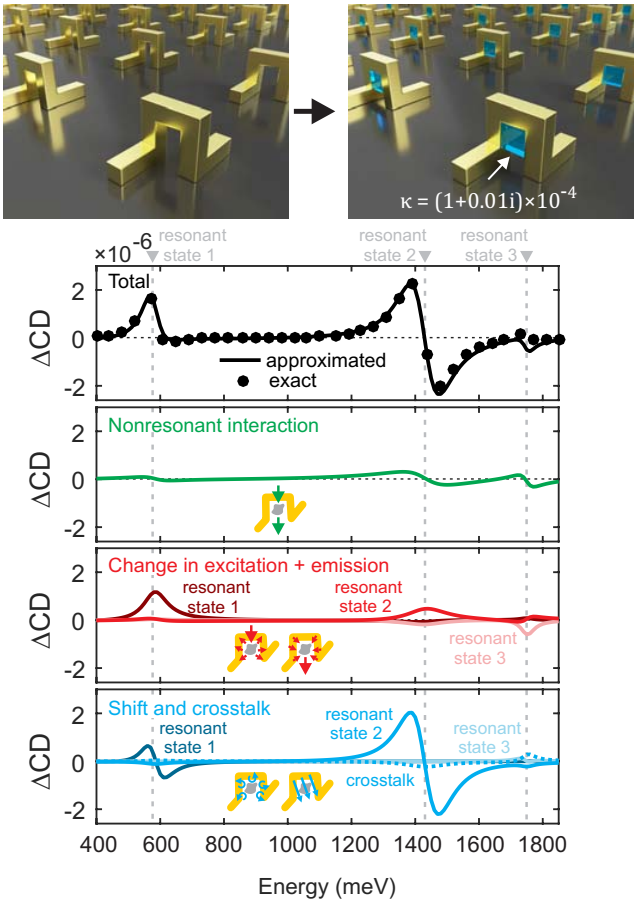

Figure C.7. Results from Fig 5.8, but with the energy range on the x axis extended such that resonant state 3 is visible. Note, however, that for high photon energies, the prediction of the perturbation theory is not so accurate when considering only these three resonant states, since the spectrum is influenced by the nearby Rayleigh anomaly [99] at 1864.4 meV [given as $hc/(n_{\text{water}}P)$, where h is the Planck constant, n_{water} is the surrounding refractive index, and P is the period of the antenna array], which effectively acts as an ensemble of additional resonant states [89, 229].

C.2 CALCULATION OF ΔCD FROM THE SCATTERING MATRICES

This section provides the details on how the ΔCD signal and its contributions were calculated from the scattering matrices $S_{\mathbf{MN}}$ and $\delta S_{\mathbf{MN}}$. The ΔCD signal was defined as

$$\Delta\mathrm{CD} = \mathrm{CD}_\kappa - \mathrm{CD}_0, \tag{C.1}$$

where CD_κ and CD_0 represent the circular dichroism signals of the resonator with and without κ, respectively. The circular dichroism signals were defined as the absorption difference between left-handed circularly polarized (LCP) and right-handed circularly polarized (RCP) polarized light. The incidence direction was taken from the top. Under this definition, the circular dichroism signals are related to the scattering matrices via

$$\mathrm{CD}_0 = \underbrace{\left(1 - \sum_{\mathbf{M}} \left|S_{\mathbf{M},\mathrm{LCP\ top}}\right|^2\right)}_{\text{Absorption for LCP top input}} - \underbrace{\left(1 - \sum_{\mathbf{M}} \left|S_{\mathbf{M},\mathrm{RCP\ top}}\right|^2\right)}_{\text{Absorption for RCP top input}} \tag{C.2}$$

and

$$\mathrm{CD}_\kappa = \underbrace{\left(1 - \sum_{\mathbf{M}} \left|S_{\mathbf{M},\mathrm{LCP\ top}} + \delta S_{\mathbf{M},\mathrm{LCP\ top}}\right|^2\right)}_{\text{Absorption for LCP top input}} - \underbrace{\left(1 - \sum_{\mathbf{M}} \left|S_{\mathbf{M},\mathrm{RCP\ top}} + \delta S_{\mathbf{M},\mathrm{RCP\ top}}\right|^2\right)}_{\text{Absorption for RCP top input}}, \tag{C.3}$$

where the sum goes over all energy-carrying output channels **M**. The contributions of the ΔCD signal were defined as

$$\Delta\mathrm{CD}_\mathrm{x} = \Delta\mathrm{CD}\big|_{\delta S_{\mathbf{MN}} = \delta S^\mathrm{x}_{\mathbf{MN}}}, \tag{C.4}$$

where x = {nr, ex, em, shift, cross}.

In the end, let us consider the case $|\delta S_{\mathbf{MN}}| \ll |S_{\mathbf{MN}}|$. With very few exceptions, this condition is automatically fulfilled in scenarios, where the first-order perturbation theory is applicable. In particular, this condition holds for all example systems discussed in this work. Under the above assumption, Eqs. (C.1) to (C.4) simplify to more intuitive expressions:

$$\Delta\mathrm{CD} \approx \sum_{\mathbf{M}} 2\,\mathrm{Re}\left(S^*_{\mathbf{M},\mathrm{RCP\ top}} \delta S_{\mathbf{M},\mathrm{RCP\ top}}\right) - \sum_{\mathbf{M}} 2\,\mathrm{Re}\left(S^*_{\mathbf{M},\mathrm{LCP\ top}} \delta S_{\mathbf{M},\mathrm{LCP\ top}}\right), \tag{C.5}$$

$$\Delta \mathrm{CD}_{\mathrm{x}} \approx \sum_{\mathbf{M}} 2\,\mathrm{Re}\left(S^{*}_{\mathbf{M},\mathrm{RCP\ top}}\delta S^{\mathrm{x}}_{\mathbf{M},\mathrm{RCP\ top}}\right) - \sum_{\mathbf{M}} 2\,\mathrm{Re}\left(S^{*}_{\mathbf{M},\mathrm{LCP\ top}}\delta S^{\mathrm{x}}_{\mathbf{M},\mathrm{LCP\ top}}\right). \tag{C.6}$$

D

DYE POSITIONS IN THE DNA SLIDER SYSTEM

In the following, we provide details about the dye positions that were assumed in the calculations for the DNA slider from Fig. 6.16.

As shown in Fig. 6.15, the DNA slider consists of two parallel DNA origami filaments with a distance of 12 nm. Based on this value and the geometry of the structure in state '0', we assume that the dyes are bound to single stranded DNA with a length of 6 nm. The location at which the single DNA strands are attached to the DNA origami filaments is explained in Fig. 6.15. Since those single DNA strands are highly flexible, there is an uncertainty of the dye position. The single stranded DNA has a length of 26 nucleotides. In order to keep the model simple, it is assumed that the strands are standing perpendicular to the origami filaments. This configuration will be henceforth referred to as unbound state.

When the two dyes come close to each other, the DNA strands can stick together via a transient binding and form a bound state. In this transient binding, the expected distance of the two strands is about 2 nm. However; since the dyes do actually not sit directly at the end of the single DNA strands, but are connected to them by linkers of estimated length 2 nm, there is an additional source for position uncertainty. It was assumed that the effective distance between the donor and the acceptor in the bound state is about 5 nm.

As shown in Fig. 6.16(a), the DNA slider has five different sliding states. Figure D.1 depicts the dye positions that were used in the simulation to represent the individual sliding states. In order to quantitatively describe the positions, a coordinate system is depicted, with the origin corresponding to the center of the nanoparticle (diameter 10 nm). The coordinates can be found in Table D.1, together with the corresponding distance between

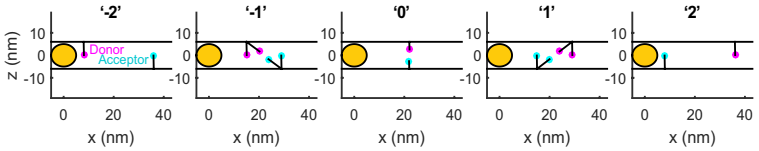

Figure D.1. Dye positions during the individual sliding states. There are two parallel DNA origami filaments with a distance of 12 nm. The dyes are connected to the filaments by single DNA strands of length 6 nm. The dye positions that are used in the calculation are drawn into a coordinate system with the origin being chosen as the center of the nanoparticle. The coordinates can be found in Table D.1. The '−2' and '2' sliding states were described with the DNA strands standing perpendicular to the filaments. This configuration is referred to as unbound state. For the '0' sliding states, it was assumed that the dyes form a bound state with a distance of 5 nm between the donor and the acceptor, due to a transient binding of the single DNA strands. The '−1' and '1' sliding state were modeled as a 50%:50% distribution of dye pairs in a bound state and dye pairs in an unbound state.

the dye and the nanoparticle (labeled as Dye-NP) and the corresponding distance between the two dyes (labeled as D-A).

In the '−2' and '2' sliding states, the dyes are very far apart, so they cannot form a bound state. Hence, those sliding states were modeled as an unbound state with the dyes standing perpendicular to the origami filaments. In the '0' sliding state, the dyes are very close to each other and a transient binding is highly likely. Hence, this sliding state was modeled as a bound state with a distance of 5 nm, as explained above. The '−1' and '1' sliding states are slightly more complicated: Due to the intermediate distance, it is expected to be possible that the dyes can be in a bound state as well as in an unbound state. Note that in the '−1' and '1' state, the sliding displacement is 14 nm and geometrical considerations would hence suggest that the single DNA strands with expected length of 6 nm are not long enough to form a bound state. However, it is known that the single DNA strands are stretchable and can in fact be longer than 6 nm. In the simulation, we found, that neither the assumption that all dyes are in an unbound state, nor the assumption that all dyes are in a bound state can explain the experimental results. For an unbound state, with the DNA strands standing perpendicular to the filaments, the distance between the donor and the acceptor is 14 nm, which is much larger than the Förster radius. In this case, the calculated acceptor intensity is close to zero. For a bound state, the calculation yields an acceptor intensity that is comparable to the one in the '0' sliding state (only slightly

altered by the different quenching of donor and acceptor compared to the '0' sliding state). In the experiment, the acceptor intensity in the '−1' and '1' sliding states is in between the one from the '0' and the one from the -2' and '2' sliding states. For this reason, it was concluded that there is a combination of dye pairs in a bound state and dye pairs in an unbound state. Since no exact ratio is known, it was assumed that both states are equally likely (50%:50% distribution).

Table D.1. Dye positions as drawn in Fig. D.1. For each sliding state, the table lists the sliding displacement (displ.), the coordinates of donor and acceptor, the distance of the individual dye to the surface of the nanoparticle (labeled as Dye-NP) and the distance between the donor and the acceptor (labeled as A-D). All distances are given in nm. The '−1' and '1' sliding states are special in a sense that for them, it is assumed that there is a 50%:50% distribution of two different dye configurations.

State	Displ.		Donor			Acceptor			D-A
			x	z	Dye-NP	x	z	Dye-NP	
-2	**-28**		-2.0	0.0	8.0	26.0	0.0	36.0	28.0
-1	**-14**	50%	5.0	0.0	15.0	19.0	0.0	29.0	14.0
		50%	10.1	1.6	20.2	13.9	-1.6	24.0	5.0
0	**0**		12.0	2.5	22.1	12.0	-2.5	22.1	5.0
1	**14**	50%	19.0	0.0	29.0	5.0	0.0	15.0	14.0
		50%	13.9	1.6	24.0	10.1	-1.6	20.2	5.0
2	**28**		26.0	0.0	36.0	-2.0	0.0	8.0	28.0

BIBLIOGRAPHY

[1] B. Kuswandi, Nuriman, J. Huskens, and W. Verboom: *Optical sensing systems for microfluidic devices: A review.* Analytica Chimica Acta **601**, 141–155 (2007),
Cit. on p. 1.

[2] S. M. Borisov and O. S. Wolfbeis: *Optical Biosensors.* Chemical Reviews **108**, 423–461 (2008),
Cit. on p. 1.

[3] J. Hodgkinson and R. P. Tatam: *Optical gas sensing: a review.* Measurement Science and Technology **24**, 012004 (2012),
Cit. on p. 1.

[4] M. A. Butler: *Fiber Optic Sensor for Hydrogen Concentrations near the Explosive Limit.* Journal of The Electrochemical Society **138**, L46–L47 (1991),
Cit. on p. 1.

[5] H. Altug, S.-H. Oh, S. A. Maier, and J. Homola: *Advances and applications of nanophotonic biosensors.* Nature Nanotechnology **17**, 5–16 (2022),
Cit. on pp. 1, 3, 159.

[6] M. Mesch, B. Metzger, M. Hentschel, and H. Giessen: *Nonlinear Plasmonic Sensing.* Nano Letters **16**, 3155–3159 (2016),
Cit. on p. 2.

[7] W. D. Wilson: *Analyzing biomolecular interactions.* Science **295**, 2103–2105 (2002),
Cit. on pp. 3, 66, 89, 92.

[8] D. Dorfner, T. Zabel, T. Hürlimann, N. Hauke, L. Frandsen, U. Rant, G. Abstreiter, and J. Finley: *Photonic crystal nanostructures for optical biosensing applications.* Biosensors and Bioelectronics **24**, 3688–3692 (2009),
Cit. on p. 3.

[9] N. Liu, T. Weiss, M. Mesch, L. Langguth, U. Eigenthaler, M. Hirscher, C. Sönnichsen, and H. Giessen: *Planar metamaterial analogue of electromagnetically induced transparency for plasmonic sensing.* Nano Lett. **10**, 1103–1107 (2010),
Cit. on pp. 3, 46, 92.

[10] N. Liu, M. Mesch, T. Weiss, M. Hentschel, and H. Giessen: *Infrared perfect absorber and its application as plasmonic sensor.* Nano Lett. **10**, 2342–2348 (2010),
Cit. on pp. 3, 92.

[11] S. Arnold, M. Khoshsima, I. Teraoka, S. Holler, and F. Vollmer: *Shift of whispering-gallery modes in microspheres by protein adsorption.* Opt. Lett. **28**, 272–274 (2003),
Cit. on pp. 3, 6, 7, 66, 89, 92.

[12] C. Rosman, J. Prasad, A. Neiser, A. Henkel, J. Edgar, and C. Sönnichsen: *Multiplexed Plasmon Sensor for Rapid Label-Free Analyte Detection.* Nano Letters **13**, 3243–3247 (2013),
Cit. on pp. 3, 92.

[13] A. E. Cetin, A. F. Coskun, B. C. Galarreta, M. Huang, D. Herman, A. Ozcan, and H. Altug: *Handheld high-throughput plasmonic biosensor using computational on-chip imaging.* Light: Science & Applications **3**, e122 (2014),
Cit. on pp. 3, 66, 89, 92.

[14] Y. nan Zhang, Y. Zhao, and R. qing Lv: *A review for optical sensors based on photonic crystal cavities.* Sensors and Actuators A: Physical **233**, 374–389 (2015),
Cit. on p. 3.

[15] N. Bontempi, K. E. Chong, H. W. Orton, I. Staude, D.-Y. Choi, I. Alessandri, Y. S. Kivshar, and D. N. Neshev: *Highly sensitive biosensors based on all-dielectric nanoresonators.* Nanoscale **9**, 4972–4980 (2017),
Cit. on p. 3.

[16] O. Yavas, M. Svedendahl, P. Dobosz, V. Sanz, and R. Quidant: *On-a-chip Biosensing Based on All-Dielectric Nanoresonators.* Nano Letters **17**, 4421–4426 (2017),
Cit. on p. 3.

[17] R. Semenyshyn, M. Hentschel, C. Stanglmair, T. Teutsch, C. Tarin, C. Pacholski, H. Giessen, and F. Neubrech: *In Vitro Monitoring Conformational Changes of Polypeptide Monolayers Using Infrared Plasmonic Nanoantennas.* Nano Letters **19**, 1–7 (2019),
Cit. on pp. 3, 92, 159.

[18] L. K, R. Semenyshyn, M. Hentschel, F. Neubrech, C. Tarín, and H. Giessen: *Vibrational Sensing Using Infrared Nanoantennas: Toward the Noninvasive Quantitation of Physiological Levels of Glucose and Fructose.* ACS Sensors **4**, 1973–1979 (2019),
Cit. on pp. 3, 159.

[19] M. L. Tseng, Y. Jahani, A. Leitis, and H. Altug: *Dielectric Metasurfaces Enabling Advanced Optical Biosensors.* ACS Photonics **8**, 47–60 (2021),
Cit. on p. 3.

[20] A. Tittl, P. Mai, R. Taubert, D. Dregely, N. Liu, and H. Giessen: *Palladium-Based Plasmonic Perfect Absorber in the Visible Wavelength Range and Its Application to Hydrogen Sensing*. Nano Letters **11**, 4366–4369 (2011),
Cit. on p. 3.

[21] T. Pohl, F. Sterl, N. Strohfeldt, and H. Giessen: *Optical Carbon Dioxide Detection in the Visible Down to the Single Digit ppm Range Using Plasmonic Perfect Absorbers*. ACS Sensors **5**, 2628–2635 (2020),
Cit. on pp. 3, 92.

[22] E. Herkert, F. Sterl, N. Strohfeldt, R. Walter, and H. Giessen: *Low-Cost Hydrogen Sensor in the ppm Range with Purely Optical Readout*. ACS Sensors **5**, 978–983 (2020),
Cit. on p. 3.

[23] B. Gallinet, T. Siegfried, H. Sigg, P. Nordlander, and O. J. F. Martin: *Plasmonic radiance: Probing structure at the Angstrom scale with visible light*. Nano Lett. **12**, 497–503 (2013),
Cit. on pp. 3, 92.

[24] J. Prasad, I. Zins, R. Branscheid, J. Becker, A. H. R. Koch, G. Fytas, U. Kolb, and C. Sönnichsen: *Plasmonic core satellite assemblies as highly sensitive refractive index sensors*. J. Phys. Chem. C **119**, 5577–5582 (2015),
Cit. on pp. 3, 92.

[25] M. Mesch, T. Weiss, M. Schäferling, M. Hentschel, R. S. Hegde, and H. Giessen: *Highly sensitive refractive index sensors with plasmonic nanoantennas–utilization of optimal spectral detuning of Fano resonances*. ACS Sensors **3**, 960–966 (2018),
Cit. on pp. 3, 10, 46, 50–53, 66, 67, 89, 92.

[26] E. Hendry, T. Carpy, J. Johnston, M. Popland, R. V. Mikhaylovskiy, A. J. Lapthorn, S. M. Kelly, L. D. Barron, N. Gadegaard, and M. Kadodwala: *Ultrasensitive detection and characterization of biomolecules using superchiral fields*. Nature Nanotech. **5**, 783–787 (2010),
Cit. on pp. 3, 92, 94, 99, 102.

[27] B. M. Maoz, Y. Chaikin, A. B. Tesler, O. Bar Elli, Z. Fan, A. O. Govorov, and G. Markovich: *Amplification of Chiroptical Activity of Chiral Biomolecules by Surface Plasmons*. Nano Letters **13**, 1203–1209 (2013),
Cit. on pp. 3, 92.

[28] J. García-Guirado, M. Svedendahl, J. Puigdollers, and R. Quidant: *Enantiomer-Selective Molecular Sensing Using Racemic Nanoplasmonic Arrays*. Nano Letters **18**, 6279–6285 (2018),
Cit. on pp. 3, 92, 93, 109.

[29] J. García-Guirado, M. Svedendahl, J. Puigdollers, and R. Quidant: *Enhanced Chiral Sensing with Dielectric Nanoresonators*. Nano Letters **20**, 585–591 (2020),
Cit. on pp. 3, 92–94, 97, 109.

[30] S. Yoo and Q.-H. Park: *Metamaterials and chiral sensing: a review of fundamentals and applications.* Nanophotonics **8**, 249 –261 (2019),
Cit. on pp. 3, 92, 94.

[31] F. Vollmer and S. Arnold: *Whispering-gallery-mode biosensing: Labelfree detection down to single molecules.* Nat. Meth. **5**, 591–596 (2008),
Cit. on pp. 3, 6.

[32] J. Wiersig: *Enhancing the sensitivity of frequency and energy splitting detection by using exceptional points: Application to microcavity sensors for single-particle detection.* Phys. Rev. Lett. **112**, 203901 (2014),
Cit. on pp. 3, 6, 9.

[33] N. Toropov, G. Cabello, M. P. Serrano, R. R. Gutha, M. Rafti, and F. Vollmer: *Review of biosensing with whispering-gallery mode lasers.* Light Sci. Appl. **10**, 42 (2021),
Cit. on pp. 3, 6.

[34] D. Rodrigo, O. Limaj, D. Janner, D. Etezadi, F. J. G. de Abajo, V. Pruneri, and H. Altug: *Mid-infrared plasmonic biosensing with graphene.* Science **349**, 165–168 (2015),
Cit. on p. 3.

[35] E. A. Muljarov, W. Langbein, and R. Zimmermann: *Brillouin-Wigner perturbation theory in open electromagnetic systems.* Europhys. Lett. **92**, 50010 (2010),
Cit. on pp. 3, 6, 9, 10, 18, 27–29, 46–48, 54.

[36] C. Sauvan, J. P. Hugonin, I. S. Maksymov, and P. Lalanne: *Theory of the spontaneous optical emission of nanosize photonic and plasmon resonators.* Phys. Rev. Lett. **110**, 237401 (2013),
Cit. on pp. 3, 6, 9, 24, 25, 31, 35, 54–57, 120.

[37] E. A. Muljarov and T. Weiss: *Resonant-state expansion for open optical systems: Generalization to magnetic, chiral, and bi-anisotropic materials.* Opt. Lett. **43**, 1978–1981 (2018),
Cit. on pp. 3, 6, 9, 10, 12, 18, 19, 22, 25, 27–29, 47, 61.

[38] P. Lalanne, W. Yan, K. Vynck, C. Sauvan, and J. Hugonin: *Light Interaction with Photonic and Plasmonic Resonances.* Laser Photonics Rev. **12**, 1700113 (2018),
Cit. on pp. 3, 6, 9, 13, 17, 21, 24, 30–32, 35, 36, 54, 55, 61.

[39] P. T. Kristensen, K. Herrmann, F. Intravaia, and K. Busch: *Modelling electromagnetic resonators using quasinormal modes.* Adv. Opt. Photonics **12**, 612–708 (2020),
Cit. on pp. 3, 6, 9, 10, 13, 16, 20, 35, 56, 60.

[40] P. T. Kristensen and S. Hughes: *Modes and mode volumes of leaky optical cavities and plasmonic nanoresonators.* ACS Photonics **1**, 2–10 (2014),
Cit. on pp. 3, 54, 56, 57.

[41] E. A. Muljarov and W. Langbein: *Exact mode volume and Purcell factor of open optical systems*. Phys. Rev. B **94**, 235438 (2016),
Cit. on pp. 3, 9, 22, 27–29, 31, 53, 54, 56.

[42] L. Zschiedrich, F. Binkowski, N. Nikolay, O. Benson, G. Kewes, and S. Burger: *Riesz-projection-based theory of light-matter interaction in dispersive nanoresonators*. Phys. Rev. A **98**, 043806 (2018),
Cit. on pp. 3, 44.

[43] F. Alpeggiani, N. Parappurath, E. Verhagen, and L. Kuipers: *Quasinormal-mode expansion of the scattering matrix*. Phys. Rev. X **7**, 021035 (2017),
Cit. on pp. 3, 37, 44.

[44] S. V. Lobanov, W. Langbein, and E. A. Muljarov: *Resonant-state expansion of three-dimensional open optical systems: Light scattering*. Phys. Rev. A **98**, 033820 (2018),
Cit. on pp. 3, 37, 43.

[45] T. Weiss and E. A. Muljarov: *How to calculate the pole expansion of the optical scattering matrix from the resonant states*. Phys. Rev. B **98**, 085433 (2018),
Cit. on pp. 3, 10, 14, 15, 19, 20, 27, 31, 32, 37–45, 71, 161, 170.

[46] S. Upendar, I. Allayarov, M. A. Schmidt, and T. Weiss: *Analytical mode normalization and resonant state expansion for bound and leaky modes in optical fibers – an efficient tool to model transverse disorder*. Opt. Express **26**, 22536–22546 (2018),
Cit. on pp. 3, 9, 19, 60, 61.

[47] S. Upendar, M. A. Schmidt, and T. Weiss: *What optical fiber modes reveal: Group velocity and effective index for external perturbations*. J. Opt. Soc. Am. B **38**, 1097–1103 (2021),
Cit. on pp. 3, 19, 78.

[48] M. B. Doost, W. Langbein, and E. A. Muljarov: *Resonant-state expansion applied to planar open optical systems*. Phys. Rev. A **85**, 023835 (2012),
Cit. on pp. 3, 48.

[49] M. B. Doost, W. Langbein, and E. A. Muljarov: *Resonant state expansion applied to two-dimensional open optical systems*. Phys. Rev. A **87**, 043827 (2013),
Cit. on pp. 3, 9, 36, 48.

[50] M. B. Doost, W. Langbein, and E. A. Muljarov: *Resonant-state expansion applied to three-dimensional open optical systems*. Phys. Rev. A **90**, 013834 (2014),
Cit. on pp. 3, 9, 29, 30, 48, 50, 54, 66, 67, 72.

[51] J. Yang, H. Giessen, and P. Lalanne: *Simple analytical expression for the peak-frequency shifts of plasmonic resonances for sensing*. Nano Lett. **15**, 3439–3444 (2015),
Cit. on pp. 3, 10, 50, 51, 57, 66, 67, 89.

[52] T. Weiss, M. Mesch, M. Schäferling, H. Giessen, W. Langbein, and E. A. Muljarov: *From dark to bright: First-order perturbation theory with analytical mode normalization for plasmonic nanoantenna arrays applied to refractive index sensing*. Phys. Rev. Lett. **116**, 237401 (2016),
Cit. on pp. 3, 9, 10, 20, 27–29, 50–52, 66, 67, 74, 76, 89.

[53] W. H. Louisell: *Analysis of the single tapered mode coupler*. The Bell System Technical Journal **34**, 853–870 (1955),
Cit. on p. 6.

[54] J. S. Maybee: *Normal and quasi-normal modes in damped linear dynamic systems*. J. Appl. Mech. **33**, 413–416 (1966),
Cit. on p. 6.

[55] K. S. Thorne and A. Campolattaro: *Nonradial pulsation of general-relativistic stellar models. I. Analytic analysis for $l \geq 2*$*. Ap. J. **149**, 591 (1967),
Cit. on p. 6.

[56] J. Humblet and L. Rosenfeld: *Theory of nuclear reactions: I. Resonant states and collision matrix*. Nuclear Physics **26**, 529–578 (1961),
Cit. on p. 6.

[57] W. L. Barnes, A. Dereux, and T. W. Ebbesen: *Surface plasmon subwavelength optics*. Nature **424**, 824–830 (2003),
Cit. on p. 7.

[58] M. I. Stockman, S. V. Faleev, and D. J. Bergman: *Localization versus delocalization of surface plasmons in nanosystems: Can one state have both characteristics?* Phys. Rev. Lett. **87**, 167401–1–14 (2001a),
Cit. on p. 7.

[59] V. Podolskiy, A. Sarychev, and V. Shalaev: *Plasmon modes and negative refraction in metal nanowire composites*. Opt. Express **11**, 735–745 (2003),
Cit. on p. 7.

[60] P. Nordlander, C. Oubre, E. Prodan, K. Li, and M. I. Stockman: *Plasmon hybridization in nanoparticle dimers*. Nano Lett. **4**, 899–903 (2004),
Cit. on p. 7.

[61] W. A. Murray and W. L. Barnes: *Plasmonic materials*. Advanced Materials **19**, 3771–3782 (2007),
Cit. on p. 7.

[62] J. M. McMahon, J. Henzie, T. W. Odom, G. C. Schatz, and S. K. Gray: *Tailoring the sensing capabilities of nanohole arrays in gold films with Rayleigh anomaly-surface plasmon polaritons*. Opt. Express **15**, 18119–18129 (2007),
Cit. on pp. 7, 9.

[63] K. M. Mayer and J. H. Hafner: *Localized surface plasmon resonance sensors*. Chem. Rev. **111**, 3828–3857 (2011),
Cit. on p. 7.

[64] M. L. Juan, M. Righini, and R. Quidant: *Plasmon nano-optical tweezers*. Nat. Phys. **5**, 349–356 (2011),
Cit. on p. 7.

[65] I. Staude, A. E. Miroshnichenko, M. Decker, N. T. Fofang, L. Sheng, E. Gonzales, J. Dominguez, T. S. Luk, D. N. Neshev, I. Brener, and Y. Kivshar: *Tailoring directional scattering through magnetic and electric resonances in subwavelength silicon nanodisks*. ACS Nano **7**, 7824–7832 (2013),
Cit. on p. 7.

[66] J. Eismann, M. Neugebauer, and P. Banzer: *Exciting a chiral dipole moment in an achiral nanostructure*. Optica **5**, 954–959 (2018),
Cit. on p. 7.

[67] D. Tzarouchis and A. Sihvola: *Light scattering by a dielectric sphere: Perspectives on the Mie Resonances*. Apl. Sci. **8**, 184 (2018),
Cit. on p. 7.

[68] M. F. Picardi, M. Neugebauer, J. S. Eismann, G. Leuchs, P. Banzer, F. J. Rodríguez-Fortuño, and A. V. Zayats: *Experimental demonstration of linear and spinning Janus dipoles for polarisation- and wavelength-selective near-field coupling*. Light Sci. Appl. **8**, 52 (2019),
Cit. on p. 7.

[69] K. Koshelev and Y. Kivshar: *Dielectric resonant metaphtononics*. ACS Photonics **8**, 102–112 (2021),
Cit. on p. 7.

[70] E. Yablonovitch, T. J. Gmitter, and K. M. Leung: *Photonic band structure: The face-centered-cubic case employing nonspherical atoms*. Phys. Rev. Lett. **67**, 2295–2298 (1991),
Cit. on p. 7.

[71] T. F. Krauss, R. M. DeLaRue, and S. Brand: *Two-dimensional photonic-bandgap structures operating at near-infrared wavelengths*. Nature **383**, 699–702 (1996),
Cit. on p. 7.

[72] P. St.J. Russell: *Photonic crystal fibers*. Science **299**, 358–362 (2003),
Cit. on p. 7.

[73] Y. Akahane, T. Asano, B.-S. Song, and S. Noda: *High-Q photonic nanocavity in a two-dimensional photonic crystal*. Nature **425**, 944–947 (2003),
Cit. on p. 7.

[74] R. Alaee, C. Rockstuhl, and I. Fernandez-Corbaton: *Exact multipolar decompositions with applications in nanophotonics*. Adv. Optical Mater. **7**, 1800783 (2019),
Cit. on p. 8.

[75] T. Kaelberer, V. A. Fedotov, N. Papasimakis, D. P. Tsai, and N. I. Zheludev: *Toroidal Dipolar Response in a Metamaterial*. Science **330**, 1510–1512 (2010),
Cit. on p. 8.

[76] A. Ahmadivand, B. Gerislioglu, R. Ahuja, and Y. K. Mishra: *Terahertz plasmonics: The rise of toroidal metadevices towards immunobiosensings*. Materials Today **32**, 108–130 (2020),
Cit. on p. 8.

[77] A. Ahmadivand, B. Gerislioglu, R. Ahuja, and Y. K. Mishra: *Toroidal Metaphotonics and Metadevices*. Laser & Photonics Reviews **14**, 1900326 (2020),
Cit. on p. 8.

[78] I. Fernandez-Corbaton, S. Nanz, and C. Rockstuhl: *On the dynamic toroidal multipoles from localized electric current distributions*. Scientific Reports **7**, 7527 (2017),
Cit. on p. 8.

[79] P. C. Wu, C. Y. Liao, V. Savinov, T. L. Chung, W. T. Chen, Y.-W. Huang, P. R. Wu, Y.-H. Chen, A.-Q. Liu, N. I. Zheludev, and D. P. Tsai: *Optical Anapole Metamaterial*. ACS Nano **12**, 1920–1927 (2018),
Cit. on p. 8.

[80] E. A. Gurvitz, K. S. Ladutenko, P. A. Dergachev, A. B. Evlyukhin, A. E. Miroshnichenko, and A. S. Shalin: *The High-Order Toroidal Moments and Anapole States in All-Dielectric Photonics*. Laser & Photonics Reviews **13**, 1800266 (2019),
Cit. on p. 8.

[81] X. Cui, Y. Lai, R. Ai, H. Wang, L. Shao, H. Chen, W. Zhang, and J. Wang: *Anapole States and Toroidal Resonances Realized in Simple Gold Nanoplate-on-Mirror Structures*. Advanced Optical Materials **8**, 2001173 (2020),
Cit. on p. 8.

[82] D. C. Marinica, A. G. Borisov, and S. V. Shabanov: *Bound States in the Continuum in Photonics*. Phys. Rev. Lett. **100**, 183902 (2008),
Cit. on p. 8.

[83] C. W. Hsu, B. Zhen, A. D. Stone, J. D. Joannopoulos, and M. Soljačić: *Bound states in the continuum*. Nat. Rev. Mater. **1**, 16048 (2016),
Cit. on p. 8.

[84] A. S. Pilipchuka and A. F. Sadreeva: *Accidental bound states in the continuum in an open Sinai billiard.* Phys. Lett. A **381**, 720–724 (2017), Cit. on pp. 8, 9.

[85] A. Krasnok and A. Alú: *Embedded scattering eigenstates using resonant metasurfaces.* J. Opt. **20**, 064002 (2018), Cit. on p. 8.

[86] Z. Yu, Y. Wang, B. Sun, Y. Tong, J.-B. Xu, H. K. Tsang, and X. Sun: *Hybrid 2D-Material Photonics with Bound States in the Continuum.* Advanced Optical Materials **7**, 1901306 (2019), Cit. on p. 8.

[87] S. Murai, D. R. Abujetas, G. W. Castellanos, J. A. Sánchez-Gil, F. Zhang, and J. G. Rivas: *Bound States in the Continuum in the Visible Emerging from out-of-Plane Magnetic Dipoles.* ACS Photonics **7**, 2204–2210 (2020), Cit. on p. 8.

[88] S. Neale and E. Muljarov: *Accidental and symmetry-protected bound states in the continuum in a photonic-crystal slab: A resonant-state expansion study.* Phys. Rev. B **103**, 155112 (2021), Cit. on pp. 8, 48.

[89] S. Neale and E. Muljarov: *Resonant-state expansion for planar photonic crystal structures.* Phys. Rev. B **101**, 155128 (2020), Cit. on pp. 9, 48, 49, 78, 109, 176.

[90] D. D. Solnyshkov, T. Weiss, G. Malpuech, and N. A. Gippius: *Polariton laser based on a ZnO photonic crystal slab.* Appl. Phys. Lett **99**, 111110 (2011), Cit. on p. 9.

[91] J. Doppler, A. A. Mailybaev, J. Böhm, U. Kuhl, A. Girschik, F. Libisch, T. J. Milburn, P. Rabl, N. Moiseyev, and S. Rotter: *Dynamically encircling an exceptional point for asymmetric mode switching.* Nature **537**, 76–80 (2016), Cit. on p. 9.

[92] W. Langbein: *No exceptional precision of exceptional-point sensors.* Phys. Rev. A **98**, 023805 (2018), Cit. on p. 9.

[93] J. Wiersig: *Review of exceptional point-based sensors.* Photonics Res. **8**, 1457–1467 (2020), Cit. on p. 9.

[94] A. D. Humphrey and W. L. Barnes: *Plasmonic surface lattice resonances on arrays of different lattice symmetry.* Phys. Rev. B **90**, 075404 (2014), Cit. on p. 9.

[95] V. Tretnak, U. Hohenester, J. R. Krenn, and A. Hohenau: *The role of particle size in the dispersion engineering of plasmonic arrays.* J. Phys. Chem. C **124**, 2104–2112 (2020), Cit. on p. 9.

[96] M. S. Bin-Alam, O. Reshef, Y. Mamchur, M. Z. Alam, G. Carlow, J. Upham, B. T. Sullivan, J.-M. Ménard, M. J. Huttunen, R. W. Boyd, and K. Dolgaleva: *Ultra-high-Q resonances in plasmonic metasurfaces.* Nature Communications **12** (2021),
Cit. on p. 9.

[97] B. Wang, P. Yu, W. Wang, X. Zhang, H.-C. Kuo, H. Xu, and Z. M. Wang: *High-Q Plasmonic Resonances: Fundamentals and Applications.* Advanced Optical Materials **9**, 2001520 (2021),
Cit. on p. 9.

[98] R. W. Wood: *On a remarkable case of uneven distribution of light in a diffraction grating spectrum.* Philos. Mag. **4**, 396–402 (1902),
Cit. on pp. 9, 17.

[99] L. Rayleigh: *Note on the remarkable case of diffraction spectra described by Prof. Wood.* Philos. Mag. **14**, 60–65 (1907),
Cit. on pp. 9, 17, 76, 109, 176.

[100] L. Rayleigh: *On the dynamical theory of gratings.* Proc. R. Soc. Lond. **79**, 399–416 (1907),
Cit. on pp. 9, 17.

[101] G. Gamov: *Zur Quantentheorie des Atomkerns.* Zeitschrift für Physik **51**, 204–212 (1928),
Cit. on p. 9.

[102] Y. B. Zel'dovich: *On the theory of unstable states.* Sov. Phys. JETP **12**, 542–545 (1961),
Cit. on pp. 9, 24.

[103] È. È. Shnol: *Remarks on the theory of quasistationary states.* Theoret. and Math. Phys. **8**, 729–736 (1971),
Cit. on pp. 9, 24.

[104] R. Sammut and A. W. Snyder: *Leaky modes on circular optical waveguides.* Appl. Opt. **15**, 477–482 (1976),
Cit. on pp. 9, 24, 61.

[105] R. Sammut and A. W. Snyder: *Leaky modes on a dielectric waveguide: Orthogonality and excitation.* Appl. Opt. **15**, 1040–1044 (1976),
Cit. on pp. 9, 24, 61.

[106] S. V. Lobanov, G. Zoriniants, W. Langbein, and E. A. Muljarov: *Resonant-state expansion of light propagation in nonuniform waveguides.* Phys. Rev. A **95**, 053848 (2017),
Cit. on pp. 9, 17, 36, 48, 61.

[107] H. M. Lai, P. T. Leung, K. Young, P. W. Barber, and S. C. Hill: *Time-independent perturbation for leaking electromagnetic modes in open systems with application to resonances in microdroplets.* Phys. Rev. A **41**, 5187–5198 (1990),
Cit. on p. 9.

[108] L. A. Weinstein: *Open resonators and open waveguides*, Golem Press (Boulder, Col.), 1969.
Cit. on p. 9.

[109] L. J. Armitage, M. B. Doost, W. Langbein, and E. A. Muljarov: *Resonant-state expansion applied to planar waveguides*. Phys. Rev. A **89**, 053832 (2014),
Cit. on pp. 9, 17, 29, 36, 48.

[110] E. A. Muljarov and W. Langbein: *Resonant-state expansion of dispersive open optical systems: Creating gold from sand*. Phys. Rev. B **93**, 075417 (2016),
Cit. on pp. 9, 26, 29, 48, 55, 72.

[111] T. Weiss, M. Schäferling, H. Giessen, N. A. Gippius, S. G. Tikhodeev, W. Langbein, and E. A. Muljarov: *Analytical normalization of resonant states in photonic crystal slabs and periodic arrays of nanoantennas at oblique incidence*. Phys. Rev. B **96**, 045129 (2017),
Cit. on pp. 9, 10, 19, 26–29, 36, 48, 50, 51, 66, 67, 75–78.

[112] Q. Bai, M. Perrin, C. Sauvan, J. P. Hugonin, and P. Lalanne: *Efficient and intuitive method for the analysis of light scattering by a resonant nanostructure*. Opt. Express **21**, 27371–27382 (2013),
Cit. on pp. 9, 30, 32, 54.

[113] P. T. Kristensen, C. V. Vlack, and S. Hughes: *Generalized effective mode volume for leaky optical cavities*. Opt. Lett. **37**, 1649–1651 (2012),
Cit. on pp. 9, 54, 55, 57.

[114] P. T. Kristensen, R.-C. Ge, and S. Hughes: *Normalization of quasinormal modes in leaky optical cavities and plasmonic resonators*. Phys. Rev. A **92**, 053810 (2015),
Cit. on pp. 9, 54.

[115] E. A. Muljarov and W. Langbein: *Comment on "Normalization of quasinormal modes in leaky optical cavities and plasmonic resonators"*. Phys. Rev. A **96**, 017801 (2017),
Cit. on pp. 9, 16, 54.

[116] P. T. Kristensen, R.-C. Ge, and S. Hughes: *Reply to "Comment on 'Normalization of quasinormal modes in leaky optical cavities and plasmonic resonators' "*. Phys. Rev. A **96**, 017802 (2017),
Cit. on pp. 9, 54.

[117] P. Lalanne: *Mode volume of electromagnetic resonators: let us try giving credit where it is due*. arXiv:2011.00218 [physics.optics] (2020),
Cit. on pp. 9, 54.

[118] P. Lind: *Completeness relations and resonant state expansions*. Phys. Rev. C **47**, 1903–1920 (1993),
Cit. on pp. 10, 22, 36.

[119] P. Lind, R. J. Liotta, E. Maglione, and I. Vertse: *Resonant state expansions of the continuum.* Z. Phys. A **9**, 231–236 (1994),
Cit. on p. 10.

[120] S. V. Lobanov, W. Langbein, and E. A. Muljarov: *Resonant-state expansion applied to three-dimensional open optical systems: Complete set of static modes.* Phys. Rev. A **100**, 063811 (2019),
Cit. on pp. 10, 37, 49, 50.

[121] H. A. Haus and W. Huang: *Coupled-mode theory.* Proc. IEEE **79**, 1505–1518 (1991),
Cit. on p. 10.

[122] A. Unger and M. Kreiter: *Analyzing the performance of plasmonic resonators for dielectric sensing.* J. Phys. Chem. C **113**, 12243–12251 (2009),
Cit. on pp. 10, 24, 66, 89.

[123] B. Gallinet and O. J. F. Martin: *Refractive index sensing with subradiant modes: A framework to reduce losses in plasmonic nanostructures.* ACS Nano **7**, 6978–6987 (2013),
Cit. on pp. 10, 66, 90.

[124] V. S. Asadchy, M. S. Mirmoosa, A. Díaz-Rubio, S. Fan, and S. A. Tretyakov: *Tutorial on electromagnetic nonreciprocity and its origins.* Proc. IEEE **108**, 1684–1727 (2020),
Cit. on pp. 12, 19–21, 61.

[125] H. Zhang and O. D. Miller: *Quasinormal coupled mode theory.* arXiv:2010.08650 [physics.optics] (2020),
Cit. on pp. 13, 37, 40, 42–44.

[126] G. Hergert, J. Vogelsang, F. Schwarz, D. Wang, H. Kollmann, P. Groß, C. Lienau, E. Runge, and P. Schaaf: *Long-lived electron emission reveals localized plasmon modes in disordered nanosponge antennas.* Light: Science & Applications **6**, e17075 (2017),
Cit. on p. 15.

[127] S. Silver: *Radiation from current distributions*, McGraw-Hill (New York), 1949.
Cit. on p. 16.

[128] A. B. Akimov, N. A. Gippius, and S. G. Tikhodeev: *Optical Fano resonances in photonic crystal slabs near diffraction threshold anomalies.* JETP Lett. **93**, 427–430 (2011),
Cit. on pp. 17, 36, 75, 76.

[129] J. Defrance and T. Weiss: *On the pole expansion of electromagnetic fields.* Opt. Express **28**, 32363–32376 (2020),
Cit. on pp. 17–19, 22, 31–34.

[130] P. Lalanne, W. Yan, A. Gras, C. Sauvan, J.-P. Hugonin, M. Besbes, G. Demésy, M. D. Truong, B. Gralak, F. Zolla, A. Nicolet, F. Binkowski, L. Zschiedrich, S. Burger, J. Zimmerling, R. Remis, P. Urbach, H. T. Liu, and T. Weiss: *Quasinormal mode solvers for resonators with dispersive materials*. J. Opt. Soc. Am A **36**, 686–704 (2019),
Cit. on p. 18.

[131] G. B. Arfken and H. J. Weber: *Mathematical methods for physicists*, 6th edition, Elsevier (London), 2011.
Cit. on p. 18.

[132] I. Allayarov, S. Upendar, M. A. Schmidt, and T. Weiss: *Analytic mode normalization for the Kerr nonlinearity parameter: Prediction of nonlinear gain for leaky modes*. Phys. Rev. Lett. **121**, 213905 (2018),
Cit. on pp. 19, 62.

[133] I. Allayarov, M. A. Schmidt, and T. Weiss: *Theory of four-wave mixing for bound and leaky modes*. Physical Review A **101**, 043806 (2020),
Cit. on pp. 19, 62.

[134] L. Onsager: *Reciprocal relations in irreversible processes. I.* Phys. Rev. **37**, 405–426 (1931),
Cit. on p. 20.

[135] L. Onsager: *Reciprocal relations in irreversible processes. II.* Phys. Rev. **38**, 2265–2279 (1931),
Cit. on p. 20.

[136] H. B. G. Casimir: *On Onsager's principle of microscopic reversibility*. Rev. Mod. Phys. **17**, 343–350 (1945),
Cit. on p. 20.

[137] F. Zolla, A. Nicolet, and G. Demésy: *Photonics in highly dispersive media: the exact modal expansion*. Opt. Lett. **43**, 5813–5816 (2018),
Cit. on p. 21.

[138] M. D. Truong, G. Demésy, F. Zolla, and A. Nicolet: *Quasi-normal mode (DQNM) expansion in open and periodic nanophotonic structures*. 2019 22nd International Conference on the Computation of Electromagnetic Fields (COMPUMAG) **29**, 29016–29032 (2020),
Cit. on p. 21.

[139] M. D. Truong, A. Nicolet, G. Demésy, and F. Zolla: *A continuous family of exact dispersive quasi-normal modal (DQNM) expansions for dispersive photonic structures*. Opt. Express **29**, 29016–29032 (2020),
Cit. on pp. 21, 32.

[140] M. V. Keldysh: *On eigenvalues and eigenfunctions of some classes of non self-adjoint equations*. Dokl. Akad. Nauk SSSR **77**, 11–14 (1951),
Cit. on p. 21.

[141] M. V. Keldysh: *On the completeness of the eigenfunctions of some classes of non-selfadjoint linear operators*. Russian Mathematical Surveys **26**, 15 (1971), Cit. on p. 21.

[142] H. S. Sehmi, W. Langbein, and E. A. Muljarov: *Optimizing the Drude-Lorentz model for material permittivity: Method, program, and examples for gold, silver, and copper*. Phys. Rev. B **95**, 115444 (2017), Cit. on p. 22.

[143] R. Colom, R. Mcphedran, B. Stout, and N. Bonod: *Modal expansion of the scattered field: Causality, nondivergence, and nonresonant contribution*. Phys. Rev. B **98**, 085418 (2018), Cit. on p. 23.

[144] J. M. Gérard: *Solid-state cavity-quantum electrodynamics with self-assembled quantum dots*. In: Single Quantum Dots, Topics in Applied Physics, Springer (Berlin), 2003. Cit. on pp. 24, 53.

[145] A. F. Koenderink: *On the use of Purcell factors for plasmon antennas*. Opt. Lett. **35**, 4208–4210 (2010), Cit. on p. 24.

[146] T. Vertse, P. Curutchet, and R. J. Liotta: *The use of Gamow functions in nuclear problems*. In: Resonances – the unifying route towards the formulation of dynamical processes foundations and applications in nuclear, atomic, and molecular physics, Lecture Notes in Physics, ed. by E. Brändas and N. Elander, Springer (Cham), 1989. Cit. on p. 24.

[147] J. P. Hugonin and P. Lalanne: *Perfectly matched layers as nonlinear coordinate transforms: A generalized formalization*. J. Opt. Soc. Am. A **22**, 1844–1849 (2005), Cit. on p. 24.

[148] R. C. Mcphedran and B. Stout: *Killing Mie softly: Analytic integrals for complex resonant states*. QJMAM **73**, 119–139 (2020), Cit. on p. 25.

[149] R.-C. Ge, P. T. Kristensen, J. F Young, and S. Hughes: *Quasinormal mode approach to modelling light-emission and propagation in nanoplasmonics*. New Journal of Physics **16**, 113048 (2014), Cit. on pp. 28, 56, 57.

[150] M. Perrin: *Eigen-energy effects and non-orthogonality in the quasi-normal mode expansion of Maxwell equations*. Opt. Express **24**, 27137–27151 (2016), Cit. on p. 30.

[151] G. Unger, A. Trügler, and U. Hohenester: *Novel modal approximation scheme for plasmonic transmission problems*. Phys. Rev. Lett. **121**, 246802 (2018), Cit. on p. 32.

[152] A. Gras, P. Lalanne, and M. Duruflé: *Non-uniqueness of the quasi-normal mode expansion of electromagnetic Lorentz-dispersive materials*. J. Opt. Soc. Am. A **37**, 1219–1228 (2020),
Cit. on p. 32.

[153] W. Yan, R. Faggiani, and P. Lalanne: *Rigorous modal analysis of plasmonic nanoresonators*. Phys. Rev. B **97**, 205422 (2018),
Cit. on pp. 35, 36, 54, 57, 86, 120.

[154] G. García-Calderón: *On the over-completeness of the set of bound, antibound, and resonant states*. Lett. Nuovo Cimento **33**, 253–257 (1982),
Cit. on p. 36.

[155] L. Li: *Use of Fourier series in the analysis of discontinuous periodic structures*. J. Opt. Soc. Am. A **13**, 1870–1876 (1996),
Cit. on p. 37.

[156] L. Li: *New formulation of the Fourier modal method for crossed surface-relief gratings*. J. Opt. Soc. Am. A **14**, 2758–2767 (1997),
Cit. on p. 37.

[157] G. Granet: *Reformulation of the lamellar grating problem through the concept of adaptive spatial resolution*. J. Opt. Soc. Am. A **16**, 2510–2516 (1999),
Cit. on p. 37.

[158] L. Li: *Fourier modal method for crossed anisotropic gratings with arbitrary permittivity and permeability tensors*. J. Opt. A: Pure Appl. Opt. **5**, 345–355 (2003),
Cit. on p. 37.

[159] C. Sauvan, T. Wu, R. Zarouf, E. A. Muljarov, and P. Lalanne: *Normalization, orthogonality, and completeness of quasinormal modes of open systems: the case of electromagnetism [Invited]*. Opt. Express **30**, 6846–6885 (2022),
Cit. on p. 37.

[160] M. Benzaouia, J. D. Joannopoulos, S. G. Johnson, and A. Karalis: *Quasi-normal mode theory of the scattering matrix, enforcing fundamental constraints for truncated expansions*. Phys. Rev. Research **3**, 033228 (2021),
Cit. on pp. 37, 44.

[161] F. Binkowski, F. Betz, R. Colom, M. Hammerschmidt, L. Zschiedrich, and S. Burger: *Quasinormal mode expansion of optical far-field quantities*. Phys. Rev. B **102**, 035432 (2020),
Cit. on pp. 37, 44.

[162] J. Yang, J. P. Hugonin, and P. Lalanne: *Near-to-far field transformations for radiative and guided waves*. ACS Photonics **3**, 395–402 (2016),
Cit. on p. 37.

[163] N. A. Gippius, S. G. Tikhodeev, and T. Ishihara: *Optical properties of photonic crystal slabs with an asymmetrical unit cell.* Phys. Rev. B **72**, 45138 (2005),
Cit. on p. 44.

[164] T. Weiss, G. Granet, N. A. Gippius, S. G. Tikhodeev, and H. Giessen: *Matched coordinates and adaptive spatial resolution in the Fourier modal method.* Opt. Express **17**, 8051–8061 (2009),
Cit. on pp. 45, 74, 76.

[165] T. Weiss, N. A. Gippius, S. G. Tikhodeev, G. Granet, and H. Giessen: *Derivation of plasmonic resonances in the Fourier modal method with adaptive spatial resolution and matched coordinates.* J. Opt. Soc. Am. A **28**, 238–244 (2011),
Cit. on pp. 45, 74, 76.

[166] M. F. Limonov, M. V. Rybin, A. N. Poddubny, and Y. S. Kivshar: *Fano resonances in photonics.* Nature Photonics **11**, 543–554 (2017),
Cit. on p. 46.

[167] A. E. Miroshnichenko, S. Flach, and Y. S. Kivshar: *Fano resonances in nanoscale structures.* Rev. Mod. Phys. **82**, 2257–2298 (2010),
Cit. on p. 46.

[168] B. Luk'yanchuk, N. I. Zheludev, S. A. Maier, N. J. Halas, P. Nordlander, H. Giessen, and C. T. Chong: *The Fano resonance in plasmonic nanostructures and metamaterials.* Nat. Mater. **9**, 707–715 (2010),
Cit. on p. 46.

[169] B. Gallinet and O. J. F. Martin: *Relation between near-field and far-field properties of plasmonic Fano resonances.* Opt. Express **19**, 22167–22175 (2011),
Cit. on p. 46.

[170] D. Bekele, Y. Yu, K. Yvind, and J. Mork: *In-Plane Photonic Crystal Devices using Fano Resonances.* Laser & Photonics Reviews **13**, 1900054 (2019),
Cit. on p. 46.

[171] N. Papasimakis, V. A. Fedotov, N. I. Zheludev, and S. L. Prosvirnin: *Metamaterial analog of electromagnetically induced transparency.* Phys. Rev. Lett. **101**, 253903 (2008),
Cit. on p. 46.

[172] N. Liu, L. Langguth, T. Weiss, J. Kästel, M. Fleischhauer, T. Pfau, and H. Giessen: *Plasmonic electromagnetically induced transparency at the Drude damping limit.* Nature Materials **8**, 758–762 (2009),
Cit. on p. 46.

[173] S. G. Tikhodeev, E. A. Muljarov, W. Langbein, N. A. Gippius, H. Giessen, and T. Weiss: *Influence of disorder on a Bragg microcavity.* J. Opt. Soc. Am. B **38**, 139–150 (2021),
Cit. on pp. 48, 50, 67.

[174] E. A. Muljarov: *Full electromagnetic Green's dyadic of spherically symmetric open optical systems and elimination of static modes from the resonant-state expansion*. Phys. Rev. A **101**, 053854 (2020),
Cit. on pp. 49, 50.

[175] H. T. Dung, L. Knöll, and D.-G. Welsch: *Spontaneous decay in the presence of dispersing and absorbing bodies: General theory and application to a spherical cavity*. Phys. Rev. A **62**, 053804 (2000),
Cit. on p. 53.

[176] H. T. Dung, L. Knöll, and D.-G. Welsch: *Decay of an excited atom near an absorbing microsphere*. Phys. Rev. A **64**, 013804 (2001),
Cit. on p. 53.

[177] A. G. Curto, G. Volpe, T. H. Taminiau, M. P. Kreuzer, R. Quidant, and N. F. van Hulst: *Unidirectional emission of a quantum dot coupled to a nanoantenna*. Science **329**, 930–933 (2010),
Cit. on pp. 53, 114.

[178] G. M. Akselrod, C. Argyropoulos, T. B. Hoang, C. Ciraci, C. Fang, J. Huang, D. R. Smith, and M. H. Mikkelsen: *Probing the mechanisms of large Purcell enhancement in plasmonic nanoantennas*. Nat. Phot. **8**, 835–840 (2014),
Cit. on p. 53.

[179] Y.-Y. Cai, S. S. E. Collins, M. J. Gallagher, U. Bhattacharjee, R. Zhang, T. H. Chow, A. Ahmadivand, B. Ostovar, A. Al-Zubeidi, J. Wang, P. Nordlander, C. F. Landes, and S. Link: *Single-Particle Emission Spectroscopy Resolves d-Hole Relaxation in Copper Nanocubes*. ACS Energy Letters **4**, 2458–2465 (2019),
Cit. on pp. 53, 55.

[180] B. Ostovar, Y.-Y. Cai, L. J. Tauzin, S. A. Lee, A. Ahmadivand, R. Zhang, P. Nordlander, and S. Link: *Increased Intraband Transitions in Smaller Gold Nanorods Enhance Light Emission*. ACS Nano **14**, 15757–15765 (2020),
Cit. on pp. 53, 55.

[181] A. S. Solntsev, G. S. Agarwal, and Y. S. Kivshar: *Metasurfaces for quantum photonics*. Nature Photonics **15**, 327–336 (2021),
Cit. on p. 53.

[182] H. Wei, X. Yan, Y. Niu, Q. Li, Z. Jia, and H. Xu: *Plasmon–Exciton Interactions: Spontaneous Emission and Strong Coupling*. Advanced Functional Materials, 2100889 (2021),
Cit. on p. 53.

[183] E. M. Purcell: *Spontaneous emission probabilities at radio frequencies*. Phys. Rev. **69**, 681 (1946),
Cit. on p. 53.

[184] R. Coccioli, M. Boroditsky, K. W. Kim, Y. Rahmat-Samii, and E. Yablonovitch: *Smallest possible electromagnetic mode volume in a dielectric cavity*. IEE Proceedings - Optoelectronics **145** (1998), Cit. on p. 53.

[185] J. D. Joannopoulos, S. G. Johnson, J. N. Winn, and R. D. Meade: *Photonic Crystals: Molding the Flow of Light (Second Edition)*, second edition, Princeton University Press (Princeton), 2008. Cit. on p. 53.

[186] P. T. Leung, S. Y. Liu, and K. Young: *Completeness and orthogonality of quasinormal modes in leaky optical cavities*. Phys. Rev. A **49**, 3057–3067 (1994), Cit. on p. 54.

[187] P. T. Leung and K. M. Pang: *Completeness and time-independent perturbation of morphology-dependent resonances in dielectric spheres*. J. Opt. Soc. Am. B **13**, 805–817 (1996), Cit. on p. 54.

[188] K. M. Lee, P. T. Leung, and K. M. Pang: *Dyadic formulation of morphology-dependent resonances. I. Completeness relation*. J. Opt. Soc. Am. B **16**, 1409–1417 (1999), Cit. on p. 54.

[189] S. Franke, S. Hughes, M. K. Dezfouli, P. T. Kristensen, K. Busch, A. Knorr, and M. Richter: *Quantization of quasinormal modes for open cavities and plasmonic cavity quantum electrodynamics*. Phys. Rev. Lett. **122**, 213901 (2019), Cit. on p. 54.

[190] X. Zambrana-Puyalto and N. Bonod: *Purcell factor of spherical Mie resonators*. Phys. Rev. B **91**, 195422 (2015), Cit. on p. 54.

[191] T. Wu, M. Gurioli, and P. Lalanne: *Nanoscale Light Confinement: the Q's and V's*. ACS Photonics **8**, 1522–1538 (2021), Cit. on pp. 54, 55.

[192] L. Novotny and B. Hecht: *Principles of Nano-Optics*, 2nd edition, Cambridge University Press (Cambridge), 2012. Cit. on pp. 55, 147–149, 153.

[193] M. K. Dezfouli and S. Hughes: *Regularized quasinormal modes for plasmonic resonators and open cavities*. Phys. Rev. B **97**, 115302 (2018), Cit. on p. 57.

[194] K. G. Cognée, W. Yan, F. L. China, D. Balestri, F. Intonti, M. Gurioli, A. F. Koenderink, and P. Lalanne: *Mapping complex mode volumes with cavity perturbation theory*. Optica **6**, 269–273 (2019), Cit. on pp. 57, 58.

[195] N. Caselli, T. Wu, G. Arregui, N. Granchi, F. Intonti, P. Lalanne, and M. Gurioli: *Near-Field Imaging of Magnetic Complex Mode Volume*. ACS Photonics **8**, 1258–1263 (2021),
Cit. on p. 58.

[196] D. J. Bergman: *Dielectric constant of a two-component granular composite: A practical scheme for calculating the pole spectrum*. Phys. Rev. B **19**, 2359 (1979),
Cit. on p. 58.

[197] D. J. Bergman: *The dielectric constant of a simple cubic array of identical spheres*. J. Phys. C: Solid State Phys. **12**, 4947 (1979),
Cit. on p. 58.

[198] D. J. Bergman and D. Stroud: *Theory of resonances in the electromagnetic scattering by macroscopic bodies*. Phys. Rev. B **22**, 3527 (1980),
Cit. on p. 58.

[199] A. Farhi and D. J. Bergman: *Electromagnetic eigenstates and the field of an oscillating point electric dipole in a flat-slab composite structure*. Phys. Rev. A **93**, 063844 (2016),
Cit. on p. 58.

[200] J. D. Jackson: *Classical electrodynamics*, third edition, John Wiley & Sons (Hoboken), 1999.
Cit. on pp. 59, 100.

[201] P. Y. Chen, D. J. Bergman, and Y. Sivan: *Generalizing normal mode expansion of electromagnetic Green's tensor to open systems*. Phys. Rev. Appl. **11**, 044018 (2019),
Cit. on p. 59.

[202] P. Y. Chen, Y. Sivan, and E. A. Muljarov: *An efficient solver for the generalized normal modes of non-uniform open optical resonators*. Journal of Computational Physics **422**, 109754 (2020),
Cit. on p. 59.

[203] P. Y. Chen and Y. Sivan: *Resolving the Gibbs phenomenon via a discontinuous basis in a mode solver for open optical systems*. Journal of Computational Physics **429**, 110004 (2021),
Cit. on p. 59.

[204] M. Pascale, G. Miano, R. Tricarico, and C. Forestiere: *Full-wave electromagnetic modes and hybridization in nanoparticle dimers*. Sci. Rep. **9**, 14524 (2019),
Cit. on p. 59.

[205] E. Prodan, C. Radloff, N. J. Halas, and P. Nordlander: *A hybridization model for the plasmon response of complex nanostructures*. Science **302**, 419–422 (2003),
Cit. on p. 59.

[206] E. Prodan and P. Nordlander: *Plasmon hybridization in spherical nanoparticles*. The Journal of Chemical Physics **120**, 5444–5454 (2004),
Cit. on p. 59.

[207] N. A. Gippius, T. Weiss, S. G. Tikhodeev, and H. Giessen: *Resonant mode coupling of optical resonances in stacked nanostructures*. Opt. Express **18**, 7569–7574 (2010),
Cit. on p. 59.

[208] B. Vial and Y. Hao: *A coupling model for quasi-normal modes of photonic resonators*. J. Opt. **18**, 115004 (2016),
Cit. on p. 59.

[209] C. Tao, J. Zhu, Y. Zhong, and H. Liu: *Coupling theory of quasinormal modes for lossy and dispersive plasmonic nanoresonators*. Phys. Rev. B **102**, 045430 (2020),
Cit. on p. 59.

[210] Q. Li, T. Wu, J. van de Groep, P. Lalanne, and M. L. Brongersma: *Structural color from a coupled nanowire pair beyond the bonding and antibonding model*. Optica **8**, 464–470 (2021),
Cit. on p. 60.

[211] T. Weiss, N. A. Gippius, G. Granet, S. G. Tikhodeev, R. Taubert, L. Fu, H. Schweizer, and H. Giessen: *Strong resonant mode coupling of Fabry-Perot and grating resonances in stacked two-layer systems*. Photonics and Nanostructures–Fundamentals and Applications **9**, 390–397 (2011),
Cit. on p. 60.

[212] T. Weiss, G. K. L. Wong, F. Biancalana, S. M. Barnett, X. M. Xi, and P. St.J. Russell: *Topological Zeeman effect and circular birefringence in twisted photonic crystal fibers*. J. Opt. Soc. Am. B **30**, 2921–2927 (2013),
Cit. on p. 60.

[213] A. W. Snyder and J. Love: *Optical waveguide theory*, Chapman & Hall (London), 1983.
Cit. on pp. 60, 61.

[214] G. Agrawal: *Nonlinear fiber optics*, 3rd edition, Academic Press (San Diego), 2001.
Cit. on pp. 61, 62.

[215] A. V. Maslov: *Rigorous calculation of the nonlinear Kerr coefficient for a waveguide using power-dependent dispersion modification*. Opt. Lett. **39**, 4396–4399 (2014),
Cit. on p. 62.

[216] G. Li, C. M. de Sterke, and S. Palomba: *General analytic expression and numerical approach for the Kerr nonlinear coefficient of optical waveguides*. Opt. Lett. **42**, 1329–1332 (2017),
Cit. on p. 62.

[217] M. M. Elsawy and G. Renversez: *Exact calculation of the nonlinear characteristics of 2D isotropic and anisotropic waveguides*. Opt. Lett. **43**, 2446–2449 (2018),
Cit. on p. 62.

[218] R. W. Boyd: *Nonlinear optics*, 2nd edition, Academic Press (San Diego), 2003.
Cit. on p. 62.

[219] T. Paul, C. Rockstuhl, and F. Lederer: *A numerical approach for analyzing higher harmonic generation in multilayer nanostructures*. J. Opt. Soc. Am. B **27**, 1118–1130 (2010),
Cit. on p. 62.

[220] T. Paul, C. Rockstuhl, and F. Lederer: *Integrating cold plasma equations into the Fourier modal method to analyze second harmonic generation at metallic nanostructures*. Journal of Modern Optics **58**, 438–448 (2010),
Cit. on p. 62.

[221] J. Defrance, M. Schäferling, and T. Weiss: *Modeling of second-harmonic generation in periodic nanostructures by the Fourier modal method with matched coordinates*. Opt. Express **26**, 13746–13758 (2020),
Cit. on p. 62.

[222] C. Gigli, T. Wu, G. Marino, A. Borne, G. Leo, and P. Lalanne: *Quasinormal-mode non-Hermitian modeling and design in nonlinear nano-optics*. ACS Photonics **7**, 1197–1205 (2020),
Cit. on p. 62.

[223] T. Christopoulos, O. Tsilipakos, and E. E. Kriezis: *Perturbation theory for Kerr nonlinear leaky cavities*. Opt. Lett. **45**, 6442–6445 (2020),
Cit. on p. 62.

[224] W. Zhang and O. J. F. Martin: *A universal law for plasmon resonance shift in biosensing*. ACS Photonics **2**, 144–150 (2015),
Cit. on pp. 66, 90.

[225] C. Cohen-Tannoudji: *Quantum mechanics*, Hermann (Paris), 1991.
Cit. on p. 68.

[226] P. G. Etchegoin, E. C. Le Ru, and M. Meyer: *An analytic model for the optical properties of gold*. J. Chem. Phys. **125**, 164705–1–3 (2006),
Cit. on p. 74.

[227] D. A. Bykov and L. L. Doskolovich: *Numerical methods for calculating poles of the scattering matrix with applications in grating theory*. J. Lightwave Technol. **31**, 793–801 (2013),
Cit. on pp. 74, 76.

[228] S. G. Tikhodeev, A. L. Yablonskii, E. A. Muljarov, N. A. Gippius, and T. Ishihara: *Quasiguided modes and optical properties of photonic crystal slabs*. Phys. Rev. B **66**, 045102–1–17 (2002),
Cit. on p. 76.

[229] B. Vial, F. Zolla, A. Nicolet, and M. Commandré: *Quasimodal expansion of electromagnetic fields in open two-dimensional structures*. Phys. Rev. A **89**, 023829 (2014),
Cit. on pp. 78, 109, 176.

[230] S. F. Almousa and E. A. Muljarov: *Varying the medium surrounding an optical resonator: An efficient and rigorous way to calculate its spectral changes*. arXiv:2109.07026 [physics.optics] (2021),
Cit. on p. 78.

[231] N. Liu, H. Guo, L. Fu, S. Kaiser, H. Schweizer, and H. Giessen: *Three-dimensional photonic metamaterials at optical frequencies*. Nature Materials **7**, 31–37 (2008),
Cit. on p. 86.

[232] W. T. Kelvin: *Baltimore Lectures on Molecular Dynamics and the Wave Theory of Light*, CJ Clay and Sons (London), 1904.
Cit. on p. 91.

[233] U. Meierhenrich: *Amino Acids and the Asymmetry of Life*. Advances in astrobiology and biogeophysics, Springer (Berlin), 2008.
Cit. on p. 91.

[234] J. S. Siegel: *Single-handed cooperation*. Nature **409**, 777–778 (2001),
Cit. on p. 91.

[235] L. A. Nguyen, H. He, and C. Pham-Huy: *Chiral drugs: an overview*. International journal of biomedical science : IJBS **2**, 85–100 (2006),
Cit. on p. 91.

[236] J. Aronson: *Meyler's Side Effects of Drugs: The International Encyclopedia of Adverse Drug Reactions and Interactions*, Elsevier Science (Amsterdam), 2015.
Cit. on p. 91.

[237] K. N. Nina Berova and R. W. Woody: *Circular Dichroism. Principles and Applications*, 2nd ed. edition, Wiley-VCH (New York), 2000.
Cit. on p. 91.

[238] I. Lindell, A. Sihvola, S. Tretyakov, and A. Viitanen: *Electromagnetic waves in chiral and bi-isotropic media*, Artech House (Boston), 1994.
Cit. on pp. 92, 94.

[239] A. H. Sihvola and I. V. Lindell: *BI-isotropic constitutive relations*. Microwave and Optical Technology Letters **4**, 295–297 (1991),
Cit. on p. 92.

[240] F. Lu, Y. Tian, M. Liu, D. Su, H. Zhang, A. O. Govorov, and O. Gang: *Discrete Nanocubes as Plasmonic Reporters of Molecular Chirality*. Nano Letters **13**, 3145–3151 (2013),
Cit. on p. 92.

[241] R.-Y. Wang, P. Wang, Y. Liu, W. Zhao, D. Zhai, X. Hong, Y. Ji, X. Wu, F. Wang, D. Zhang, W. Zhang, R. Liu, and X. Zhang: *Experimental Observation of Giant Chiroptical Amplification of Small Chiral Molecules by Gold Nanosphere Clusters*. The Journal of Physical Chemistry C **118**, 9690–9695 (2014),
Cit. on p. 92.

[242] R. Tullius, A. S. Karimullah, M. Rodier, B. Fitzpatrick, N. Gadegaard, L. D. Barron, V. M. Rotello, G. Cooke, A. Lapthorn, and M. Kadodwala: *"Superchiral" Spectroscopy: Detection of Protein Higher Order Hierarchical Structure with Chiral Plasmonic Nanostructures*. Journal of the American Chemical Society **137**, 8380–8383 (2015),
Cit. on pp. 92, 99.

[243] Y. Zhao, A. N. Askarpour, L. Sun, J. Shi, X. Li, and A. Alù: *Chirality detection of enantiomers using twisted optical metamaterials*. Nature Communications **8**, 14180 (2017),
Cit. on p. 92.

[244] C. Kelly, R. Tullius, A. J. Lapthorn, N. Gadegaard, G. Cooke, L. D. Barron, A. S. Karimullah, V. M. Rotello, and M. Kadodwala: *Chiral Plasmonic Fields Probe Structural Order of Biointerfaces*. Journal of the American Chemical Society **140**, 8509–8517 (2018),
Cit. on pp. 92, 94, 95, 99.

[245] L. V. Poulikakos, P. Gutsche, K. M. McPeak, S. Burger, J. Niegemann, C. Hafner, and D. J. Norris: *Optical Chirality Flux as a Useful Far-Field Probe of Chiral Near Fields*. ACS Photonics **3**, 1619–1625 (2016),
Cit. on pp. 92, 94.

[246] K. M. McPeak, C. D. van Engers, S. Bianchi, A. Rossinelli, L. V. Poulikakos, L. Bernard, S. Herrmann, D. K. Kim, S. Burger, M. Blome, S. V. Jayanti, and D. J. Norris: *Ultraviolet Plasmonic Chirality from Colloidal Aluminum Nanoparticles Exhibiting Charge-Selective Protein Detection*. Advanced Materials **27**, 6244–6250 (2015),
Cit. on p. 92.

[247] H.-H. Jeong, A. G. Mark, and P. Fischer: *Magnesium plasmonics for UV applications and chiral sensing*. Chem. Commun. **52**, 12179–12182 (2016),
Cit. on p. 92.

[248] U. Kilic, M. Hilfiker, A. Ruder, R. Feder, E. Schubert, M. Schubert, and C. Argyropoulos: *Broadband Enhanced Chirality with Tunable Response in Hybrid Plasmonic Helical Metamaterials*. Advanced Functional Materials **n/a**, 2010329 (2021),
Cit. on p. 92.

[249] M. Schäferling: *Chiral Nanophotonics: Chiral Optical Properties of Plasmonic Systems*, Springer (Cham), 2016.
Cit. on pp. 92, 99, 108.

[250] Y. Tang and A. E. Cohen: *Optical chirality and its interaction with matter.* Phys. Rev. Lett. **104**, 163901 (2010),
Cit. on pp. 92, 94, 108.

[251] A. O. Govorov, Z. Fan, P. Hernandez, J. M. Slocik, and R. R. Naik: *Theory of circular dichroism of nanomaterials comprising chiral molecules and nanocrystals: Plasmon enhancement, dipole interactions, and dielectric effects.* Nano Lett. **10**, 374–1382 (2010),
Cit. on pp. 92, 94.

[252] A. O. Govorov: *Plasmon-Induced Circular Dichroism of a Chiral Molecule in the Vicinity of Metal Nanocrystals. Application to Various Geometries.* The Journal of Physical Chemistry C **115**, 7914–7923 (2011),
Cit. on pp. 92, 94.

[253] E. Hendry, R. V. Mikhaylovskiy, L. D. Barron, M. Kadodwala, and T. J. Davis: *Chiral Electromagnetic Fields Generated by Arrays of Nanoslits.* Nano Letters **12**, 3640–3644 (2012),
Cit. on pp. 92, 99, 102.

[254] M. Schäferling, D. Dregely, M. Hentschel, and H. Giessen: *Tailoring Enhanced Optical Chirality: Design Principles for Chiral Plasmonic Nanostructures.* Phys. Rev. X **2**, 031010 (2012),
Cit. on pp. 92, 94, 102.

[255] M. Schäferling, X. Yin, and H. Giessen: *Formation of chiral fields in a symmetric environment.* Opt. Express **20**, 26326–26336 (2012),
Cit. on pp. 92, 102.

[256] A. García-Etxarri and J. A. Dionne: *Surface-enhanced circular dichroism spectroscopy mediated by nonchiral nanoantennas.* Phys. Rev. B **87**, 235409 (2013),
Cit. on pp. 92, 94, 111, 159.

[257] T. J. Davis and E. Hendry: *Superchiral electromagnetic fields created by surface plasmons in nonchiral metallic nanostructures.* Phys. Rev. B **87**, 085405 (2013),
Cit. on pp. 92, 102.

[258] T. J. Davis and D. E. Gómez: *Interaction of localized surface plasmons with chiral molecules.* Phys. Rev. B **90**, 235424 (2014),
Cit. on p. 92.

[259] M. Schäferling, X. Yin, N. Engheta, and H. Giessen: *Helical Plasmonic Nanostructures as Prototypical Chiral Near-Field Sources.* ACS Photonics **1**, 530–537 (2014),
Cit. on pp. 92, 94, 102.

[260] T. Wu, J. Ren, R. Wang, and X. Zhang: *Competition of Chiroptical Effect Caused by Nanostructure and Chiral Molecules.* The Journal of Physical Chemistry C **118**, 20529–20537 (2014),
Cit. on p. 92.

[261] M. Schäferling, N. Engheta, H. Giessen, and T. Weiss: *Reducing the Complexity: Enantioselective Chiral Near-Fields by Diagonal Slit and Mirror Configuration.* ACS Photonics **3**, 1076–1084 (2016),
Cit. on pp. 92, 94, 102.

[262] L. V. Poulikakos, P. Thureja, A. Stollmann, E. De Leo, and D. J. Norris: *Chiral Light Design and Detection Inspired by Optical Antenna Theory.* Nano Letters **18**, 4633–4640 (2018),
Cit. on pp. 92, 94.

[263] L. V. Poulikakos, J. A. Dionne, and A. García-Etxarri: *Optical Helicity and Optical Chirality in Free Space and in the Presence of Matter.* Symmetry **11** (2019),
Cit. on pp. 92, 94.

[264] E. Mohammadi, K. L. Tsakmakidis, A. N. Askarpour, P. Dehkhoda, A. Tavakoli, and H. Altug: *Nanophotonic Platforms for Enhanced Chiral Sensing.* ACS Photonics **5**, 2669–2675 (2018),
Cit. on pp. 92, 94.

[265] E. Mohammadi, A. Tittl, K. L. Tsakmakidis, T. V. Raziman, and A. G. Curto: *Dual Nanoresonators for Ultrasensitive Chiral Detection.* ACS Photonics **8**, 1754–1762 (2021),
Cit. on p. 92.

[266] S. Lee, J.-H. Kang, S. Yoo, and Q.-H. Park: *Robust numerical evaluation of circular dichroism from chiral medium/nanostructure coupled systems using the finite-element method.* Scientific Reports **8**, 8406 (2018),
Cit. on pp. 92, 94, 111.

[267] M. L. Solomon, J. Hu, M. Lawrence, A. García-Etxarri, and J. A. Dionne: *Enantiospecific Optical Enhancement of Chiral Sensing and Separation with Dielectric Metasurfaces.* ACS Photonics **6**, 43–49 (2019),
Cit. on p. 92.

[268] F. Graf, J. Feis, X. Garcia-Santiago, M. Wegener, C. Rockstuhl, and I. Fernandez-Corbaton: *Achiral, Helicity Preserving, and Resonant Structures for Enhanced Sensing of Chiral Molecules.* ACS Photonics **6**, 482–491 (2019),
Cit. on pp. 92, 111, 159.

[269] S. Droulias and L. Bougas: *Absolute Chiral Sensing in Dielectric Metasurfaces Using Signal Reversals.* Nano Letters **20**, 5960–5966 (2020),
Cit. on p. 92.

[270] J. Lasa-Alonso, D. R. Abujetas, l. Nodar, J. A. Dionne, J. J. Sáenz, G. Molina-Terriza, J. Aizpurua, and A. García-Etxarri: *Surface-Enhanced Circular Dichroism Spectroscopy on Periodic Dual Nanostructures.* ACS Photonics **7**, 2978–2986 (2020),
Cit. on p. 92.

[271] J. Feis, D. Beutel, J. Köpfler, X. Garcia-Santiago, C. Rockstuhl, M. Wegener, and I. Fernandez-Corbaton: *Helicity-Preserving Optical Cavity Modes for Enhanced Sensing of Chiral Molecules.* Phys. Rev. Lett. **124**, 033201 (2020), Cit. on pp. 92, 111, 159.

[272] P. Scott, X. Garcia-Santiago, D. Beutel, C. Rockstuhl, M. Wegener, and I. Fernandez-Corbaton: *On enhanced sensing of chiral molecules in optical cavities.* Applied Physics Reviews **7**, 041413 (2020), Cit. on pp. 92, 94, 111, 159.

[273] D. Beutel, P. Scott, M. Wegener, C. Rockstuhl, and I. Fernandez-Corbaton: *Enhancing the optical rotation of chiral molecules using helicity preserving all-dielectric metasurfaces.* Applied Physics Letters **118**, 221108 (2021), Cit. on pp. 92, 111, 159.

[274] A. O. Govorov, Y. K. Gun'ko, J. M. Slocik, V. A. Gérard, Z. Fan, and R. R. Naik: *Chiral nanoparticle assemblies: circular dichroism, plasmonic interactions, and exciton effects.* J. Mater. Chem. **21**, 16806–16818 (2011), Cit. on p. 92.

[275] A. Ben-Moshe, B. M. Maoz, A. O. Govorov, and G. Markovich: *Chirality and chiroptical effects in inorganic nanocrystal systems with plasmon and exciton resonances.* Chem. Soc. Rev. **42**, 7028–7041 (2013), Cit. on p. 92.

[276] M. Hentschel, M. Schäferling, X. Duan, H. Giessen, and N. Liu: *Chiral plasmonics.* Science Advances **3**, e1602735 (2017), Cit. on p. 92.

[277] M. Qiu, L. Zhang, Z. Tang, W. Jin, C.-W. Qiu, and D. Lei: *3D Metaphotonic Nanostructures with Intrinsic Chirality.* Advanced Functional Materials **28**, 1803147 (2018), Cit. on p. 92.

[278] M. L. Solomon, A. A. E. Saleh, L. V. Poulikakos, J. M. Abendroth, L. F. Tadesse, and J. A. Dionne: *Nanophotonic Platforms for Chiral Sensing and Separation.* Accounts of Chemical Research **53**, 588–598 (2020), Cit. on p. 92.

[279] Z. Cao, H. Gao, M. Qiu, W. Jin, S. Deng, K.-Y. Wong, and D. Lei: *Chirality Transfer from Sub-Nanometer Biochemical Molecules to Sub-Micrometer Plasmonic Metastructures: Physiochemical Mechanisms, Biosensing, and Bioimaging Opportunities.* Advanced Materials **32**, 1907151 (2020), Cit. on pp. 92, 94.

[280] A. Kakkanattu, N. Eerqing, S. Ghamari, and F. Vollmer: *Review of optical sensing and manipulation of chiral molecules and nanostructures with the focus on plasmonic enhancements [Invited].* Opt. Express **29**, 12543–12579 (2021), Cit. on p. 92.

[281] S. A. Tretyakov, F. Mariotte, C. R. Simovski, T. G. Kharina, and J. Heliot: *Analytical antenna model for chiral scatterers: comparison with numerical and experimental data.* IEEE Transactions on Antennas and Propagation **44**, 1006–1014 (1996),
Cit. on pp. 93, 103.

[282] C. Rockstuhl, C. Menzel, T. Paul, and F. Lederer: *Optical activity in chiral media composed of three-dimensional metallic meta-atoms.* Phys. Rev. B **79**, 035321–1–5 (2009),
Cit. on pp. 93, 103.

[283] C. Helgert, E. Pshenay-Severin, M. Falkner, C. Menzel, C. Rockstuhl, E.-B. Kley, A. Tünnermann, F. Lederer, and T. Pertsch: *Chiral Metamaterial Composed of Three-Dimensional Plasmonic Nanostructures.* Nano Letters **11**, 4400–4404 (2011),
Cit. on pp. 93, 103.

[284] I. Sakellari, X. Yin, M. L. Nesterov, K. Terzaki, A. Xomalis, and M. Farsari: *3D Chiral Plasmonic Metamaterials Fabricated by Direct Laser Writing: The Twisted Omega Particle.* Advanced Optical Materials **5**, 1700200 (2017),
Cit. on pp. 93, 103.

[285] S. Lee, S. Yoo, and Q.-H. Park: *Microscopic Origin of Surface-Enhanced Circular Dichroism.* ACS Photonics **4**, 2047–2052 (2017),
Cit. on p. 94.

[286] M. L. Nesterov, X. Yin, M. Schäferling, H. Giessen, and T. Weiss: *The role of plasmon-generated near fields for enhanced circular dichroism spectroscopy.* ACS Photonics **4**, 578–583 (2016),
Cit. on pp. 94, 97, 99, 107, 108, 111.

[287] M. Onishi, K. Crabtree, and R. A. Chipman: *Formulation of rigorous coupled-wave theory for gratings in bianisotropic media.* J. Opt. Soc. Am. A **28**, 1747–1758 (2011),
Cit. on p. 94.

[288] V. Klimov, I. Zabkov, A. Pavlov, and D. Guzatov: *Eigen oscillations of a chiral sphere and their influence on radiation of chiral molecules.* Opt. Express **22**, 18564–18578 (2014),
Cit. on p. 94.

[289] W. Zhang, T. Wu, R. Wang, and X. Zhang: *Surface-Enhanced Circular Dichroism of Oriented Chiral Molecules by Plasmonic Nanostructures.* The Journal of Physical Chemistry C **121**, 666–675 (2017),
Cit. on pp. 94, 95.

[290] A. O. Govorov and Z. Fan: *Theory of Chiral Plasmonic Nanostructures Comprising Metal Nanocrystals and Chiral Molecular Media.* ChemPhysChem **13**, 2551–2560 (2012),
Cit. on p. 94.

[291] M. Schäferling and H. Giessen: *Comment on "Enantioselective Optical Trapping of Chiral Nanoparticles with Plasmonic Tweezers"*. ACS Photonics **5**, 2533–2534 (2018),
Cit. on p. 97.

[292] J. K. Gansel, M. Thiel, M. S. Rill., M. Decker, K. Bade, V. Saile, G. von Freymann, S. Linden, and M. Wegener: *Gold helix photonic metamaterial as broadband circular polarizer*. Science **325**, 1513–1515 (2009),
Cit. on p. 103.

[293] J. Kaschke and M. Wegener: *Gold triple-helix mid-infrared metamaterial by STED-inspired laser lithography*. Opt. Lett. **40**, 3986–3989 (2015),
Cit. on p. 103.

[294] Y. Tang and A. E. Cohen: *Enhanced Enantioselectivity in Excitation of Chiral Molecules by Superchiral Light*. Science **332**, 333–336 (2011),
Cit. on p. 108.

[295] J. N. Farahani, D. W. Pohl, H.-J. Eisler, and B. Hecht: *Single Quantum Dot Coupled to a Scanning Optical Antenna: A Tunable Superemitter*. Phys. Rev. Lett. **95**, 017402 (2005),
Cit. on pp. 114, 156.

[296] S. Kühn, U. Håkanson, L. Rogobete, and V. Sandoghdar: *Enhancement of Single-Molecule Fluorescence Using a Gold Nanoparticle as an Optical Nanoantenna*. Phys. Rev. Lett. **97**, 017402 (2006),
Cit. on pp. 114, 156.

[297] P. Anger, P. Bharadwaj, and L. Novotny: *Enhancement and Quenching of Single-Molecule Fluorescence*. Phys. Rev. Lett. **96**, 113002 (2006),
Cit. on pp. 114, 156.

[298] M. Ringler, A. Schwemer, M. Wunderlich, A. Nichtl, K. Kürzinger, T. A. Klar, and J. Feldmann: *Shaping Emission Spectra of Fluorescent Molecules with Single Plasmonic Nanoresonators*. Phys. Rev. Lett. **100**, 203002 (2008),
Cit. on pp. 114, 120.

[299] R. Chikkaraddy, B. de Nijs, F. Benz, S. J. Barrow, O. A. Scherman, E. Rosta, A. Demetriadou, P. Fox, O. Hess, and J. J. Baumberg: *Single-molecule strong coupling at room temperature in plasmonic nanocavities*. Nature **535**, 127–130 (2016),
Cit. on pp. 114, 156.

[300] P. W. K. Rothemund: *Folding DNA to create nanoscale shapes and patterns*. Nature **440**, 297–302 (2006),
Cit. on p. 115.

[301] S. M. Douglas, H. Dietz, T. Liedl, B. Högberg, F. Graf, and W. M. Shih: *Self-assembly of DNA into nanoscale three-dimensional shapes*. Nature **459** (2009),
Cit. on p. 115.

[302] B. Saccà and C. M. Niemeyer: *DNA Origami: The Art of Folding DNA*. Angewandte Chemie International Edition **51**, 58–66 (2012),
Cit. on p. 115.

[303] A. Kuzyk, R. Jungmann, G. P. Acuna, and N. Liu: *DNA Origami Route for Nanophotonics*. ACS Photonics **5**, 1151–1163 (2018),
Cit. on p. 116.

[304] S. Nummelin, B. Shen, P. Piskunen, Q. Liu, M. A. Kostiainen, and V. Linko: *Robotic DNA Nanostructures*. ACS Synthetic Biology **9**, 1923–1940 (2020),
Cit. on pp. 116, 133.

[305] S. Dey, C. Fan, K. V. Gothelf, J. Li, C. Lin, L. Liu, N. Liu, M. A. D. Nijenhuis, B. Saccà, F. C. Simmel, H. Yan, and P. Zhan: *DNA origami*. Nature Reviews Methods Primers **1**, 13 (2021),
Cit. on p. 116.

[306] P. Bharadwaj and L. Novotny: *Spectral dependence of single molecule fluorescence enhancement*. Opt. Express **15**, 14266–14274 (2007),
Cit. on pp. 116, 118.

[307] T. H. Taminiau, F. D. Stefani, and N. F. van Hulst: *Single emitters coupled to plasmonic nano-antennas: angular emission and collection efficiency*. New Journal of Physics **10**, 105005 (2008),
Cit. on p. 117.

[308] S. V. Lobanov, T. Weiss, D. Dregely, H. Giessen, N. A. Gippius, and S. G. Tikhodeev: *Emission properties of an oscillating point dipole from a gold Yagi-Uda nanoantenna array*. Phys. Rev. B **85**, 155137 (2012),
Cit. on p. 119.

[309] N. Di Fiori and A. Meller: *The Effect of Dye-Dye Interactions on the Spatial Resolution of Single-Molecule FRET Measurements in Nucleic Acids*. Biophysical Journal **98**, 2265–2272 (2010),
Cit. on pp. 121, 122, 128.

[310] A. Gust, A. Zander, A. Gietl, P. Holzmeister, S. Schulz, B. Lalkens, P. Tinnefeld, and D. Grohmann: *A Starting Point for Fluorescence-Based Single-Molecule Measurements in Biomolecular Research*. Molecules **19**, 15824–15865 (2014),
Cit. on p. 121.

[311] W. L. Barnes: *Fluorescence near interfaces: The role of photonic mode density*. Journal of Modern Optics **45**, 661–699 (1998),
Cit. on p. 121.

[312] J. Lakowicz: *Principles of Fluorescence Spectroscopy*, Springer US (New York), 2007.
Cit. on p. 121.

[313] W. L. Vos, A. F. Koenderink, and I. S. Nikolaev: *Orientation-dependent spontaneous emission rates of a two-level quantum emitter in any nanophotonic environment.* Phys. Rev. A **80**, 053802 (2009),
Cit. on pp. 124, 125.

[314] P. B Johnson and R. W. Christy: *Optical constants of the noble metals.* Phys. Rev. B **6**, 4370–4379 (1972),
Cit. on p. 128.

[315] G. P. Acuna, F. M. Möller, P. Holzmeister, S. Beater, B. Lalkens, and P. Tinnefeld: *Fluorescence Enhancement at Docking Sites of DNA-Directed Self-Assembled Nanoantennas.* Science **338**, 506–510 (2012),
Cit. on p. 131.

[316] S. Bidault, A. Devilez, V. Maillard, L. Lermusiaux, J.-M. Guigner, N. Bonod, and J. Wenger: *Picosecond Lifetimes with High Quantum Yields from Single-Photon-Emitting Colloidal Nanostructures at Room Temperature.* ACS Nano **10**, 4806–4815 (2016),
Cit. on p. 131.

[317] D. Sun, Y. Tian, Y. Zhang, Z. Xu, M. Y. Sfeir, M. Cotlet, and O. Gang: *Light-Harvesting Nanoparticle Core–Shell Clusters with Controllable Optical Output.* ACS Nano **9**, 5657–5665 (2015),
Cit. on p. 131.

[318] R. R. F. Machinek, T. E. Ouldridge, N. E. C. Haley, J. Bath, and A. J. Turberfield: *Programmable energy landscapes for kinetic control of DNA strand displacement.* Nature Communications **5**, 5324 (2014),
Cit. on p. 141.

[319] P. W. Atkins and J. De Paula: *Atkins' physical chemistry*, Tenth edition edition, Oxford University Press (Oxford), 2014.
Cit. on p. 141.

[320] J. A. Gonzaga-Galeana and J. R. Zurita-Sánchez: *A revisitation of the Förster energy transfer near a metallic spherical nanoparticle: (1) Efficiency enhancement or reduction? (2) The control of the Förster radius of the unbounded medium. (3) The impact of the local density of states.* The Journal of Chemical Physics **139**, 244302 (2013),
Cit. on pp. 148, 153.

[321] J. J. Funke and H. Dietz: *Placing molecules with Bohr radius resolution using DNA origami.* Nature Nanotechnology **11**, 47–52 (2016),
Cit. on p. 149.

[322] A. D. Rakić, A. B. Djurišić, J. M. Elazar, and M. L. Majewski: *Optical properties of metallic films for vertical-cavity optoelectronic devices.* Appl. Opt. **37**, 5271–5283 (1998),
Cit. on p. 152.

[323] D. Pfezer, J. Karst, L. Kühner, M. Hentschel, and H. Giessen: *SEIRA Sensing of Different Sugars at Physiological Concentrations*, Conference on Lasers and Electro-Optics, Optica Publishing Group, 2021,
Cit. on p. 159.

[324] E. Corcione, D. Pfezer, M. Hentschel, H. Giessen, and C. Tarín: *Machine Learning Methods of Regression for Plasmonic Nanoantenna Glucose Sensing*. Sensors **22** (2022),
Cit. on p. 159.

ACKNOWLEDGMENTS

At this point, I would like to thank all people who contributed to this thesis as well as everyone who helped and supported me throughout this journey:

- First and foremost, Prof. Dr. Thomas Weiss, for making everything possible, for the constant supply with ideas and suggestions, for the opportunity to learn many things, ranging from nanophotonics to physics in general to paper writing to all aspects of scientific workflow, as well as for all his guidance and for the great supervision over the last five years.
- Prof. Dr. Eric Lutz and Prof. Dr. Carsten Rockstuhl for kindly agreeing to be second supervisor and external reviewer, respectively, and Prof. Dr. Sebastian Loth for offering to be the head of the examination committee.
- Prof. Dr. Harald Giessen, for a lot of helpful input, for teaching me many things about physics and scientific workflow as well, for his constant enthusiasm, and for the fantastic working environment at the 4^{th}-physics institute.
- Prof. Dr. Na Liu and her team, Dr. Max Urban, Dr. Ling Yin, Dr. Pengfei Zhan, and Andreas Peil for the fascinating and highly productive experimental collaboration in the DNA-nanotechnology projects. In this context, I especially want to acknowledge the numerous fruitful discussions with Dr. Max Urban during the initial stages of the collaboration.
- Prof. Dr. Klas Lindfors and his team, Dr. Mo Lu and Dr. Markus Pfeiffer for the experimental cooperation with the DNA-walker project and several related discussions.
- Dr. Martin Schäferling for a lot of valuable input with his expertise on chiral nanophotonics.
- Dr. Egor A. Muljarov for several useful discussions and comments about resonant states.
- Dr. Maxim Nesterov for introducing me to COMSOL Multiphysics and for various tips regarding simulations.

- Dr. Florian Sterl and Tobias Pohl for their fantastic rendering jobs.
- Dr. Christine von Rekowski for the steady help with all sorts of administrative matters.
- All proofreaders of this thesis, namely Dr. Andy Steinman, Lida Shamsafar, Dr. Swaathi Upendar, Paul Ruchka, Dr. Florian Sterl, Dr. Qi Ai, for their valuable comments and corrections.
- All colleagues of the former theory group, Dr. Josselin Defrance, Dr. Swaathi Upendar, Dr. Izzatjon Allayarov (alias "party guy"), and Sascha Böhrkircher, for the great atmosphere, for many physics- and non-physics related discussions, as well as for our numerous activities outside the institute. At this point, I also want to take the opportunity to thank Dr. Swaathi Upendar for 39 cups of coffee.
- The running team, Dr. Mario Hentschel and Simon Ristok, for the enjoyable discussions during our sport activities. The former, I also want to thank for the regular supply with chocolate bars.
- The old PI4 biking group, Dr. Florian Sterl, Dr. Josselin Defrance, Philipp Geser, and Sascha Börkircher, for our adventurous cycling events, as well as the PI4 AOE gang, Dr. Tobias Steinle, Paul Ruchka, Dr. Florian Sterl, etc., for many entertaining Friday nights.
- My former office mates, Dr. Rostyslav Semenyshyn, Sascha Börkircher, and Lida Shamsafar, for the great atmosphere and the incredibly fun time.
- The different lunch groups we had over the years (involving Dr. Qi Ai, Dr. Andy Steinman, Dr. Rostyslav Semenyshyn, Dr. Izzatjon Allayarov, Dr. Josselin Defrance, Dr. Swaathi Upendar, Sascha Böhrkircher, Dr. Florian Sterl, Dr. Asa Asadollahbaik, Ksenia Weber, Simon Mangold, Florian Mangold, Paul Ruchka, Lida Shamsafar, and all others) for countless random discussions as well as many activities beyond physics.
- All current and former institute colleagues for the nice time together.
- Finally, all my friends and family for their constant support over the years.

CURRICULUM VITÆ

NAME	Steffen Both
BORN	October 27, 1990 in Bad Mergentheim
CITIZENSHIP	German
ADDRESS	Unteres Tor 1, 97953 Königheim, Germany
E-MAIL	steffenboth.unistuttgart @gmail.com

2022	Ph.D thesis: "Theory of resonant light-matter interactions in nanophotonic sensing", University of Stuttgart, advisor: Prof. Dr. Thomas Weiss.
2017 - 2022	Research assistant, group of Prof. Dr. Thomas Weiss, 4^{th} Physics Institute and Research Center SCoPE, University of Stuttgart, Germany.
2016	Master thesis: "Fabrication of Plasmonic Metasurfaces for Quantum Optical Experiments", Karlsruhe Institute of Technology (KIT), advisor: Prof. Dr. Martin Wegener.
2015	Industry Internship at TRUMPF Inc.,Farmington, Connecticut, USA.
2013 - 2016	Studies of Optics and Photonics, Karlsruhe Institute of Technology (KIT), Germany; Master of Science.
2013	Bachelor thesis: "Erbium Based Light Emission in Silicon-on-Insulator Waveguides", Karlsruhe Institute of Technology (KIT), advisor: Prof. Dr. Christian Koos.
2010 - 2013	Studies of Electrical Engineering and Information Technology, Karlsruhe Institute of Technology (KIT), Germany; Bachelor of Science.
2001 - 2010	Matthias-Grünewald-Gymnasium Tauberbischofsheim; Allgemeine Hochschulreife.

COLOPHON

This thesis was typeset with LaTeX 2_ε using Robert Slimbach's Minion Pro font. The style was inspired by Robert Bringhurst's "*The Elements of Typographic Style*". It is available for LaTeX via CTAN as CLASSICTHESIS.